

ABSTRACT

LAUGHLIN, BRIAN JAMES. *Sputtered (Ba_x, Sr_{1-x})TiO₃, BST, Thin Films on Flexible Copper Foils for Use as a Non-Linear Dielectric.* (Under the direction of Jon-Paul Maria.)

Ferroelectric thin film dielectrics have a non-linear DC bias dependent permittivity and can be used as the dielectric between metal electrodes to make tunable Metal-Insulator-Metal (MIM) capacitors. Varactors can be used to change the resonance frequency of a circuit allowing high speed frequency switching intra- and inter-band. 2-D geometric arrays of circuitry, where resonant frequency is independently controlled by tunable elements in each section of the array, allow electromagnetic radiation to be focused and the wave front spatial trajectory controlled. BST thin films varactors allow large DC fields to be applied with modest voltages providing large tunabilities. If ferroelectric thin film based devices are to compliment or supplant semiconductor varactors as tunable elements then devices must be synthesized using a low cost processing techniques.

The Film on Foil process methodology for depositing BST thin films on copper foil substrates was used to create BST/Cu specimens. Sputtering conditions were determined via BST deposition on platinized silicon. Sputtered BST thin films were synthesized on Cu foil substrates and densified using high T , controlled pO_2 anneals. XRD showed the absence of Cu_2O in as-deposited, post crystallization annealed, and post “re-ox” annealed state. Data showed a polycrystalline BST microstructure with a 55 - 80 nm grain size and no copper oxidation. HRTEM imaging qualitatively showed evidence of an abrupt BST/Cu interface free from oxide formation. Dielectric properties of Cu/BST/Pt MIM devices were measured as a function of DC bias, frequency, and temperature. A permittivity of 725 was observed with tunability >3:1 while zero bias $\tan \delta$ of 0.02 saturating to $\tan \delta < 0.003$ at high DC bias. No significant frequency dispersion was observed over five decades of frequency. Temperature dependent measurements revealed a broad ferroelectric transition with a maximum at -32 °C which sustains a large tunability over -150 °C to 150 °C. Sputtered BST thin films on copper foils show comparable dielectric properties to CVD deposited films on platinized silicon substrates

proving sputtered BST/Cu specimens can reproduce excellent properties using a more cost-effective processing approach.

A concept for reducing the temperature dependence was explored. Stacks of multiple compositions of BST thin films were considered as an extension of core-shell structures to a thin film format. Temperature profiles of BST/Cu films were modeled and mathematically combined in simulations of multi-composition film stacks. Simulations showed singular composition BST thin films could meet X7R specifications if a film has a $292 \text{ K} < T_C < 330 \text{ K}$. Simulations of series connected film stacks show only modest temperature profile broadening. Parallel connected dual composition film stacks showed a $75 \text{ }^\circ\text{C}$ temperature range with essentially flat capacitance by simulating compositions that create a $\Delta T_C = 283 \text{ }^\circ\text{C}$. Maximum permittivity and temperature profile shape independent of film thickness or composition were assumed for simulations. BST/Cu thickness and compositions series were fabricated and dielectric properties characterized. These studies showed films could be grown from 300 nm and approaching 1 μm without changing the dielectric temperature response. In studying BST composition, an increasing T_C shift was observed when increasing Ba mole fraction in BST thin films while tunability $>3:1$ was maintained. These results provide a route for creating temperature stable capacitors using a BST/Cu embodiment.

An effort to reduce surface roughness of copper foil substrates adversely impacted BST film integrity by impairing adhesion. XPS analysis of high surface roughness commercially obtained Cu foils revealed a surface treatment of Zn-Cu-O that was not present on smooth Cu, thus an investigation of surface chemistry was conducted. Sessile drop experiments were performed to characterize Cu-BST adhesion and the effects of metallic Zn and ZnO in this system. The study revealed the work of adhesion of Cu-BST, $W_a^{\text{Cu-BST}} \approx 0.60 \text{ J m}^{-2}$, an intermediate value relative to noble metals commonly used as electrodes and substrates for electroceramics. Examination of metallic Zn-BST adhesion revealed a dramatic decrease of $W_a^{\text{Zn-BST}} \approx 0.13 \text{ J m}^{-2}$, while increasing the content of Zn in metallic $(\text{Cu}_x\text{Zn}_{1-x})$ alloys monotonically reduced $W_a^{(\text{Cu}_x\text{Zn}_{1-x})\text{-BST}}$. Conversely, a Cu-ZnO interface showed a large work of adhesion, $W_a^{\text{Cu-ZnO}} = 2.0 \text{ J m}^{-2}$. These results indicate that a ZnO interlayer between the substrate Cu and the BST thin film provides adequate

adhesion for robust films on flexible copper foil substrates. Additionally, this study provided characterization of adhesion for Zn-Al₂O₃ and Zn-BST; data that does not exist in the open literature.

A process has been developed for preparing ultra-smooth copper foils by evaporation and subsequent peel-off of copper metal layers from glass slides. These 15 μm thick substrates exhibited roughness values between 1 and 2 nm RMS and 9 nm RMS over 25 μm^2 and 100 μm^2 analysis areas, respectively. The deposition and crystallization of BST layers on these ultra-smooth foils is demonstrated. The fully processed dielectric layers exhibited field tunability >5:1, and could withstand fields >750 kV cm⁻¹. High field loss tangents below 0.007 were observed, making these materials excellent candidates for microwave devices. Finally, a process of lamination and contact lithography was used to demonstrate patterning of micron-scale features suitable for microwave circuit element designs.

**SPUTTERED (BA_x, SR_{1-x})TiO₃, BST, THIN FILMS ON FLEXIBLE
COPPER FOILS FOR USE AS A NON-LINEAR DIELECTRIC**

By:

BRIAN JAMES LAUGHLIN

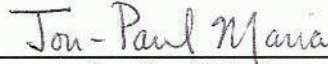
A dissertation submitted to the Graduate Faculty
of North Carolina State University
in partial fulfillment of the requirements for the
Degree of Doctor of Philosophy

MATERIALS SCIENCE AND ENGINEERING

Raleigh

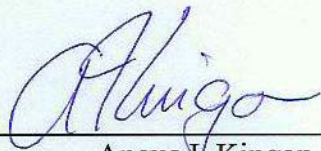
2006

APPROVED BY:



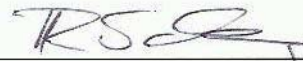
Jon-Paul Maria

Associate Professor of Materials Science & Engineering
Chair of Advisory Committee



Angus V. Kingon

Professor of Materials Science &
Engineering



Raoul Schlessler

Research Associate Professor
of Materials Science & Engineering



Michael B. Steer

Lampe Professor of Electrical &
Computer Engineering



Alexei Gruverman

Research Associate Professor
of Materials Science & Engineering

DEDICATION

To my wife,

Harmony Ann Laughlin

BIOGRAPHY

Brian James Laughlin was born February 6, 1977 to parents Richard and Patricia Laughlin in Englewood, NJ. At age 12 and raised Yankee, he moved to the northern most part of the Deep South, suburbs of Richmond, VA. While surviving indoctrination into southern culture, he received a degree from Atlee HS in 1995. Dreams of playing collegiate soccer were quashed by 4 broken foot injuries, which he believes stunted his growth to 5' 8" whereas all other Laughlin males are 6'+. Instead, Brian nurtured his second love, science, by enrolling in the Department of Materials Science & Engineering at North Carolina State University. While at NC State, he was mentored by Dr. Jerome Cuomo learning thin film sputter deposition. During a sabbatical, he interned at Intel, AZ and learned the excitement and stress of semiconductor fabs. While attending school, he interned in IBM's Personal Computing Division analyzing failure computer components. During his senior design project on DuPont 951 Green Tape, Brian met Harmony McLean who later agreed to marry him. Brian graduated with a Bachelor of Science from NC State in 2000. After graduation, he accepted a position as a TEM/FIB microscopist at IBM Microelectronics in Vermont. Although the extreme winters did not bother him, the small town atmosphere did, and in strangely fortunate circumstances he was laid off from IBM in June of 2002. Although the semiconductor business instability halted his career, this provided an opportunity to return to school and pursue a graduate degree. Dr. Jon-Paul Maria of NC State extended an offer to return to Raleigh where he began research into high-K gate dielectrics. Funding was short lived and his research switched focus to ferroelectric thin films. This avoided loathsome interaction with a MBE in a cleanroom, allowing him to help build Prof. Maria's laboratory. Brian received his Masters of Materials Science & Engineering in May 2005 and his Doctor of Philosophy in October 2006 from North Carolina State University. After receiving his Ph.D., he accepted a research scientist position with the DuPont Microelectronics Division. During his career at DuPont, he hopes to oversee the continuation of his thesis research as it grows into a commercial enterprise while exploring the intricacies of glass science.

ACKNOWLEDGEMENTS

First I would like to thank my wife, Harmony Laughlin, for untiring support and ultimate patience. She has held me up when I needed fortitude and comforted me in my most trying times. Not the least of her contributions to this work, was acting as my editor. Without her help, I would never have achieved what I have.

I would like to express extreme gratitude to my advisor, Prof. Jon-Paul Maria, for his tutelage. Four years ago I possessed only a cursory understanding of ferroelectrics, and only through Prof. Maria's help and teachings this work was possible. Prof. Maria gave me the freedom to allow my curiosity to direct my research. The knowledge of equipment building Prof. Maria instilled in me is art that not many graduate students have the pleasure of learning and is as valuable as the scientific knowledge I gained.

Dr. Jon Ihlefeld was a constant companion and colleague. Since we started and finished our thesis work at almost the same time, we had many invaluable discussions about theory and results. He, along with Prof. Maria, was always available to imbibe a few (maybe more than a few) fermented beverages in celebration, or relief of frustration. Mark Losego and I had more conversations about the chemistry of sol-gel than I ever asked for, but I appreciated his excitement for research in every exchange. The rest of the research group: Dr. Charles Parker, Dr. Taeyun Kim, Dr. Dipankar Ghosh, Alisa Hunt-Lowery, Leslie Jimison, Spalding Craft, Seymen Aygun, Peter Lam, Patrick Daniel, Erin Gross, and Michele Casper helped make my graduate school experience remarkable.

Dr. Baxter Moody, Dr. Rafael Dalmau, Dr. Raoul Schlessler, and Dr. Dave Cann provided invaluable help with sessile drop experiments. Spalding Craft and Ramón Callazo offered their expertise through XPS characterization when needed.

I would like to thank the Earth Science Technology Office of NASA Goddard who provided funding in a collaborative effort between North Carolina State, The Pennsylvania State University, and QorTek, Inc. that supported this work. Additionally, I would like to thank Dr. Bill Borland of DuPont Microelectronics for providing financial support while consulting about the needs for high volume manufacturing.

TABLE OF CONTENTS

List of Tables	viii
List of Figures.....	x
List of Terms	xxii
1. Introduction.....	1
1.1. Statement of Purpose.....	3
2. Literature Review.....	4
2.1. Dielectric Materials	4
2.2. Ferroelectric/Paraelectric Materials	10
2.2.1. Polar dielectrics	10
2.2.2. Pyroelectricity.....	12
2.2.3. Piezoelectricity.....	12
2.3. Ferroelectricity	13
2.3.1. Historical perspective of ferroelectric materials	13
2.3.2. Theory of ferroelectricity	14
2.3.3. Ferroelectric phase transition	21
2.4. Paraelectric Behavior	23
2.4.1. Non-linear dielectric response in the paraelectric regime	24
2.4.2. Losses in the paraelectric regime	26
2.5. Barium Titanate- Strontium Titanate Solid Solutions.....	31
2.5.1. Bulk BST properties	31
2.6. BST Thin Films.....	35
2.6.1. Finite size and scaling effects	35
2.6.2. BST thin film properties	36
2.7. BST Defect Chemistry	38
2.8. Sputter Deposition.....	41
2.8.1. Historical perspective of sputter deposition	41
2.8.2. Fundamentals of sputtering in a DC glow discharge	41
2.8.3. Sputtering in radio-frequency discharges.....	46
2.9. Base metals and Perovskite Oxides.....	48
2.10. Thin Film Adhesion	52
2.10.1. Sessile drop technique for quantifying adhesion	54
2.10.2. Liquid metal alloy adhesion.....	60

3. Experimental Procedures: Sputtered Film on Foil Methodology.....	64
3.1. Copper Foil Substrates	64
3.2. Sputter Deposition Equipment	66
3.3. Sputter Deposition Process.....	71
3.4. Low pO_2 , High Temperature Anneals	75
3.5. Re-oxidation Anneals	78
3.6. Device Definition	80
3.7. Physical Characterization	82
3.8. Electric Characterization	84
3.9. Experimental Procedure Summary.....	87
4. Processing - Structure - Property Relationships: Sputtered BST Thin Films on Copper Foil Substrates	88
4.1. Sputter Deposited BST Thin Film on Platinized Silicon	89
4.2. Sputter Deposited BST Thin Film on Cu Foils	93
4.2.1. <i>BST/Cu physical characterization</i>	93
4.2.2. <i>Dielectric properties of BST/Cu</i>	104
4.3. Sputtered Film on Foil Methodology Summary	112
5. Multi-Composition Stacked Films: Route to Mitigate TCC	114
5.1. Multi-Composition TCC Modeling.....	116
5.1.1. <i>Optimized BST Composition</i>	117
5.2. Temperature Profile Simulations	119
5.2.1. <i>Series connected dual composition composite simulations</i>	120
5.2.2. <i>Parallel connected dual composition composite simulations</i>	124
5.2.3. <i>Multi-composition composite temperature profiles simulations</i>	127
5.2.4. <i>Temperature profile simulations summary</i>	128
5.3. Dependence of Thickness & Composition.....	129
5.4. Dielectric Properties as a Function of Thickness	130
5.4.1. <i>Film growth of thickness series</i>	130
5.4.2. <i>Physical characterization of thickness series</i>	131
5.4.3. <i>Dielectric properties as a function of thickness</i>	134
5.4.4. <i>Thickness series summary</i>	138
5.5. Dielectric Properties as a Function of Composition.....	139
5.5.1. <i>Film growth of composition series</i>	139
5.5.2. <i>BST thin film composition</i>	139
5.5.3. <i>Dielectric properties as a function of composition</i>	142
5.5.4. <i>Composition series summary</i>	146
5.6. Summary	146

6. Adhesion in the BST/Cu System	148
6.1. Analysis of Commercial/Conventional Cu Foil Substrates.....	151
6.2. Experimental Setup for Contact Angle Measurement.....	152
6.3. Adhesion of Pure Copper & Zinc to Alumina.....	160
6.4. Adhesion of Pure Copper & Zinc to BST	162
6.5. Adhesion of (Cu _x , Zn _{1-x}) to BST	166
6.6. Adhesion of Copper to ZnO	169
6.7. Summary and Conclusions.....	170
7. Lithography-Compatible Copper Foil Substrates	173
7.1. UltraFoil Synthesis.....	173
7.2. UltraFoil/Zn/BST Thickness Dependences.....	176
7.3. BST Thin Film Properties on UltraFoil Substrates	179
7.4. Photolithographic Patterning & Device Definition.....	182
7.5. Conclusion.....	186
8. Conclusions and Future Work.....	187
8.1. Conclusions	187
8.2. Future work	189
9. Bibliography	191
Appendices.....	213
A. Certificate of Analysis for BST sputter targets	214
B. Phase Diagrams	215
C. Powder Diffraction Files	218
D. Reox Study <i>C-V</i> Results.....	229
E. BST-UltraFoil Thickness Study: Raw <i>C-V</i> Data.....	232

LIST OF TABLES

Table 2.1: List of polar point groups	10
Table 2.2: Curie groups defining the symmetry of morphology and applied field. The notation is given with the corresponding geometric representation and examples of representative situation displaying the symmetry. Curie groups with requiring handedness are not included as do not apply to this thesis.....	11
Table 2.3: List of room temperature ionic radii pertinent to this these taken from the tabulations of Shannon. ^{27, 28} The ions of barium strontium titanate are included along with those of zinc to be referenced in the adhesion sections of this thesis.	16
Table 3.1: World mine production and cost of noble metals and copper according the Minerals Commodity Summaries 2006 published by the U.S Department of the Interior and U.S. Geological Survey. ²²³	66
Table 3.2: Optimized sputter deposition conditions.	73
Table 6.1: Experimental conditions used for all wetting experiments.....	159
Table 6.2: Contact angle and W_a values measured by sessile drop experiments for pure Cu on alumina (sapphire and polycrystalline Al_2O_3). Cu- Al_2O_3 values are compared to those found in the literature for 1100 °C, $\sim 10^{-19}$ atm pO_2 . ^{189, 199}	161
Table 6.3: Measured contact angle and W_a of Cu and Zn on alumina substrates. Values for other common BST electrode metals are given from the literature. ^{209, 211}	162
Table 6.4: Measured contact angle and W_a of Cu and Zn on BST/ Al_2O_3 substrates. Values for Cu on polished bulk $BaTiO_3$ substrates are given from the literature. ^{206, 208}	165
Table 6.5: Adhesion measurements of Cu on three ceramic substrates measured at 1100 °C while flowing 5% H_2 (balance N_2) forming gas.	170
Table A.1: Measured impurity levels in raw powders to make BST sputter targets. Values are reported by the manufacturer.	214

Table C.1: Powder diffraction file for FCC Cu.	218
Table C.2: Powder diffraction file for copper oxide, Cu ₂ O.	218
Table C.3: Powder diffraction file for copper oxide, CuO.	219
Table C.4: Powder diffraction file for perovskite barium titanate.	220
Table C.5: Powder diffraction file for perovskite strontium titanate.	221
Table C.6: Powder diffraction file for perovskite barium strontium titanate, (Ba _{0.5} , Sr _{0.5})TiO ₃	222
Table C.7: Powder diffraction file for corundum alumina.	222
Table C.8: Powder diffraction file for reaction product of strontium oxide and alumina.	223
Table C.9: Powder diffraction file for reaction product of strontium titanate and alumina.	225
Table C.10: Powder diffraction file for hexagonal metallic zinc.	227
Table C.11: Powder diffraction file for zinc oxide.	227

LIST OF FIGURES

Figure 2.1: Schematic of parallel electrodes separated by a dielectric material. Shown are individual dipoles with their dipole moments and polarization and applied electric field vectors.	4
Figure 2.2: Theoretical frequency dispersion for a dielectric showing all possible polarization mechanisms and the expected frequencies for their relaxation.....	8
Figure 2.3: Parallel plate capacitor configuration.....	9
Figure 2.4: Schematic representation of a perovskite unit cell. Lattice positions of the ions comprising BST are labeled in the figure.....	15
Figure 2.5: Schematic of a model 2-D polarized lattice. Red spheres are anions and blue spheres are cations. The dashed line represents a domain wall where above this the polarization is horizontal to the left and below horizontal to the right.	17
Figure 2.6: Schematic of the double potential well which describes the equilibrium position of cations relative to the anions in the model 2-D polarized lattice. The energy barrier, ΔE , is on the order of eE_C allowing for polarization reversal when $\bar{E} \geq eE_C$ is applied.....	18
Figure 2.7: Characteristic hysteresis loops for a) a ceramic ferroelectric (blue) and b) single crystal, mono-domain ferroelectric (red).	19
Figure 2.8: Non-linear dielectric response with respect to biasing field. In the ferroelectric phase the response is hysteretic with the peak permittivity, or capacitance, occurring at the coercive field, E_C	20
Figure 2.9: Temperature response of permittivity for a single crystal mono-domain ferroelectric crystal.	21
Figure 2.10: P - E loops in the paraelectric phase and the corresponding ϵ - E curve (dotted line represents $\tan \delta$).	25
Figure 2.11: Experimental data for the temperature dependence the 3-quantum loss mechanism in SrTiO_3 . Figure is adapted from Tagantsev et al ³⁸ based on data from Buzin. ⁴²	28

Figure 2.12: Figure adapted from Tagantsev et al.³⁸ Plot a) gives a schematic comparison between 1) 3 quantum interactions, 2) 4 quantum interactions and 3) quasi-Debye contributions to loss. Plot b) gives the calculated functional dependence and magnitude of the quasi-Debye loss for paraelectric Ba_{0.6}Sr_{0.4}TiO₃ tested at 300K and 1 GHz (actual data from Sengupta et al⁴³)..... 29

Figure 2.13: ϵ - E curve where the response in the grey area is due to extrinsic contributions to permittivity and loss and regions outside of the grey area the intrinsic response can be observed. 30

Figure 2.14: Smolenskii's data showing the linear ferroelectric transition temperature shift with increasing mole percent SrTiO₃. Although it appears that maximum permittivity increases near equimolar ratios of BaTiO₃ and SrTiO₃, no data on microstructure is given.⁶⁵ 34

Figure 2.15: Schematic drawing of a typical DC plasma device..... 42

Figure 2.16: Dielectric properties of PZT film on metal substrates of titanium (Ti), brass (BR), and stainless steel (SS).¹⁶⁷ 51

Figure 2.17: Diagram of a liquid drop contacting a solid surface surrounded by a vapor. The contact angle, Θ , at the 3 phase triple point is determined by a balance of the two phase surface energies. 54

Figure 2.18: Contact angle versus oxygen activity for metal-oxide systems reported in the open literature. At low oxygen activity large contact angles predominate giving low work of adhesion and “non-wetting” behavior. At large oxygen activity low contact angles are observed since work of adhesion is large and reaction layer formation leads to wetting behavior..... 56

Figure 2.19: Data for Cu-Al₂O₃(sapphire) reported by Ghetta as a function of oxygen activity at 1365 K. a) At oxygen activity $> 10^{-6}$ the contact angle discontinuously reduces and (not shown) the surface tension of liquid copper linearly decreases. b) At this critical oxygen activity a discontinuous jump in work of adhesion is observed followed by a linear decrease in work of adhesion with increasing oxygen activity.¹⁹⁹ 57

Figure 2.20: Wulff plot equilibrium crystallite shape and anisotropy in crystallite surface energy. The equilibrium facets are changed by the existence of an interface with a rigid substrate of surface energy $\gamma_{substrate}$ to create an interface of surface energy $\gamma_{interface}$.	59
Figure 3.1: Top: 3-D rendering of 10 μm X 10 μm AFM scan. Bottom left: 2-D AFM data over 5 μm X 5 μm . Bottom right: 2-D AFM data over 20 μm X 20 μm .	65
Figure 3.2: Diagram showing the important features of the sputter system used for BST thin film deposition. Blue labels are used for clarification for the discussion of the system and its operation.	67
Figure 3.3: Detailed diagram of the sputter gun. The entire gun is oriented 30° from the substrate normal and an 8.5 cm center to center distance of the target to the substrate. Also highlighted are the magnetic field lines with respect to the target surface. The electrical connections show how the target is isolated from the grounding shield which is at common ground with the substrate stage via the chamber walls.	69
Figure 3.4: A singular 1" X 2" copper foil clamped in a stainless steel frame.	72
Figure 3.5: $p\text{O}_2$ - T phase diagram for the Cu - BST system. Gray area shows the set of process conditions to maintain metallic copper in equilibrium with molecular oxygen and oxidized BST cations.	76
Figure 3.6: Schematic diagram of the crystallization furnace showing the gas delivery system and the position of the <i>in situ</i> oxygen sensor.	77
Figure 3.7: Schematic diagram of the sealed vacuum furnace used for re-ox anneals.	79
Figure 3.8: Calibrated optical image (taken at 100X) of sputtered top Pt electrodes defined by a shadow mask.	81
Figure 4.1: XRD of a 250 nm thick BST film on platinized silicon. In the as-deposited state (green) peaks corresponding to the substrate platinum and intensity from the amorphous film are identifiable. After 650 °C 30 min. air anneal (blue) reflections from the BST perovskite phase can be seen peaks of Pt and BST with peaks for the platinum substrate and the zirconia adhesion layer between the Pt and Si.	90
Figure 4.2: Room temperature permittivity and loss versus DC bias field measured at 100 kHz with 4 kV cm ⁻¹ oscillation level on a Pt/BST/Pt MIM device.	91

Figure 4.3: Room temperature dielectric constant and loss frequency dispersion data measured with 4 kV cm^{-1} oscillation level on a Pt/BST/Pt MIM device.....	92
Figure 4.4: XRD data for an as-deposited 800 nm thick $(\text{Ba}_{0.6}, \text{Sr}_{0.4})\text{TiO}_3$ film. Guidelines show the exact 2θ peak position and peak height according to the JCPDS PDF card. Note no reflections from the most likely copper oxide phase, cuprite Cu_2O . The vertical solid lines are given as guides to the expected peak position and intensities given by the powder diffraction cards.	94
Figure 4.5: XRD data for the crystallized sample (blue solid line). The data is displayed above the data shown in figure 4.4 (blue dotted line) to exemplify the increase in peak intensity for perovskite $(\text{Ba}_{0.6}, \text{Sr}_{0.4})\text{TiO}_3$. The vertical solid lines are given as guides to the expected peak position and intensities given by the powder diffraction cards.	95
Figure 4.6: XRD data for the same sample shown in figures 4.4 and 4.5 yet after a “re-ox” anneal of $550 \text{ }^\circ\text{C}$, $10^{-8} \text{ atm } p\text{O}_2$ for 30 min. (blue solid line). The data is displayed above the data shown in figure 4.4 for the as-deposited state (gray dotted line) and figure 4.5 for the crystallized state (blue dotted line) to show there is no change in crystallinity and no formation of copper oxide when the sample is subjected to a “re-ox” anneal. The vertical solid lines are given as guides to the expected peak position and intensities given by the powder diffraction cards.	96
Figure 4.7: a) XRD area image of an as-deposited 800 nm BST film showing out-of-plane $\{111\}$ texturing and diffuse, low diffracted intensity. b) XRD area image of a fully processed 800 nm BST film showing narrow out-of-plane $\{111\}$ textured diffraction intensity. The Cu $\{111\}$ reflection goes from intensity consistent with fine grained microstructure to discrete spots after annealing indicating substantial copper grain growth.	98
Figure 4.8: BF TEM taken at 120 kX. The copper substrate was mostly removed during specimen preparation yet still can partially be seen in the lower right of the image. See the DF TEM image in figure 4.9 for more detail.....	99

Figure 4.9: DF TEM using the $\{111\}$, $\{110\}$, $\{002\}$, and $\{102\}$ reflections (see the SAD diffraction image in figure 4.10) taken at 80 kX. The majority of the copper was removed by the ion milling yet still can be seen in the lower right of each image. Show in the complimentary images is a fine grained polycrystalline region adjacent to the copper substrate and a columnar $\{111\}$ textured region for the remaining film thickness.....	99
Figure 4.10: Indexed SAD pattern taken at 60 cm camera length. The shaded region shows the approximate position of the objective aperture position for the DF image shown in figure 4.9.	100
Figure 4.11: Topographical AFM data of a fully processed 800 nm thick BST film.	101
Figure 4.12: HRTEM image of the BST/Cu interface. Arrows highlight the position of the interface. Both sides of the interface have multiple grains with random orientation making simultaneous zone axis alignment impossible. Evident from the image is an abrupt BST/Cu absent of interfacial phases.	102
Figure 4.13: AFM of polished cross section. The substrate copper is on the left side of the image and the silicon support on the right. The BST thin film is mated directly to the copper and epoxy is seen between the BST film and the silicon.	103
Figure 4.14: Uncalibrated BF TEM image of a BST/Cu film sputtered for 120 min. digitally captured at 590kX.	104
Figure 4.15: Room temperature DC bias dependent permittivity measurement taken at 100 kHz and 1.25 kV cm^{-1} oscillation field for a fully processed 800 nm thick BST thin film deposited on copper foil.	105
Figure 4.16: Room temperature permittivity frequency dispersion measurement taken at 0 V DC bias and 1.25 kV cm^{-1} oscillation field for a fully processed 800 nm thick BST thin film deposited on copper foil.	107
Figure 4.17: Permittivity (solid blue line) and $\tan \delta$ (dotted blue line) as a function of temperature. Measurements were conducted from 100 K to 500 K using 10 kHz and a 1.25 kV cm^{-1} oscillation field. The maximum permittivity occurs at approximately $-32 \text{ }^\circ\text{C}$	108

Figure 4.18: 0 V to 10 V tunability measured at discrete temperatures at 10 kHz and 1.25 kV cm^{-1} . Tunability is maximized at the temperature where permittivity peaks, $-32 \text{ }^\circ\text{C}$, yet remains greater than 1½:1 over the entire temperature range. The ultimate tunability is substantially greater than displayed here since measurements were not extended to DC biases that reached saturation. 109

Figure 4.19: Eighteen individual DC leakage current measurements along an arbitrary row of MIM capacitors on one BST/Cu sample. No dead shorts were observed during the experiment and all data are displayed without excluding or selectively including any MIM devices along the row. 111

Figure 4.20: Room temperature DC bias dependent permittivity measurements for a fully processed 800 nm BST thin on Cu foil substrate (green) compared to a 600 nm thick fully fiber textured BST thin film on platinized silicon processed at $700 \text{ }^\circ\text{C}$ (red). 113

Figure 5.1: Temperature profile data for a 400 nm $(\text{Ba}_{0.5}, \text{Sr}_{0.5})\text{TiO}_3$ film deposited on a Cu foil substrate (dashed black line). The Smolenskii model is fit to the data (blue) showing a high degree of fit. 116

Figure 5.2: Simulated temperature dependence of capacitance for the limiting case of maximum and minimum T_C meeting X7R specifications. The shaded area shows the X7R temperature and capacitance change boundaries. a) Simulation of $T_C = 291.8 \text{ K}$ and b) $T_C = 329.3 \text{ K}$. In both cases the capacitance change is $\leq \pm 15\%$ from the room temperature capacitance within the temperature boundaries. 117

Figure 5.3: Simulation result for $T_C = 310.6 \text{ K}$ (red) exactly between the limiting cases for X7R compliance. The temperature boundaries are shown for Y5 by only the purple regions, the X5 by the combined blue & purple regions, and the X7 by the entire region shaded by blue, purple & green regions. The percentage capacitance change from room temperature capacitances are shown by the regions labeled $\pm F$, $\pm P$, and $\pm R$ 118

Figure 5.4: a) Schematic representation of series connected equi-thickness dual composition composite in a MIM configuration. b) Schematic representation of a parallel connected equi-thickness, equi-area dual composition composite in a MIM configuration. 119

Figure 5.5: Simulated temperature profiles for series connected composites of equi-thickness dual composition films. BST films with a T_C of $-173\text{ }^\circ\text{C}$ (blue), $-73\text{ }^\circ\text{C}$ (red), and $27\text{ }^\circ\text{C}$ (green), are series connected to a pure BaTiO_3 film ($T_C = 120\text{ }^\circ\text{C}$).....	122
Figure 5.6: Simulated capacitance change relative to room temperature capacitance of series connected composites of equi-thickness dual composition films. BST films with a T_C of $-173\text{ }^\circ\text{C}$ (blue), $-73\text{ }^\circ\text{C}$ (red), and $27\text{ }^\circ\text{C}$ (green), are series connected to a pure BaTiO_3 film ($T_C = 120\text{ }^\circ\text{C}$). The shaded area shows the percent capacitance change and temperature range of X7R compliance.	122
Figure 5.7: Simulated capacitance change relative to room temperature capacitance of series connected composites of equi-thickness dual composition films. BST films with a T_C of $-93\text{ }^\circ\text{C}$ (yellow), $-53\text{ }^\circ\text{C}$ (red), and $-13\text{ }^\circ\text{C}$ (purple), are series connected to a pure BaTiO_3 film ($T_C = 120\text{ }^\circ\text{C}$). The shaded area shows the percent capacity change and temperature range of X7R compliance. These results show the minimum and maximum T_C of the BST film to comply with X7R specifications.....	123
Figure 5.8: Simulated temperature profile for a series connected composite of equal thicknesses of pure BaTiO_3 and SrTiO_3 (black). The result is compared to a simulated BST film with an identical $T_C = -76.5\text{ }^\circ\text{C}$ (blue). Relative capacitance is plotted versus temperature to achieve exact overlap at the T_C	124
Figure 5.9: Simulated temperature profiles for parallel connected composites of equi-thickness, equi-area dual composition films. A BST film with a T_C of $-163\text{ }^\circ\text{C}$ is parallel connected to a pure BaTiO_3 film ($T_C = 120\text{ }^\circ\text{C}$).	125
Figure 5.10: Simulated temperature profiles for parallel connected composites of equi-thickness, equi-area dual composition films. Shown in green, a BST film with a $T_C = -163\text{ }^\circ\text{C}$ is parallel connected to a pure BaTiO_3 film ($T_C = 120\text{ }^\circ\text{C}$). Shown in blue, a BST film with a $T_C = 33\text{ }^\circ\text{C}$ is parallel connected to a pure SrTiO_3 film ($T_C \sim 0\text{ }^\circ\text{C}$).....	126

Figure 5.12: Three representative SEM images of the BST thin films in cross section. The films are fractured and aligned parallel to the electron beam when imaging. Left: 60 min. deposition. Center: 90 min. deposition, Right: 120 min. deposition. The scale bar in the center is valid for all three images. The fracture surface allows qualitative insight into the film microstructure since the fracture occurs by intergranular fracture, intragranular fracture, and grain pull out. Equiaxial grain morphology is observed throughout the film thickness and is consistent for all films in the thickness series.	132
Figure 5.13: Uncalibrated BF TEM image of a BST/Cu film sputtered for 120 min. digitally captured at 590kX.	133
Figure 5.14: 1 μm X 1 μm topographical AFM image of a BST film sputtered for 75 min.	133
Figure 5.15: Measured ASTM grain diameter measured by AFM versus SEM measured film thickness for the thickness series.	134
Figure 5.16: Room temperature permittivity versus DC bias for the thickness series. See the inset legend for the thicknesses associated with each curve.	135
Figure 5.17: Room temperature inverse capacitance density versus film thickness. The data has a high degree of fit to a linear function with a zero intercept evident by the displayed equation and R^2 value of 0.9847.	136
Figure 5.18: Permittivity temperature dependence for the thickness series. Film thicknesses are given in the inset.	137
Figure 5.19: Lattice parameter of BST thin films based on extrapolation by the Nelson-Riley function. The dotted line shows the expected lattice parameter for all compositions based on Vegard's Law and the accepted values of the end members.	141
Figure 5.20: Room temperature unit cell volume of BST thin films from XRD data and extrapolation using the Nelson-Riley function. The dotted line shows the accepted values for bulk room temperature BST unit cell volume. ⁶³	141
Figure 5.21: Relative capacitance temperature dependence for the composition series. Target composition used to grow each film are given in the inset.	143

Figure 5.22: Observed T_C (closed circles) and the shift from the accepted bulk BST values, ΔT_C (open circles), versus film composition. The grey line represents the accepted T_C values for bulk BST and is given as reference to comparing the observed T_C for the films in this study.....	143
Figure 5.23: C-V curves for films in the composition series. The multiple curves for each film are from successive forward and reverse sweeps of voltage to display any apparent hysteresis. The axis on the extreme right, relative capacitance (closed circles), and extreme left, $\tan \delta$ (open circles), are valid for all four data sets.....	145
Figure 6.1: XPS spectra of the PLSP copper foil surface. a) XPS peak for the binding energy associated with the Cu 2p electrons. b) XPS peak for the binding energy associated with the Zn 2p electrons. c) XPS peak for the binding energy associated with the O 1s electrons showing a binding energy shift due to metal-oxide bonds.....	152
Figure 6.2: a) Vapor pressure curves for pure metallic Zn and Cu. The melting point for each metal is labeled on the plot. b) pO_2 -T plots of zero free energy of formation for the oxidation reactions of the binary oxides of Cu and Zn.....	153
Figure 6.3: Schematic of furnace designed to measure contact angle.....	154
Figure 6.4: pO_2 versus temperature curves for the free energy of oxide formation for Cu (black) and Zn (green). These curves are compared the pO_2 conditions created by the 8.55% H_2 :balance He (red), and 5% H_2 :balance N_2 (blue) forming gas measured <i>in situ</i> in a sealed tube furnace.....	155
Figure 6.5: Temperature profile created by sliding the furnace at 1035 °C over a room temperature sample. The <i>in situ</i> temperature (blue) is compared to the furnace temperature (red).....	156
Figure 6.6: Images of a) molten Zn on Al_2O_3 at 725 °C and b) molten Cu on Al_2O_3 at 1100 °C.....	160
Figure 6.7: a) Cu wrapped Zn on BST/ Al_2O_3 sealed in the furnace tube prior to the experiment. The white color of the substrate is alumina ceramic viewed through the transparent BST thin film. b) A solidified (Cu_x, Zn_{1-x}) drop on a BST/ Al_2O_3 substrate viewed after an experiment and still sealed in the furnace tube. The substrate appears dark due to the change in optical properties of BST from the extreme reducing, high T conditions the sample encounters during experiment.....	163

Figure 6.8: XRD θ - 2θ of the BST/Al ₂ O ₃ substrate after a sessile drop experiment. The BST and alumina phases are clearly evident. Weak intensity from a secondary phase could not be identified as reflection from any one particular phase. It is proposed that these data show a small interfacial reaction of BST and Al ₂ O ₃ but by peak intensities it appears this phase is confined to the interface.....	164
Figure 6.9: XPS survey scan of the BST surface after a sessile drop experiment. No signal from Al can be seen assuring that the reaction phase observed in XRD is confined to the interface and does not affect contact angle measurements on BST thin films.....	165
Figure 6.10: Contact angle for (Cu _x , Zn _{1-x}) on BST/Al ₂ O ₃ substrates given versus the mass percent Zn in the molten alloy.	167
Figure 6.11: SEM backscattered electron images and EDS line scan data for three intermediate (Cu _x , Zn _{1-x}) alloys. a) $x = 75$ mass% Zn b) $x = 50$ mass% Zn c) $x = 25$ mass% Zn.....	168
Figure 6.12: Images of molten Cu on a) Al ₂ O ₃ , b) BST/Al ₂ O ₃ , and c) ZnO. Cu-ZnO represents a wetting system where $\theta < 90^\circ$ whereas Cu-Al ₂ O ₃ and Cu-BST are non-wetting systems ($\theta > 90^\circ$).	170
Figure 7.1: Schematic representation of the thermal evaporator system used to produce copper foils on glass slides.....	174
Figure 7.2: a) 10 μm X 10 μm AFM scan (rendered in 3-D) for the smooth (or shiny) side of Oak Mitsui PLSP $\frac{1}{2}$ oz. Cu foil. b) 10 μm X 10 μm AFM scan (rendered in 3-D) for thermally evaporated UltraFoil. Data taken of the smooth side of the UltraFoil originally mated to the glass slide and is the intended deposition surface. Roughness values were measured at 150 nm and 9.0 nm RMS, respectively.....	175
Figure 7.3: a) Room temperature C-V data versus Zn adhesion layer thickness measured at 10 kHz and 1.11 kV cm ⁻¹ oscillator field. b) Critical parameters extracted from the raw data including maximum capacitance, tunability, dielectric loss at 0 V DC bias and dielectric loss at 25 V DC bias. Dielectric properties are maximized using 50 Å of deposited Zn as an adhesion layer.	177
Figure 7.4: XRD θ - 2θ data for a 450 nm BST thin film as-deposited on UltraFoil Cu (gray) and the same BST/Cu stack after full processing (blue).....	179

Figure 7.5: Dielectric constant verses DC electric field data for an MIM dot capacitor with Pt top electrode taken at room temperature. The oscillator voltage was 2.22 kV/cm RMS, and the measurement frequency was 10 kHz. This film was 450 nm in thickness, thus the maximum field applied was approximately 750 kV cm ⁻¹	180
Figure 7.6: Permittivity frequency dispersion measurements for the same sample in figure 7.5. Note that the increase in loss above 10 kHz corresponds to the onset of capacitor resonance, not an increase in the material's loss tangent.....	181
Figure 7.7: Permittivity temperature response for a fully processed 700 nm BST thin film deposited on an UltraFoil Cu substrate. The broad temperature profile allows > 3:1 tunability by 30 V applied over the entire temperature range.....	181
Figure 7.8: Schematic representation of the vice used to laminate BST/UltraFoil Cu specimens to Si wafer carriers.....	183
Figure 7.9: a) Optical micrograph of an interdigitated Pt electrode patterned by contact lithography and lift-off. 4 μm gaps and features are demonstrated. Prior to lithographic patterning, the foil-BST capacitor stack was laminated onto a silicon wafer. B) Large area optical micrograph of IDC Pt electrodes defined by photolithography. Few pattern transfer flaws are seen over a large area although the BST/Cu stack was processed outside of the cleanroom environment.....	184
Figure 7.10: Room temperature C-V data of IDE structures. These data show an electrical MIM response due to the existence of the high conductivity Cu substrate.....	185
Figure B.1: The BaO - TiO ₂ phase diagram showing the line compound BaTiO ₃ . ^{255, 256}	215
Figure B.2: The SrO - TiO ₂ phase diagram showing the line compound SrTiO ₃ . ²⁵⁷	215
Figure B.3: BaTiO ₃ - SrTiO ₃ phase diagram showing full miscibility between the two perovskite oxides. ⁶²	216
Figure B.4: The BaO - SrO - TiO ₂ ternary phase diagram at 1400 °C. The labels in the figure correspond to: B = BaO, S = SrO, T = TiO ₂ , BT = BaTiO ₃ , ST = SrTiO ₃ , (B, S)T = (Ba _x , Sr _{1-x})TiO ₃ . ²⁵⁸	216

Figure B.5: SrO - Al ₂ O ₃ phase diagram showing possible reaction products of BST on alumina. The entire composition range is shown in a) while b) shows the details of the phase field from 18 < mole % Al ₂ O ₃ < 24 ²⁵⁹	217
Figure B.6: The copper - zinc phase diagram showing total solid and liquid miscibility over the entire composition range. ²¹⁹	217
Figure D.1: C-V data from sample reoxed by a range of <i>p</i> O ₂ -T combinations.	230
Figure D.2: Similar data set to figure D.1 for a different sample of identical composition and thickness. Reox anneals were all performed at 550 °C and total O ₂ systematically varied.	231
Figure E.1: Raw C-V data for BST thickness of 450 - 1350 nm on UltraFoil substrates 10 - 18 μm. Data along row in the figure are plotted on the sample capacitance scale and all plots have a voltage range of -30 to 30 V.	232

LIST OF TERMS

2θ	[degrees]	Bragg angle
A	[cm ⁻²]	area
A	[V Torr ⁻¹ cm ⁻¹]	Paschen gas constant
$A^{substrate}$	[cm ²]	area of electrode counter to target
A^{target}	[cm ²]	target area
a	[² / ₃ for low P, ³ / ₄ for high P]	cathode sheath exponent
a	[Å]	measured lattice parameter
a_i	[unitless]	activity of the i th component
a_0	[Å]	actual lattice parameter
B	[V Torr ⁻¹ cm ⁻¹]	Paschen gas constant
C	[F]	capacitance
C_{C-W}	[°C]	Curie-Weiss constant
C_{MAX}	[F]	maximum capacitance over all temperatures
$C(T)$	[F]	temperature dependent capacitance
c_{bulk}^A	[mole fraction]	concentration of solute in the bulk
$c_{surface}^A$	[mole fraction]	concentration of solute at a surface
d	[cm]	distance
d_{ijk}	[C N ⁻¹]	direction piezoelectric coefficient
d_s	[cm]	cathode sheath length
\mathbf{D}	[C m ⁻²]	dielectric displacement vector
$\bar{\mathbf{d}}$	[cm]	charge separation vector
e	[1.602 • 10 ⁻¹⁹ C]	fundamental electron charge
$\bar{\mathbf{E}}, E_k$	[V m ⁻¹]	electric field vector
E_0	[V m ⁻¹]	electric field amplitude
E'	[V m ⁻¹]	real part of electric field
E''	[V m ⁻¹]	imaginary part of electric field
E_i	[eV]	ion energy
E_T	[eV]	target atom energy
E_C	[kV cm ⁻¹]	coercive field
F_a	[N]	adhesion force
f	[unitless]	surface segregation constant in enthalpy relation
G	[J mol ⁻¹]	Gibb's free energy
g	[unitless]	surface segregation constant in surface tension relation
ΔH_{Sub}	[kJ mol ⁻¹]	heat of sublimation
$\Delta H_{f(MO)}^0$	[kJ mol ⁻¹]	enthalpy of oxidation of a metal
$\Delta \bar{H}_{A(B)}^\infty$	[kJ mol ⁻¹]	enthalpy of mixing
h	[cm]	center-to-center target to substrate distance
Δh_v	[kJ mol ⁻¹]	formation enthalpy
\hbar	[1.055 • 10 ⁻³⁴ J sec ⁻¹]	Plank constant

i	[unitless]	$\sqrt{-1}$
j^+	[A cm ⁻²]	ion current density
k_B	[1.381 • 10 ⁻²³ J K ⁻¹]	Boltzmann constant
k	[cm ⁻¹]	wave number
k_{rxn}	[unitless]	reaction rate constant
K	[unitless]	dielectric constant
\bar{K}	[GPa]	average bulk modulus
m	[unitless]	structure parameter
m_e	[9.109 • 10 ⁻³¹ kg]	electron mass
m_i	[kg]	ion mass
m_T	[kg]	target atom mass
N	[# cm ⁻³]	number density
n	[unitless]	absolute tunability
n_e	[cm ⁻³]	density of free electrons
n_i	[cm ⁻³]	density of ions
P	[Torr]	gas pressure
$\bar{\mathbf{P}}, P_i$	[C cm ⁻²]	polarization vector
$\langle P_{loc} \rangle$	[C cm ⁻²]	average local polarization
P_S	[C cm ⁻²]	spontaneous polarization
$\bar{\mathbf{p}}$	[C cm]	dipole moment vector
p_i	[C cm ⁻² K ⁻¹]	pyroelectric coefficient
pH_2	[atm]	partial pressure of hydrogen gas
pH_2O	[atm]	partial pressure of water vapor
pO_2	[atm]	partial pressure of oxygen gas
q	[C]	charge
q_i	[C]	ion charge
R	[8.314 J mol ⁻¹ K ⁻¹]	gas constant
R^2	[unitless]	fitting metric
r_i	[nm]	distance
$\bar{\mathbf{r}}$	[cm]	spatial position vector
r_A	[Å]	A-site ionic radius
r_B	[Å]	B-site ionic radius
r_O	[Å]	oxygen ionic radius
$S_n(E_i)$	[keV amu ⁻¹]	energy dependent nuclear stopping power
T	[°C or K]	temperature
T_C	[°C or K]	Curie temperature
TCC	[F °C ⁻¹]	temperature coefficient of capacitance
ΔT_C	[°C or K]	difference between Curie temperatures
T_e	[eV]	electron temperature
T_0	[°C]	Curie-Weiss temperature
T_{MAX}	[°C or K]	temperature at maximum capacitance/permittivity
t	[unitless]	perovskite tolerance factor
t	[sec.]	time

t_i	[nm]	thickness of the i^{th} film
V	[V]	voltage
V_B	[V]	plasma breakdown voltage
V_C	[V]	negative cathode potential
V_i	[m ³ mol ⁻¹]	molar volume of i^{th} component
\bar{V}_m	[m ³ mol ⁻¹]	average molar volume
$[V_o^{\bullet\bullet}]$	[ppb]	concentration of oxygen vacancies
V_P	[V]	Plasma potential
V_S	[V]	sheath potential
V_S^{target}	[V]	sheath potential at the target electrode
$V_S^{\text{substrate}}$	[V]	sheath potential at the substrate
v	[cm ³]	volume
W_a	[J m ⁻²]	work of adhesion
x	[fraction]	molar fraction (<i>i.e.</i> composition)
x_{ij}	[unitless]	strain tensor
$\tan \delta$	[unitless]	dielectric loss
Z	[unitless]	atomic number
α	[C cm ² V ⁻¹]	polarizability
α	[unitless]	sputter yield constant
δ	[°C]	Smolenskii's broadness parameter
γ_{Se}	[unitless]	secondary electron yield
γ_{hkl}	[J m ⁻²]	surface energy of specific crystallographic plane
$\gamma_{\text{interface}}$	[J m ⁻²]	surface energy between substrate and film
γ_{lv}	[J m ⁻²]	liquid-vapor surface tension
γ_{sl}	[J m ⁻²]	solid-liquid surface energy
$\gamma_{\text{substrate}}$	[J m ⁻²]	solid-vapor surface energy
γ_{sv}	[J m ⁻²]	solid-vapor surface energy
ϵ	[F m ⁻¹]	permittivity
ϵ'	[F m ⁻¹]	real part of the permittivity
ϵ''	[F m ⁻¹]	imaginary part of the permittivity
ϵ_0	[8.854 • 10 ⁻¹² F m ⁻¹]	permittivity of free space
ϵ_{MAX}	[F]	maximum relative permittivity over all temperatures
ϵ_r	[F m ⁻¹]	relative permittivity
$\epsilon(T)$	[unitless]	temperature dependent relative permittivity
λ	[kJ mol ⁻¹]	pair-wise molar exchange energy
$\langle \lambda \rangle$	[cm]	mean free path
λ_D	[cm]	Debye length
η	[unitless]	relative tunability
θ	[degrees]	contact angle
ρ	[C cm ³]	charge density
σ_{jk}	[Pa]	stress vector
χ	[F m ⁻¹]	dielectric susceptibility
Ω_M	[m ² mol ⁻¹]	molar interfacial area

ω [Hz]frequency
 ω_S [Hz]soft mode frequency
 ω_{TO} [Hz]transverse optical mode frequency
 ω_{pe} [Hz]electron plasma frequency

1. INTRODUCTION

This thesis outlines a commercially compatible methodology to deposit barium strontium titanate, BST, thin films on copper foil substrates. This technology provides a means to synthesize ferroelectric thin film based tunable capacitors for frequency-agile circuits. This work progressed through collaboration with scientists in academia: North Carolina State University and The Pennsylvania State University, and industry representatives: QorTek (a NASA contractor) and DuPont.

Wireless communications rely on the transmission and receipt of electromagnetic radiation. This requires front end circuitry that can operate within predefined frequency bands established by the FCC for communications, telemetry, and defense. Current technologies require high performance varactors in complex circuits to achieve signal transmission in multiple frequency bands and high speed frequency shifting within those bands. The majority of medium and low cost wireless devices employ omni-directional antennae where radiation is sent and received equally in all directions in space: this occurs at the expense of low efficiency. 2-D geometric arrays of circuitry, where resonant frequency is independently controlled by tunable elements in each section of the array, allow electromagnetic radiation to be focused and the wave front spatial trajectory controlled.

Semiconductor varactors are the primary component currently used to handle frequency shifting in medium and low cost wireless devices. The semiconductor processing required to make these p-n junction based varactors makes this technology costly. Additionally, there are concerns that high dielectric losses at increasing frequencies will make this technology obsolete as communications evolve into the microwave regime. Recent success and subsequent commercialization of ferroelectric thin film based varactors have been shown by nGimatTM¹ and Agile Materials & Technologies, Inc.² These varactors are based on deposition of ferroelectric thin films on single crystal substrates and noble metal electrodes; restricting their use to applications where cost is not a limiting factor.

Ferroelectric thin film dielectrics have a non-linear dependence of permittivity with the application of a DC bias superimposed on the high frequency voltage signal. This allows their use as a tunable dielectric in capacitors controlled by voltage signals. The use of a thin film format allows application of large DC fields applied with modest voltages thereby allowing a large tunability with modest electrical drive. Since capacitance tuning is handled electronically, the shifting of the resonant frequency can be achieved on very short time scales. The permittivity and dielectric loss typically does not show relaxation or significant dispersion until well beyond the 10 GHz. Though the technology is appropriate for device design and operation, the limiting factor for commercialization of ferroelectric thin film varactors is the current high processing costs associated with this technology.

An embodiment of a ferroelectric thin film deposited over a wide area on a mechanically flexible metal substrate allows processing at high temperatures irrespective of the temperature constraints of packaging materials. These sheets can then be integrated into a circuit for frequency agile operation and allow tunable capacitors to be realized with high tunability and low dielectric losses combined with thick, low resistivity metallization to realize low insertion losses and high quality factors.

If ferroelectric thin film based devices are to complement or supplant semiconductor varactors, device elements must be synthesized using a low cost processing techniques. Additionally, ferroelectrics undergo a phase transition imparting temperature dependent dielectric properties. The phase transition temperature of BST can be manipulated around room temperature by adjusting the composition, BaTiO₃ to SrTiO₃ mole ratio. Having the transition temperature near room temperature provides large permittivity and tunability over intended device operating temperatures but also exacerbates the temperature dependence of dielectric properties; consequently some compositional engineering is needed for property stability.

1.1. STATEMENT OF PURPOSE

The manuscript outlines research into barium strontium titanate, BST, thin films deposited on copper foils. The process methodology was developed considering the viability of commercializing the technology. Metal-insulator-metal, MIM, devices were fabricated from BST/Cu specimens and dielectric properties are compared to microstructure found through physical characterization. These experiments allow formation of processing-structure-property relationships. A concept of stacked multi-composition dielectric composites was explored through simulation to investigate the ability to mitigate the temperature coefficient of capacitance, TCC. The simulations can only be extended to device synthesis if dielectric film thickness and composition can be manipulated with suitable dielectric properties. These dielectric properties were experimentally explored as a function of film thickness and composition to assess plausibility of TCC mitigation. Ferroelectric thin films have high permittivity making it impossible to form impedance matched capacitors in high frequency circuits without micron scale electrode definition. Initial, BST/Cu specimen synthesis was developed on Cu foil substrates with large surface roughness which is incompatible with the photolithography required for micron scale dimension. A process for synthesizing advanced Cu foil substrates with reduced surface roughness was explored. BST thin films deposited on reduced surface roughness substrates allowed assessments of the ability to define required electrode dimensions. The use of Cu substrates represents a significant shift from oxide and noble metal substrates. As such, several fundamental issues of this novel embodiment warranted exploration. One particularly important issue is mechanical stability, which is very strongly influenced by film-substrate adhesion. Adhesion was explored through wetting experiments to characterize the BST-Cu adhesion and the affect of surface treatments to improve thin film adhesion.

Studies are intended to give insight into the practicality and commercial viability of ferroelectric based thin film capacitors providing tunability to circuits for frequency-agile circuits. Areas of practical concern are addressed and material solutions and concepts are presented to overcome potential barriers.

2. LITERATURE REVIEW

2.1. DIELECTRIC MATERIALS

Dielectric materials commonly referred to as insulators, resist the flow of current in a circuit and can store electric charge. When a dielectric is immersed in an electric field a material responds by shifting internal charge density, separating positive and negative charge centers and creating internal dipoles. Defining the vector quantity, \bar{p} , dipole moment for a single dipole equivalent to the amount of charge, q , multiplied by the vector separating positive and negative charge centers, \bar{d} .

$$\bar{p} = q\bar{d} \quad \text{eqn [2.1]}$$

Extending this to the collection of the many dipoles that exist in a dielectric material the total polarization, \bar{P} , is simply equivalent to the number density of dipoles, N , multiplied by \bar{p} . This polarization is described by the material specific parameter polarizability, α , describing the polarization with a unit electric field.

$$\bar{P} = Nq\bar{d} = \alpha\bar{E} \quad \text{eqn [2.2]}$$

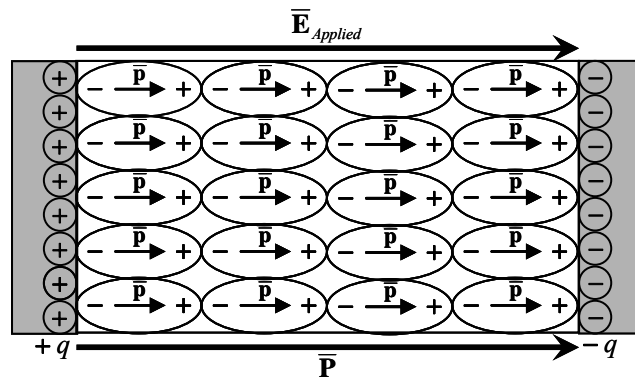


Figure 2.1: Schematic of parallel electrodes separated by a dielectric material. Shown are individual dipoles with their dipole moments and polarization and applied electric field vectors.

The quantification of a dielectric material's ability to store charge is not often done in terms of polarizability but instead the dielectric susceptibility, χ , or the permittivity, ϵ . These material parameters are intimately linked by equation 2.3.

$$\epsilon = \epsilon_0 \epsilon_r = \epsilon_0 (1 + \chi) = \epsilon_0 \left(1 + \frac{N\alpha}{\epsilon_0} \right) \quad \text{eqn [2.3]}$$

To be fully accurate the dielectric displacement, \bar{D} , is vector quantifying the amount of charge stored per unit area given by equation 2.4 and can be defined thermodynamically as the change in Gibbs free energy with a change in electric field at constant temperature and mechanical stress.

$$\bar{D} = \epsilon \bar{E} + \bar{P} = \left(\frac{\partial G}{\partial \bar{E}} \right)_{T,\sigma} \quad \text{eqn [2.4]}$$

In most cases, the product of the electric field and the permittivity of free space is much smaller than the polarization and the valid assumption $\bar{D} \approx \bar{P}$ can be made. From this thermodynamic description of stored charge the relative permittivity can be defined in a thermodynamic means by the following relation.³

$$\epsilon_r = \left(\frac{\partial^2 G}{\partial \bar{E}_1 \partial \bar{E}_2} \right)_{T,\sigma} = \left(\frac{\partial \bar{D}}{\partial \bar{E}} \right)_{T,\sigma} \quad \text{eqn [2.5]}$$

Ultimately, permittivity is used to describe how a material responds to electrical stimuli.

In most practical cases, electrical signals are transient thus the effect of non-zero frequency is important to consider. To describe a transient electric field we can assume a sine wave to mathematically describe behavior terms of a complex numbers.

$$E = E_0 \sin(\omega t) = E_0 \exp[i\omega t] = E' + i\omega E'' \quad \text{eqn [2.6]}$$

When this complex definition of an electric field is inserted into the preceding equations the permittivity also becomes a complex quantity.

$$\varepsilon(\omega) = \varepsilon'(\omega) + i\varepsilon''(\omega) \quad \text{eqn [2.7]}$$

This definition of the permittivity includes a real, ε' , and imaginary, ε'' , contribution, both being frequency dependent. The real part of the permittivity is what determines the measured dielectric constant in a physical circuit whereas the imaginary part represents lost energy. The energy loss is quantified by the loss tangent, otherwise known as the dissipation loss factor or simply dielectric loss, $\tan \delta$.

$$\tan \delta = \frac{\varepsilon''}{\varepsilon'} \quad \text{eqn [2.8]}$$

When considering the use of dielectric materials in practical circuits, permittivity is the primary parameter used in the material selection or circuit design while minimum dielectric loss is nearly always paramount.

The frequency dependence of permittivity and dielectric loss is due to several different polarization mechanisms which are responsible for dipole creation within a material. The effect of an individual mechanism on permittivity and is determined by the amount of charge that is displaced and the displacement distance as shown from equations 2.1 through 2.5. In situations where multiple mechanisms act concomitantly, the effect is additive and the resulting permittivity is the sum of the contributions from each mechanism. In all cases, polarization involves the movement of charges with finite mass bound to at rest positions by a restoring force akin to a simple harmonic oscillator yet the driving force is electronic and the restoring force is the charged species desire to be at the position corresponding to the lowest free energy. When the drive force frequency increases beyond a resonant condition the polarizations cannot be fully achieved within the time period before the field reversal and relaxation occurs. At resonance large amounts of energy are absorbed and dielectric loss experiences maxima with frequency.

An analysis of the individual mechanisms responsible for frequency dispersion will give insight into material behavior. At very high frequencies in the optical regime the negatively charged electron cloud around individual atoms can be displaced from the

positive atomic nuclei creating dipoles at each atom. Since electrons have an extremely small mass this electronic polarization mechanism can respond to applied fields at high frequencies. The dipole moments created in this process are small due the small number of charges surrounding individual atoms and the small displacements allowed by the balance between electron binding energy thus the increase of permittivity above ϵ_0 is small. In materials where bonding is primary ionic an applied field can displace anions and cations oppositely creating a polarization. Here the charged species, ions, are more massive than electrons and the restoring force is determined by the ionic bonds. The larger mass and displacements force relaxation to occur at lower frequencies, typically in the infra red regime. Here the dipole moments created are larger and the contribution to permittivity is greater. In materials where individual molecules have a permanent dipole moment or in crystals where the structure includes an array of permanent re-orientable dipoles the effective dipole moment of entire specimen will be zero if these dipoles are randomly oriented. Under an applied field these dipoles can align creating large polarizations in the directions of the applied field. In this situation dipoles are not created but rather the orientation changed toward the applied field. This movement involves multiple species with a large collective mass and there is not necessarily a restoring force, but in some cases, a common equilibrium orientation for an ensemble of these individual dipoles. The dipole contribution can be large yet the large mass and slow movement of the species causes relaxation somewhere in the regime of radio frequency and possibly as high as microwave frequencies. At the lowest frequencies space charge effects can contribute to the observed permittivity. Space charges exists to a degree in all practical insulators since some amount of free charge carriers with a certain mobility are present and move in response to the applied field accumulating at internal boundaries or interfaces. The relaxation for space charge and interfacial charge contributions can occur within a large frequency regime but typically occurs in the kHz range or below since mobilities are small in insulators. Since the low frequency contribution is attributed to conduction it is typically undesirable when considering dielectric materials and in high

frequency operation the contribution to permittivity is non-operable or contribute to high loss at the desired frequency.⁴

The resulting dispersion for a material where all contributions to permittivity can operate is shown in figure 2.2.

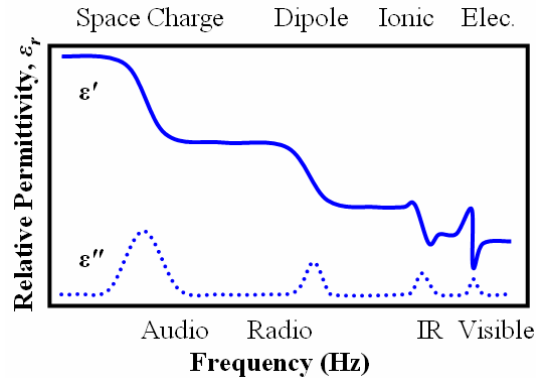


Figure 2.2: Theoretical frequency dispersion for a dielectric showing all possible polarization mechanisms and the expected frequencies for their relaxation.

Although it is important to note that not all materials are ionically bonded, possess permanent dipoles, or have significant number of free charges, so the dispersion for a specific specimen may not include all the features shown in figure 2.2. However, the concept of dispersion is important when evaluating dielectric materials for operation in a device or circuit at high frequencies and the achievement of the lowest possible dielectric loss.

Permittivity is of paramount importance when discussing dielectric materials yet a real material's ability to resist current flow is never perfect. When a material has finite conductivity the ability to store charge is mitigated by the loss of charge through conduction. The wideband gap of insulators gives low concentrations of intrinsic charge carriers at room temperature if free from defects. Any existence of defects allowing energy levels in the band gap on the order of $k_B T$ from the conduction band minimum or valence band maximum and substantial loss of resistivity results. Additionally, features of the microstructure, including grain boundaries, dislocation, and secondary phases, and macroscopic defects, such as porosity or cracking, can cause high conductivity paths through the material.

Beyond supplying simple electrical isolation, dielectric materials are employed as capacitive elements to store and/or supply charge and to manipulate a circuit's characteristic resonant frequency. The simplest form capacitive structure is that of a parallel plate capacitor.

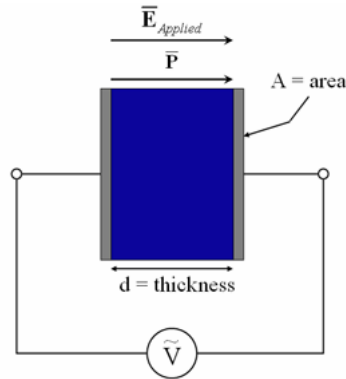


Figure 2.3: Parallel plate capacitor configuration.

The circuit designer's main concern is the capacitance, C , yet beyond geometry of the plate area, A , and the separation between the plates, d , the material permittivity determines the capacitance.

$$C = \frac{K\epsilon_0 A}{d} \text{ where } K = \frac{\epsilon_r}{\epsilon_0} \quad \text{eqn [2.9]}$$

Here the dielectric constant, K , is defined as parameter common to design engineers which is analogous and in many cases essentially identical to relative permittivity. Given potential restrictions on capacitor physical dimensions, the material parameter permittivity must be engineered to suit the needs of a device design. This thesis will outline a methodology to synthesize non-linear and tunable dielectric thin films considering the practical restraints of high volume manufacturing and using optimal materials (substrate and film).

2.2. FERROELECTRIC/PARAELECTRIC MATERIALS

2.2.1. Polar dielectrics

The symmetry of any material can be defined by one of the 32 point groups or crystal classes. Yet only 10 crystal classes contain symmetry consistent with the spontaneous formation of dipoles. All dielectric materials become polarized in the presence of external electric fields, yet only the 10 polar crystal classes support spontaneous dipoles in the absence of external stimuli.⁵

Table 2.1: List of polar point groups

Polar Crystal Classes	
1	<i>4mm</i>
2	3
<i>m</i>	<i>3m</i>
<i>mm2</i>	6
4	<i>6mm</i>

In polar crystalline materials a dipole moment can be defined for each unit cell. Generically there is a separation of the positive and negative charge distributions within the unit cell, and by defining an arbitrary origin, the position of the positive and negative charge centers, and their spatial separation can be found by the following volume integral.⁶

$$q(\bar{\mathbf{r}}) = \iiint \rho(\bar{\mathbf{r}}) \cdot \bar{\mathbf{r}} \cdot d\mathbf{v} \quad \text{eqn [2.10]}$$

Either through rigorous theoretical calculation or experimental means the polar properties of a material can be known the polar axis identified.

The existence of a unique polar axis fundamentally imparts property anisotropy in polar dielectrics. The point group symmetry can fully describe anisotropy in single crystal mono-domain specimen. Of the 10 polar crystal classes all but point group 1 allows for multiple polarization directions which can lead to a multi-domain state even in a single crystal specimen. A domain being homogeneous regions within a crystal with consistent polarization separated from adjacent regions with polarization along a different crystallographic direction while not destroying the coherence of the crystal structure. In polycrystalline specimens, individual grains are most often randomly oriented, with the possibility for single or multiple domains within each grain.

The symmetry of material properties must include the symmetry of the point group and the symmetry of the physical microstructure. The symmetry considerations with microstructural origins are defined by the Curie groups.

Table 2.2: Curie groups defining the symmetry of morphology and applied field. The notation is given with the corresponding geometric representation and examples of representative situation displaying the symmetry. Curie groups with requiring handedness are not included as do not apply to this thesis.

Curie Group	Geometric symmetry	Example
∞m	conical	poled polar crystal
∞/mm	cylindrical	uniaxial applied field or fiber textured grain morphology
$\infty\infty m$	spherical	equiaxial random grain morphology or amorphous materials

Neumann's Principle predicates that property symmetry must reflect unit cell symmetry, the symmetry imposed by microstructure, and the symmetry imposed by external forces.³ Therefore, it is important to consider electrical polarization in terms of crystallographic orientation, applied electric and mechanical fields, and grain/domain morphology.

2.2.2. Pyroelectricity

The recognition of polar materials dates to antiquity when the Greek philosopher Teophrastus observed how the mineral “lyngourion,” which is suspected to be tourmaline the complex silicate $(Ca, Na, K)(Al, Fe, Li, Mg, Mn)_3(Al, Cr, Fe, V)_6(BO_3)_3Si_6O_{18}(O, OH, F)_4$, attracted small fragments of wood. The definition of polar dielectrics in terms of modern physics developed through the 17th and 18th centuries where researchers connected electrical effects with temperature changes.⁷ These effects are now known as pyroelectricity. Pyroelectricity describes the net change in polarization with change in temperature.

$$d\bar{P} = d\bar{D} = p_i dT \quad \text{eqn [2.11]}$$

In a response to the polarization change a small current must to flow to accumulate the compensating charges on the surfaces of the specimen.

The observation of pyroelectricity provides unambiguous proof for spontaneous polarization, yet this observation cannot be made in a material with randomly oriented polar domains. This is due to the fact there is no macroscopic polar axis even though spontaneous dipoles exist within domains and grains. All polar materials are pyroelectric therefore only crystals with non-centrosymmetric symmetry can display pyroelectricity. Pyroelectric materials, a term synonymous with polar materials, are the general classification from which other specific polar materials are grouped.

2.2.3. Piezoelectricity

Of the 32 crystal classes, 21 lack a center of symmetry and all but one of these classes support direct piezoelectricity (point group 432 being the exception). Direct piezoelectricity is the ability of these materials to develop an induced polarization proportional to a mechanical stress.

$$P_i = d_{ijk} \sigma_{jk} \quad \text{eqn [2.12]}$$

Here the tensor notation is appropriate since stress, σ_{jk} , is a second rank tensor and the polarization, P_i , is a first rank tensor which requires the piezoelectric tensor, d_{jkl} , having 9 independent coefficients in the generic asymmetric case. Since stresses can be tensile, positive, or compressive, negative, the polarization can switch directions when the stress state changes. The converse piezoelectric effect is the development of a mechanical strain proportional to the application of an electric field.

$$x_{ij} = d_{ijk} E_k \quad \text{eqn [2.13]}$$

Although the relation involves different specific variables the piezoelectric coefficients are identical. All materials with the required symmetry can be piezoelectric unless the morphology imparts the spherical symmetry of the $\infty\infty m$ Curie group. This is the case for randomly oriented grain morphology or domain structure.

The existence of piezoelectric behavior can have implications on the measurement of permittivity in inhomogeneous systems. In many situations, material syntheses or testing, mechanical stresses and strains are unavoidable and can contribute to the polarization and the measured dielectric response. One possible way to avoid this is to create conditions where the material is in a centrosymmetric phase or has an unpoled random orientation which makes the macroscopic specimen isotropic.⁸

2.3. FERROELECTRICITY

2.3.1. Historical perspective of ferroelectric materials

A subset of polar materials was first observed by Valasek in 1921 in single crystals of Rochelle salt, $\text{KNa}(\text{C}_4\text{H}_4\text{O}_6) \cdot 4\text{H}_2\text{O}$.⁹ The hysteretic behavior observed between polarization and applied electric field was analogous to the magnetism versus magnetic field behavior in ferromagnetic materials which were previously understood. Therefore the phenomenon was termed “ferroelectricity.” The earliest research identified only two

types of ferroelectric materials, tartrates such as Rochelle salt (*e.g.* sodium ammonium tartrate tetrahydrate $\text{Na NH}_4(\text{C}_4\text{H}_4\text{O}_6) \cdot 4\text{H}_2\text{O}$ in 1928¹⁰ and lithium ammonium tartrate monohydrate $\text{LiNH}_4(\text{C}_4\text{H}_4\text{O}_6) \cdot \text{H}_2\text{O}$ in 1951^{11, 12}), and potassium dihydrogen phosphate (*e.g.* KH_2PO_4 in 1935¹³) and its isomorphs (*e.g.* ammonium dihydrogen phosphate $\text{NH}_4\text{H}_2\text{PO}_4$ in 1938¹⁴). These materials' water solubility made them impractical for use in electronic devices and the ferroelectric phenomenon could only be observed at low temperatures.

In 1940, the first refractory oxide ferroelectric with room temperature ferroelectricity was discovered in the perovskite barium titanate, BaTiO_3 , by Thurnauer and Deaderick at the American Lava Co.^{15, 16} Publication of the high permittivity of BaTiO_3 in the open literature came from the U.S.¹⁷⁻¹⁹ and Europe²⁰⁻²² in concurrent independent reports and the determination that the high permittivity was due to ferroelectricity in BaTiO_3 was given by von Hippel of the Laboratory for Insulation Research at MIT.²³ The discovery of ferroelectric barium titanate represented a breakthrough in ferroelectric research and fueled development of high permittivity devices. Piezoelectric transducers were facilitated by the discovery of the ferroelectric perovskite solid solution lead zirconate titanate, $\text{Pb}(\text{Zr}, \text{Ti})\text{O}_3$ or PZT,²⁴ and the existence of a temperature independent polymorphic phase boundary at Zr:Ti mole ratios of 52:48.²⁵ To date, perovskite based ferroelectrics are the mostly widely utilized class of solid-state materials for high capacitance density capacitors and high strain/sensitivity transducers. Despite the large number of publications each year, their potential for commercial electronics is yet to be exhausted.

2.3.2. Theory of ferroelectricity

The class of materials known as ferroelectric is a subset of polar dielectrics which possess a switchable spontaneous polarization below a characteristic temperature known as the Curie temperature. Non-ferroelectric, polar dielectrics are spontaneously polarized but do not possess energetically equivalent options for the orientation of their spontaneous dipole within the unit cell. In ferroelectric materials the dielectric response is hysteretic

below the Curie temperature where the direction of polarization is reoriented when applying an electric field with a greater magnitude than the coercive field, E_C .

The most utilized and studied ferroelectric materials are oxides based on the perovskite crystal structure.

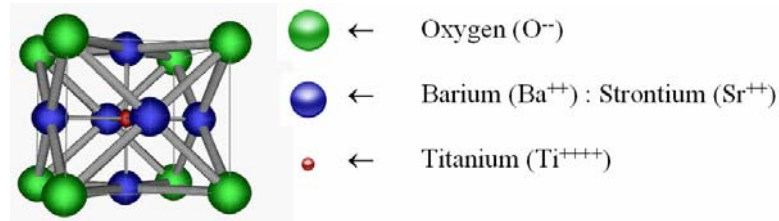


Figure 2.4: Schematic representation of a perovskite unit cell. Lattice positions of the ions comprising BST are labeled in the figure.

All further discussions, will concern only perovskite oxide ferroelectric materials. Oxides with the perovskite structure, shown in fig 2.4, consist of a cubic close packed oxygen sub-lattice where the unit cell is drawn as a face centered cubic unit cell with oxygen anions occupying the cell faces and a B-type cation at the octahedral site and A-type cations occupying the cuboctahedral cube corners coordinated by oxygen. This unit cell definition is the simplest to view the crystallographic distortions which underpin the hysteretic physical phenomenon. The high temperature aristotype structure was first observed in the mineral named perovskite, CaTiO_3 . Using simple geometry and knowledge of crystal chemistry Goldschmidt defined a tolerance factor for the perovskite structure adapted below for oxides.²⁶

$$t = \frac{r_A + r_O}{\sqrt{2}(r_B + r_O)} \quad \text{eqn [2.14]}$$

This tolerance factor, t , calculated from known ionic radii can be used to gauge the structural stability of compositions with stoichiometry ABO_3 in the perovskite phase. Ionic radii at room temperature have been tabulated by Shannon^{27, 28} and pertinent data is included in Table 2.3.

Table 2.3: List of room temperature ionic radii pertinent to these taken from the tabulations of Shannon.^{27, 28} The ions of barium strontium titanate are included along with those of zinc to be referenced in the adhesion sections of this thesis.

Ion	Valence	Coordination	Ionic radius (Å)
O	2-	6	1.40
Ba	2+	12	1.61
Sr	2+	12	1.44
Ti	4+	6	0.605
Ti	3+	6	0.670
Ti	2+	6	0.86
Zn	2+	6	0.704
Zn	4+	6	0.72

The perovskite strontium titanate, SrTiO₃, which is cubic at room temperature has a tolerance factor, $t_{SrTiO_3} = 1.002$. SrTiO₃ follows closely with Goldschmidt's prediction that when the tolerance factor is close to unity, cubic perovskite structure is observed. Barium titanate, BaTiO₃, is tetragonal at room temperature and has a tolerance factor $t_{BaTiO_3} = 1.062$. This again follows Goldschmidt's predictions that tetragonal distortions occur for perovskites with $t > 1$ and result from either the A-site cation being too large or the B-site cation being too small for their respective interstice volume. For tolerance factors $t < 0$ where the A-site cation is small or the B-site cation too large Goldschmidt predicts octahedral tilting and distortions from cubic symmetry which is precisely what occurs in many AScO₃, A = {Bi, Pb, Th, Y}, perovskite oxides.²⁹

Although Goldschmidt predicts the crystallographic distortions of most ferroelectric perovskites it does not adequately explain the instability that leads to spontaneous polarization. The degree of bond covalency also contributes to structural distortions and polarization anisotropy. As in all ionic solids short range repulsive forces are balanced by long range attractive forces and in ferroelectric materials the short range

forces tend to stabilize the cubic non-ferroelectric structures while the long range forces stabilize the spontaneously polarized ferroelectric structure.³⁰ Modern computing power gives the ability to formulate sufficiently exact Hamiltonians using the local density approximation (LDA) of density functional theory (DFT) to calculate *ab-initio* the microscopic bonding occurring within the unit cell of perovskites. Cohen found in barium titanate the ferroelectric instability arises from the covalent hybridization between the Ti 3d and O 2p electron states while the Ba-O bond are largely ionic in character.³¹ Conversely, in perovskites where occupation of the A-site is by p-block ions (Pb, Bi, etc) the lone pair electrons form homo-bonds which hybridize with the electronic states of the neighboring oxygen anions imparting directional bonds and supporting spontaneous polarization.³⁰ Cohen's *ab-initio* calculations are only valid at $T = 0$ K since they were performed without the inclusion of molecular dynamics. The results have been confirmed for non-zero temperatures by Rabe.^{32,33}

The switchable polarization can be understood by the examination of simplified model of a hypothetical 2-D polar dielectric.

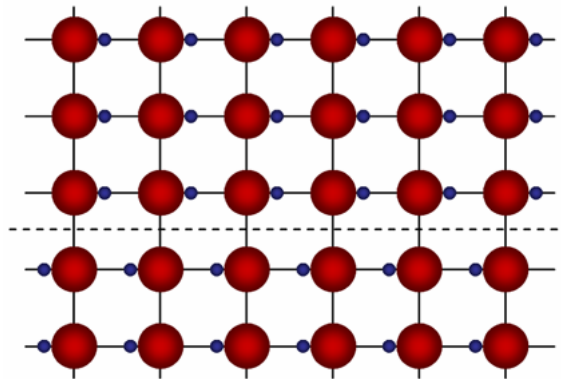


Figure 2.5: Schematic of a model 2-D polarized lattice. Red spheres are anions and blue spheres are cations. The dashed line represents a domain wall where above this the polarization is horizontal to the left and below horizontal to the right.

Shown in figure 2.5 is such a hypothetical lattice where the cations equilibrium position is shifted toward one of the neighboring anions. This non-centered cation position is equally likely to be shift toward any of its neighbors. In any primary direction this situation is described energetically by a double potential well. The isotropic configuration sits at

local instability where an infinitesimal perturbation would shift the cation position towards an anion neighbor minimizing free energy thus establishing the spontaneous polarization.

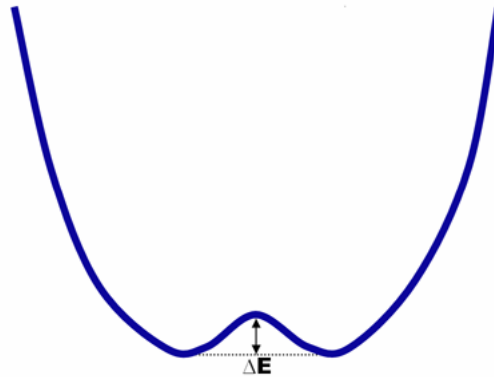


Figure 2.6: Schematic of the double potential well which describes the equilibrium position of cations relative to the anions in the model 2-D polarized lattice. The energy barrier, ΔE , is on the order of eE_C allowing for polarization reversal when $\bar{E} \geq eE_C$ is applied.

A finite energy barrier separates the two stable energy minima and in a ferroelectric this energy barrier is on the order of eE_C where E_C is the coercive field necessary to switch the polarization. This concepts established by this simplified model extend to the 3-D case actual ferroelectric crystals.⁶

The existence of switchable spontaneous polarization manifests in non-linear and hysteretic relationship between electrical polarization and applied field. In the case of a mono-domain single crystal the hysteretic response would produce a square loop seen in figure 2.7.

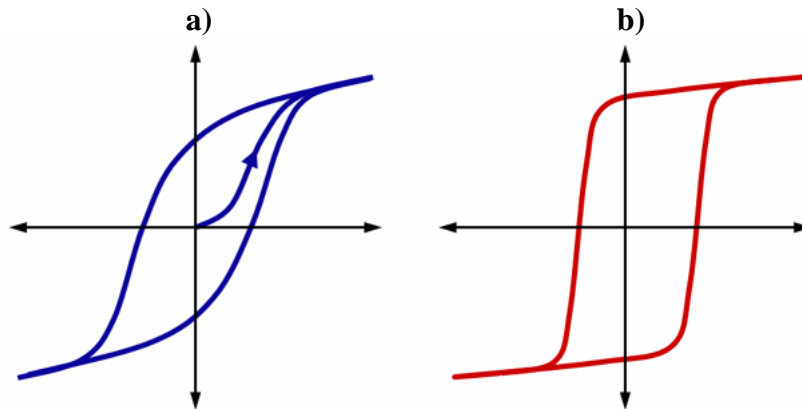


Figure 2.7: Characteristic hysteresis loops for a) a ceramic ferroelectric (**blue**) and b) single crystal, mono-domain ferroelectric (**red**).

Starting at high positive field all dipoles are aligned with the field and the polarization is saturated. As the field is reduced to zero the material retains some of the polarization and the remnant polarization is measured at $\bar{E} = 0$; the polarization direction is maintained even in small fields opposite in direction to the polarization up to the point $-E_C$ is reached, i.e., the coercive field. This field is sufficient to overcome the energy barrier in the double potential well and ions shift to align the dipoles with the applied field. At large negative fields the situation is identical to large positive fields although the directions are reversed. In reality, measured P - E loops of polycrystalline, polydomain ceramic ferroelectrics create a smoother response. In this case the collection grains are randomly oriented. At high fields the dipoles align to the field as much as the polar directions allow. As the field is decreased the polarization drops with a non-zero slope since various inhomogeneities (*viz.* crystalline defects, internal strains, temperature gradient, and depolarization fields) promote backswitching. Since this occurs the remnant polarization substantially smaller than the saturated polarization. Near E_C the P - E response has a much lower slope due to the kinetics of domain wall movement and domain nucleation necessary to switch the polarization. Although P - E loops exemplify the connection of crystallographic distortions and ferroelectricity to macroscopic electrical response the extension to permittivity is more meaningful to capacitors.

Permittivity can be calculated from the relationship between field and polarization. Assuming that all other contributions to dielectric displacement are insignificant compared to dipoles then the permittivity at any value of electric field is simply the instantaneous slope of the P-E loop.⁶

$$\epsilon_r = \left(\frac{\partial \bar{P}}{\partial \bar{E}} \right) \quad \text{eqn [2.15]}$$

Assuming the ferroelectric is inserted as the dielectric in a parallel plate capacitor, the capacitance is directly proportional to permittivity only by constants of capacitor dimension. The hysteretic behavior seen in a P-E loops is still seen in permittivity verses electric field, ϵ -E, or capacitance verses voltage, C-V, measurements.

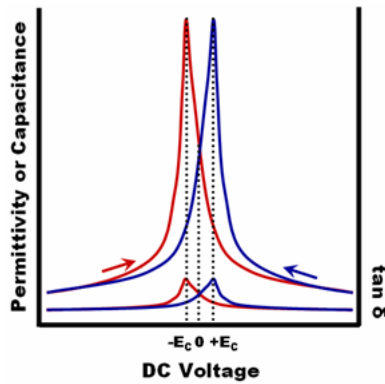


Figure 2.8: Non-linear dielectric response with respect to biasing field. In the ferroelectric phase the response is hysteretic with the peak permittivity, or capacitance, occurring at the coercive field, E_C .

The response is non-linear with the permittivity peaking at the coercive field when domain wall movement is maximized and saturates to a minimum value at high fields. Any device exploiting this non-linear response would operate in the regions where the permittivity changes most rapidly yet this does not occur at zero fields which can become a major problem in device design as hysteresis always adds complexity to circuit operation. If the high permittivity and high degree of non-linearity of ferroelectric materials can be maintained while eliminating hysteresis an optimal condition for

frequency agile device design would exist. Fortunately, the last criterion for ferroelectricity, the phase transition to higher symmetry at T_C , allows this.

2.3.3. Ferroelectric phase transition

A necessary criterion for classification for ferroelectricity is the existence of a phase transition from a low temperature low symmetry ferroelectric phase to a higher symmetry non-polar paraelectric phase above a transition temperature called the Curie temperature. The temperature dependence of permittivity for a ferroelectric is given by figure 2.9.

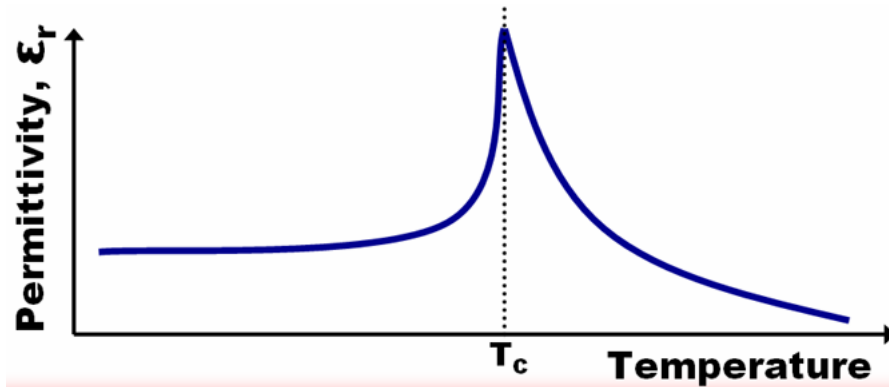


Figure 2.9: Temperature response of permittivity for a single crystal mono-domain ferroelectric crystal.

Beginning at high temperatures, the permittivity increases as the temperature is reduced following the Curie-Weiss law.

$$\epsilon \cong \frac{C_{C-W}}{T - T_0} \quad \text{eqn [2.16]}$$

The Curie constant, C_{C-W} , and the Curie-Weiss temperature, T_0 , are empirically determined to describe the magnitude of the inverse proportionality of permittivity with temperature. For barium titanate, no exact indisputable value for $C_{C-W}^{BaTiO_3}$ has been determined yet all measurements are on the order of 10^5 and the Curie-Weiss temperature $T_0^{BaTiO_3}$ is typically 10 °C lower than the transition temperature.⁶ Curie-Weiss behavior is valid for many other non-linear dielectrics for example, strontium titanate, $SrTiO_3$, which

is considered an incipient ferroelectric since the predicted transition temperature is less than 0 K. The Curie-Weiss constants have been measured for SrTiO₃ to be $C_{C-W}^{SrTiO_3}$ slightly less than 10^5 and $T_0^{SrTiO_3} \sim 20$ °C.^{34, 35}

Near and at the transition temperature, T_C , anomalies in dielectric, elastic, optical, and thermal properties are observed. The transitions can be of first or second order. These classifications constitute a transition that occurs discontinuously in first order cases, or smoothly over a range of temperatures in the second order scenario. Both scenarios were modeled by Devonshire in 1954. This phenomenological theory is based on the thermodynamic function for a ferroelectric system. The equations of state for ferroelectric crystals relate the system free energy to polarization based on the influences of temperature, stress and external electric fields. The results of these calculations show that polarization has equivalent minima at $P \neq 0$ at temperatures below T_C supporting the observation of spontaneous polarization. Results of the calculations show for a second order transition the minima slowly collapse toward $P = 0$ yet for a first order transition free energy minima move very little yet a localized reduction of the free energy appears at $P = 0$ and becomes a global minima at $T \geq T_C$.³⁶ First order ferroelectric transitions are associated with discontinuous changes in polarization, latent heat, and specific heat. Most perovskite oxide ferroelectric show first order transition behavior.

Devonshire's description adequately describes the behavior of measured parameters though the phase transition yet a more complete understanding of the physical phenomenon can be proposed using the dynamics of lattice vibrations. The transverse optical vibrational mode in perovskites showing displacive transitions is associated with the vibration of the B-site cation and is defined as the “soft mode.” As the temperature is lowered from a temperature above the transition temperature this mode decreases in frequency (increases in wavelength) at the Brillouin Zone center at zero wave number.

$$\omega_{TO}^2 = K(T - T_0) \quad \text{eqn [2.17]}$$

Here ω_{TO} is the angular frequency of the transverse optical mode or soft mode, T_0 is the temperature where the frequency of the mode falls to zero, and K is a constant that

determines the how fast the frequency falls with T . The non-zero frequency of the soft mode above the transition shows that the cations are free to vibrate around their respective unit cell centers and therefore the time and spatially averaged charge density is located at the unit cell center, thus polarization cannot be supported. As the soft mode frequency falls to zero the mode is frozen and all cations vibrate in phase over a longer distance within the crystal. This can interpreted as an overall spontaneous polarization since at a low enough temperature (where frequency goes to zero, or wavelength goes to infinity) all cations are displaced away from the center of the unit cell at any point in time. The permittivity is a result of the linear combination of all displacements which can be described by all the optic modes at $k = 0$ yet the soft mode contributes the most significantly to the permittivity in ferroelectrics as seen in equation 2.18.

$$\varepsilon = \frac{1}{\omega_s^2} \quad \text{eqn [2.18]}$$

As the temperature is lowered below the transition temperature the soft mode decreases in wavelength leading to vibrations including longer-range coordination of polarizing displacements and the permittivity increases. At the transition temperature the permittivity peaks and spontaneous polarization is supported. If hysteretic behavior is to be avoided then a device can be operated just above the transition temperature while still taking advantage of high permittivity.

2.4. PARAELECTRIC BEHAVIOR

Above the transition temperature paraelectric behavior is observed. This phase is characterized by zero values of coercive field, no spontaneous polarization, and the absence of hysteresis. In the paraelectric state the material is centrosymmetric and therefore non-polar, yet the non-linear dielectric behavior is still maintained. Since spontaneous polarization, and therefore domains, do not exist in the paraelectric phase the dielectric losses are reduced. This combination of a highly non-linear dielectric response,

lack of hysteresis, and low losses make formulations displaying paraelectric behavior at operation temperatures superior to formulations where the ferroelectric phase is stable.

2.4.1. Non-linear dielectric response in the paraelectric regime

Given the explanation of lattice vibrations, at temperatures near yet above the transition temperature the soft mode frequency is low and there is some semblance of coordinated ion vibrations over short distances. The higher temperatures give rise to greater thermal oscillations and allow the ionic character of bonds to provide greater restoring force to an isotropic arrangement than the directional covalent bonds within the unit cell. Above the transition temperature there is sufficient restoring force to stabilize the non-polar state in the absence of external fields. The application of an external field can induce a large polarization since the susceptibility is still large and the wavelength of optic mode vibrations is still comparatively long. Since essentially the same fundamental forces are interacting in the material the dielectric response is analogous to that of a ferroelectric yet absent of hysteresis.

The Devonshire theory of ferroelectricity suggests that the application of an electric field can shift the transition temperature and stability of the ferroelectric phase to higher temperatures. When measuring the permittivity just above the equilibrium T_C the application of an external electric field stabilizes the polarization to a higher temperature.³⁶ Since the material is isotropic when the field is applied the polarization is necessarily aligned with the applied field. This lowers the measured permittivity and as the applied field is increased the permittivity reduces toward the permittivity found at saturated polarization. Using either the thermodynamic model of Devonshire or the model of lattice dynamics a similar prediction for the non-linear response of permittivity is made.

See in figure 2.10 is a P - E and ϵ - E curves for a typical paraelectric material. Notice the similarities to figures 2.7 and 2.8 for the ferroelectric case.

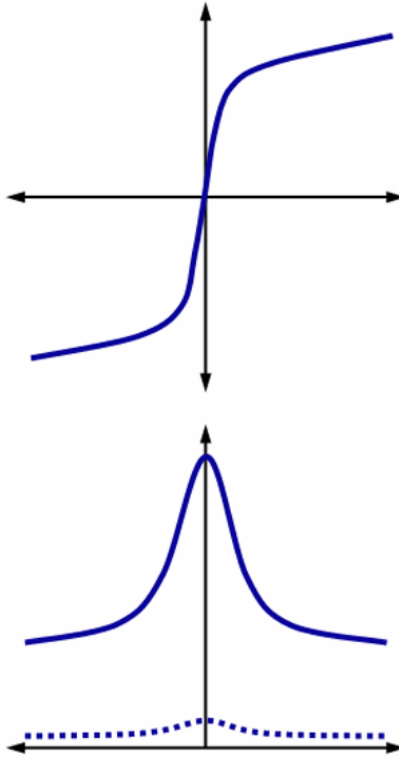


Figure 2.10: P - E loops in the paraelectric phase and the corresponding ε - E curve (dotted line represents $\tan \delta$).

The most notable feature with respect to a ferroelectric response is the absence of polarization hysteresis. The low field limit is characterized by large slope which saturates at high fields. This saturation occurs when polarization can no longer increase because ions and associated charge are far from low energy positions and restoring forces due to bonding restriction further charge separation.. The derivative of polarization with respect to the field gives the ε - E curve of a paraelectric material, where again, the form is similar to that of a ferroelectric yet without hysteresis. The paraelectric response is more practical for designing tunable devices where frequency agility is the main goal and hysteretic behavior would cause complication with control algorithms.

From this ε - E or the adapted C - V curve the metric of tunability can be defined.

$$n = \frac{\varepsilon(\bar{\mathbf{E}} = 0)}{\varepsilon(\bar{\mathbf{E}} = E_{SAT})} = \frac{C(V = 0)}{C(V = V_{SAT})} \quad \text{eqn [2.19]}$$

Alternatively, relative tunability is reported as a quantification of tunability.

$$\eta = \frac{\varepsilon(\bar{\mathbf{E}} = 0) - \varepsilon(\bar{\mathbf{E}} = E_{SAT})}{\varepsilon(\bar{\mathbf{E}} = E_{SAT})} = \frac{C(V = 0) - C(V = V_{SAT})}{C(V = V_{SAT})} = \frac{n-1}{n} \quad \text{eqn [2.20]}$$

Where absolute tunability, n , is greater than one and is useful to describe the magnitude of permittivity change with field. The relative tunability, η , is less than one and listed as a fraction or a percentage to the differences in modest tunabilities. Here tunability is defined as the ratio of permittivity or capacitance in the lack of an external electric field of voltage to the permittivity or capacitance at saturation. The choice of field to measure the saturated value is arbitrary yet the functional dependence of permittivity saturates at high fields thus only slight increases in tunability are appreciated by extending the saturation field. The fundamental limit for saturated permittivity for a ferroelectric is established by the permittivity measured in a fully poled material along the poled direction. For barium titanate this is the c-axis permittivity has been measured at 160.³⁷ This value can be used as a guide to the saturated permittivity that would be observed for paraelectric barium titanate (measured above the transition temperature). One important trend observed for tunable paraelectric materials is that tunability increases proportionally to the maximum observed permittivity.³⁸ The effective tunability is a measure of the extrinsic dielectric response creating high permittivity at zero bias and the ability to applied large DC electric fields and approach saturation. Any crystalline imperfections or secondary phases which dilute the electromechanical response will reduce the dielectric tunability.³⁸ The tunability and lack of hysteresis in the paraelectric phase enable the use of these materials in tunable frequency-agile devices yet permittivity is not the only concern; dielectric losses must also be considered.

2.4.2. Losses in the paraelectric regime

Of equal importance to the tunability is dielectric loss tangent. The reduction of loss tangent is the central motivation for choosing a paraelectric phase. All losses can be

divided into intrinsic losses or extrinsic origins. Intrinsic loss is due to the interaction of the AC field with the lattice vibrations, or phonons, present in the material. Extrinsic loss arises from interactions of the electric field with defects. These defects can not be avoided entirely and can be exacerbated by the processing, stoichiometry, and microstructure. The following discussion follows the concepts outlined in extensive reviews on the subject for displacive ferroelectric materials.³⁸⁻⁴¹

Intrinsic contributions to loss involve the interaction of phonons, typically the transverse optical lattice vibrations of the soft mode, of frequency, ω_{TO} , with the oscillating electric field of frequency, ω . For displacive ferroelectrics in the paraelectric phase there is a large disparity in frequency between the soft mode and electric field frequencies. Conservation laws are difficult to satisfy when $\omega_{TO} \gg \omega$ and only three types of interactions are likely to occur and contribute to loss: 3-quantum, 4-quantum, and quasi-Debye interactions. For a two-phonon mechanism, interactions with an oscillation field can only occur when the two phonon differ very little in frequency; a situation which only occurs when there is degeneracy between the various branches of the soft mode. This degeneracy arises from the centrosymmetric symmetry associated with the paraelectric phase. The function dependence of loss with respect to ω , T , ϵ for a displacive ferroelectric in the paraelectric phase is given below.

$$\tan \delta \equiv \frac{\epsilon''}{\epsilon'} \propto \omega T^2 \epsilon^{3/2} \quad \text{eqn [2.21]}$$

Figure 2.11 shows actual data for SrTiO₃ measured at high frequency. In this case, the reduction in permittivity as temperature increases from 0 K causes a drop in loss tangent via the $\epsilon^{3/2}$ dependence. Above 150 K, the loss begins to increase, and is associated with the T^2 dependency in equation 2.21.

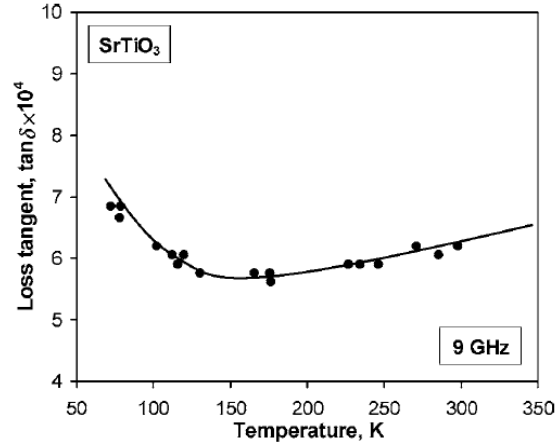


Figure 2.11: Experimental data for the temperature dependence the 3-quantum loss mechanism in SrTiO₃. Figure is adapted from Tagantsev et al³⁸ based on data from Buzin.⁴²

Conservation laws are less restrictive and insensitive to crystal symmetry when 3 phonons interact with an electric field. In the high temperature limit $T \geq \hbar\omega_{TO} k_B^{-1}$, which is valid at near and above room temperature, the functional dependence of this mechanism is identical to equation 2.21 yet the magnitude is smaller than the 3-quantum (or two phonon) case. The quasi-Debye mechanism is only valid for non-centrosymmetric crystals and operates in paraelectric crystals only when the electric field induces dipoles and crystal distortions. When the electric field is applied a phonon dispersion relaxation occurs and the phonon distribution deviates from the equilibrium value. The dependence is a complex function depending on the phonon damping constant, the amount of electric field applied to break the centrosymmetric symmetry, and exact phonon distribution. In the case of a displacive ferroelectric the contribution is an order of magnitude greater than 3 and 4 quantum mechanisms. Figure 2.12b shows the results of a quasi-Debye calculation of loss versus applied biasing field and AC field frequency.

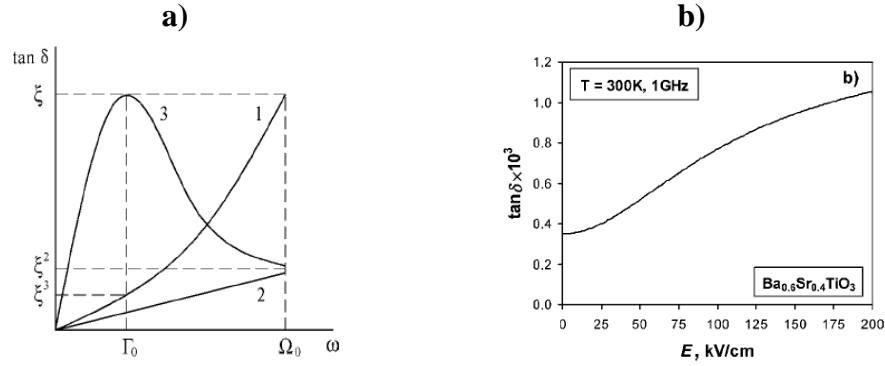


Figure 2.12: Figure adapted from Tagantsev et al.³⁸ Plot a) gives a schematic comparison between 1) 3 quantum interactions, 2) 4 quantum interactions and 3) quasi-Debye contributions to loss. Plot b) gives the calculated functional dependence and magnitude of the quasi-Debye loss for paraelectric Ba_{0.6}Sr_{0.4}TiO₃ tested at 300K and 1 GHz (actual data from Sengupta et al⁴³).

Figure 2.12a gives a comparison the pertinent intrinsic loss mechanisms for a paraelectric material. The overall intrinsic loss the linear superposition of all significant mechanisms and therefore the intrinsic loss of these materials should be no greater than $\tan \delta \sim 10^2$.

The losses typically measured in ferroelectric crystals is often an order of magnitude or greater than the expected intrinsic values. This disparity can be attributed to extrinsic sources. Extrinsic losses include those caused by charged defects, quasi-Debye losses incurred by the random local polar regions caused by defects, structural imperfections, and microstructure, and those based on universal relaxation. Entropic considerations and limitations of processing of electroceramic materials predicts finite point defect concentrations which by necessity exist in equilibrium with compensating electronic and ionic charge carriers. These defects routinely occur in the ppm to ppt level. Additionally, the purity levels of raw materials impart substantial concentrations of isovalent and aliovalent impurity cations and anions. The discrete and often mobile charges associated with impurities also contribute to losses in paraelectric materials. These losses increase according to the square of the electro-active defect's charge and directly proportional to their number density in the lattice.

$$\tan \delta \propto Z^2 N_{defects} \quad \text{eqn [2.22]}$$

This loss mechanism increases proportionally with the permittivity thus complicating the optimization for high tunability and low loss yet in paraelectric materials the permittivity quickly drops with the application of an electric biasing field.

$$\tan \delta \propto \epsilon \propto \frac{1}{E} \quad \text{eqn [2.23]}$$

This allows identification of different regions in the characteristic ϵ - E curve for a paraelectric crystal.

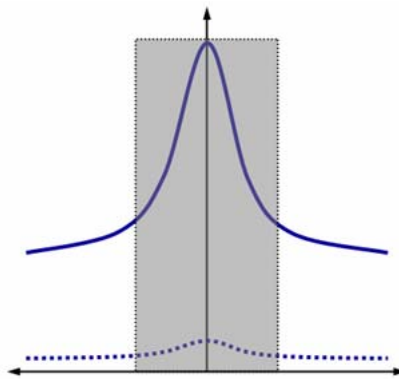


Figure 2.13: ϵ - E curve where the response in the grey area is due to extrinsic contributions to permittivity and loss and regions outside of the grey area the intrinsic response can be observed.

At low bias fields the loss is dominated by extrinsic effects that are present in real materials and the high field regions show intrinsic permittivity and loss from intrinsic mechanisms. Structural defects such as planar defects (i.e. surfaces, grain boundaries, stacking faults, twinning, etc.), line defects (i.e. dislocations), and neutral point defects can impart localized regions which assume polar characteristics. These randomly distributed and aligned polar regions reduce local symmetry and therefore lead to quasi-Debye losses. The loss mechanism is identical as described above yet they are caused by extrinsic defect and hence considered an extrinsic loss mechanism. This loss also contributes mainly to the high permittivity region of a ϵ - E curve following the

following relation where $\langle P_{loc} \rangle$ is the average polarization of the polar regions in the material.

$$\tan \delta \propto \varepsilon^{3/2} \langle P_{loc}^2 \rangle \quad \text{eqn [2.24]}$$

When considering high frequencies the relaxation of the polarization mechanism inherent in paraelectric materials increases losses as described the previous section, as seen in figure 2.2. At microwave frequencies between 10^1 - 10^2 GHz the ionic mechanism responsible for the high permittivity can relax. Little theory has been established on exactly what frequency this should occur and much of the knowledge about this relaxation is gleaned experimentally.⁴⁴ In most experimentally observed samples the extrinsic losses dominate thus obfuscate the onset of relaxation in the microwave frequency regime.

The paramount goal of this thesis is to synthesize barium strontium titanate thin films in a configuration which gives the optimal tunability with the lowest levels of loss. The review of ferroelectric and paraelectric theory indicates that efforts to increase the peak permittivity will also increase the tunability. This methodology may lead to increased levels of dielectric loss especially if extrinsic loss mechanisms are not controlled. Intrinsic losses are of a magnitude acceptable particularly in the case where device designs can employ mainly the high field region of the ε - E curves.

2.5. BARIUM TITANATE- STRONTIUM TITANATE SOLID SOLUTIONS

2.5.1. Bulk BST properties

This section will review reported values for bulk ceramic and single crystals of BST. Since the dielectric properties are highly sensitive to any deviation from purity, structural perfection, or mechanical boundary conditions no absolute value for dielectric properties can be stated. Mechanical, thermal, and optical properties are also sensitive to microstructure and chemistry to varying degrees.⁸ These deviations from ideality are

often exacerbated in thin films, therefore results of bulk properties provide comparative property values with which to view thin film results.

Barium titanate, BaTiO_3 , is a ferroelectric perovskite oxide. At high temperature, barium titanate is cubic with $m3m$ cubic symmetry and displays paraelectric behavior. When cooled below the ferroelectric transition temperature, a transformation to tetragonal $4mm$ symmetry occurs and the material is ferroelectric with the primary polarization directions parallel to the cubic $\langle 001 \rangle$ directions. The ferroelectric transition temperature was originally believed to be 120°C , yet observations of $T_C = 130^\circ\text{C}$ ⁸ have been observed in high purity single crystal specimen grown by Remeika's process.⁴⁵ Although the precise ferroelectric phase transition temperature depends on purity and the particle or crystallite size, T_C values $\sim 120^\circ\text{C}$ are routinely observed. At room temperature, barium titanate is ferroelectric with tetragonal symmetry. The maximum spontaneous polarization, $P_S = 26 \mu\text{C cm}^{-2}$, was observed in a single crystal specimen.⁴⁶ The coercive field is dependent on microstructure, including domain structure, and length of time an electric field is applied yet careful measurements give $\frac{1}{2} \text{ kV cm}^{-2} < E_C < 2 \text{ kV cm}^{-2}$.^{37, 46, 47} Single crystals show c-axis permittivity of 4000 and a-axis permittivity of 400.^{48, 49} Square hysteresis loops are routinely observed in single crystal mono-domain specimens, but the incongruent melting of BaTiO_3 makes single crystals difficult to grow in appreciable sizes. Much larger spontaneous polarization values and coercive fields can be achieved in compositions of lead zirconate titanate, PZT, with a morphotropic phase boundary near room temperature, $\text{Pb}(\text{Zr}_{0.48}, \text{Ti}_{0.52})\text{O}_3$, making PZT better suited for non-volatile memory and transducer applications.^{50, 51} Barium titanate is more useful as a high permittivity ceramic dielectric for capacitive applications.

Ceramic barium titanate gives slanted hysteresis loops with remnant polarizations of $8 \mu\text{C cm}^{-2}$.⁵² At room temperature, energy minimization requires formation of domains and barium titanate samples have 90° ferroelastic domain walls and 180° domain walls free from strain. In ceramic specimens, the complex mechanical boundary conditions of grain boundaries necessitate both domain wall types. This microstructure mechanical clamps crystallites leading to deviations of dielectric properties from the single crystal,

mono-domain measured values.^{6, 8} Maximum permittivity of 6000 is observed in fine grained ceramic specimens when the grain size is $\sim 1 \mu\text{m}$.⁵³ The ease of producing barium titanate ceramics allows its use in a wide array of applications requiring high permittivity, yet dielectric properties are dependent on microstructure (specifically crystallite size) forcing the need to carefully consider structure-property relationships for any application.

Two additional transformations are encountered in barium titanate upon cooling, from $5 \text{ }^\circ\text{C}$ to $-90 \text{ }^\circ\text{C}$ an orthorhombic symmetry with the primary polarization axis along cubic $\langle 110 \rangle$ directions, and below $-90 \text{ }^\circ\text{C}$ a rhombohedral symmetry with the primary polarization axis along cubic $\langle 111 \rangle$ directions. Anomalous permittivity peaks are associated with all phase transitions maintaining high permittivity values over a large temperature range ($\sim -100 \text{ }^\circ\text{C}$ to $> 120 \text{ }^\circ\text{C}$). In the cubic phase above the transition temperature, the permittivity shows Curie-Weiss behavior with constants of C_{C-W} on the order of $10^5 \text{ }^\circ\text{C}$ and T_0 roughly $10 \text{ }^\circ\text{C}$ less than the Curie temperature.^{46, 54, 55} Although permittivity remains large, over typical device operation temperature ranges, pure barium titanate shows substantial temperature dependent permittivity.

Strontium titanate, SrTiO_3 , is an incipient ferroelectric material with perovskite structure. It is termed an incipient ferroelectric since at all temperatures it is cubic and supports no spontaneous polarization, yet the permittivity temperature dependence displays Curie-Weiss behavior.^{56, 57} The room temperature permittivity of strontium titanate is on the order of 250.^{23, 58, 59} At low temperatures, a tetragonal ferroelectric phase can be stabilized by strain⁶⁰ or electrical fields.^{36, 61} Recent experiments on biaxially strained SrTiO_3 epitaxial thin films reveal the ability to shift the T_C of SrTiO_3 to room temperature.⁶⁰ Strontium titanate is fully miscible in barium titanate allowing solid solutions of $(\text{Ba}_x, \text{Sr}_{1-x})\text{TiO}_3$, BST, to be synthesized from $0 < x < 1$.⁶² When alloyed, Sr^{2+} substitutes for Ba^{2+} in the perovskite lattice; the isovalent substitution reduces the perovskite lattice parameter since the Sr^{2+} cation is smaller than the Ba^{2+} cation that was replaced.⁶³ Similar to subjecting BaTiO_3 to hydrostatic pressure, the T_C of BST is a linear function of strontium titanate composition.^{23, 64-68} The T_C of BST can be linearly reduced $3.7 \text{ }^\circ\text{C}$ per mole percent strontium titanate and concurrently the tetragonal to orthorhombic

transition temperature is linearly reduced approximately 2 °C per mole percent strontium titanate while the orthorhombic to rhombohedral transition is relatively invariant with strontium titanate content.^{8, 64} The temperature dependent permittivity was characterized for ceramic BST by Smolenskii over a large composition range.⁶⁵ No microstructural characterization is given; therefore, no conclusion can be made regarding the apparent increase of permittivity near $x = 0.5$.

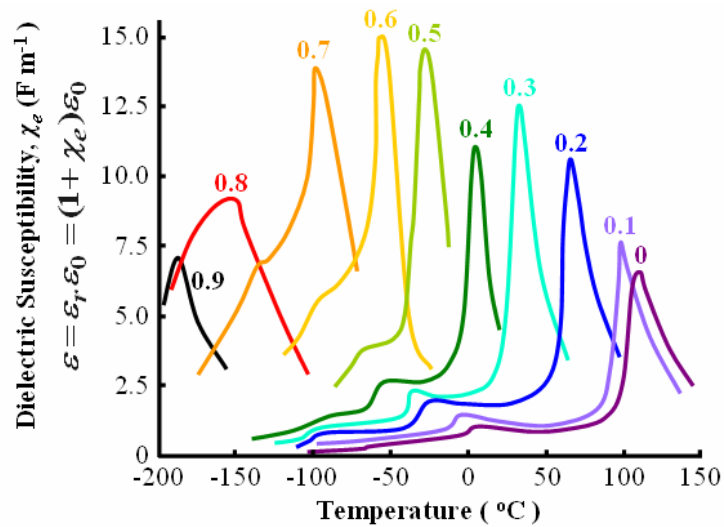


Figure 2.14: Smolenskii’s data showing the linear ferroelectric transition temperature shift with increasing mole percent SrTiO₃. Although it appears that maximum permittivity increases near equimolar ratios of BaTiO₃ and SrTiO₃, no data on microstructure is given.⁶⁵

The affect of alloying agents to manipulate the temperature profile of barium titanate based compositions is well understood.^{6, 8} Mass produced multilayer capacitors utilize a host of alloying agents in a barium titanate based dielectric with a microstructure termed “core-shell.” This microstructure allows tailoring of the temperature coefficient of capacitance while concurrently realizing high effective permittivity. The dielectric layers are synthesized starting from BaTiO₃ powder coated with specific molar ratios of alloying agents. When heat treated, a dense microstructure results where the interior of grains, the core, is nearly pure BaTiO₃ and the regions adjacent to the grain boundaries, the shell, contain the majority of alloying agents. This microstructure gives high apparent permittivity from the nearly pure core volumes and engineered temperature profiles from

the shell volume. By superposition the resulting permittivity and temperature profile meet specifications set by the Electronics Industry Association (EIA).⁶⁹⁻⁷¹

2.6. BST THIN FILMS

The use of thin film based devices allows the realization of large applied electric fields by modest applied voltages. In a MIM device where the electrode spacing is determined by the dielectric thickness, on the scale of $< 1 \mu\text{m}$, 30 V can generate 300 kV cm^{-1} . This can allow for the realization of large variations of DC bias dependent properties with voltages available in common circuits. Conversely, dielectrics with reduced resistivity as a result of processing allow unacceptable leakage current levels in a thin film format. Additionally, the Curie temperature, temperature profile broadness, and permittivity are largely affected by strain, microstructure, and purity. Extrinsic effects which are more difficult to control in thin films than in bulk.

2.6.1. Finite size and scaling effects

The effects of reducing crystallite size on features of the ferroelectric phase transition are well documented. By lattice dynamic arguments, the condensation of a soft mode which supports spontaneous polarization requires a collection of sufficient dipoles. This requires the presence of multiple unit cells to observed ferroelectricity^{72, 73} yet this hypothesis has yet to be fully proven experimentally. Also, depolarization fields at ferroelectric surfaces in the presence of electrodes destabilize spontaneous polarization at length scales approaching several unit cells.⁷⁴ Theoretical calculations and highly controlled studies on specimens with small crystallite size give a minimum volume on the order of $10 - 1000 \text{ nm}^3$ to support spontaneous polarization.⁷⁴⁻⁷⁸ These studies establish a fundamental crystallite size limit for the observation of ferroelectricity, yet many studies have observed reduced polarization and T_C shifts in much larger length scales. The room temperature permittivity was observed to approach a maximum for grain sizes $\sim 1 \mu\text{m}$.^{53, 79-81} Additional, as crystallite size is reduced below 100 nm, a shift of T_C to lower temperatures have been observed^{75, 77, 78, 82-86} which is consistent with theoretical

treatments.^{36, 87-90} Similar effects on longer length scales are increasingly being termed “scaling” effects, since they are due to extrinsic forces frustrating the ferroelectric phase transition.⁹¹ Since these scaling effects are observed in dimensions encompassing the thin film regime they are of particular interest to this study.

2.6.2. BST thin film properties

Study of BST thin films has been an active area of research for the approximately 3 decades. The desire to integrate high permittivity thin film into microelectronics has driven these studies, specifically high K dielectrics for large charge storage capacitors in DRAM devices.^{92, 93} First attempts to form BaTiO₃ thin films was by evaporation resulting in $\epsilon = 100 - 200$ and a reduced T_C by 40 °C below bulk values^{94, 95}; the poor observed dielectric properties can be attributed to non-ideal stoichiometry. Stoichiometric BST thin film deposition has been demonstrated by sputtering,⁹⁶⁻¹⁰⁸ pulsed laser deposition (PLD),¹⁰⁹⁻¹¹¹ metal-organic chemical vapor deposition (MOCVD),^{84, 85, 112-114} and chemical solution deposition (CSD).¹¹⁵⁻¹¹⁷ These studies can routinely achieve room temperature permittivity > 600 with loss tangents $\tan \delta < 0.02$. These values are significantly lower than observed for bulk BST.

Thickness dependent dielectric properties are analyzed by plotting inverse capacitance density versus thickness. A linear relationship indicates permittivity is not a function of film thickness and a zero thickness intercept that does not cross the origin indicates the possibility of a low permittivity interfacial phase that does not scale with thickness. Shin *et al* explored sputtered BST (composition unspecified) thin films 30 - 150 nm deposited at 490 °C on Pt and IrO₂ coated Si substrates. A sub-linear inverse capacitance density was observed with film thickness and attributed to a interfacial layer ($\epsilon_i = 52$, $t_i = 10$ Å) by a circuit model. The result was attributed to Schottky barriers at the electrode interfaces yet no temperature dependent data or microstructure is reported.¹⁰⁷ Lee *et al* reported reduction of grain size with decreasing film thickness of sputtered (Ba_{0.5}, Sr_{0.5})TiO₃ thin films deposited on platinized Si at 400 °C from targets with excess BaO and SrO to achieve stoichiometric films. The {110} fiber textured microstructure

had a lateral grain size of 20 nm for 25 nm thick films increasing monotonically to 80 nm for 300 nm thick films. Stoichiometry was confirmed by RBS yet no temperature dependent measurements were reported. Inverse capacitance density analysis revealed a positive deviation from linearity below 100 nm (linear above this thickness).¹⁰² PLD epitaxial $(\text{Ba}_{0.7}, \text{Sr}_{0.3})\text{TiO}_3$ films on $\text{YBa}_2\text{Cu}_3\text{O}_{7-\delta}$ superconducting substrates were explored by Chen *et al* as a function of thickness from 100 - 300 nm. Inverse capacitance density versus thickness was linear with an intercept of $t_i/\epsilon_i = 0.08$ nm. Results are explained by the existence of low permittivity interfacial phase although no microscopic or spectroscopic evidence is given and no temperature dependent measurements were provided.¹¹¹ Sinnamon *et al*¹⁰⁹ and Lookman *et al*¹¹⁰ explored the thickness dependence of PLD epitaxial $(\text{Ba}_{0.5}, \text{Sr}_{0.5})\text{TiO}_3$ thin films deposited on conducting oxide substrates. The observed non-linear inverse capacitance density thickness dependence and absence of an intercept through the origin is attributed to scaling effects where T_C and maximum permittivity decrease as film thickness is reduced and the temperature profile broadens. Basceri *et al* report on the thickness dependence of MOCVD deposited $\text{Si}/\text{SiO}_2/\text{ZrO}_2/\text{Pt}/(\text{Ba}_{0.7}, \text{Sr}_{0.3})\text{TiO}_3/\text{Pt}$ structures where the BST films, 24 - 160 nm thick, are {100} fiber textured. Linear inverse capacitance density with an intercept of 0.01 nm is observed.¹¹² The authors recognize that films are grown Ti rich to improve leakage current and provide the following possible explanations for an intercept not through the origin. A combination of extrinsic and intrinsic phenomenon including low permittivity interface layer, finite size effects giving decreasing permittivity with decreasing thickness, reduced polarizability due to Ti non-stoichiometry, and/or changes in polarizability due to biaxial mechanical strain imparted by the substrate.¹¹⁸ These studies exemplify how scaling effects can shift the ferroelectric transition temperature with decreasing crystallite size realizing a change of room temperature permittivity with film thickness. In many of the studies a low permittivity interfacial layer is proposed while the action of scaling effects is exacerbated by extrinsic factors associated with details of the film deposition technique and the mechanical boundary conditions³⁵ imparted by the choice of substrate.

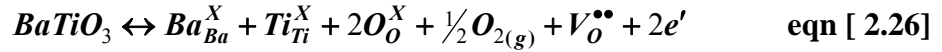
Two recent studies of BaTiO₃ at small dimensions reveal that bulk like permittivity and ferroelectric transition temperatures can be realized on the length scales of thin films. Ihlefeld showed a similar dependence of permittivity and T_C on grain size as observed by Frey *et al*⁸¹ and Arlt *et al*⁵³ in bulk systems by deposition of randomly oriented BaTiO₃ thin films, 600 nm thick film, on Cu foil substrates by CSD. This result was achieved by deposition on free standing Cu foils that imparted low values of biaxial strain and allowed crystallization temperatures > 900 °C.^{116, 119} This combination of high process temperatures with minimized substrate mechanical clamping cannot be achieved in rigid substrate systems employing Pt or conductive oxide electrodes. Electrical measurements on BaTiO₃ single crystals thinned to 75 nm by a focused ion beam (FIB) gave a 25,000 permittivity and temperature dependent dielectric properties identical to macroscopic single crystal BaTiO₃ specimens reported by Saad *et al*.¹²⁰ These studies exemplify that no intrinsic size effect is responsible for reduced permittivity or frustrations of the ferroelectric transition temperature in (Ba_x, Sr_{1-x})TiO₃ thin film with grain sizes or fiber texture/epitaxial film thickness $> 60 - 75$ nm. Most observations can be attributed to extrinsic effects imparted by the synthesis technique and choice of substrate system.

2.7. BST DEFECT CHEMISTRY

At thermodynamic equilibrium, free energy calculations predict non-zero concentrations of point defects. Point defect concentrations increase as temperature increases and when specifically speaking of oxygen stoichiometry is further increased by low pO_2 conditions. These thermodynamic implications are particularly problematic for electroceramic oxides. In perovskite oxides, Frenkel disorder is highly unlikely since open interstice volumes are too small for Ba²⁺ and O²⁻ ions and electrostatics prohibit Ti⁴⁺. Absent of impurities, this leaves oxygen vacancies as the most likely point defect.¹²¹ The generic Schottky defect reaction for oxygen vacancies with compensation by electrons is given below.



This reaction is written using Kroger-Vink notation.¹²² The reaction shows that as oxygen leaves the lattice, a 2+ oxygen vacancy is left behind compensated by free electrons to maintain electroneutrality. Inserting this Schottky reaction into a reaction considering the BaTiO₃ lattice gives the following reaction.



Using these reactions, a mass-action expression can be written.

$$[V_o^{\bullet\bullet}] n^2 = K p O_2^{-1/2} \quad \text{eqn [2.27]}$$

Electron compensation is typically favored in pure perovskite oxides; therefore the following electroneutrality condition is valid.

$$n \approx 2[V_o^{\bullet\bullet}] \quad \text{eqn [2.28]}$$

Combining the electroneutrality condition with the mass-action equation gives the dependence of oxygen vacancy concentration on temperature and pO_2 .

$$[V_o^{\bullet\bullet}] = \left[\frac{1}{4} p O_2^{-1/2} \exp\left(\frac{-\Delta h_v}{kT}\right) \right]^{1/3}$$

As pO_2 is reduced the concentration of oxygen vacancies increases proportional to $(pO_2)^{1/6}$ and as temperature is increased the concentration of oxygen vacancies is proportional to $[\exp(-\Delta h_v/kT)]^{1/3}$, where Δh_v is the enthalpy of formation for an oxygen vacancy equal to -568 kJ mol⁻¹.¹²³ Since the formation of oxygen vacancies is associated with free electrons by electroneutrality then resistivity is expected to decrease as process temperature increases and pO_2 decreases.

Chan & Smyth's thoroughly studied conductivity in pure bulk barium titanate where a maximum resistivity of 0.27 Ω•cm was reported for samples annealed at 900 °C

and 10^{-5} atm pO_2 .¹²⁴ The reason for maximum resistivity at slightly reducing conditions is currently under considerable debate. Tsur and Randall attribute these findings to oxygen vacancies compensating for cation vacancies from intrinsic full Schottky defects¹²⁵ where Smyth *et al* propose that oxygen vacancies compensate extrinsic point defects from acceptor type impurities.¹²⁴ In the review by Nowotny *et al* both situations are considered and states cation vacancy diffusivities are small limiting the previous studies' ability to achieve equilibrium conditions.¹²⁶

Assuming the specimen reaches equilibrium at the peak anneal temperature and oxygen activity, an oxygen vacancy concentration can be calculated. Conservative estimates assume this level is quenched into the dielectric upon cooling. Using thermodynamic, electrochemical, and semiconductor physics, anneal conditions of 900 °C and 10^{-12} atm pO_2 give an oxygen vacancy concentration and conductivity of 220 ppb and $2.42 \cdot 10^{-5}$ ($\Omega \cdot \text{cm}$)⁻¹ in BaTiO₃ (and assumed to be similar for BST).

Sputter deposition and subsequent low pO_2 , high temperature anneals create a situation where an inauspicious low resistivity could result in BST with unacceptably low resistivity - which can be attributed to oxygen non-stoichiometry. Additionally, 10 - 100 ppm levels of BST sputter target impurities, mostly acceptor impurities in BST (see appendix A for sputter target representative assay), create undesirable electro-active defects in BST thin films affecting the final resistivity.

Lower temperature, higher pO_2 processing can potentially reduce oxygen vacancy concentrations, yet the use of copper substrate necessitates a methodology that avoids copper oxidation. These anneals can be performed after a dense dielectric is formed, creating an oxygen diffusion barrier that kinetically limits transport of oxygen to the dielectric-metal substrate interface. Reports of oxygen diffusivity in the open literature are of little agreement, yet two particular studies report $5 \cdot 10^{-10}$ cm² sec⁻¹¹²⁷ and $8 \cdot 10^{-13}$ cm² sec⁻¹¹²⁸ at 900 °C. If these data are extrapolated to low temperatures, unfortunately outside the temperature range of the studies, oxygen diffusivity can be estimated as $\sim 6 \cdot 10^{-13}$ cm² sec⁻¹ by the low temperature equation given by Paladino.¹²⁷ This value gives a diffusion length, \sqrt{Dt} , for the re-ox anneal of $\sim \frac{1}{3}$ μm . These data

suggest that the oxygen activity at the dielectric/substrate interface is significantly lower than in the vapor phase given the anneal time and film thickness.

2.8. SPUTTER DEPOSITION

2.8.1. Historical perspective of sputter deposition

Early into the study of low pressure cathode ray tubes and plasmas it was noted that the cathodes within the tube can react and/or disintegrate during operation.^{129, 130} The first report on utilizing this effect to generate thin coatings to platinize glass was in 1877.¹³¹ This effect was quantified for a variety of metals by Sir William Crookes in 1891.¹³² In these early reports, what is modernly termed “sputtering” lacked an accurate phenomenological explanation since the full determination of atomic structure was not decided upon until ~1900 after J.J. Thompson’s discovery of the electron.^{133, 134} With this knowledge, the mechanisms of momentum transfer from plasma ions that can cause the ejection of target materials from a cathode into the gas phase and subsequent deposition of a thin film onto an anodic substrate could be understood. The utility of sputter deposition was recognized before a physical understanding was developed as evident by Edison’s patents for coating phonograph mandrels with gold.^{135, 136} Today, sputter deposition has matured into widely used technology for the formation of thin films of various materials onto numerous substrates. Many authoritative reviews and texts have been published about sputter deposition¹³⁷⁻¹⁴¹; the following discussion will specifically outline important details of sputtering perovskite oxide materials.

2.8.2. Fundamentals of sputtering in a DC glow discharge

The simplest configuration with which to understand the physical mechanisms occurring during sputter deposition is shown in figure 2.15.

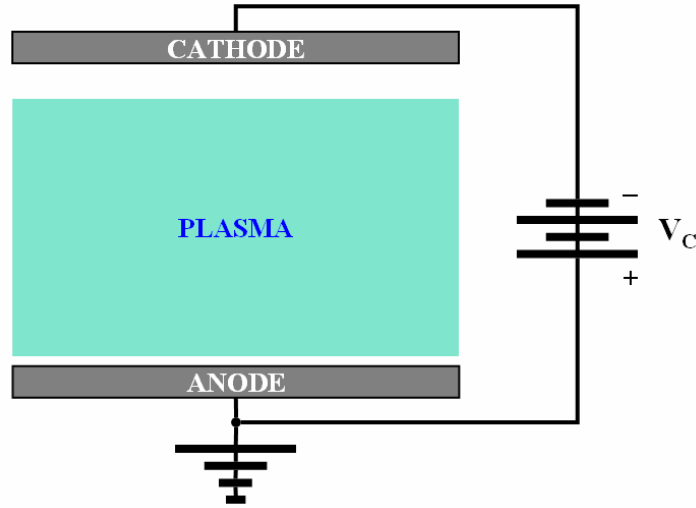


Figure 2.15: Schematic drawing of a typical DC plasma device.

This schematic represents two conducting electrodes biased by a DC power supply and immersed a vacuum chamber filled with a low pressure inert gas, i.e. 30 mTorr Ar. The gas molecules are ionized when a sufficient voltage across the electrodes is maintained, described by Paschen's Law.¹⁴² Paschen theories applied to concepts of Townsend for secondary electron emission¹⁴³ gives the required voltage to form the plasma, V_B ,

$$V_B = \frac{B(Pd)}{\ln[A(Pd)] - \ln\left(\ln\left(1 + \frac{1}{\gamma_{se}}\right)\right)} \quad \text{eqn [2.29]}$$

is a function of the Pd product, where P is the pressure of the gas, d is the distance between the electrodes, γ_{se} is the number of secondary electrons ejected during an ionizing event or the collision event of a gaseous atom, molecule, or ion with the electrode, and A and B are constants specific to the gas (i.e. $A = 13.6$ and $B = 235$ for argon). This breakdown voltage is mainly a function of the Pd product since this is a measure of the number of collision gas molecules will have with ionizing free electrons based on the mean free path between collisions and is adjusted by the variables specific to the

ionization of the gas. Once this voltage is created between the electrodes the plasma is self sustaining by the large number of secondary electrons created during collisions.

A plasma is defined as a quasi-neutral ionized gas dominated by collective behavior determined by electrostatics. Plasmas commonly employed for thin film deposition are have a low fraction of ionized molecules, $\sim 10^{-4}$, and are termed “cold plasmas” since the free electron energies are typically 1 to 10 eV yet the ion energies are roughly the room temperature value of 25 meV. These plasmas can be quantitatively characterized by the plasma frequency, ω_{pe} ,

$$\omega_{pe} = \sqrt{\frac{e^2 n_e}{\epsilon_0 m_e}} \quad \text{eqn [2.30]}$$

which is the direct result of the collective behavior of an ionized gas and determined by the free electron density, n_e . Since electrons have much greater velocities relative to the comparatively motionless ions and neutrals, any surface submersed in the plasma will charge negatively to a potential $-V_p$ from the high flux of electrons and form a region adjacent to the surface which is deficient of electrons. The plasma is required by electrostatics to remain quasi-neutral in the plasma bulk, therefore requiring screening of the negatively charge with a region of positive charge, i.e. $n_i < n_e$. The size of this screened region around a point charge is characterized by the Debye length, λ_D ,

$$\lambda_D = \sqrt{\frac{\epsilon_0 k_B T_e}{n_i e^2}} = \frac{1}{\omega_{pe}} \sqrt{\frac{k_B T_e}{m_e}} \quad \text{eqn [2.31]}$$

derived using the Boltzmann relation for the distribution of charged particles and Poisson’s equation of electromagnetism. Equation 2.31 shows how the Debye length is proportional to the electron temperature, T_e , yet inversely proportional to the density of ions. Electrostatics mandates a voltage must exist within this sheath which accelerates the positive ions towards the surface. Ejection of the atoms from the surface occurs when the

plasma ions are accelerated across this sheath and gain energy greater than the binding energy of the atoms of the surface in a process termed sputtering.

In a device designed for thin film deposition, a negative potential, V_C , is applied to a target of the material of which a thin film is desired. As a consequence, the target surface has a potential relative to the plasma bulk then the sheath potential is V_S .

$$V_S = V_P - V_C \quad \text{eqn [2.32]}$$

This is somewhat of an oversimplification since ambipolar diffusion must be considered; eV_S is several times the electron temperature since the ion mass is more than three orders of magnitude greater than the electron mass¹⁴⁰ which gives the following relation for the potential across the target sheath.

$$V_P - V_C = \frac{k_B T_e}{2q_i \ln\left(\frac{m_i}{2.3m_e}\right)} \quad \text{eqn [2.33]}$$

This increased potential drop along with the fact that the target is planar surface and not a point charge makes the size of the cathode sheath, d_S , considerably larger than the Debye length.

$$d_S \approx \left(\frac{q_i(V_P - V_C)}{k_B T_e}\right)^a \lambda_D \quad \text{eqn [2.34]}$$

Ions entering the sheath are accelerated by the electric field in the sheath toward the target surface at a current described by the Child-Langmuir law.

$$j^+ = \frac{4\epsilon_0}{9} \sqrt{\frac{2e}{m_i}} \frac{V_S^{3/2}}{d_S^2} \quad \text{eqn [2.35]}$$

This expression assumes a collision-less path of ions from the sheath edge toward the negative surface which only can occur when the mean-free path, $\langle\lambda\rangle$ determined primarily by its inverse relation to overall pressure, of these ions is greater than d_S . Often this is not

a valid assumption for sputtering discharges since higher pressures are desirable to control certain aspects of film growth and higher pressures allow for collisions to occur in the sheath effecting the number of ions and a mitigated average energy of ions when impinging on the target surface. Hence, the current can be adjusted assuming mobility limited flux of ions through the sheath.

$$j^+ = \frac{9\epsilon_0 V_s^{3/2}}{8 d_s^3} \quad \text{eqn [2.36]}$$

As the ions impinge on the target surface collision physics describe energy and momentum interplay from accelerated ions and target atoms. Assuming only elastic collisions, a valid assumption considering the relatively small mass difference between ions and target atoms, energy transfer is described by kinematics.

$$\frac{E_T}{E_i} = 4 \frac{m_i m_T}{(m_i + m_T)^2} \cos^2 \theta \quad \text{eqn [2.37]}$$

From equation 2.37 it can be seen that the energy transfer is maximized when $\theta = 0$, a direct collision trajectory, and when the ion and target atom masses are approximately equal. When E_T is greater than the binding energy of an atom, which is approximately target material's heat of sublimation ΔH_{Sub} , the solid target atoms can be ejected into the gas phase. The parameter sputtering yield, S , is used to describe the effect of many collisions over a large target area and is used to estimate the thin film deposition rate.

$$S = \frac{\# \text{ of sputtered atoms}}{\# \text{ of incident particles}} = \frac{4.2\alpha S_n(E_i)}{\Delta H_{Sub}} \approx \frac{3\alpha}{4\pi} \frac{4m_i m_T}{(m_i + m_T)^2} \frac{E_i}{\Delta H_{Sub}} \quad \text{eqn [2.38]}$$

To accurately know the sputter yield the energy dependent nuclear stopping power of the ion in the target, $S_n(E_i)$, needs to be known exactly since impinging ions experience numerous collisions along their trajectory. These data are in most cases not known but Sigmund theory¹⁴⁴ can be used for the approximation and has been used with great success. In this approximation α is a constant typically 0.2 - 0.4 dependent on the ratio of

the ion and target atoms masses, m_i/m_T , and the angle of impingement, θ . By knowing the sputter yield and ion current density, j^+ , which is equivalent to the flux of ions at the target, the flux of sputtered material can be estimated.

Equations 2.29 through 2.38 describe the basic physics of sputtering in DC plasmas yet their application to actual sputtering systems is at best an approximation.^{140,}

¹⁴¹ Many of the assumption used to derive these relations are not fully satisfied in practical thin film deposition systems yet the general trends give sufficient explanation for system design toward the goal of particular thin film deposition parameters.

2.8.3. Sputtering in radio-frequency discharges

The preceding discussion of plasma physics in a constant current regime is invalid for case of an insulating target. An insulating electrode surface prohibits the necessary electron current to sustain the plasma yet the impedance of a material lowers with increasing frequency. Therefore plasmas can be sustained at high frequencies since displacement currents compensate for the loss of DC current - i.e., the cathode is capacitively coupled to the plasma. The plasma maintains sufficient ionization not only by secondary electron emission but also by increased electron energy from the oscillating field. In this high frequency plasma at any point in time one electrode acts as a cathode and the other as an anode yet in the next half high cycle of the drive voltage the situation reverses. Screening and the formation of sheaths at each electrode creating a rectifying situation where the plasma bulk remains at a positive potential relative to either electrode yet the thickness of the sheath is varying in time at a frequency equal to the driving potential. This moving sheath edge can transfer additional velocity to electrons in the regions near the sheath allowing for a sufficient number of ionizing events to stabilize the plasma. The existences of sheaths at each electrode allow the driving circuit to be coupled capacitively to the plasma bulk and current continuity is maintained primarily by displacement currents not conduction of ions or electronics. Typically, high frequency plasmas are operated at the 13.56 MHz radio-frequency, RF, band allowed by the FCC for

industrial uses which allows RF plasmas to be sustained at lower system pressures than DC plasmas.¹⁴¹

At first glance, it would seem that RF plasmas are symmetric and do not allow for thin film deposition from the target to the substrate, and that when the drive potential is in the half cycle where the intended substrate is negatively biased this electrode would be sputtered, damaging the substrate. In practice the situation is not symmetric due to the geometry of a system designed for thin film deposition. The area of the target electrode is much smaller than the opposing grounded electrode comprised of not only the substrate but the substrate holding stage and the system walls. Since no DC voltage can be maintained in the grounded external circuit, and assuming space-charge limited ion current, the ratio of target sheath voltage to substrate sheath voltage are determined by the ratio of the respective areas by the capacitive division of voltage by equation 2.39.

$$\frac{V_S^{target}}{V_S^{substrate}} = \left(\frac{A^{substrate}}{A^{target}} \right)^4 \quad \text{eqn [2.39]}$$

Additionally, the capacitive coupling at the target is adjusted by the target capacitance as well as the sheath, whereas the counter electrode is coupled only by the plasma sheath. Again, these are approximations based on an idealized situation yet full analysis of the total impedance of the discharge and coupled RF circuit shows that a substantially larger potential exists at the target surface allowing for the sputtering of the desired material. An important point is that in a RF discharge the substrate and growing film are bombarded by ions due the formation of a sheath at both electrodes and this bombardment can impart dramatic effects during film growth.¹⁴⁵⁻¹⁴⁷

RF plasmas can be used to sputter from insulating targets. The processes of film growth and microstructure evolution are conceptually similar to sputtering using DC plasma discharges. The major differences being stable plasmas at lower background pressures leading to potentially larger mean free paths of species. Since energy transfer to plasma species is less efficient in RF plasmas the resulting particle energies are similar to DC discharges. When sputtering oxide insulators, the existence of oxygen plays a

significant role. The tendency for oxygen species to ionize negatively causes them to acceleration toward the anode, where the growing film is located, and hence increased film bombardment results causing film compaction or erosion. Deposition rates of oxide films is typical an order of magnitude lower than conducting films deposited using DC discharges. Since oxygen is volatile, oxygen species have sticking coefficient less than unity reducing the rate at which oxide film can be grown. This concept also leads to oxygen substoichiometry if process conditions are compensated by oxygen. Therefore molecular oxygen is added in the gas as a mixture with inert species. The inert species ionize positively and are responsible for the moment transfer at the target surface the majority of sputtering and oxygen compensates for the low sticking coefficients. This additional gas phase oxygen further exacerbates bombardment with the growing film. When low substrate temperatures are used, this bombardment along with insufficient energy for adatoms to reach low energy lattice sites before encountering new adsorbed species typically results in amorphous films of films with low crystallinity. These factors must all be considered when analyzing physical characterization of as-deposited films.

2.9. BASE METALS AND PEROVSKITE OXIDES

Traditionally, noble metals or conducting oxides electrodes are used to form capacitors with perovskite oxide dielectrics to avoid undesirable chemical interface reactions during oxidizing process conditions. These materials are commonly incorporated as substrates in ferroelectric thin films. The success of BaTiO₃ in multilayered capacitors (MLC) also relied on alloys of palladium and silver in early stages of development. Due to increasing costs and limited availability of palladium as demand for MLCs increased, a shift to lower cost materials was needed. The chosen metallization needed to withstand the high sintering temperatures of BaTiO₃.^{148, 149} Herbert gave the first demonstration that Ni/BaTiO₃ stacks could be processed at the required temperatures if the oxygen activity during anneals was carefully controlled.^{150, 151} If a hydrogen annealing ambient was used for sintering, the low pO_2 environment avoided

oxidation of the Ni electrodes avoiding degradation of electrode conductivity while the dielectric could be sufficiently densified and desired dielectric properties result.

Currently, the MLC industry produces billions of devices annually with internal Ni electrodes and a BaTiO₃ dielectric incorporating dopants used to achieve maximum density at temperatures below the melting point of Ni and optimum dielectric resistivity in a core-shell microstructure.^{148, 152} Research is currently underway to explore a higher conductivity, lower cost, and more widely available electrode material, copper.¹⁵³

Thermodynamic treatments show that base metals can be processed at the high temperatures needed to form a dense perovskite oxide layer while avoiding metal oxidation. The free energy of formation for the oxidation of a metal species and the law of mass action can be used to determine the pO_2 where equilibrium between molecular oxygen, metallic state, and oxidized metal exists. Writing a generic metal oxidation reaction:



$$\Delta G^0 = -RT \ln(k_{rxn}) \quad \text{eqn [2.41]}$$

A rate constant, k_{rxn} , is exponentially dependent on the negative of the free energy of formation at standard state, ΔG^0 , and exponentially dependent on the inverse of temperature, T (in Kelvin), and the gas constant, R . Using the generic chemical reaction and the law of mass action, the rate constant can be written as a ratio of activities of reactants and products (activity of condensed phases is assumed unity).

$$k_{rxn} = \frac{a_{MO}^2}{a_M^2 pO_2} = \frac{1}{pO_2} \quad \text{eqn [2.42]}$$

Combining equations 2.41 and 2.42 gives a pO_2 - T dependence of zero free energy, or an equilibrium line on a pO_2 - T phase diagram.

$$\Delta G^0 = RT \ln\left(\frac{1}{pO_2}\right) \quad \text{eqn [2.43]}$$

The free energy of reactions for numerous binary oxides are available in published tables.¹⁵⁴⁻¹⁵⁸ When considering the oxidation of Cu or Ni versus the cations of BST, a large range of pO_2 and T are available to process base metal-perovskite oxide stacks.^{149, 159} If pO_2 is carefully controlled, then BST can be processed at high temperatures and the BST cation oxidized state is stable with metallic base metals and molecular oxygen (see section 3.4 for a phase diagram and processing details for the Cu-BST system).

Thin film perovskite oxides on base metals research followed the trends of the MLC industry with initially less success. Initial attempts utilized lead containing perovskite oxides since densification requires only 550 - 600 °C. The first reports in this effort were PZT thin films deposited on stainless steel plates by alkoxide based CSD and air annealeds.¹⁶⁰ No results on stainless steel are reported but a permittivity of 260 was achieved on glass substrates using this process. This same process route was used to coat Alumel wires which were driven to resonance by a piezoelectric response.¹⁶¹ A study from The Pennsylvania State University, deposited a 52/48 PZT film by CSD onto a TiNi shape memory alloy and stacks annealed at 500 °C in air. The report states samples were analyzed by XRD and do no mention observation of nickel or titanium oxides while reporting a grain size of less than 1 μm for a 600 nm thick film. Dielectric measurements gave permittivity of 700 and $\tan \delta$ of 0.3 at 100 kHz. Ferroelectric measurements gave a remnant polarization of 15 $\mu\text{C cm}^{-2}$.¹⁶² Similar to Chen's report, Mercado and Jardine report XRD data for CSD PZT on TiNi alloys showing no reflections from substrate oxides after 5 minute anneals at 600 °C in air. Ferroelectric P - E loop measurements of these films show a rounded shape characteristic of a lossy dielectric.¹⁶³ PZT films on various substrates have been reported using similar anneals, less than 650 °C in air, on a host of metallic substrates including stainless steel, titanium, brass, nickel alloys, and lanthanum aluminate, LaNiO_3 , coated Ni foils.¹⁶⁴⁻¹⁶⁷ Figure 2.16 shows ϵ - E curves for PZT deposited on Ti, brass (BR), and stainless steel (SS) substrates where $\tan \delta$ is 0.05 - 0.15.¹⁶⁷

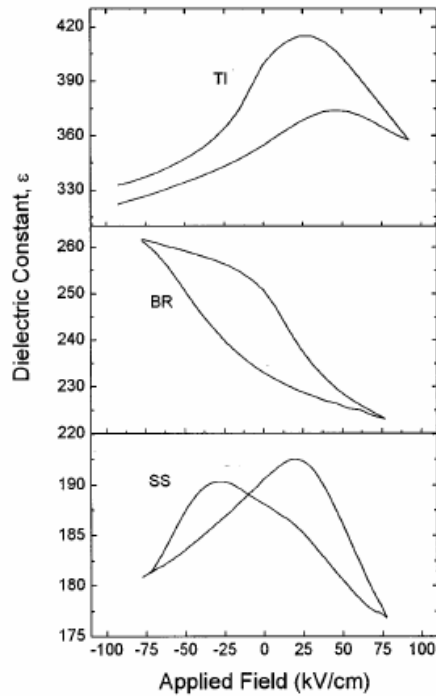


Figure 2.16: Dielectric properties of PZT film on metal substrates of titanium (Ti), brass (BR), and stainless steel (SS).¹⁶⁷

Only in the last several years have perovskite oxide thin films been processed on base metals while achieving sufficient dielectric properties for practical use. Kim annealed CSD PZT thin films on electro-less Ni foils in flowing nitrogen and achieved permittivity of 400 with low loss tangents resulting from a low permittivity interface layer of NiP from the substrate.^{168, 169} Dawley used the thermodynamic approach outline above to process BST thin films by CSD on biaxially textured {100} Ni tapes. Anneals at 10^{-18} atm pO_2 and 900 °C gave permittivity of 450 for random microstructures and when fiber textured microstructures were achieved from substrate templating, 1500 permittivity could be achieved at room temperature.^{159, 170} A modified processing route considering PbO loss was developed by Losego to deposit PZT by CSD on pure Cu foils. Reports show no copper oxidation by this technique while achieving dielectric properties comparable to PZT thin films on platinized silicon.^{171, 172} Efforts to deposit BaTiO₃ by CSD on Cu foils using a thermodynamic approach are outlined in the thesis by Ihlefeld.¹¹⁹ This study reports for the first time, dielectric properties of BaTiO₃ similar to those

observed in bulk due to the ability to anneal at higher temperatures than afforded by conventional substrates achieving high crystallinity with equiaxial grain sizes large for BaTiO₃ thin films. Anomalous grain growth is achieved by barium borate flux showing unambiguous tetragonality in a film for the first time in the open literature.

This thesis outlines a processing methodology to sputter deposit BST over a wide composition range directly on Cu foil substrates. A thermodynamic approach is used to densify low temperature deposited films. This effort will represent the first attempt to sputter deposit BST thin films directly on base metal substrates.

2.10. THIN FILM ADHESION

A thin film is not mechanically robust if free standing and relies on the mechanical properties of a substrate to provide strength. A thin film based device must be durable enough to withstand the rigors of service, and avoid the deleterious effects of poor adhesion between the two materials which could lead to device failure,¹⁷³ Adhesion must be adequate to overcome not only forces imparted by use, but also internal stresses induced thermally and from the deposition mechanisms.¹⁷⁴ There is no accepted convention for defining adhesion strength. Generally, adhesion force, F_a , describes the maximum force needed to separate the thin film from its substrate over some distance (usually a molecular distance) and work of adhesion, W_a , is a quantitative description of the amount of energy needed to destroy the film-substrate interface and create two new free surfaces. These two quantities are related by the following integral.

$$W_a = \int F_a(r) dr \quad \text{eqn [2.44]}$$

Regardless if adhesion is considered as force or energy, the strength of the interface is fundamentally due to the chemical bonding across the interface. In practicality, the measured adhesion strength is typically dominated by external factors. Interfaces can be classified into three major categories: 1) atomically flat, abrupt interface, 2) bonding interlayers due to chemical reaction, inter-diffusion, and chemical mixing of the constitute phases, or 3) high roughness interfaces where the film and

substrate are mechanically interlocked in reentrant sections. In smooth abrupt interfaces the chemical forces between the film and substrate dominate the measured adhesion strength, yet this situation is idealized and cannot be realized in most systems. When interlayers or concentration gradients exist, definition of an interface is ambiguous. This case also describes a layer of trapped surface contamination which can lead to very low measured adhesion strength uncharacteristic of the film-substrate system. When rough interfaces are present, regions of material in reentrant features are under compression and keep the film adhered to the substrate until the fracture strength of the weaker material is surpassed. For thin film capacitor structures, rough interfaces and interlayers are not desirable. Of more interest are the chemical forces across the interface to quantify adhesion strength. In all cases, structural flaws at the interface (including voids, micro-cracks, vacancies, small regions of impurities, etc.) can dominate the measured adhesion force giving extreme low values.¹⁷³

Methods to quantify adhesion strength are of two types, mechanical and thermodynamic. Mechanical tests involve peeling, pulling, or scratching a thin film adhered to a substrate.¹⁷³⁻¹⁷⁶ The force required to cause delamination allows quantification of adhesion force. This force is determined by the chemical bonding across the interface and mechanical/physical interlocking due to interface morphology. The film and substrate can interlock in the reentrant sections caused by substrate roughness and conformal thin film growth. The peeling stresses can cause plastic deformation and/or fracture of these interlocked regions and add to the measured adhesion force.¹⁷³ Interface roughness can also allow more bonding sites per apparent interface area leading to a potential artifact. The need for external attachment to both the film and substrate to be stronger than the adhesion force makes mechanical adhesion tests impractical for flexible systems.¹⁷⁵ The existence of graded composition interfaces or interlayers gives adhesion force measurement of the weakest part of an interface at an arbitrary plane in the ambiguous interface region.

All mechanical tests are subject to measurement errors from internal stress. Internal stress can overcome the adhesion strength of the interface causing failure before

applied stresses. Conversely, internal stress can counteract applied stresses giving adhesion force values unrepresentative of the material couple. Additionally, no tests have been devised to repeatedly and accurately control the homogeneity of stresses and alleviate the loss of mechanical energy due to plastic deformation. Therefore, adhesion tests based on equilibrium shapes of solid crystallites or liquid drops give work of adhesion in a situation absent of internal stress and mechanical deformation or fracture. Since tests are performed at equilibrium, thermodynamic concepts can be applied to results and fundamental adhesion strength can be quantified in terms of the chemical bonding across the material couple interface. Although mechanical tests more accurately reproduce service conditions, knowledge of the thermodynamic chemical adhesion must first be established for new systems. Then the interface structure can be engineered to balance the need for a durable interface versus the electrical, thermal, and mechanical properties desired for a thin film based device.

2.10.1. Sessile drop technique for quantifying adhesion

The geometry of liquid drops was determined by Laplace where drop shape is determined by the difference in pressure across a liquid surface balanced by the surface tension of the liquid.¹⁷⁷ Further study by Young and Dupré showed that in a three phase system of solid, liquid, and vapor the angle of contact at the triple point is a circumstance of a balance of two phase surface energies.^{178, 179}

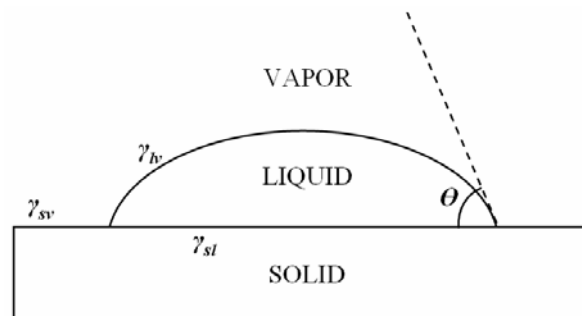


Figure 2.17: Diagram of a liquid drop contacting a solid surface surrounded by a vapor. The contact angle, Θ , at the 3 phase triple point is determined by a balance of the two phase surface energies.

$$\gamma_{lv} \cos \theta = \gamma_{sv} - \gamma_{sl} \quad \text{eqn [2.45]}$$

The formalism established by the Young-Dupré equation allows calculation of energy per unit interfacial area between the liquid and the solid, the work of adhesion, W_a , if the contact angle and liquid-vapor surface energy are known.

$$W_a = \gamma_{lv}(1 + \cos \theta) \quad \text{eqn [2.46]}$$

The work of adhesion is a thermodynamic quantity defining the free energy released to form the liquid-solid interface. The larger W_a , the more energy (and hence, more force) is required to separate the liquid from the solid. The theory was further extended by Bashforth and Adams where gravitational forces were considered in how drop shape is affected. Characterizing the radius of curvature at the drop meridian, the height of the meridian, the meridian radius, and the radius of the contact area gives a parameter β .¹⁸⁰ Knowing the liquid density, contact angle, and characteristics of shape give W_a and γ_{lv} . Dorsey simplified this model by using simplified drop measurement schemes.¹⁸¹ This procedure was used by Kingery to measure the surface tension of silicon, iron, and nickel.¹⁸² Liquid surface tensions for all pure elements measured by various methods including those described above are summarized in the review by Keene.¹⁸³

Sessile drop experiments quantify W_a by melting the lower melting point component of a system on the higher melting point component's surface and the contact angle measured optically. These experiments are also commonly referred to as wetting experiments. This method has been used extensively to characterize adhesion between metals and binary oxides in an effort to improve brazed metal-ceramic bonds. Typically, strong adhesion exists between oxides since bonding in both materials is mainly ionic-covalent. Metals primarily have bonding through delocalized electrons which results in large differences in thermal, mechanical, and chemical properties across metal-oxide interfaces and hence poorer adhesion.^{184, 185} A large literature base exists for metal-oxide adhesion allowing detailed reviews of experimental procedures, established results, and efforts to form predictive theories.¹⁸⁶⁻¹⁸⁹ Single crystal sapphire (Al_2O_3) is often used as the model oxide surface since wafers are widely available with atomically flat surfaces.

Thermodynamic concepts are applied to empirical results and are used to explain a large dependence on W_a with the activity of oxygen in the experimental ambient. At low oxygen activities, large contact angles and low W_a are observed in situation termed “non-wetting,” and at high oxygen activities, low contact angles and large W_a in a “wetting” situation accompanied by the formation of a reaction layer at the interface.¹⁹⁰

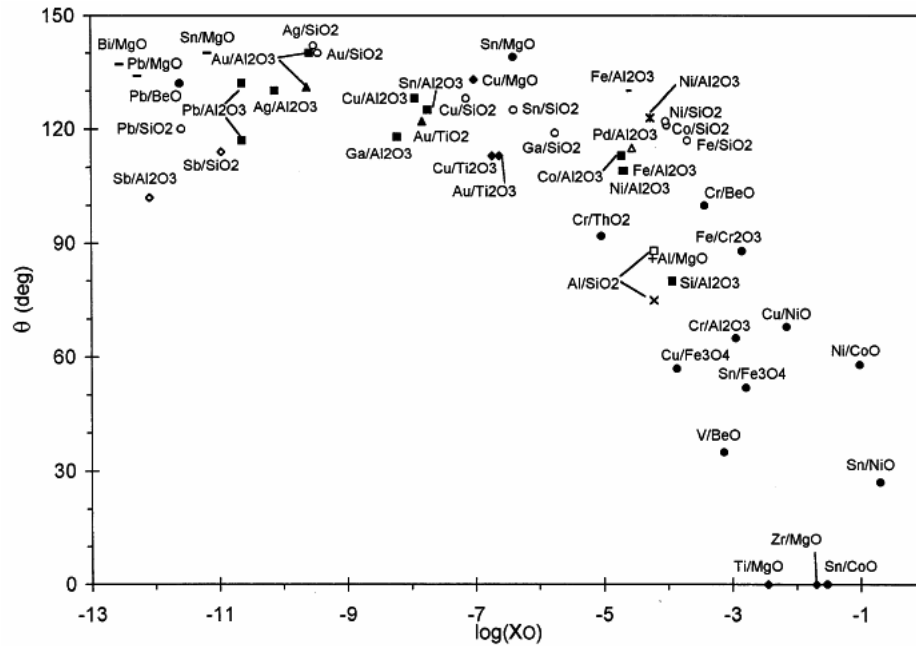


Figure 2.18: Contact angle versus oxygen activity for metal-oxide systems reported in the open literature. At low oxygen activity large contact angles predominate giving low work of adhesion and “non-wetting” behavior. At large oxygen activity low contact angles are observed since work of adhesion is large and reaction layer formation leads to wetting behavior.

Many attempts have been made to fully describe all metal-oxide interfaces through fundamental thermodynamic quantities. Although no theory can fully explain all observations, Eustathopoulos states generally W_a increases with the partial enthalpy of mixing at infinite dilution of the oxide’s cation in the liquid metal and W_a increases with enthalpy of oxidation of the metal, $\Delta H^0_{f(MO)}$.¹⁸⁶

Although sessile drop experiments are widely used to quantify adhesion, several experimental difficulties make these measurements non-trivial. Accurate measurement of W_a by sessile drop methods necessitates that the liquid drop has an equilibrium

axisymmetric shape. In non-reactive and non-wetting systems, drop spreading occurs on the scale of milliseconds; whereas in systems where significant reactions occur at the interface, the need to diffusion reacting species to the interface causes equilibrium drop shapes to develop on the scale of 10s - 100s of seconds.^{191, 192} This necessitates the measurement of contact angle over time scales greater than the speed of drop spreading. When specimens are on an inclined plane relative the direction of gravity $>10^\circ$, significant drop asymmetry is observed making the contact angle on the leading triple point significantly different than measured at the trailing triple point.^{193, 194} Asymmetry can also arise from the wetting front conforming to surface asperities, creating an irregular meniscus, and a non-equilibrium drop shape.¹⁹⁵ A rough solid surface causes hysteretic drop spreading and hence large errors in contacts angle measurement from non-equilibrium shaped drops.^{196, 197} Additionally, the Young-Dupré equation is derived from a balance of surface energies, a per unit area energy term. Interface roughness makes the interfacial area greater than the apparent area and larger contact angles can be observed.¹⁹⁸

Vapor phase contaminants are particularly problematic in sessile drop experiments since a large surface area of the liquid phase at high temperature is exposed to the experimental ambient. Of most concern is impurity oxygen. As Ghetta shows for wetting of Cu on sapphire, there is a discontinuous change of surface tension and contact angle at a critical partial pressure of oxygen.¹⁹⁹

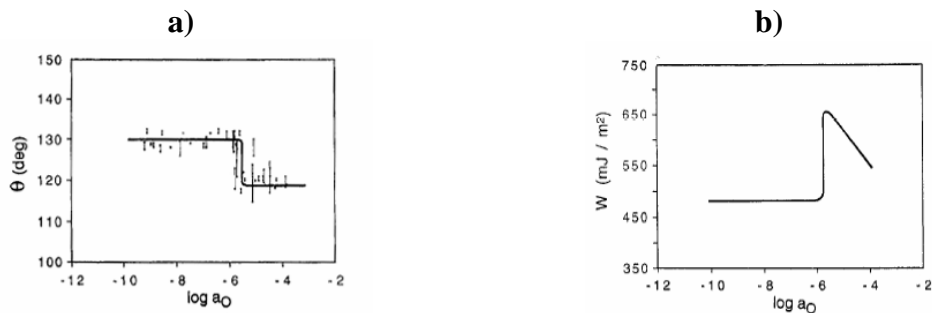


Figure 2.19: Data for Cu-Al₂O₃(sapphire) reported by Ghetta as a function of oxygen activity at 1365 K. a) At oxygen activity $> 10^{-6}$ the contact angle discontinuously reduces and (not shown) the surface tension of liquid copper linearly decreases. b) At this critical oxygen activity a discontinuous jump in work of adhesion is observed followed by a linear decrease in work of adhesion with increasing oxygen activity.¹⁹⁹

Contamination also plays a role at the liquid-solid interface. Since metal-oxide samples are solid before measurement and the metal is melted forming a continuous solid-liquid interface, surface contamination can be trapped at the interface. Ownby observed this phenomenon when measuring silicon wetting on silicon carbide surfaces.¹⁸⁹ When the surface was allowed an unobstructed path to desorb all surface contaminants at high temperature a more accurate measurement of wetting was made. The experimental considerations outlined above must be critically assessed in any sessile drop experiment so that accurate measurements of W_a can be obtained.

Alternatively, interfacial energy in solid-solid systems can be measured using a Wulff construction. In the solid state symmetry imparts property anisotropy and different surface energies for different crystallographic planes. This necessitates a characteristic crystallite shape that minimizes total surface free energy. Wulff showed a polar plot of surface energy of all planes gives this equilibrium shape in the so-called Wulff construction.^{200, 201} The equilibrium shapes of metallic crystallites were experimentally verified and compared to Wulff constructions by several authors.²⁰²⁻²⁰⁴ Pillar and Nutting studied the effect of a substrate surface on the equilibrium shape of metal solid crystallites to determine the interfacial energy between the metal and substrate. In this study, ~ 200 Å metal films were deposited on α -Al₂O₃ substrates by evaporation then heated to just below the metal melting point to agglomerate the contiguous films into isolated islands. The islands were analyzed by TEM to assess if an equilibrium shape results and measure the distance between the crystallite center and the substrate along a line orthogonal to the interface shown schematically in figure 2.20.

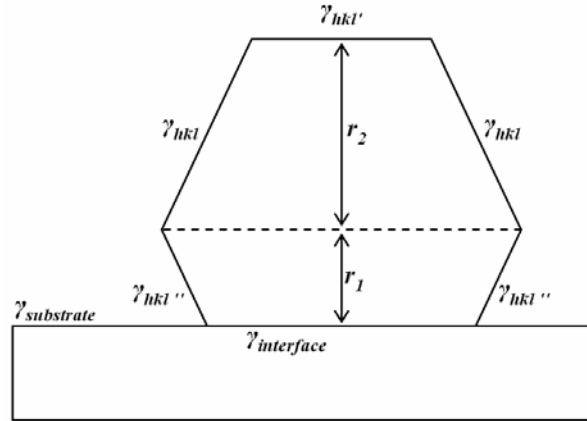


Figure 2.20: Wulff plot equilibrium crystallite shape and anisotropy in crystallite surface energy. The equilibrium facets are changed by the existence of an interface with a rigid substrate of surface energy $\gamma_{substrate}$ to create an interface of surface energy $\gamma_{interface}$.

The interfacial surface energy was determined by knowing the substrate surface energy and the surface energy of the crystallite plane parallel to the interface by the using the following relation.

$$\gamma_{interface} = \gamma_{substrate} + \frac{r_1}{r_2} \gamma_{hkl'} \quad \text{eqn [2.47]}$$

Experiments revealed that the interfacial surface energy measured by Pillar's and Nutting's method just below the melting point differs by less than 20% from W_a measurements performed in liquid drop just above the melting point.²⁰⁵

For thin film adhesion, if W_a between a thin film and its substrate is large then this interface should be strong and require a proportional amount of force to separate. Sessile drop experiments can be used to quantify W_a for the metal-oxide system of interest and an appropriate corollary to the strength of a thin film-substrate interface. This thesis is primarily concerned with the Cu-BST system. Cann *et al* measured metal adhesion with sintered oxide samples in a 10^{-6} Torr vacuum furnace with a graphite setter to achieve sufficiently low oxygen activity and high temperature to melt the metals of interest. This study found a Cu-BaTiO₃ contact angle of $102^\circ \pm 4^\circ$ and $W_a^{Cu-BaTiO_3} = 1.080 \pm 0.090 \text{ J m}^{-2}$ at the melting point of Cu. This results is compared to

$W_a^{Ag-BaTiO_3} = 0.620 \pm 0.100 \text{ J m}^{-2}$ and $W_a^{Au-BaTiO_3} = 0.520 \pm 0.040 \text{ J m}^{-2}$ found using the same experimental setup and at the respective melting points of the metals. The major conclusion of this work is Cu-BaTiO₃ adhesion is comparable in W_a to other metals commonly used for electrodes on electroceramics.^{206, 207} Wang *et al* used the sessile drop method to measure Ag, Au, Cu, Pb, Sn, and (Ag_{0.7}, Pd_{0.3}) wetting on polished ceramic BaTiO₃ substrates. Cu-BaTiO₃ contact angle is reported as 102° when using purified Ar (low oxygen activity) and reduced to 64° when measurements were made in air (high oxygen activity). This study verifies that Cu-BaTiO₃ work of adhesion is comparable to other electroceramic electrode metals on BaTiO₃.²⁰⁸ These are the only two studies of adhesion between Cu and barium titanate based perovskite oxides found in the open literature.

Surveys of reports of Cu adhesion on binary oxides are available in the open literature. The most commonly reported binary oxide in these studies is single crystal alumina (sapphire). These reports provide a verified contact angle for a Cu-oxide system, $118^\circ < \theta^{Cu-Al_2O_3} < 120^\circ$.^{186, 189, 199, 209, 210} Temperatures close to the melting point of Cu and oxygen activity $< 10^{-5}$ are used in these experiments. Any experimental procedure to measure work of adhesion using the sessile drop technique can be validated by measuring Cu-Al₂O₃ and comparing results to those obtained in the above mentioned studies. W_a for metals commonly used for electroceramics have been measured on alumina. Chatain reports W_a of 0.277 and 0.737 J m⁻² for Au and Pd, respectively, on alumina.²⁰⁹ McLean and Hondros report W_a of $1.050 \pm 0.080 \text{ J m}^{-2}$ for Pt on alumina measured by grain boundary grooving.²¹¹ W_a for metals appropriate for electroceramic electrodes needs to be explored experimentally for BST as data is not reported in the open literature.

2.10.2. Liquid metal alloy adhesion

Metal alloys have been explored by sessile drop experiments to assess the effect of solute additions on adhesion to oxide substrates.^{190, 199, 212-216} Generally, small contents of highly wetting or reactively wetting elements increase W_a of the alloy without degrading properties of the solvent material in its pure state. Some concept of superposition of

wetting characteristics seems apparent, but it is an over simplification to use only superposition to explain the ability engineer W_a by solute addition.

In most alloys, a significant thermodynamic driving force exists for surface segregation. Enthalpy of mixing, surface energy mismatch, and atomic size mismatches in the alloy system can all drive surface segregation. Consider solute (A) in solvent (B). The surface concentration of the solute, $c_{surface}^A$, relative to the bulk concentration, c_{bulk}^A , is determined by the enthalpy of mixing by the following relation.

$$\frac{c_{surface}^A}{c_{bulk}^A} = \exp\left(\frac{f\Delta\bar{H}_{A(B)}^\infty}{3RT}\right) \quad \text{eqn [2.48]}$$

Here f is a dimensionless constant ($f = 0.71$), R is the gas constant, and T is the temperature in Kelvin. If the enthalpy of mixing is negative and mixing is preferred then the surface concentration is identical to the bulk, yet in alloys with a positive enthalpy of mixing and mixing is not preferred then significant surface segregation of the solute is observed. The driving force for surface segregation due to surface tension mismatch is seen in the following equation.

$$\frac{c_{surface}^A}{c_{bulk}^A} = \exp\left[\frac{-g(\gamma_{lv}^A - \gamma_{lv}^B)V_A^{2/3}}{3RT}\right] \quad \text{eqn [2.49]}$$

Here g is a dimensionless constant ($g = 4.0 \cdot 10^8$) and V_A is the molar volume of the solute atom. When the surface tension of pure solvent (B) is larger than the surface tension of pure solute (A) then surface segregation is favored. A size difference between the solute and solvent atoms creates a driving force for surface segregation as seen below.

$$\frac{c_{surface}^A}{c_{bulk}^A} = \exp\left(\frac{0.42\bar{K}\bar{V}_m\delta^2}{RT}\right) \quad \text{eqn [2.50]}$$

where:

$$\delta = \frac{(V_A^{1/3} - V_B^{1/3})}{\bar{V}_m^{1/3}} \quad \text{eqn [2.51]}$$

In the above relations, \bar{k} is the average bulk modulus, V_i is the molar volume, \bar{V}_m is the average molar volume. When the molar volume of the solute atom is larger than the solvent atom, a driving force exists for surface enrichment of solute. These driving forces can be assessed through known physical and thermodynamic properties of the system to predict if surface segregation will be observed in an alloy.²¹⁷

W_a is strongly correlated with the surface tension of the liquid drop and addition of solutes can affect the surface tension in alloys.²¹⁸ A model presented by Li *et al* proposes the following relation for the effect of solute concentration on the alloy surface tension.²¹⁴

$$\left(\frac{\partial \gamma_{lv}}{\partial x_A} \right) = \frac{RT}{\Omega_M} \left[1 - \exp \left(\frac{-(\gamma_{lv}^A - \gamma_{lv}^B) \Omega_M - m \lambda}{RT} \right) \right] \quad \text{eqn [2.52]}$$

where:

$$\lambda = - \frac{\Delta \bar{H}_{A(B)}^\infty + \Delta \bar{H}_{B(A)}^\infty}{2} \quad \text{eqn [2.53]}$$

Here m is a structure parameter ($m \sim 0.25$ for liquid metals), Ω_M is the molar interfacial area, and λ is pair-wise molar exchange energy calculated as the mean value of partial enthalpy of mixing at infinite dilution of the solution dilution extremes.

Copper-zinc alloys will be studied in this thesis. In this system, mixing is preferred over all the full concentration range therefore the enthalpy of mixing can be assumed to be negative at all concentrations.^{158, 219, 220} The molar volume of zinc is larger than the molar volume of copper and the surface tension of copper is larger than the surface tension of zinc. In this alloy a driving force for surface segregation exists for Cu rich alloys. Surface segregation is not expected to be large since only two of the three driving forces of segregation are significant. In Li's model for predicting surface tension changes due to alloying, insufficient data could be found for predicting the resulting surface tension. The surface tension of copper is greater than the surface tension of zinc yet partial enthalpy of mixing at infinite dilution for concentration extremes could not be found. The relative W_a between the two pure components can lead to an understanding of pair-wise change energy, yet W_a of zinc on perovskite oxides could not be found in the

literature. This thesis will outline experiments to measure W_a of zinc and the full range of compositions in the Cu-Zn system on alumina and BST.

3. EXPERIMENTAL PROCEDURES: SPUTTERED FILM ON FOIL

METHODOLOGY

This chapter describes the methodology for the synthesis of barium strontium titanate (BST), $(\text{Ba}_x, \text{Sr}_{1-x})\text{TiO}_3$, thin films by sputter deposition onto copper foils. The sputter system configuration is outlined below. Specific equipment features unique to this work and which lead to the success of the process are highlighted. An annealing procedure to transform the amorphous or “proto-”crystalline as-deposited films into a ceramic film with a high degree of crystallinity while preserving the metallic character of the substrate is presented. The key of this processing step is precise control of temperature and $p\text{O}_2$ during the entire thermal cycle. A secondary re-oxidation anneal is intended to reduce the high concentration of oxygen vacancies in the films created by the conditions present during the crystallization. Methods for characterizing the physical structure and electrical properties of samples are presented which provide data to form process-structure-property relationships.

3.1. COPPER FOIL SUBSTRATES

Copper foil substrates were used in this study; the low resistivity, low cost, and flexibility of Cu foil were factors of primary consideration. These foils have been engineered as interlayer ground planes in modern printed wiring boards (PWB). Choosing a material that is already in common use, available in large quantities, and well understood should facilitate commercialization. Additionally, the configuration of a free-standing foil makes capacitor stacks on foils suitable for flexible applications. This subsection will outline the properties of a specific variant of copper foil used in this study.

Copper foils were obtained from Oak-Mitsui, Hoosick Falls, NY via DuPont Electronics, Research Triangle Park, NC. These foils are produced in large volumes under the product name PLSP and in this study the “½ oz. weight” is used. Copper is electroplated onto a continuously rotating mandrel and the final product is a

polycrystalline foil with a total thickness of 18 μm . The “back” side of the foil is intentionally roughened to aid in lamination to the polymers of a PWB and bears no further discussion within the context of this study. The “top” side is significantly smoother and more appropriate for dielectric thin film deposition. The root mean square (RMS) roughness of the foil surface is 25 nm over a 25 μm^2 area and 150 nm over a 100 μm^2 area measured using an atomic force microscope (AFM). This analysis indicates that the foils have large long range undulations with substantially lower roughness on the micron scale. Figure 3.1 shows an AFM of the foil surface over a 5 $\mu\text{m} \times 5 \mu\text{m}$ area.

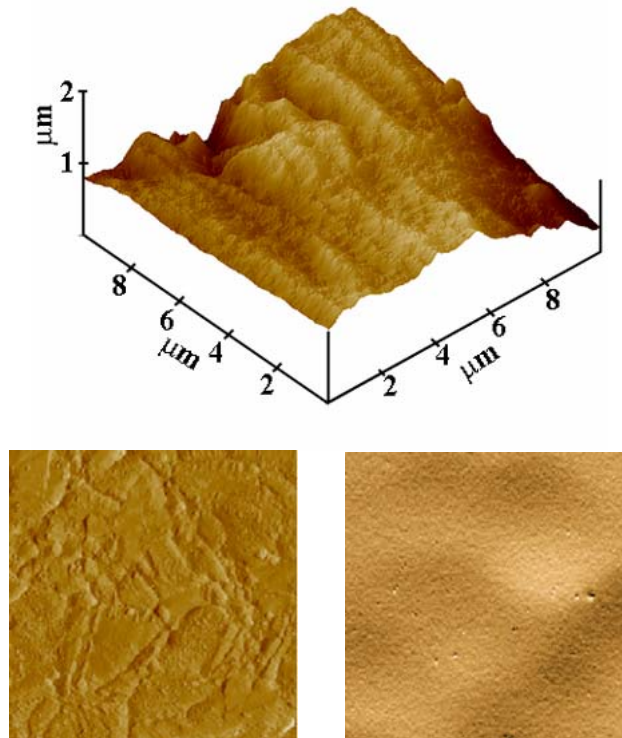


Figure 3.1: Top: 3-D rendering of 10 $\mu\text{m} \times 10 \mu\text{m}$ AFM scan. Bottom left: 2-D AFM data over 5 $\mu\text{m} \times 5 \mu\text{m}$. Bottom right: 2-D AFM data over 20 $\mu\text{m} \times 20 \mu\text{m}$.

This surface is at least an order of magnitude rougher than single crystal substrates typically used for BST thin film substrates.²²¹

These substrates are substantially different in structure and properties from those common for thin film ferroelectrics. The copper foil flexibility allows for free body

movement, while the combination of a small foil thickness and a low copper shear modulus dramatically reduces the residual film strain that typically arises from thermal expansion mismatch. This is in contrast to the more common situation of a thin film on a thick and rigid substrate. Anneal temperatures approaching the melting point of Cu, $T_M^{Cu} = 1084\text{ }^\circ\text{C}$, are achievable on copper, as compared to platinized silicon which suffers from hillocking or delamination after thermal excursions above $\sim 700\text{ }^\circ\text{C}$.²²² The low resistivity of pure copper is exceeded only by superconductors or metallic silver. Superconductors exhibit lower resistivity than copper only when below a transition temperature; yet no materials have displayed superconductor behavior above cryogenic temperatures.

Metallic silver is limited by the high raw material cost. Copper is much less expensive and more readily available in large volumes.²²³ Thus, copper far outweighs the potential advantages of superconductors, precious metals, and single crystal oxide substrates.

Table 3.1: World mine production and cost of noble metals and copper according the Minerals Commodity Summaries 2006 published by the U.S Department of the Interior and U.S. Geological Survey.²²³

	2005 World Mine Production (annual metric tons)	2005 Average Price (US\$ • tr. oz. ⁻¹)
Platinum	218	890.00
Silver	20,300	7.15
Copper	14,900,000	0.12

3.2. SPUTTER DEPOSITION EQUIPMENT

A sputter system has been constructed considering the requirements for sputtering insulating oxides. Figure 3.2 shows this system in schematic form. A 25 L stainless steel cylindrical chamber (a) forms the system body. This chamber is evacuated using a rotary vane mechanical pump (b) lubricated with inert perfluorinated polyether based oil. The

mechanical pump (MP), with an approximate pumping speed of 10 L s^{-1} , is capable of evacuating the main chamber from atmospheric pressure to $< 1 \cdot 10^{-3} \text{ Torr}$. A welded 4" diameter port to the main chamber is attached to a mechanical screw driven gate valve (c) by Conflat flanges with a copper gasket. Behind the gate valve is a turbomolecular pump (TMP) (d) connected by elastomer sealed K-style ISO flanges. The chamber and pumping system can maintain a base pressure of $2 \cdot 10^{-7} \text{ Torr}$ by the following procedure.

The system is sealed by closing the main door (not shown) and the N_2 vent valve (e) and the small gate valve (f) opened.

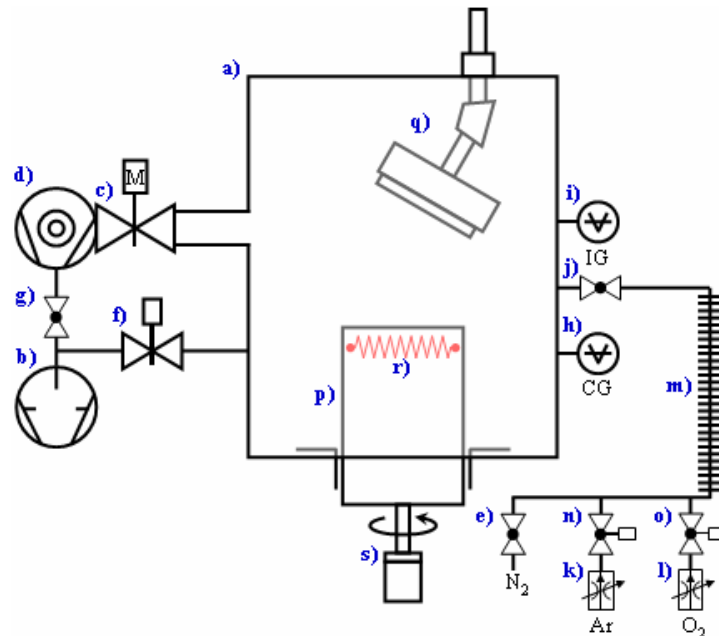


Figure 3.2: Diagram showing the important features of the sputter system used for BST thin film deposition. Blue labels are used for clarification for the discussion of the system and its operation.

To ensure isolation of the TMP, the large gate valve (c) and the isolation valve (g) between the MP and TMP remain closed. The falling pressure is observed by a convectron gauge (h) connected to the main chamber. When the pressure in the main chamber reaches $5 \cdot 10^{-3} \text{ Torr}$, the small gate valve (f) is closed, the TMP backing valve (g) opened, and the large gate valve (c) opened. The system can then pump into the high vacuum regime and pressure is monitored by a Granville-Philips (Brooks Automation,

Chelmsford, MA, USA) Micro-Ion Gauge™ (i). A base pressure of $3 \cdot 10^{-7}$ Torr can be achieved in 8 hours with the main gas manifold isolation valve closed (j) or a base pressure of $1 \cdot 10^{-6}$ Torr in the same time period with this valve open. The system is vented to atmosphere with dry N₂ gas by closing all valves to isolate the pumps (c & f) from the main chamber and the vent valve opened (e).

Typically, the system is pumped to $\sim 1 \cdot 10^{-5}$ Torr in 30 min. prior to depositions. The plasma is initiated and maintained by a supply of 13.56 MHz RF power and purified gases. Independently controlled flows of UHP argon (Ar 99.999% purity) and UHP molecular oxygen (O₂ 99.999% purity) are introduced into the chamber using MKS Instruments (Andover, MA, USA) mass-flow controllers (k & l) via a manifold constructed of welded or metal sealed stainless steel tubing and flexible bellows (m). Individual gas supplies can be isolated from the system using pneumatically driven isolation valves (n & o). The use of a gas mixture of inert argon and reactive oxygen helps to maintain the target's stoichiometry in the growing film. Inert argon acts as the main sputtering species and always supplied in the greater balance. The atomic weight of argon is $39.948 \text{ g mol}^{-1}$ and although not matched to any of the elements of BST (Ba $137.327 \text{ g mol}^{-1}$, Sr 37.62 g mol^{-1} , Ti $47.867 \text{ g mol}^{-1}$, O 16.00 g mol^{-1}) the intermediate atomic weight allows sufficient kinematic factor of all the species in sputtering the compound (Ba, Sr)TiO₃. Additionally, argon is significantly less expensive than other inert gases due to its greater abundance and ease of distillation. Small amounts of oxygen in the process gas mixture are necessary to compensate for the low sticking coefficient of oxygen adatoms and admolecules to the growing film. Oxygen species have a high electron affinity and tend to ionize with negative charge. Excessive concentrations of oxygen in the plasma can cause deleterious effects due to bombardment of negative ions accelerated by electric field supplied at the electrodes. The Ar:O₂ ratio influences the deposition rate, film morphology, and as-deposited stoichiometry making precise control of this parameter of paramount importance. The gas delivery system outlined here allows for $\pm 3\%$ control over this ratio. The total pressure during sputtering is controlled in part by adjusting the total input flow and reducing the pumping speed of the TMP by partially

closing the manual gate valve (c) during deposition. Once the necessary total pressure and sputtering ambient is supplied in the predetermined gas ratio the plasma can be initiated.

Radio frequency energy is supplied between two internal electrodes immersed in the process gases. A sinusoidal waveform is supplied at 13.56 MHz by an Advanced Energy® (Fort Collins, CO, USA) RFX-600 power supply operated in a power control mode. The chamber walls and substrate stage (p) form a grounded electrode. The driven counter electrode is a Kurt J. Lesker (Pittsburg, PA, USA) Torus 4 sputter gun (q). This assembly shown by figure 3.3 is a water cooled magnetron assembly capable of holding a 4" diameter sputtering target.

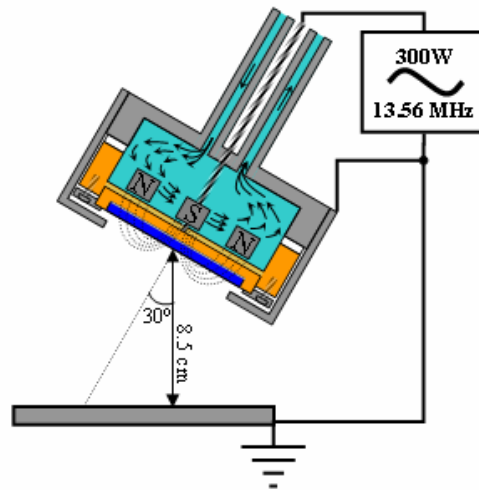


Figure 3.3: Detailed diagram of the sputter gun. The entire gun is oriented 30° from the substrate normal and an 8.5 cm center to center distance of the target to the substrate. Also highlighted are the magnetic field lines with respect to the target surface. The electrical connections show how the target is isolated from the grounding shield which is at common ground with the substrate stage via the chamber walls.

This configuration transfers heat from the target by conduction to the water cooled copper heat sink via silver particle loaded vacuum grease, and is mechanically clamped by a mechanically clamped stainless steel retaining ring.

Targets of stoichiometric barium titanate were obtained from Super Conducting Materials, Inc. (Suffern, NY, USA). The target used for this study had a composition of $(\text{Ba}_{0.4}, \text{Sr}_{0.6})\text{TiO}_3$ of $\geq 95\%$ theoretical density. The 3.81" diameter ceramic disc was indium bonded into a copper backing plate with a cup shaped depression. The high

density and backing plate design allow efficient cooling of the brittle target to avoid thermal shock during long depositions where large amounts of heat could evolve. Other simpler target/Cu backing plate assemblies were used; however, none offered the longevity of the Cu-cup configuration.

The 30° off-axis gun arrangement and the magnetic field at the target surface serve two distinct advantages for sputter deposition of oxides. The rare-earth metal permanent magnets supply a radial symmetric magnet field in the vicinity of the target surface as seen in figure 3.3. Electrons are trapped in helical orbits by $\vec{E} \otimes \vec{B}$ drift where the magnetic field lines are roughly parallel to the target surface and perpendicular to the applied electric field. This increases the lifetime of plasma electrons and raises the probability of ionizing collisions with the gas atoms and molecules. The result is an increased plasma density near the target surface. The increased ion density increases the ion current at the cathode, allowing high sputter rates to be achieved. This increased density manifests in a ring on the target surface known as the erosion track, which is the location of maximum material removal, and is characteristic to all magnetron sputtering sources. The off-axis geometric orientation of the target relative to the substrate is chosen to mitigate the bombardment of negative ions accelerated toward the substrate. The gun is tilted 30° away from the substrate normal thus kinetic energy transfer to the substrate is reduced by $\cos(60^\circ)$. This geometry reduces the amount of energetic bombardment experienced by the growing film, especially that bombardment arising from oxygen anions. The optimum total pressure and substrate to target center to center distance will also serve to avoid film bombard through thermalization.

The substrate manipulator (p) also functions as the plasma anode. This stage consists of a UHV linear and rotation motion feed through and an internal boron nitride resistive heater (q) with a K-type bare thermocouple for measuring temperature. The stage surface area adjacent to the plasma is wrapped in tantalum foil for thermal insulation. A stainless steel plate above the heater uses clamps to hold down the substrates. Copper foil substrates are clamped into 2" X 1" stainless steel or titanium frames to fully stabilize the perimeter of the flexible foils. The stage is centered in the

cylindrical chamber, yet the target is slightly off center. The conventional dimension of target-to-substrate distance is irrelevant in this configuration and a center-to-center target to substrate distance is defined by h . For this study $h = 8.5$ cm. This parameter can be adjusted by sliding the sputter gun support shaft in the compression seal at the chamber top, or fine tuned by a dial on the linear motion feed through outside of the vacuum system. Note, the substrate heating element is in a fixed position in the chamber and adjusting the stage dial will raise or lower the substrate stage relative to the heater. Moving the substrate stage relative to the heater changes the magnitude of radiative thermal heat transfer making the samples lower or higher temperature, yet since the thermocouple is fixed to the heating element the temperature readout is unaffected by any change in the position of the substrate stage relative to the fixed heater. The stage is rotated during deposition by a DC motor connected to the atmosphere side of the motion feed through. The rotation speed is a linear function of the supplied DC voltage. For this study, 12V are applied to the motor creating a rotation speed of 2 rpm.

The sputter deposition system is capable of depositing oxide films at temperatures ranging from room temperature up to 700 °C. Electrical measurements from two 2" X 1" samples simultaneously deposited shows at least a ~ 4 sq. in. area is uniformly deposited. The following section outlines the deposition conditions found to produce the highest quality BST thin films.

3.3. SPUTTER DEPOSITION PROCESS

Preliminary exploration of deposition conditions were performed on platinized silicon substrates. Results are not included for brevity and are not particularly significant to the goals of this thesis. Outlined below are the deposition conditions to synthesize BST thin films on copper foils that, once annealed, give dielectric properties comparable to those reported elsewhere.

Copper foil substrates are used in the "as-received" state. Appropriate sized foils are cut in a rectangle with clipped corners to allow for placement in the metal frames. The foils are placed in frames to minimize curling from any film strain induced in the

deposition process and to fix the substrates from shifting during pumping/venting cycles and substrate rotation. A photograph of a copper foil clamped in a frame is shown in figure 3.4.

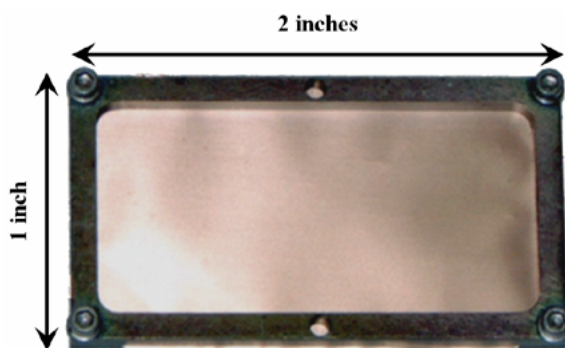


Figure 3.4: A singular 1" X 2" copper foil clamped in a stainless steel frame.

Two frames can fit in the region of uniform deposition on the center of the stage. The samples are loaded into the system with no cleaning except for a blast with dry compressed N_2 to remove loose particles. The system is then sealed by the procedure in the previous section to a base pressure of $<1 \cdot 10^{-5}$ Torr with the gas manifold isolation valve open. When this pressure is reached, the stage is heated in a controlled $30 \text{ }^\circ\text{C min.}^{-1}$ ramp until the thermocouple reads $130 \text{ }^\circ\text{C}$. With the samples loaded and sufficient background pressure reached, the samples are ready for deposition.

The plasma is initiated at process conditions different from the deposition conditions. Process gases are flowed at rates that will remain constant for the entire deposition and the manual gate valve is closed, increasing the total pressure above $1.5 \cdot 10^{-2}$ Torr. The RF generator is set to the desired power and turned on. The high total pressure increases the likelihood of a random ionizing event to start the cascade which forms the stable plasma. The system is viewed through a quartz window until the glow discharge is observed. The manual gate valve is opened until the desired deposition pressure is achieved. The pressure can be normalized to the desired total pressure in less than 5 seconds. Considering deposition times are a minimum of 15 min. (and more typically 1 - 2 hours) this initial pressure fluctuation represents an insignificant period of time. A shutter was included in the system to test if this plasma stabilization period

affected film properties and no noticeable effects except for undesirable particulate contamination from the stainless steel shutter were observed. Consequently the shuttering technique was abandoned.

Initial studies of deposition conditions were evaluated based on qualitative film analysis (i.e. cracking and thickness uniformity by optical thickness fringes) and by X-ray diffraction of annealed films. Optimum conditions are given by table 3.2.

Table 3.2: Optimized sputter deposition conditions.

Parameter	Value
RF Power	300 W
total pressure	$5 \cdot 10^{-3}$ Torr
center-to-center substrate to target distance	8.5 cm
Ar flow	20 sccm
O ₂ flow	5 sccm
Ar:O ₂ ratio	5:1
deposition rate	9 nm min. ⁻¹
stage temperature	130 °C
rotation speed (supplied DC voltage)	2 rpm (12V)

The RF power was set to 300 W to achieve a reasonable deposition rate. Given a plasma transfers charge in the 10 mA range, 300 W should apply on the order of 10¹ kV or greater. Assuming a collision-less sheath this would give argon ions impingement energy >> keV. Sputter yields saturate when the impingement energy is greater than an order of magnitude above the binding energy of the target material, approximated by the heat of sublimation, which is 100 eV or less for all elements and compounds. Therefore the power supplied is sufficient to eject any component of the target and a stoichiometric ratio of species entering the gas phase can be assumed. The upper bound for input power is

determined by safe operating powers for the equipment and the ability to heat transfer the amount of thermal energy evolved at the target surface. The power chosen allows for efficient sputtering of near stoichiometric ratios of species at a reasonable deposition rate while still operating at power densities that ensure long target lifetimes.

As stated in the discussion of sputtering theory, the Pd product is a critical parameter for plasma stability, and from table 3.2, $Pd = (5 \cdot 10^{-3} \text{ Torr})(8.5 \text{ cm}) = 0.057 \text{ kg sec}^{-2}$ in SI units. This value also determines the degree that plasma species are thermalized in transit through the plasma, or reduce kinetic energy to the ambient temperature equivalent. The kinetic theory of gases would give the mean free path for the species $\langle \lambda \rangle \sim 1 \text{ cm}$ at $5 \cdot 10^{-3} \text{ Torr}$ ignoring the minute differences in the collisional cross sections of each species. On average, these particles will encounter 8 - 9 collisions as they transverse the target-to-substrate distance of 8.5 cm and transferring energy to an average value. Considering the low plasma ion density, the vast majority of species is neutral and has kinetic energy equal to room temperature. Plasma anions are accelerated toward the growing film and can cause undesirable ion bombardment yet after only a few collisions with low energy neutrals will lose energy and reach an equilibrium kinetic energy approaching room temperature. This process is statistical and the existence of a high energy tail in the Maxwell-Boltzmann distribution of kinetic energy implies high energy anions will also exist to some degree irrespective of the average number of collisions anions encounter.¹⁴¹

The exact Ar:O₂ ratio in sputter deposition of oxides is always under considerable scrutiny in any oxide system. There is a tradeoff between the ideal level of energetic impingement in an oxide containing plasma, and the risk of anion deficiency that can occur under low $p\text{O}_2$ conditions. The choice of 5:1 Ar:O₂ during deposition allows for near stoichiometric film upon deposition while accepting a moderate level of film bombardment. This bombardment will partially determine the resulting thin film grain morphology, yet is not sufficient to cause excessive amounts of sputter etching of the growing film as the deposition rate is 9 nm min^{-1} , an appreciable rate for oxide films.

The use of a copper substrate does not afford a high enough temperature to realize epitaxial film growth and avoid copper oxidation. The pO_2 in the sputtering ambient and the existence of high activity oxygen ions and free radicals allow for the oxidation of the copper substrate. Thermodynamically this should occur at 130 °C, yet at this temperature the reaction is kinetically limited. X-ray diffraction (XRD) experiments reveal that attempts to deposit films at > 130 °C cause the formation of Cu_2O .

The substrate is also rotated at 2 rpm during deposition. This rotation speed is sufficient to form a radially symmetric thickness profile in the center 3” of the stage. The off-axis configuration would cause high deposition rates at positions on the stage closer the lower edge of the target yet through rotation this effect is averaged in a circular pattern.

The deposition conditions described above are used to synthesize BST thin films of predetermined thickness by adjusting deposition time assuming a constant deposition rate. Due to the low deposition temperature, as-deposited films have low crystalline quality and require post deposition anneals.

3.4. LOW pO_2 , HIGH TEMPERATURE ANNEALS

Ex situ annealing to high temperatures fully transforms the as-deposited BST film to the equilibrium perovskite phase. To maintain the metallic character of the copper substrate, anneals must be performed using conditions that will not result in oxidation. This section will describe the equipment and methodology for *ex situ* anneals to fully crystallize the BST thin film while preserving the metallic copper substrate.

A thermodynamic analysis predicts process conditions where the desired material phases, metallic copper and perovskite BST, are at equilibrium. Extending upon the concepts of copper oxidation described in section 2.9 and equations 2.40 through 2.43, a $pO_2 - T$ phase diagram can be constructed that includes the oxidation of copper and the cations of BST (figure 3.5)¹⁵⁴⁻¹⁵⁷.

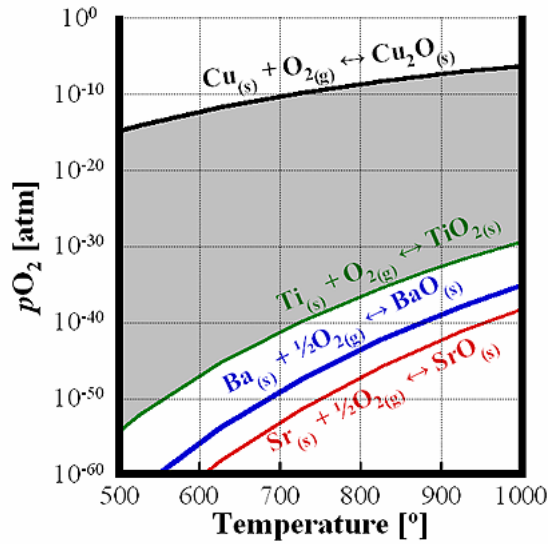


Figure 3.5: pO_2 - T phase diagram for the Cu - BST system. Gray area shows the set of process conditions to maintain metallic copper in equilibrium with molecular oxygen and oxidized BST cations.

Only the BST cations' binary oxides are displayed and this figure does not precisely locate the equilibrium conditions for the perovskite phase. However, analysis of the phase diagram of TiO_2 and BaO or SrO (see appendix figures B.1 through B.3) shows that an equimolar ratio of these compounds yields the phase of perovskite $BaTiO_3$ or $SrTiO_3$. This indicates the free energy of formation of $BaTiO_3$ is lower than any of the individual cation binary oxides inferring a stable perovskite phase at lower pO_2 for a given T . Analysis of figure 3.5 displays a large process window of pO_2 and T conditions where molecular oxygen, metallic copper, and perovskite $BaTiO_3$ are at thermodynamic equilibrium. Using this knowledge, the sputter deposited BST is annealed to temperatures approaching the melting point of the copper substrate (1084 °C) and controlled pO_2 .

A furnace was constructed to achieve the desired pO_2 - T conditions and is shown schematically in figure 3.6.

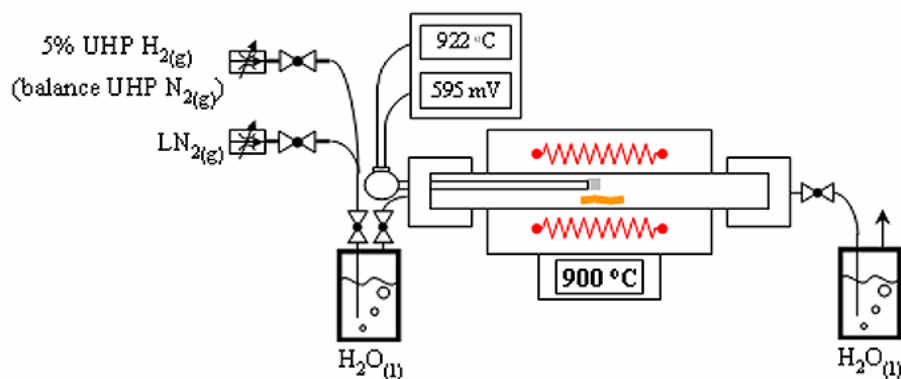


Figure 3.6: Schematic diagram of the crystallization furnace showing the gas delivery system and the position of the *in situ* oxygen sensor.

A 2" diameter fused silica tube is sealed by Viton® O-ring compression fittings to isolate samples from the ambient during anneals. The sealed tube is encapsulated in a glowbar furnace (Lindberg/Blue M, Asheville, NC, USA) with an approximately 3" long hot zone capable of reaching temperatures > 1000 °C. This furnace uses a standard PID algorithm to control temperature and time in a programmable ramp and soak cycles with feedback from an S-type thermocouple external to the seal tube. The pO_2 is controlled by supplying a mixture of H_2 , N_2 , and $H_2O_{(v)}$ gases. The flow of forming gas, 5% H_2 (99.999% purity), and N_2 gas supplied from a liquid nitrogen dewar are controlled using MKS Instruments (Andover, MA, USA) mass-flow controllers. The gas mixture is passed through a water bubbler to add water vapor prior to entering the sealed tube. H_2 and $H_2O_{(v)}$ (N_2 acts as a dilutant) establishes an equilibrium compensating for the level of oxygen impurities in the supplied gases and determines the pO_2 in the furnace hot zone by the following chemical reaction.



$$pO_2 = \frac{pH_2O^2}{pH_2^2} \exp\left(\frac{\Delta G}{RT}\right) \quad \text{eqn [3.2]}$$

A doped zirconia oxygen sensor (Australian Oxytrol Systems, Victoria, Australia, DS-Series solid-state pO_2 sensor) centered in the furnace hot zone allows monitoring of the

pO_2 *in situ* by reading the voltage drop across the sensor and the temperature from an R-type thermocouple. The following engineering equation supplied by the manufacturer allows calculation of pO_2 from voltage and temperature in the ranges 700 - 1700 °C and $1 - 10^{-24}$ atm.

$$pO_2 = 0.209 \exp\left(\frac{-46.42 \cdot V}{T}\right) \quad \text{eqn [3.3]}$$

T in Celsius [°C], V in millivolts [mV]

Samples are placed on fused silica furnace furniture, secured with copper weights, and set in the hot zone of the sealed furnace beneath the oxygen sensor. Gases are flowed at 410 sccm LN₂(g) and 20.5 sccm 5% forming gas through the DI H₂O bubbler held at 25 °C. The furnace is ramped from the standby temperature of 150 °C at 30 °C min⁻¹ to a dwell temperature of 900 °C. The total wet gas flow ratio of H₂:N₂ = 1:420 gives a 10⁻¹² atm pO_2 at 900 °C. These pO_2 - T conditions are 4 orders of magnitude lower pO_2 than thermodynamically predicted to oxidize the copper substrate and <150 °C below the melting point of copper. These conditions were chosen for all anneals to allow margin of safety and avoid substrate oxidation. The furnace described above was replicated to allow more processing capacity. Standard flows were calibrated against the original furnace and no discernable difference in specimen properties were observed from processing in either furnace.

The *ex situ* anneal using the equipment and conditions described above transformed the “proto-”crystalline as-deposited BST film to a fully crystalline perovskite (Ba_x, Sr_{1-x})TiO₃ phase while preserving the metallic Cu substrate.

3.5. RE-OXIDATION ANNEALS

Section 2.7 discusses details of BST defect chemistry, specifically how free energy minimization predicts a non-zero equilibrium concentration of oxygen defects. Considering the low pO_2 , high temperature anneals outlined above, an elevated levels of these point defects are expected which may lead to degradation of electrical properties

such as low resistivity. This section outlines the procedure for anneals to reduce the concentration of oxygen vacancies in the crystallized dielectric.

To improve the insulation resistance, a methodology for BST re-oxidation annealing the specimen was developed. Lower temperature, high oxygen activity anneals reduce the final concentration of oxygen vacancies following similar entropic considerations and assumptions used previously for calculating conductivity from crystallization anneals yet in a manner that kinetically limits substrate oxidation. A high vacuum tube furnace with a controlled $O_{2(g)}$ leak was used for these anneals.

Samples were inserted into the hot zone of a silica high vacuum evacuated tube furnace and a controlled leak of UHP $O_{2(g)}$ (99.999% purity) by means of a sapphire variable leak valve. A schematic of the vacuum tube furnace is given in figure 3.7.

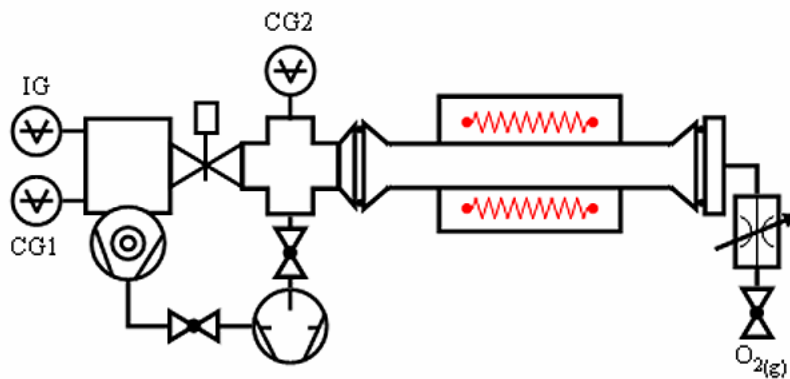


Figure 3.7: Schematic diagram of the sealed vacuum furnace used for re-ox anneals.

Samples are sealed inside the cool inlet side of the silica tube and evacuated by a rotary vane pump to the proper crossover pressure where the TMP can then evacuate the system to a base pressure of $<1 \cdot 10^{-6}$ Torr. The furnace is then ramped at $30 \text{ }^\circ\text{C min}^{-1}$ from 150 to 550 $^\circ\text{C}$. The sample is then fed into the center of the hot zone by means of a stainless steel transfer rod that allows linear motion while maintaining vacuum. The leak valve is opened until the oxygen flow stabilizes with the pumping speed to reach a stable total pressure of oxygen of 10^{-5} Torr read at the ion gauge.

To note, the actual pressure at the sample is not read by this configuration since there is a significant conductance between the position of the sample and the gauge. The

reported re-ox pressures are given as a process control parameter and the actual oxygen activity scales linearly with the ion gauge recorded pressure, and is about 4X higher than what is recorded at the ion gauge. The sample is left in this stable environment for 30 minutes and then the sample is retracted to the cool side of the silica tube without breaking vacuum or reducing the oxygen flow. When the sample is cooled, the oxygen flow is shut off and the tube vented. This second *ex situ* anneal is termed a “re-ox anneal” since the intended purpose is to reintroduce oxygen into the lattice and reduce the concentration of oxygen vacancies in the dielectric.

The re-ox anneal is intended to improve the resistivity of the dielectric yet thermodynamically is predicted to oxidize the copper substrate. The anneal conditions, 550 °C and 10^{-8} atm, are above the free energy line for Cu_2O (see figure 3.5) and therefore, predicts copper oxidation at equilibrium. The success of the anneal is due to the kinetic limitation of oxygen diffusion through the densified dielectric layer to copper in the vicinity of the dielectric/substrate interface. XRD analyses of “re-ox” annealed samples show no reflections from the most likely copper oxide (Cu_2O).

Re-ox anneals were performed to achieve the lowest loss and/or leakage current for a particular specimen. These anneals are necessary to correct raw material impurities and high T , low $p\text{O}_2$ processes conditions needed to avoid copper oxidation.

3.6. DEVICE DEFINITION

Calculation of permittivity from capacitance measurements is straightforward by equation 2.9 if a parallel plate device configuration is used and film thickness and electrode area are known. For this reason, MIM devices were fabricated by depositing a platinum film in predefined areas onto fully processed BST/Cu specimen. These devices allow high electrical fields across the BST thin film when modest voltages are applied across the top electrode the copper substrate. This allows application of electrical fields approaching the breakdown strength of the dielectric and characterization of the saturated intrinsic permittivity and the full tunability.

Fully processed BST/Cu specimens are clamped between a stainless steel shadow mask and stainless steel backing plate. The shadow masks have circular opening in a series of diameters (70 μm , 117 μm , 220 μm , 326 μm , & 522 μm). A platinum thin film is DC magnetron sputtered over the masked specimen from a 4" platinum foil target (99.999% purity, Alfa Aesar, Ward Hill, MA, USA) using a similar Torus 4 sputter gun used for BST deposition yet in a parallel target - substrate arrangement. A 1500 Å Pt film is deposited in 30 seconds using 3 W cm^{-2} , 5 cm substrate to target distance, and 30 mTorr Ar. The exact top electrode diameter is measured optically in a standard optical microscope at $\sim 500\times$ and a calibrated scale bar. Figure 3.8 is an example shadow mask defined electrode on a calibrated optical image.

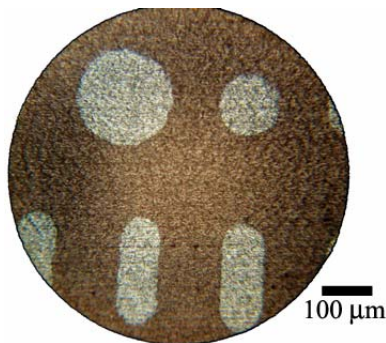


Figure 3.8: Calibrated optical image (taken at 100X) of sputtered top Pt electrodes defined by a shadow mask.

Interdigitated electrodes (IDE) are employed for two primary reasons: 1) to demonstrate fine feature photolithography on copper foil specimen and 2) to explore dielectric properties when BST thin films are deposited on insulating substrates (i.e. alumina). IDE electrodes provide a planar capacitive structure and therefore can be achieved using single step photolithography. Photo-imageable polymer films are deposited on fully processed specimens in sequential spin coatings and 140 °C baking of Shipley 1813 (Rohm and Hass Electronic Materials, Marlborough, MA, USA) and MicroChem LOR (Lift off resist) 5A (MicroChem Corp., Newton, MA, USA). This particular photo-imageable polymer stack is a positive image photoresist (PR) designed for lift off pattern transfer. Desired electrode patterns are exposed through soda lime glass/Cr photomask using a MA 6 Karl Suss (Süss MicroTec AG, Garching, Munich,

Germany) contact mask aligner operating in soft contact mode with I line UV light ($\lambda = 365$ nm). The exposed PR is developed with Shipley MF 319 developer (Rohm and Hass Electronic Materials, Marlborough, MA, USA). Upon imaged PR, 1000 Å Pt blanket films are sputter deposited as described in the previous paragraph. The Pt overlaying the residual PR is removed by an acetone PR strip leaving Pt structures as defined by the photomask. This process allows submicron linewidth control of transferred patterns.

3.7. PHYSICAL CHARACTERIZATION

Specimens are characterized by various complimentary techniques to reveal physical structure. X-ray diffraction (XRD) allows measurement of macroscopic volumes of material for phase identification and extent of crystallinity. Cross sectional transmission electron microscopy (TEM) provides electron diffraction data with high spatial resolution and direct imaging of microstructure. Atomic force microscopy (AFM) gives high resolution imaging and quantification of surface topography which can be tied to grain morphology at the sample surface.

XRD data are taken by a Bruker D5000 4-circle diffractometer fitted with a HighStar area detector controlled by GADDS v3.330 software (Bruker AXS, Karlsruhe, Germany). A 0.8 mm diameter collimated Cu K α X-ray beam is used for measurement. When the sample is orientated at a 15 ° Bragg angle, a 7.77 mm² elliptical area and a depth on the order of 10 μ m is analyzed. BST/Cu foil samples are attached to amorphous soda lime glass slides with double sided adhesive tape to avoid diffraction signal from the aluminum goniometer stage. With this equipment a 2-D map of diffracted intensity is collected where the horizontal axis is the 2θ Bragg angle, and the vertical direction is out of plane tilt denoted by χ . θ - 2θ plots are obtained by integrating counts over the χ direction. Analysis of θ - 2θ plots gives interplanar spacing that are compared against compiled powder XRD data²²⁴ for phase identification. Film texture can be quantitatively identified by calculating the intensity profile over the χ arc direction on the 2-D images or maxima in intensity versus χ plots obtained by integration over the θ direction.

Transmission electron microscopy provides diffraction information with fine spatial resolution and sub nanometer resolution imaging of film structure. TEM analysis requires thin electron transparent membranes. Cross sectional TEM specimens were made by conventional polishing techniques or focused ion beam (FIB) micromachining.

Conventionally polished TEM specimens were made by first mounting full processed films between portions of polished silicon wafers using M-bond™ 600 epoxy (Vishay Measurements Group, Malvern, PA, USA). After proper cures the samples were thinned in cross-section using a MultiPrep™ 8 automated polishing system and diamond impregnated polymer polishing films (Allied High Tech, Rancho Dominguez, CA, USA). Samples were final polished using 0.01 μm colloidal silica on a felt pad. Samples were made electron transparent with a Fischione 1010 (EA Fischione Instruments, Inc., Export, PA, USA) ion mill with the guns oriented so that ions encounter the ceramic thin film before the copper substrate in an attempt to reduce the copper removal rate. Ar ion gun parameters of 13 ° tilt, 6 KV, and 6mA were used while rotating ± 15 ° about the direction perpendicular to the sample's glue line. A final ion mill polish with gun parameters of 20° tilt, ½ kV, and 6 mA was used to remove any amorphous damage from the ion milling. The TEM specimens were made so that the final configuration was a wedge with an electron transparent region at the leading edge.

FIB made TEM cross section specimens were provided by Materials Analytical Services (Materials Analytical Services, Inc., Raleigh, NC, USA). A beam of Ga⁺ ions is produced from a liquid Ga cone with a 25kV extraction voltage and is focused by electromagnetic lenses to a sub-micron spot size (<10nm spot sizes can be achieved using apertures within the optical column). High beam currents (10 pA - 1 nA) are used remove material by momentum transfer in a similar mechanism as sputter deposition. The FIB optics raster the high energy, high current Ga⁺ beam to form deep trenches around a specific area producing a thin 100 nm membrane which can be transferred to a standard Mo TEM grid.

TEM specimens are imaged by a Topcon 002B 200kV TEM (Topcon Corp., Itabashi-ku, Tokyo, Japan) and conventional film or a JEOL 2010F 200kV TEM (JEOL

Ltd., Akishima, Tokyo, Japan) with a Gatan GIF (Gatan, Inc., Pleasanton, CA, USA) energy filtering digital imaging system. The Topcon TEM uses a LaB₆ thermionic emitter and is better suited for diffraction analysis and diffraction contrast imaging of microstructures at intermediate magnifications. The JEOL 2010F TEM has higher resolution and more sophisticated digital image acquisition system allowing for high resolution TEM (HRTEM) imaging and viewing of lattice fringes. Therefore analyses requiring fine spatial resolution, such as interface investigations, are better suited in the JEOL TEM. Samples are viewed in the cross section to reveal the film morphology through the film thickness and characterization of the BST/Cu interface.

Atomic force microscopy provides topographical imaging of specimen surfaces. A CP-Research Thermomicroscope AFM (Veeco Instruments Inc., Woodbury, NY, USA) was operated in contact mode. This technique provides sub-nanometer topographical resolution. Software based algorithms calculate surface roughness from the raw Z-height height versus lateral position data. Grain boundary grooving at the film surface provides topography related to grain morphology giving AFM contrast allowing measurement of grain size. The line intercept grain size measurement method is used on AFM images to quantify grain size of fully processed BST films. If TEM analysis reveals equiaxial grain morphology through the entire film thickness then the AFM measured grain size fully describes the average grain size throughout the specimen. Alternatively, if columnar grain morphology is present then the AFM grain size describes the average grain size in the lateral direction and the grain size normal to the film surface is provided by TEM images.

The preceding physical characterization methods are complimentary techniques providing a comprehensive understanding of the microstructure and phase composition of the thin films of BST processed on Cu foil substrates.

3.8. ELECTRIC CHARACTERIZATION

Electrical properties of BST/Cu specimens are explored by analyzing impedance versus DC bias, frequency, and temperature. These experiments reveal the dielectric

properties of the BST thin films and allow determination of electric performance at the intended operating conditions of frequency-agile circuits.

The impedance of the MIM structures is measured by a HP 4192A impedance analyzer (Agilent, Palo Alto, CA, USA). Electrical connection to MIM BST/Cu specimens are achieved by tungsten probes connected to micro manipulators. A thin tungsten probe contacts the top of a Pt electrode and a thicker probe is pierced through the thin film from the top by a separate micro manipulator to contact the Cu foil substrate. These tungsten probes comprise two counter nodes of the impedance bridge test circuit. In this way, the top and bottom electrodes of a MIM capacitor can be electrically connected to test equipment allowing straightforward calculation of permittivity by the parallel plate capacitor equation (equation 2.9).

An impedance analyzer applies a sinusoidal voltage signal and measures the current response of the circuit to calculate the impedance and phase angle. The impedance is converted to capacitance and the phase angle to $\tan \delta$ assuming an equivalent circuit of ideal capacitors and resistors to mimic a real capacitor that allows the flow of current. Capacitance and $\tan \delta$ can be measured at a range of DC bias superimposed on the sinusoidal voltage signal and is recorded by a LabView™ (National Instruments, Austin, TX, USA) program. The collected C - V data allow calculation of the permittivity, dielectric loss, and tunability of the BST film at discrete DC bias voltages.

Dielectric frequency dispersion is measured using the same impedance bridge, probe station, and data collection setup used for C - V characterization. The HP 4192A can operate between 0.5 Hz - 13 MHz yet the MIM capacitors are only impedance matched to the measurement circuit over a finite frequency range. Thus at the extremes of this range the calculated capacitance and $\tan \delta$ values are dominated by measurement artifacts.

To explore temperature dependent dielectric properties, capacitance and $\tan \delta$ were measured using the impedance bridge while the samples were placed on a controlled temperature stage. The controlled temperature stage can control temperature between 100 and 500 K by resistive heaters and cooling mechanism based on adiabatic expansion of high pressure gas. The sample is placed on a quartz stage with internal tapered channels

that when high pressure gas forced through the channels the sample is cooled by the adiabatic expansion of the gas. This device can cool to 100 K using UHP argon (99.999% purity) at $P > 1800$ psi where water and contaminants are filtered by zeolite upstream and a vacuum of <30 mTorr ambient is maintained. Controlled temperature ramps are handled by a K-20 programmable temperature controller (MMR Technologies, Mountain View, CA, USA) with feedback from a calibrated RTD temperature sensor.

To ensure the BST/Cu specimen is at the same temperature as the RTD, samples are mounted into a ceramic chip carrier (Addison Engineering, Inc., San Jose, CA, USA). The samples are mounted in the Au plated well of the chip carrier with thixotropic Ag epoxy (Epoxy Technology, Billerica, MA, USA) and cured at 150 °C for 20 min on a hot plate. Then 25 μm diameter gold wires are glued from the desired Pt top electrode to an internal bond pad in the ceramic package using Ag epoxy. This procedure repeated for a shorted device for electrical contact to the copper substrate. The wired chip carrier is again heated to cure the Ag epoxy. The mounted sample is then placed onto the temperature stage using thermal paste and the corresponding external chip carrier leads are soldered to electrical vacuum feed-throughs. The entire assembly is sealed in a vacuum chamber and evacuated with a mechanical rotary vane pump below 30 mTorr. The impedance bridge is connected to the electrical feed-throughs and temperature ramp parameters are entered into a LabView™ program which communicates with the K-20 temperature controller. The same control program facilitates data collection.

DC Leakage current measurements are made using a Keithly 617 programmable electrometer (Keithly Instruments, Cleveland, OH, USA) and electrical contact is made using a probe station in a similar configuration used with the impedance analyzer. A LabView™ program controls DC voltage sweeps including predetermined delays and repeated measurements at each voltage to statistically reduce the noise inherent to low current measurements.

This set of electrical characterization experiments allows a comprehensive understanding of the dielectric properties of BST thin films as they relate to tunable capacitors in frequency-agile circuits. Capacitance versus DC bias gives quantitative

measurement of tunability and the ability to tolerate high fields. Measurement of the frequency dispersion gives a qualitative assessment of the mobility and concentration of excess charges. Temperature dependent measurements allow determination of the Curie temperature and the broadness of the ferroelectric phase transition. Leakage current measurements quantify the dielectric resistivity while giving qualitative information about the number of free charge carriers.

3.9. EXPERIMENTAL PROCEDURE SUMMARY

The Film on Foil processing methodology outlined in this chapter allows BST thin film deposition on copper metal foils. BST thin films are sputter deposited using specialized deposition equipment and parameters which produce stoichiometric $(\text{Ba}_{0.6}, \text{Sr}_{0.4})\text{TiO}_3$ while minimizing plasma bombardment. Successive *ex situ* controlled $p\text{O}_2$ anneals crystallize the thin film while preserving the metallic phase of the copper foil substrate. This processing methodology uses equipment and processes that have proven economical in a high volume manufacturing environment. Physical and electrical characterization techniques are outlined so that process-structure-property relationships can be developed.

4. PROCESSING - STRUCTURE - PROPERTY RELATIONSHIPS: SPUTTERED BST THIN FILMS ON COPPER FOIL SUBSTRATES

The Film on Foil process methodology for depositing BST thin films on copper foil substrates employs processing techniques, equipment, and raw materials selected to obtain sufficient dielectric properties appropriate for tunable capacitors. The success of this process is assessed on the resulting material performance and the practicality and cost-effectiveness for high volume manufacturing. Any assessments of manufacturing costs are circumstantial, yet sputter deposition and post deposition anneals have proven appropriate for commercial production of optical, structural, and electronic coatings.

Chemical vapor deposited BST thin films are generally accepted to be of the highest quality.^{85, 93, 112, 113, 225-227} Historically, the bulk of BST thin film research has used platinum electrodes and silicon substrates due to the chemical inertness of Pt and the availability, quality, and uniformity of Si. Unfortunately, platinum suffers from poor adhesion to SiO₂ and a significant mismatch of thermal expansion coefficient to Si. Consequently, there is a tendency for platinum delamination when films are grown to thicknesses greater than 100 nm and process temperatures exceed ~ 600 °C. As such, the ability to make low power consumption devices is severely limited by the high electrode resistance established by the relatively thin platinum.

This chapter presents physical and electrical characterization of BST/Cu specimens allowing identification of structure-process-property relationships and demonstrates viability for commercial production. As the following results will show, PVD sputtered BST thin films on copper foils show comparable dielectric properties to CVD deposited films on platinized silicon substrates. A thorough physical characterization of fully processed BST/Cu specimens develops a comprehensive picture of microstructure, while electrical characterization establishes the connections to the dielectric response. These experiments identify of processing-structure-property

relationships for tunable capacitors synthesized by substantially less costly processes than conventional CVD or PVD techniques.

The choice of base metal copper foil substrates provides novel capabilities in processing latitude and intended applications. Polycrystalline copper substrates made by electrodeposition can be used as a substrate for a range of oxide dielectrics provided that the correct thermodynamic window can be identified. Due to improved thermo-physical stack stability, copper based BST structures can be annealed at temperatures approaching the melting point of Cu allowing for improved crystallization and densification. These dielectric/foil stacks can be subsequently laminated into printed wiring boards or become part of flexible electronics.

To date, few attempts at BST thin film sputter deposition on base metals have been published. A search of the open literature revealed success with epitaxial growth of BST on biaxially oriented Ni tapes¹⁵⁹ and the use of an interfacial buffer layer of $\text{TiO}_2/\text{Al}_2\text{O}_3$ over copper substrates²²⁸. This chapter demonstrates the ability to make low loss, highly tunable BST capacitors without interface reactions directly on copper.

4.1. SPUTTER DEPOSITED BST THIN FILM ON PLATINIZED SILICON

Initial process optimizations were performed on platinized silicon substrates. These results represent an intermediary effort to benchmark the BST process against literature examples. Low temperature sputter depositions were used to grow BST thin films as described in Chapter 3. The film stack of these substrates, $\text{Si}/\text{SiO}_2/\text{ZrO}_2/\{111\}\text{Pt}$, allows thin film deposition on conducting Pt adhered and electrically isolated from the silicon wafer carrier by silica and zirconia layers. The substrates were prepared in house using molecular beam deposition for the zirconia and $\{111\}$ textured platinum layers on 150 nm of thermal oxide. BST films are crystallized on platinized silicon using 650 °C air anneals. The use of platinized silicon substrates avoids the need for low $p\text{O}_2$ anneals allowing sole evaluation of the sputtering conditions to the resulting thin film structure as they relate to electrical properties.

Figure 4.1 shows XRD data for a 250 nm (30 min. deposition) thick $(\text{Ba}_{0.6}, \text{Sr}_{0.4})\text{TiO}_3$ thin film on platinized silicon.

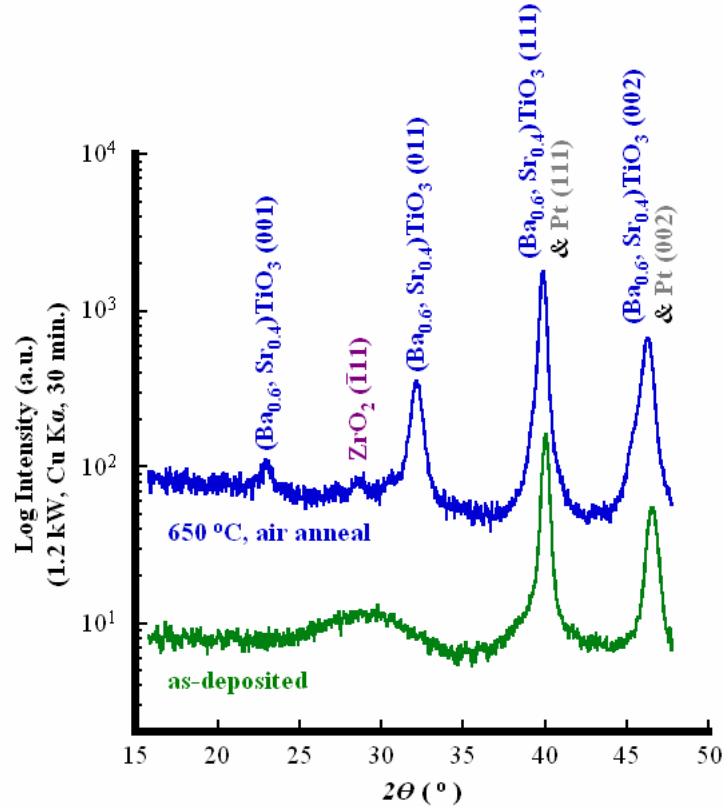


Figure 4.1: XRD of a 250 nm thick BST film on platinized silicon. In the as-deposited state (**green**) peaks corresponding to the substrate platinum and intensity from the amorphous film are identifiable. After 650 °C 30 min. air anneal (**blue**) reflections from the BST perovskite phase can be seen peaks of Pt and BST with peaks for the platinum substrate and the zirconia adhesion layer between the Pt and Si.

As-deposited, the BST thin film shows little crystallinity; evident by the broad low intensity signal at $25 < 2\theta < 35$. XRD analysis only reveals strong diffracted intensity from the substrate Pt. The low temperature deposition does not provide sufficient transport to form the equilibrium perovskite phase. When the sample was annealed at 650 °C in air, diffracted intensity is observed at 2θ values corresponding to perovskite BST and the zirconia and Pt substrate peaks (powder diffraction files in Appendix C). The (111) and (002) Pt peaks overlap the same index BST peaks. Attempts to anneal the

specimens to higher temperatures resulted in delamination of the substrate Pt from the silicon wafer destroying the BST film.

One thousand angstrom thick Pt top electrodes were sputtered through a shadow mask to form Si/SiO₂/ZrO₂/Pt/(Ba_{0.6}, Sr_{0.4})TiO₃/Pt MIM capacitors. Impedance measurements were performed as a function of DC bias and are shown in figure 4.2. Capacitance was measured at 100kHz and 0.1V oscillation level from -15 to 15V DC bias.

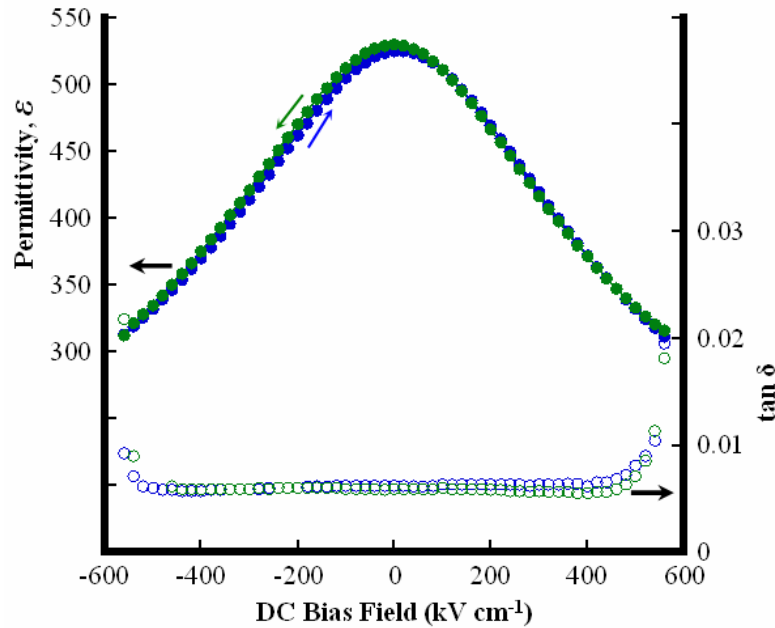


Figure 4.2: Room temperature permittivity and loss versus DC bias field measured at 100 kHz with 4 kV cm⁻¹ oscillation level on a Pt/BST/Pt MIM device.

Considering a dielectric thickness of 250nm and a 150 μm diameter Pt top electrode, these measurements revealed a peak permittivity of 530 at 0V bias and a minimum permittivity of 310 at 600 kV cm⁻¹ DC bias field using 4 kV cm⁻¹ oscillation field level. Tan δ is 0.006 for ±400 kV cm⁻¹ and at high fields increases due to current leakage through the dielectric. The 530 peak permittivity and 1³/₄:1 tunability is modest in comparison to those observed for BST thin films of similar thickness in the literature, yet the low dielectric loss is indicative of a high quality dielectric. The low tunability is not unexpected considering the comparatively low thermal budget of this process when compared against processes that achieve substantially larger values.

Pt/BST/Pt MIM devices' permittivity and $\tan \delta$ frequency dispersion was measured from 1000 Hz to 1 MHz with a 4 kV cm^{-1} oscillation field with 0 V DC bias using the impedance analyzer (figure 4.3).

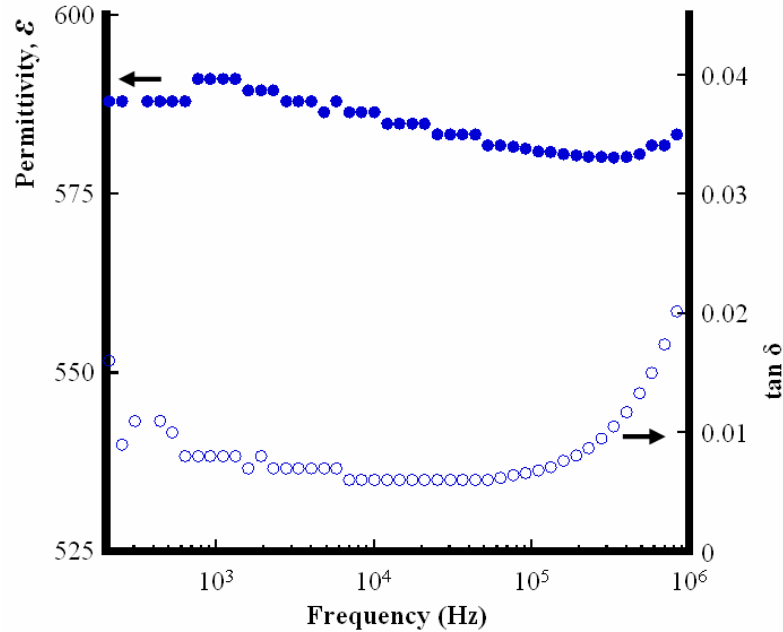


Figure 4.3: Room temperature dielectric constant and loss frequency dispersion data measured with 4 kV cm^{-1} oscillation level on a Pt/BST/Pt MIM device.

Less than 1% dispersion per decade is observed and $\tan \delta$ is consistently below 0.01 until resonance with the impedance analyzer is reached at approximately 200 kHz. No evidence of space charge dispersion is seen in the data. These data show that the above stated permittivity and tunability result from paraelectricity as opposed to large concentrations of electro-active point defects.

The XRD and dielectric property measurements establish the validity of using sputtering to deposit BST thin films. Although XRD data show the films are crystalline when annealed, the low anneal temperatures afforded by the platinized silicon substrates limits crystalline quality, and hence, permittivity and tunability are modest compared to several ferroelectric thin films in the literature.

Further development and experimentation is expected to improve dielectric properties, yet platinized silicon substrates were abandoned for copper foil substrates to

allow higher annealing temperatures and increased crystallinity. These experiments establish sputter deposition as a viable thin film synthesis technique for BST.

4.2. SPUTTER DEPOSITED BST THIN FILM ON CU FOILS

The sputter deposition conditions established using platinized silicon substrates was duplicated on Cu foil. The major processing adaptation is the need for low pO_2 post deposition anneals. The copper foils afford higher anneal temperatures since the accumulation of thermal expansion mismatch induced strain is mitigated by the compliant copper foil.

4.2.1. BST/Cu physical characterization

The metric for process optimization is the highest possible tunability with the lowest dielectric loss and leakage current. As the origin of tunability is ferroelectricity and the relation between the electromechanical response and crystal size is well documented, it is prudent to characterize crystallinity and grain morphology. This will allow comparison of data to other studies but also allow insight into the mechanisms for film growth. Also, the processing should be consistent with the economical mass production, thus, property uniformity and device robustness are considered.

The physical structure of BST/Cu specimens was characterized by various complimentary techniques to establish an understanding of microstructure evolution. XRD data were collected after each process step (as-deposited, post crystallization anneal, post “re-ox” anneal) to understand the phase development, densification, and extent of crystallization. TEM and AFM provided high resolution measurement of the microstructure and grain size. These experiments allow development of structure-property relationships.

Figure 4.4 shows XRD θ - 2θ data for an 800 nm thick (90 min.) BST thin film as-deposited on a copper foil substrate.

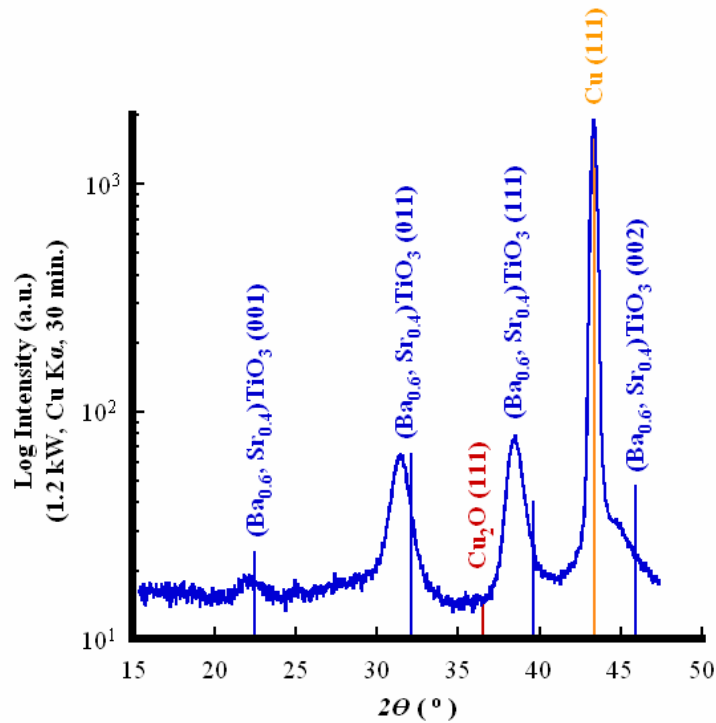


Figure 4.4: XRD data for an as-deposited 800 nm thick $(\text{Ba}_{0.6}, \text{Sr}_{0.4})\text{TiO}_3$ film. Guidelines show the exact 2θ peak position and peak height according to the JCPDS PDF card. Note no reflections from the most likely copper oxide phase, cuprite Cu_2O . The vertical solid lines are given as guides to the expected peak position and intensities given by the powder diffraction cards.

Low intensity broad peaks can be located at 2θ values associated with crystalline $(\text{Ba}_{0.6}, \text{Sr}_{0.4})\text{TiO}_3$. The low intensity broad peaks are consistent with small crystallites of the desired phase with only short range order. The extent of crystallinity, however, is noteworthy given the low temperature deposition. Very often, low temperature depositions result in amorphous thin films as seen previously for BST thin films on platinized silicon. Since the large polarizability of the perovskite crystal structure is responsible for large and non-linear permittivity, enhanced crystallinity is expected to improve dielectric properties, as such the advantage of a crystalline as-deposited film becomes apparent. To fully develop the crystalline ferroelectric phase post-deposition processing is needed.

High temperature, low pO_2 *ex situ* anneals using the equipment and conditions described previously transform the “proto-”crystalline as-deposited BST film to a fully crystalline perovskite $(Ba_x, Sr_{1-x})TiO_3$ phase while preserving metallic copper. The BST/Cu sample was annealed at 900 °C, 10^{-12} atm pO_2 for 30 minutes. Post anneal X-ray diffraction is seen in figure 4.5 where the post crystallization anneal data are presented adjacent to the data previously shown in figure 4.4.

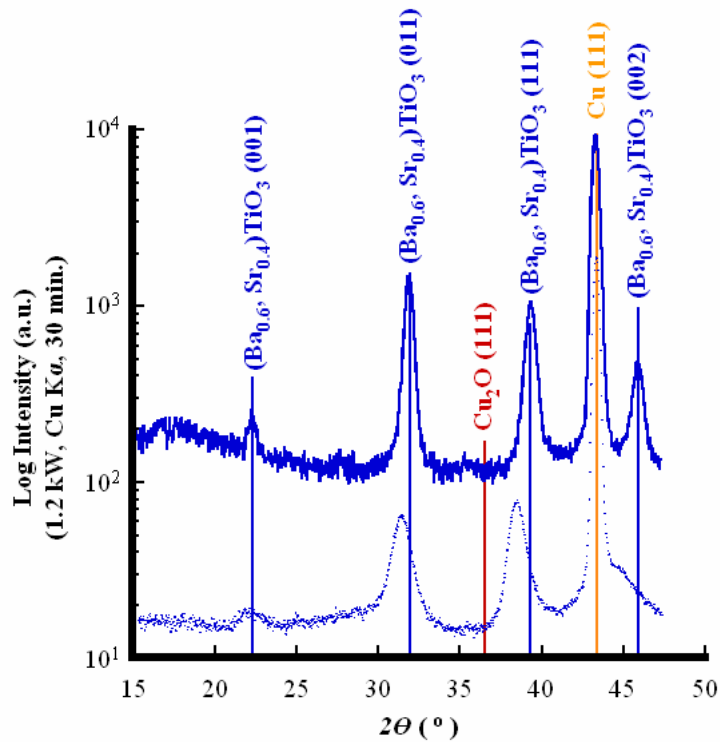


Figure 4.5: XRD data for the crystallized sample (blue solid line). The data is displayed above the data shown in figure 4.4 (blue dotted line) to exemplify the increase in peak intensity for perovskite $(Ba_{0.6}, Sr_{0.4})TiO_3$. The vertical solid lines are given as guides to the expected peak position and intensities given by the powder diffraction cards.

Comparison shows the peaks attributed to BST are sharper and more intense after the crystallization anneal indicating complete crystallization. Additionally, no intensity at 36.42° 2θ can be found. This angle corresponds to the highest intensity reflections of the lowest oxidation state of copper, Cu_2O . The high T , low pO_2 anneal is thermodynamically predicted to result in problematic concentrations of oxygen vacancies;

therefore, the sample was “re-ox” annealed *in-vacuo* at 550 °C in 10^{-8} atm of flowing O_2 . These conditions are expected to form copper oxide at equilibrium, yet copper oxidation is avoided since the dense dielectric BST thin film kinetically limits oxygen transport to the Cu-BST interface. To experimentally prove these assumptions, XRD data show that copper oxidation is avoided after the “re-ox” anneal (figure 4.6).

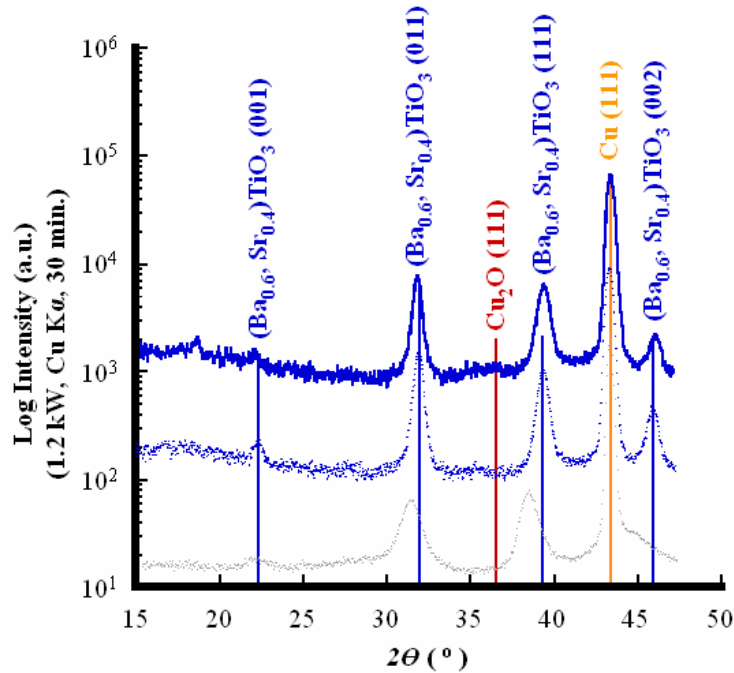


Figure 4.6: XRD data for the same sample shown in figures 4.4 and 4.5 yet after a “re-ox” anneal of 550 °C, 10^{-8} atm pO_2 for 30 min. (**blue solid line**). The data is displayed above the data shown in figure 4.4 for the as-deposited state (**gray dotted line**) and figure 4.5 for the crystallized state (**blue dotted line**) to show there is no change in crystallinity and no formation of copper oxide when the sample is subjected to a “re-ox” anneal. The vertical solid lines are given as guides to the expected peak position and intensities given by the powder diffraction cards.

Throughout the course of this study “re-ox” anneal conditions of 450 °C to 700 °C and 10^{-3} atm to 10^{-6} atm pO_2 were used to produce the lowest loss and highest resistivity BST thin films. This range of conditions shows the variability in BST defect chemistry, and the challenge associated with controlling defect levels in a pure system. In several occasions “re-ox” anneals were not necessary to observe low loss and low leakage current.

In commercial barium titanate based devices, inclusions of empirically determined dopant concentrations are used for this same reason this study employs “re-ox” anneals. This study chose to avoid intentional doping due to the high expense of purchasing many different targets with various dopants at various concentrations and the time necessary to empirically determine the appropriate dopant levels in the thin film. The connection between processing, defect chemistry, and “re-ox” conditions was beyond the scope of this study.

X-ray diffraction θ - 2θ data were shown in figures 4.4 - 4.6. These data are consistent with several literature examples of polycrystalline film data. XRD data was obtained using a 4 circle diffractometer fitted with a GADDS area detector where film texturing was easy to observe. Shown in figure 4.7 are raw x-ray detector images of as-deposited and fully processed BST thin films. The variation of intensity in the vertical arc direction of the $\{111\}$ BST reflection is indicative of texturing. The $\{111\}$ reflections are centered on the arc showing an out of plane $\{111\}$ texturing. Increased intensity at the top and bottom portions of the $\{110\}$ arc satisfy the symmetry requirement of $\{110\}$ planes inclined 35.2° to the film normal. Comparing the Cu $\{111\}$ reflections in the XRD area images from the as-deposited pre-annealed state to data taken after a 900°C anneal, the Cu $\{111\}$ arc of intensity changes from continuous intensity to separate discrete points. This results from substantial copper grain growth.

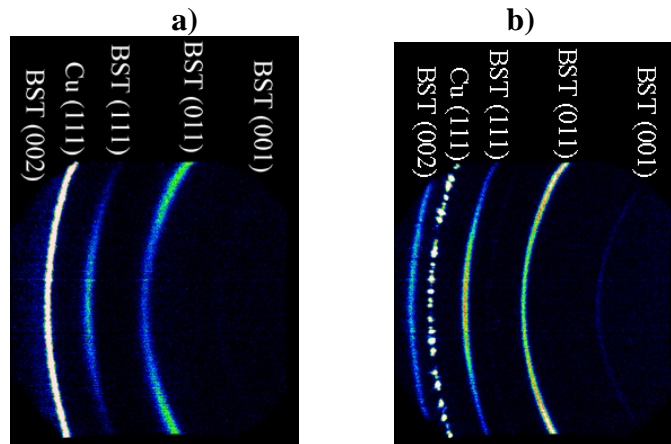


Figure 4.7: a) XRD area image of an as-deposited 800 nm BST film showing out-of-plane {111} texturing and diffuse, low diffracted intensity. b) XRD area image of a fully processed 800 nm BST film showing narrow out-of-plane {111} textured diffraction intensity. The Cu {111} reflection goes from intensity consistent with fine grained microstructure to discrete spots after annealing indicating substantial copper grain growth.

XRD characterization only analyzes macroscopic volumes of material which allow only qualitative insight into the microstructure. Higher resolution TEM and AFM allows direct observation of the BST thin film microstructure. BST/Cu films were characterized by transmission electron microscopy (TEM) to image the fully processed microstructure. Electron transparent wedge cross sections were prepared by polishing a BST/Cu specimen sandwiched between pieces of silicon. On axis bright field (BF) images and dark field (DF) using the {111}, {110}, {002}, and {102} reflections are shown in figure 4.8 and 4.9. Small area diffraction (SAD) pattern data of the BST film are shown in figure 4.10. The polycrystalline diffraction pattern is indexed using relative reciprocal distances and known interplanar distances for $(\text{Ba}_{0.6}, \text{Sr}_{0.4})\text{TiO}_3$.

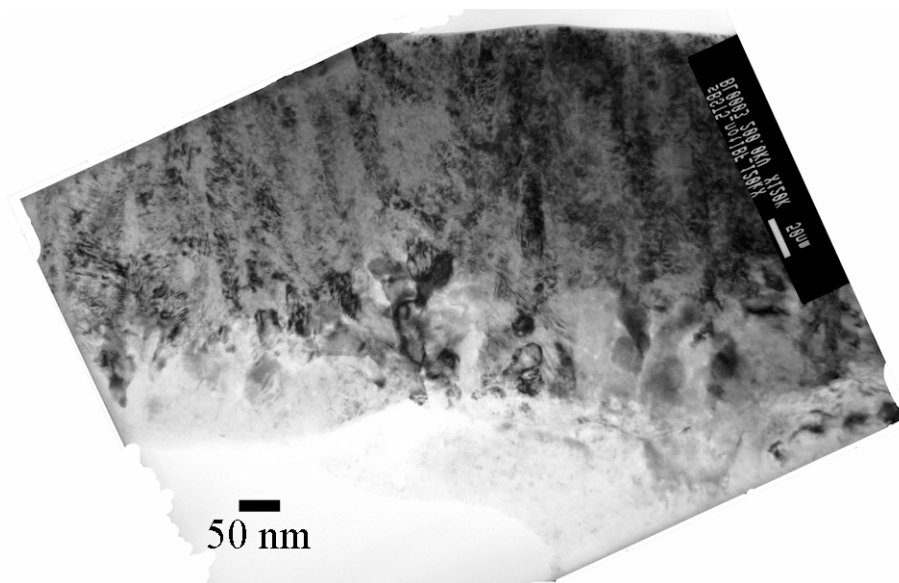


Figure 4.8: BF TEM taken at 120 kX. The copper substrate was mostly removed during specimen preparation yet still can partially be seen in the lower right of the image. See the DF TEM image in figure 4.9 for more detail.

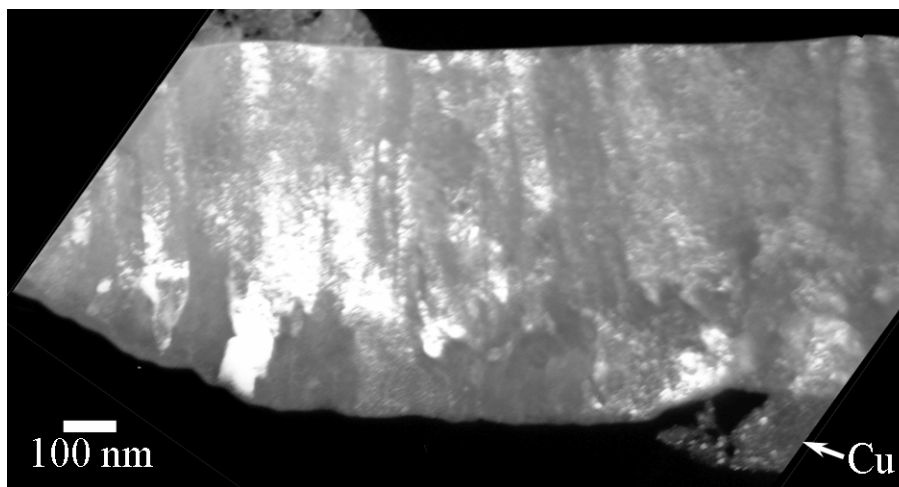


Figure 4.9: DF TEM using the $\{111\}$, $\{110\}$, $\{002\}$, and $\{102\}$ reflections (see the SAD diffraction image in figure 4.10) taken at 80 kX. The majority of the copper was removed by the ion milling yet still can be seen in the lower right of each image. Show in the complimentary images is a fine grained polycrystalline region adjacent to the copper substrate and a columnar $\{111\}$ textured region for the remaining film thickness.

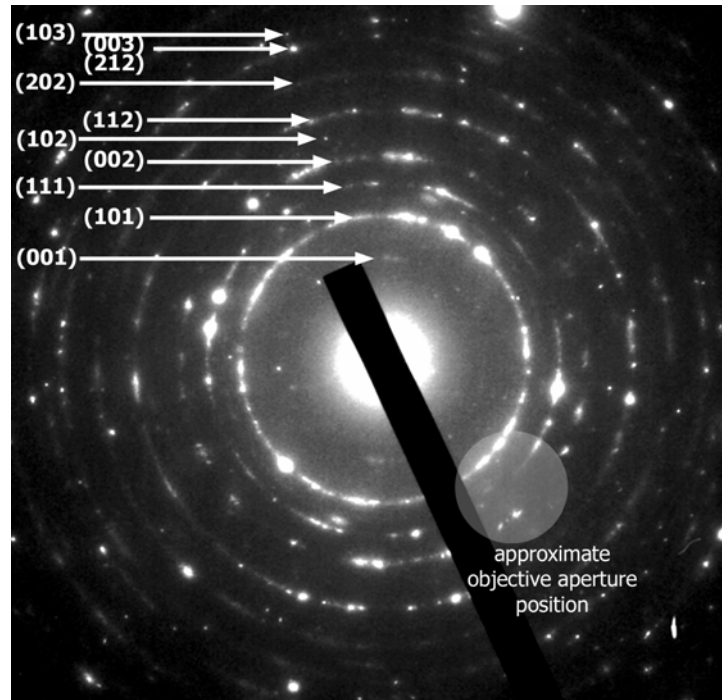


Figure 4.10: Indexed SAD pattern taken at 60 cm camera length. The shaded region shows the approximate position of the objective aperture position for the DF image shown in figure 4.9.

The incomplete rings in the SAD pattern show the film is random polycrystalline in the cross section direction and when analyzed using the complimentary XRD data indicate that the film is consistent with $\{111\}$ -oriented fiber texturing. $\{111\}$ out-of-plane texture was observed yet there was no in-plane orientation relationship in the grain boundary twist orientation. The TEM images show that an equiaxial polycrystalline region approximately 200 nm in thickness exists adjacent to the substrate/dielectric interface. The remaining 600 nm is columnar grain morphology consistent with (111) out-of-plane texturing. The average lateral grain size of the columnar region is 55 nm and grains appear to extend from the morphology transition region to the film surface.

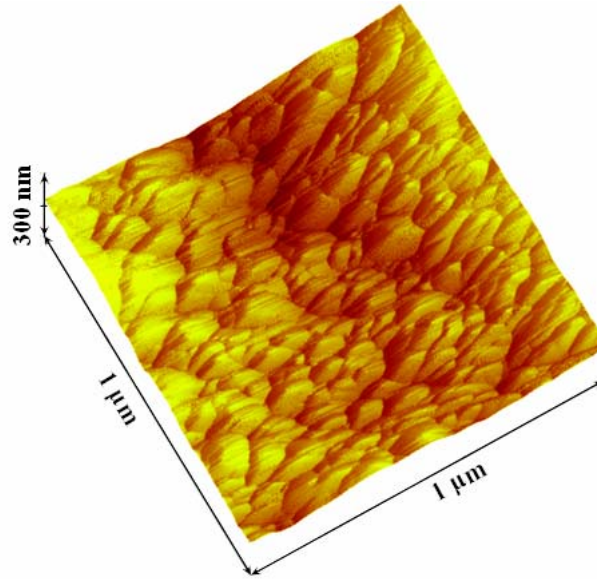


Figure 4.11: Topographical AFM data of a fully processed 800 nm thick BST film.

Figure 4.11 shows topographical AFM data with a lateral average grain size of 55 nm measured by the linear intercept method²²⁹ confirming the TEM data for the columnar region.

XRD indicates an interface free from copper oxidation yet this technique is limited in detecting minute volume fractions. Therefore the TEM specimen was imaged by high resolution TEM (HRTEM). Although the polycrystalline nature of the BST thin film and substrate copper made simultaneous zone axis alignment with alignment of the BST/Cu interface parallel to the electron beam difficult, a HRTEM image was obtained of the BST/Cu interface. Figure 4.12 shows HRTEM of this interface.

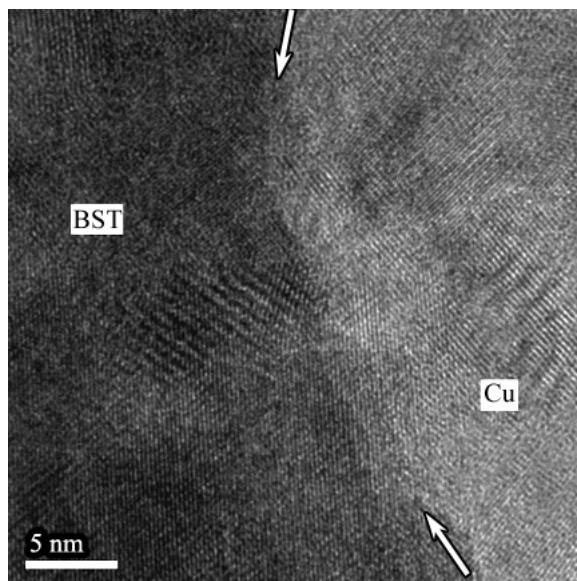


Figure 4.12: HRTEM image of the BST/Cu interface. Arrows highlight the position of the interface. Both sides of the interface have multiple grains with random orientation making simultaneous zone axis alignment impossible. Evident from the image is an abrupt BST/Cu absent of interfacial phases.

This image represents the best attempt at interface imaging and little information about the crystallographic orientation between the film and substrate can be established by these data. The BST/Cu interface is highlighted by the arrows in the figure and projection effects can be observed since the interface is not parallel to the electron beam. The figure distinctly displays the BST phase on the left with a dark contrast where multiple grains can be observed by the regions of parallel lattice fringes and the lighter contrast copper on the right. Some extension of the lattice fringes across the interface region are observed because of the interface misalignment. Most importantly, the HRTEM shows no additional contrast giving qualitative evidence of an abrupt BST-Cu interface. This finding further supports the XRD data that the processing route successfully crystallized the BST thin film while avoiding oxidation of the copper substrate.

A particularly favorable feature of sputter deposition is conformal film growth. The copper foils substrates have a comparably large rough surface and if film growth is not conformal can lead to inhomogeneities in film thickness and hence inhomogeneities in the electric field. These inhomogeneities can lead to premature device failures. To qualitatively characterize the degree of conformality in relation to the substrate roughness

a specimen was sandwiched between silicon substrates and polished in a similar procedure used to make TEM specimens. Figure 4.13 shows an AFM image of the cross section.

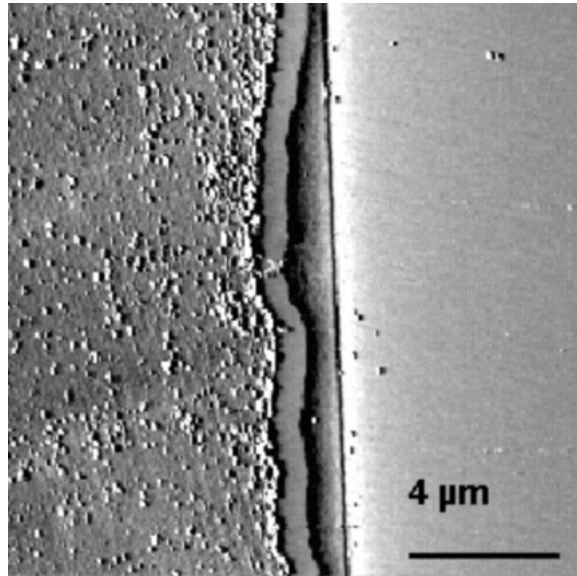


Figure 4.13: AFM of polished cross section. The substrate copper is on the left side of the image and the silicon support on the right. The BST thin film is mated directly to the copper and epoxy is seen between the BST film and the silicon.

Evident in the image is the replication of the topographical features due to the substrate roughness to the top surface of the BST thin film. This conformal BST layer allows for a consistent film thickness over large areas of the substrate irrespective of local asperities on the substrate surface. Therefore, sputter deposited BST thin films should give uniform properties over large areas while allowing for robust devices at high yields.

The transmission electron diffraction, BF/DF TEM images, XRD, and AFM data all give a consistent picture of the thin film morphology. At present, the reasons for this two-component film morphology are not well understood. The $\{111\}$ texture would not be expected since this does not correspond to the fast growth direction of perovskite oxides, and there is no substrate texturing that would promote an epitaxial growth mode. Furthermore, this texturing could not be duplicated at will in further depositions, despite rigorous attempts at adjusting and modifying processing parameters such as temperature, pressure, and gas ratios. System aging (which includes factors such as accumulation of material on chamber walls, slow changes in the magnetic field strength of the source

magnets, and target characteristics) is the suspected cause of this shift in microstructure. Most of the films in this study exhibit small equiaxial grain morphology similar to that shown in fig 4.14 below. Perhaps most importantly, the dielectric response associated with these two microstructures is nearly identical.

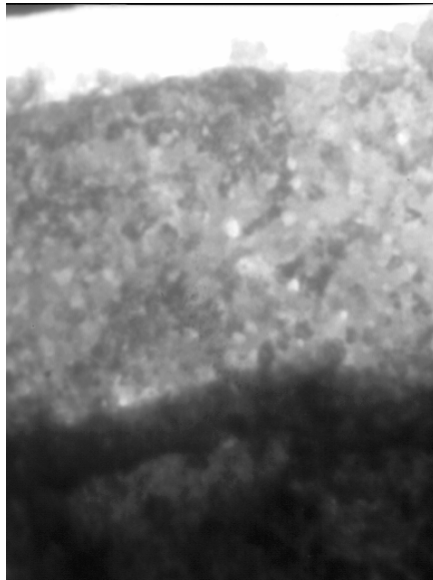


Figure 4.14: Uncalibrated BF TEM image of a BST/Cu film sputtered for 120 min. digitally captured at 590kX.

The Film on Foil process methodology produces a conformal film of “proto-”crystalline BST as-deposited. *Ex situ* anneals fully crystallize the BST thin film while control of pO_2 during anneals avoid formation of copper oxide while causing substantial copper grain growth. A grain size of 55 - 80 nm irrespective of the film thickness is consistently measured. When necessary, “re-ox” anneals were performed to control the resulting BST defect chemistry and improve dielectric properties. “Re-ox” anneals were performed while controlling pO_2 which successfully avoided degradation of the copper substrate.

4.2.2. Dielectric properties of BST/Cu

The electrical properties of BST thin films are paramount to this study where the target technology is frequency agile active capacitive elements in high frequency circuits.

The following electrical properties and their functional dependences are presented in light of these device concerns.

For this study, metal-insulator-metal (MIM) capacitors are fabricated to test the dielectric properties of the BST thin film. The permittivity, tunability, dielectric loss are characterized as a function of frequency, DC bias, and temperature. Leakage current and hence dielectric resistivity data are presented for multiple devices on a single sample to quantify property uniformity and device yield. Figure 4.15 shows the calculated ϵ - E data for a fully processed 800 nm thick $(\text{Ba}_{0.6}, \text{Sr}_{0.4})\text{TiO}_3$ film with a 96 μm diameter Pt top electrode tested using a 100 kHz 1.25 kV cm^{-1} signal measured at room temperature.

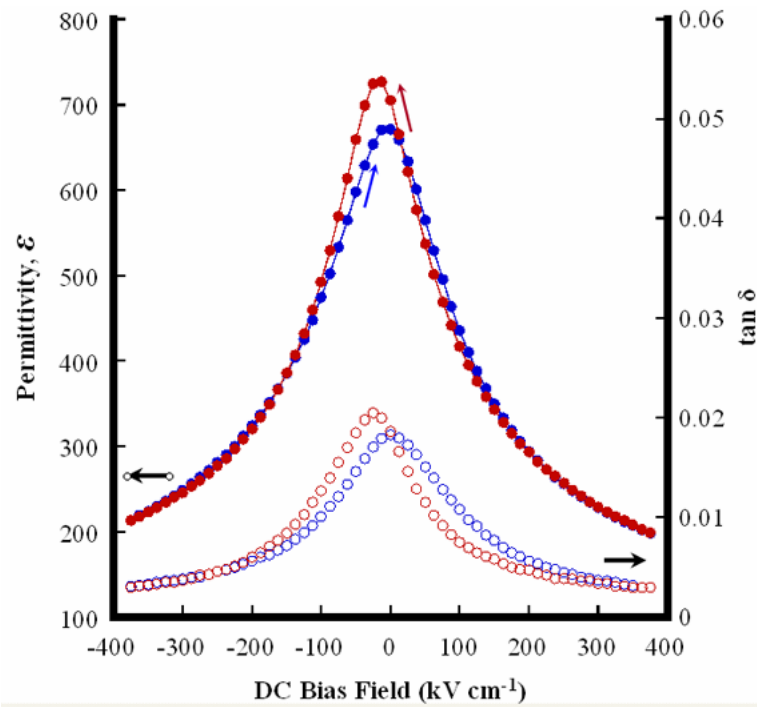


Figure 4.15: Room temperature DC bias dependent permittivity measurement taken at 100 kHz and 1.25 kV cm^{-1} oscillation field for a fully processed 800 nm thick BST thin film deposited on copper foil.

The measured permittivity displays the characteristic non-linear dependence with applied DC bias. A peak permittivity of 725 is measured at zero bias and saturates to near 200 at high applied fields of 375 kV cm^{-1} . Data are shown for a positive-to-negative and converse negative-to-positive sweep of DC bias to display the lack of hysteresis. Dielectric loss follows a similar trend as permittivity where the zero bias loss peaks at

0.02 $\tan \delta$ and saturates to 0.003 $\tan \delta$ at high field. The saturated values agree well to established values for single crystal specimens. Of particular note, the measured saturated loss value approaches the theoretically determined values for intrinsic loss mechanisms. The maximum permittivity is well below values observed in single crystal and well prepared bulk BST specimen⁶⁵ yet consistent with well prepared polycrystalline thin film BST.^{96, 100, 104} This higher observed permittivity, in comparison to films on platinized silicon substrates, is attributed to the higher annealing temperature of 900 °C (versus only 650 °C) which promotes improved crystallinity. The high maximum permittivity and the ability to reach saturated permittivity at high field values gives a tunability of > 3:1 (> 67%). The deviation of the peak permittivity at 0 V DC bias for forward and reverse sweeps in figure 4.15 is attributed to artifacts of measurement and data collection. A non-symmetric measurement time delay occurs in the impedance analyzer during the forward DC bias sweep versus the reverse sweep. This measurement artifact is routinely observed for all samples with our experimental setup. This effective "hysteresis" most likely arises from the existence of mobile defects, like oxygen vacancies, and is typically most dramatic for samples that are not re-oxidized optimally.

Comparison of the field-dependent electrical data shows that BST films are consistent with some of the best polycrystalline thin films reported in the literature. The non-linear tunability in conjunction with low dielectric loss in combination with low resistivity copper substrates makes the process attractive for frequency agile circuits where 2:1 tunability and $<0.01 \tan \delta^{230}$ are typical minimum device metrics. These properties are realized without the use of advanced substrates or complex deposition technique. The raw materials used are widely available and inexpensive while sputter deposition is consistent with large volume manufacturing.

Figure 4.16 shows permittivity and $\tan \delta$ versus for the identical film used to characterize ϵ - E .

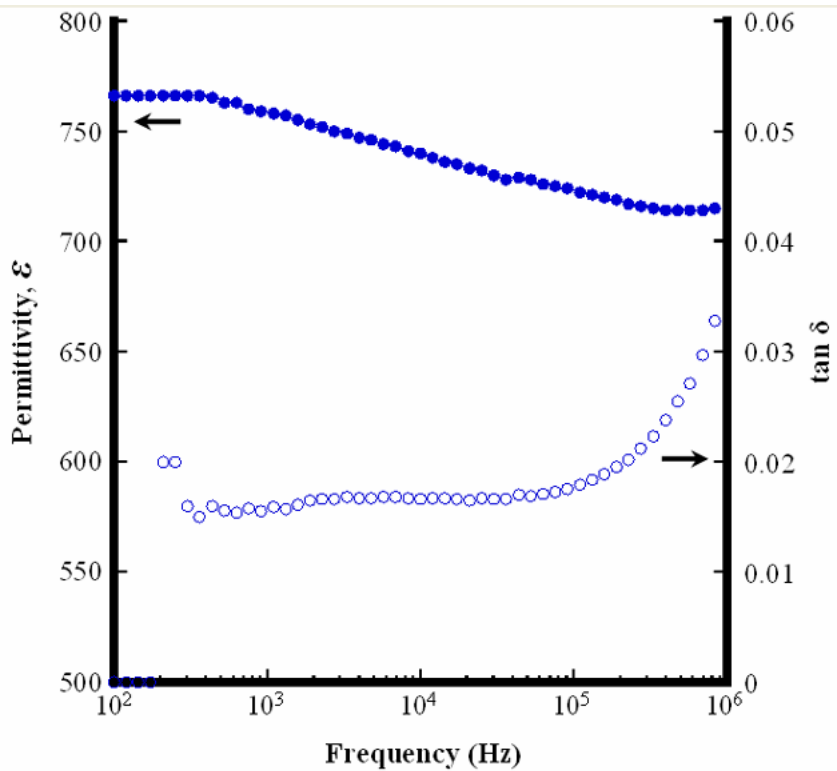


Figure 4.16: Room temperature permittivity frequency dispersion measurement taken at 0 V DC bias and 1.25 kV cm^{-1} oscillation field for a fully processed 800 nm thick BST thin film deposited on copper foil.

The data is taken using a $257 \text{ }\mu\text{m}$ diameter Pt top electrode MIM capacitor at room temperature, 0 V bias, and a 1.25 kV cm^{-1} . Below 300 Hz current response is too small to accurately measure loss and data are displayed as zero values. Above $\sim 10^5$ Hz the BST/Cu MIM and the impedance bridge approach resonance thus the measured permittivity and loss are not meaningful. The intermediate frequency range shows linear frequency dispersion with increasing logarithmic frequency where permittivity decreases $<3\%$ per decade of frequency and $\tan \delta$ is unchanged.

The absence of neither a sharp decrease in permittivity nor a peak in $\tan \delta$ over this frequency range suggests no significant contribution to the polarization from a space charge polarization mechanism. These findings are consistent with the physical characterization that showed no copper oxidation or porosity in the dielectric film. As such, we are confident that the materials produced on copper are consistent with the needs of RF and microwave devices.

Ferroelectric materials undergo a transition from a low symmetry hysteretic phase to a high symmetry paraelectric phase when traversing the Curie temperature. A permittivity peak is associated with the phase transition along with similar changes in almost all other material properties. Features of the microstructure, specifically small grain sizes, affect the magnitude and shape of the permittivity peak. The phase transition can easily be explored by analyzing permittivity and $\tan \delta$ as a function of temperature in the vicinity of the Curie temperature.

Capacitance and $\tan \delta$ were measured by means of the impedance analyzer while the samples were placed on a controlled temperature stage. Figure 4.17 shows the temperature dependent permittivity and $\tan \delta$ for a fully processed 800 nm thick $(\text{Ba}_{0.6}, \text{Sr}_{0.4})\text{TiO}_3$ film. A 0 V DC bias, 1.25 kV cm^{-1} oscillator level, 10 kHz voltage signal was used for measurement of a $344 \mu\text{m}$ diameter MIM capacitor.

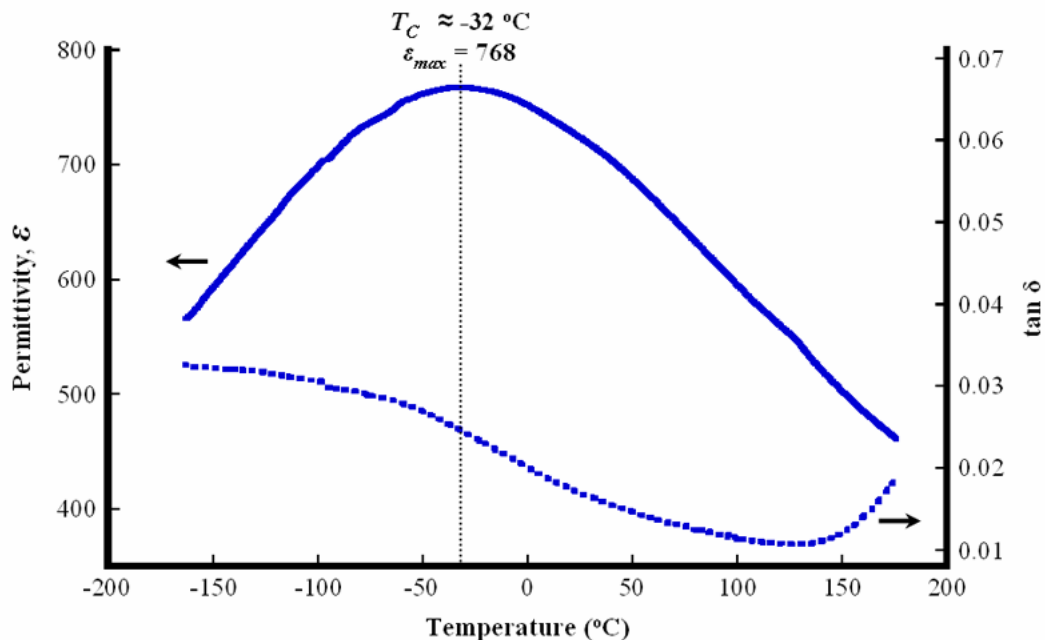


Figure 4.17: Permittivity (solid blue line) and $\tan \delta$ (dotted blue line) as a function of temperature. Measurements were conducted from 100 K to 500 K using 10 kHz and a 1.25 kV cm^{-1} oscillation field. The maximum permittivity occurs at approximately $-32 \text{ }^\circ\text{C}$.

The maximum permittivity of 768 occurs at $-32 \text{ }^\circ\text{C}$ yet there exists no sharp peak in permittivity making definition of the Curie temperature difficult. The T_C of bulk $(\text{Ba}_{0.6},$

$\text{Sr}_{0.4}\text{TiO}_3$ occurs at $5\text{ }^\circ\text{C}$ ⁶⁵ and the peak permittivity for thin film BST on copper shows a shift from this temperature of $\Delta T_C = -37\text{ }^\circ\text{C}$. The fine grained polycrystalline morphology of the film with a finite distribution of individual grain sizes is hypothesized to be responsible for the broad transition where crystallite size of each grain contributes a distinct temperature response that may possess a T_C shift based on finite size effects^{75, 87, 90, 91, 231} and collection of all the individual temperature responses for all grains where the electric field is applied under the top electrode collectively show a broad transition by superposition. If this is indeed the case, then high tunability should be observed even away from the permittivity maximum in the broad transition.

To explore this hypothesis the sample was allowed to stabilize at discrete temperatures in $50\text{ }^\circ\text{C}$ increments and C - V data collected. All data were taken from zero bias (0 V) to 125 kV cm^{-1} (10V). This lower DC bias value was used to guard against breakdown at elevated temperatures. The 0 - 10 V tunability versus temperature is shown in figure 4.18.

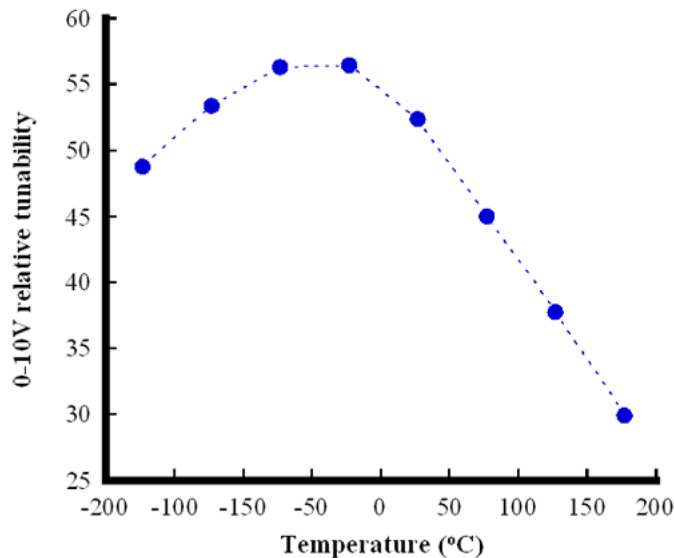


Figure 4.18: 0 V to 10 V tunability measured at discrete temperatures at 10 kHz and 1.25 kV cm^{-1} . Tunability is maximized at the temperature where permittivity peaks, $-32\text{ }^\circ\text{C}$, yet remains greater than $1\frac{1}{2}$: 1 over the entire temperature range. The ultimate tunability is substantially greater than displayed here since measurements were not extended to DC biases that reached saturation.

As expected, the tunability is greatest near the temperature corresponding to the permittivity maximum. The tunability falls off slowly below this temperature where tetragonal phase dominates and ferroelectric behavior should be observed and falls off more rapidly above this temperature where cubic symmetry and paraelectric behavior should be observed. To note, deviations of more than 150 °C from the temperature at peak permittivity still show at least 2/3 the tunability than at the peak permittivity temperature even in the high temperature paraelectric state.

Broad phase transitions are observed for BST/Cu thin films which sustain high tunability in large temperature range above the transition temperature. These results are adventitious considering device needs. The permittivity, and hence capacitance, has a weaker dependence versus temperature making circuit design simpler over a broad operating temperature range. More importantly, the tunability remains substantial over a large temperature range thereby maintaining its device practicality.

The Film on Foil processing route was designed considering ease of scaling to high volume manufacturing where processing cost must be low. Therefore reliability, repeatability, and property uniformity must meet a minimum specification. This thesis uses research scale equipment, and if high device yield and property uniformity over large areas can be achieved, there is confidence that the process can be extended to a manufacturing scale dimensions. The shadow masks used to define Pt top electrodes consist of an array of openings allowing many discrete MIM capacitors to be formed on one BST thin film covered copper foil. The BST thin film is processed as a monolith yet the MIM capacitors can be independently characterized. Figure 4.19 shows the DC leakage current data for a fully processed 800 nm thick BST thin film.

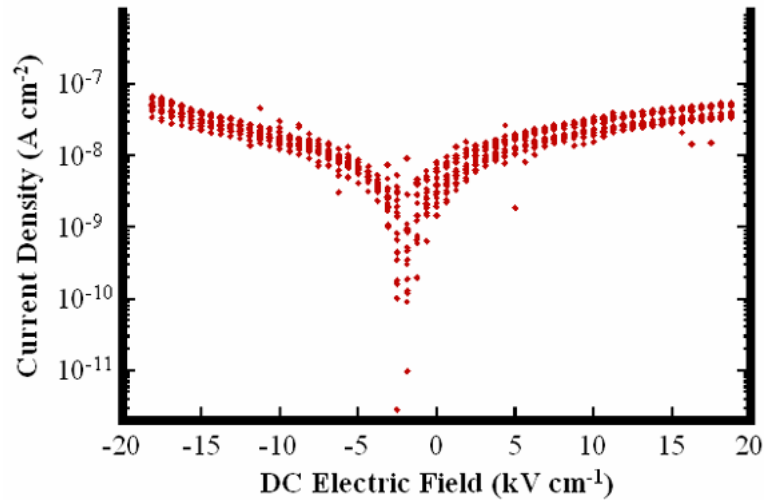


Figure 4.19: Eighteen individual DC leakage current measurements along an arbitrary row of MIM capacitors on one BST/Cu sample. No dead shorts were observed during the experiment and all data are displayed without excluding or selectively including any MIM devices along the row.

The 18 curves are data from all 18 Pt top electrodes (a 0.0147 mm^2 area for an individual electrode) along one arbitrary row of the array and no data were excluded or selectively included. No dead shorts were observed over this $\sim 3.5 \text{ mm} \times 0.2 \text{ mm}$ area of the sample. The leakage current of the 18 capacitors varies less than an order of magnitude at any voltage indicating very uniform properties over this area. The individual measurements are symmetric about 0 V indicating electronic symmetry in the MIM device and no predominance of specific polarity defects. Using the linear regions from 10V to 15V a high field resistivity can be calculated and the values range from $10^8 - 10^{10} \Omega \cdot \text{cm}$.

These data indicate the Film on Foil BST/Cu process is capable of producing high resistivity material over considerable areas relative to the processing instrumentation. These data generate confidence that scaling to commercial dimensions remains a viable concept. In a manufacturing environment these sizes can increase an order or magnitude or two yet this demonstration indicates that this scale up can be successful.

4.3. SPUTTERED FILM ON FOIL METHODOLOGY SUMMARY

Dielectric properties of Cu/BST/Pt MIM devices were measured as a function of DC bias, frequency, and temperature to complete the process-structure-property relationship determination. A permittivity of 750 with tunability $>3:1$ was observed with zero bias $\tan \delta$ of 0.02 saturating to $\tan \delta < 0.003$ at high DC bias fields. No significant frequency dispersion was observed over 5 decades of frequency. Temperature dependent measurements reveal a broad ferroelectric transition with a maximum at $-32\text{ }^{\circ}\text{C}$ which sustains a large tunability over $-150\text{ }^{\circ}\text{C}$ to $150\text{ }^{\circ}\text{C}$. The combination of fine polycrystalline grain size and high processing temperatures providing high crystalline quality are responsible for the observed dielectric properties. These dielectric properties exist on high conductivity copper foil substrates which permits high quality factor tunable capacitors to be synthesized and used in flexible frequency-agile electronics.

These properties are consistent with or surpass the properties of polycrystalline thin films processed on high quality rigid single crystal substrates, where in comparison, copper foils offer significant raw material cost savings. These findings display a real advance toward the practical implementation of frequency-agile ferroelectric thin film based tunable capacitors into commercial production. To critically compare these results to previously demonstrated BST thin film results, figure 4.20 shows permittivity versus DC bias for a sputter deposited Cu/BST/Pt MIM capacitor simultaneously plotted against a Si/SiO₂/Pt/BST/Pt MIM capacitor produced by a optimized MOCVD process.⁸⁵

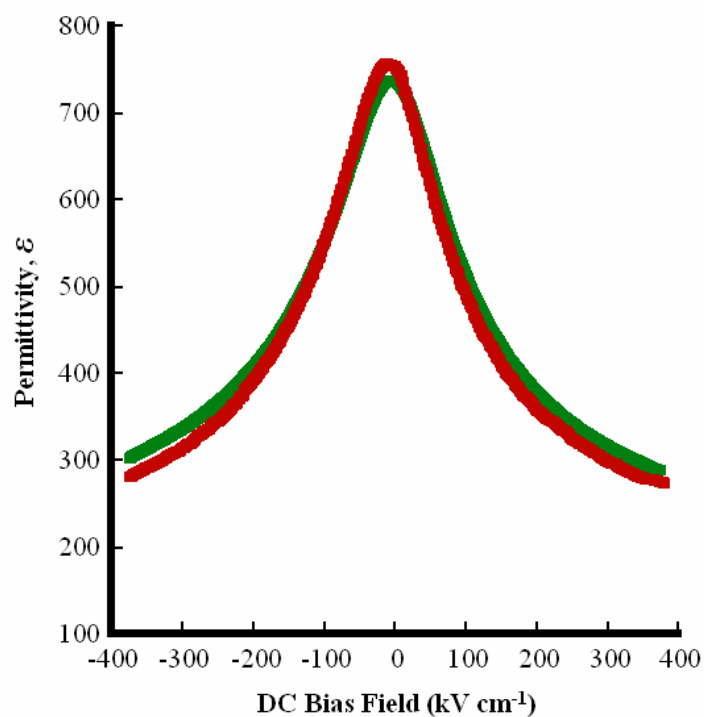


Figure 4.20: Room temperature DC bias dependent permittivity measurements for a fully processed 800 nm BST thin on Cu foil substrate (**green**) compared to a 600 nm thick fully fiber textured BST thin film on platinized silicon processed at 700 °C (**red**).

Although the MOCVD synthesized film is fully fiber textured it is grown at ~ 700 °C the ϵ - E response is comparable to a random polycrystalline BST on Cu.

5. MULTI-COMPOSITION STACKED FILMS: ROUTE TO MITIGATE TCC

A particularly problematic characteristic of ferroelectric thin films is the variation in permittivity with temperature in the vicinity of the phase transition. As temperature is increased from T_C the permittivity decreases inversely proportional to temperature. Concurrently, tunability also decreases as temperature is increased beyond T_C . Many electronic devices operate over a broad temperature range where it is desirable to have temperature independent electronic responses. Previous experiments show that of BST/Cu specimens are substantially temperature dependent.

An international consortium, Electronic Industry Association (EIA), defines a set of specifications describing limits of capacitance change from the room temperature value over defined temperature ranges. So called “Class II dielectrics” constitute high permittivity dielectrics used in numerous applications for operation around room temperature. The EIA Class II dielectric X7R specification is the most stringent specification that large value, low cost, widely used capacitors are expected to meet. The X7R specification states the change of the capacitance is less than 15% from the room temperature value over the temperature range from -55°C to $+125^\circ\text{C}$.⁶⁹⁻⁷¹ These limits are applied to evaluate if BST/Cu based capacitors are appropriate for devices that require X7R specifications. Evaluations will be extended beyond EIA specifications, to assess the ultimate temperature coefficient of capacitance, TCC. Research goals include space-borne applications; therefore, property stability over wide temperature ranges is essential.

The bulk of Class II X7R dielectric based capacitors employ a core-shell structure. These dielectrics synthesized from powder precursors of empirically determined composition based on doped BaTiO_3 - SrTiO_3 . The resulting microstructure consists of a high permittivity ferroelectric core in each grain. The grain surfaces, or shell, are doped by various elements to adjust the transition temperature of the shell volume. The permittivity temperature profile of the combined structure is engineered so that the

effective permittivity complies with X7R specifications. The core-shell microstructure consists of a continuous 3-D network of shell volume encapsulating and separating volumes of the high permittivity separated cores. This microstructure and dielectric response is described by a 3-0 connectivity.²³² The dielectric response of the composite structure can be described by a combination of discrete capacitive elements connected together in a mixture of series and parallel.

The core-shell concept can potentially be extended to thin film dielectrics where a mixture of discrete regions of different compositions can be combined in a single dielectric layer to engineer the permittivity temperature profile. The core-shell microstructure cannot be easily replicated by the BST sputtering deposition method described in this thesis. Since sputtering is an atom by atom deposition process and the BaTiO₃-SrTiO₃ has complete miscibility, deposition from a stoichiometric BST target results in a compositionally homogeneous thin film matching the composition of the target. A composite structure can be synthesized using consecutive films from different targets with different compositions. This would result in a stack of dielectric films where the T_C of discrete layers results in an engineered temperature profile. Two extreme cases are modeled: 2-2 connectivity where films are electrically in series in a MIM configuration and 1-1 connectivity where films are in parallel in a MIM device. Modeling will show which configuration has the greatest utility to produce low TCC over a wide temperature range.

This concept will be explored by mathematically modeling series and parallel connectivity. The model will assume that BST thin films can be synthesized in a range of thickness and compositions without adversely affecting dielectric properties. These assumptions are evaluated by exploring dielectric properties of BST/Cu MIM devices as a function of BST composition and film thickness.

To facilitate implementation of ferroelectric thin film devices in microwave circuits TCC should be reduced. The results of these experiments will provide direction for further research to achieve acceptable permittivity temperature dependence.

5.1. MULTI-COMPOSITION TCC MODELING

Evaluation of series versus parallel connectivity of multi-composition thin films is achieved by simple mathematical models. Temperature dependent permittivity data for a singular composition BST/Cu specimen is fit to a model developed for relaxor ferroelectrics.²³³ Although BST does not show relaxor behavior, the temperature profile shape is appropriate. A constant film thickness and capacitor area will be assumed for all simulations therefore capacitance can simply be replaced for permittivity in Smolenskii's model.

$$\frac{1}{C} = \frac{1}{C_{MAX}} + \frac{(T - T_{MAX})^2}{2C_{MAX}\delta^2} \quad \text{eqn [5.1]}$$

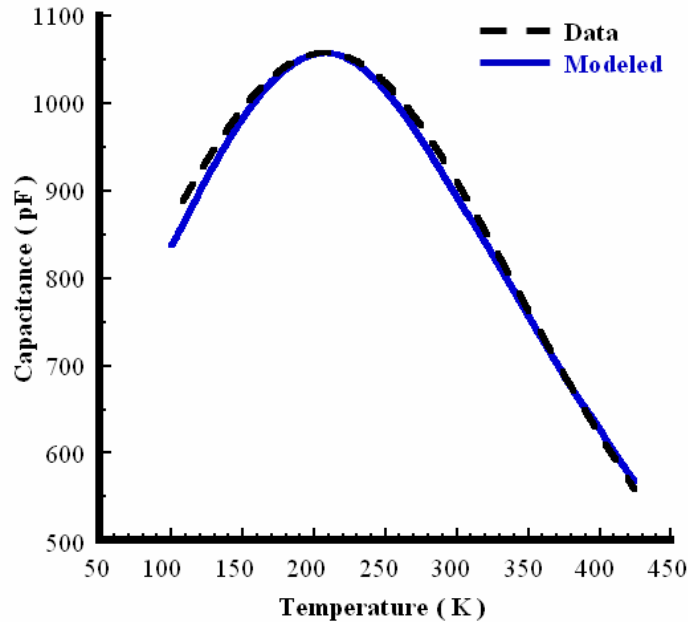


Figure 5.1: Temperature profile data for a 400 nm $(\text{Ba}_{0.5}, \text{Sr}_{0.5})\text{TiO}_3$ film deposited on a Cu foil substrate (**dashed black line**). The Smolenskii model is fit to the data (**blue**) showing a high degree of fit.

Equation 5.1 is fit to the capacitance temperature profile of a 400 nm thick $(\text{Ba}_{0.5}, \text{Sr}_{0.5})\text{TiO}_3/\text{Cu}$ sample using a $T_C = 205$ K and $C_{MAX} = 900$ pF. Fitting results in a δ broadness parameter of 170 °C. The fit is displayed in figure 5.1 where the R^2 value of the fit is 0.992. The fitting parameters were then used to shift the temperature profile

across the temperature space afforded by the BST system ($0 \text{ K} < T_C < 393 \text{ K}$). In the Smolenskii model, δ determines the broadness of the permittivity peak and if held constant, the T_C of a temperature profile can be shifted while maintaining the profile shape. The Smolenskii model is used to explore combinations of BST thin film with different compositions and different connectivity.

5.1.1. Optimized BST Composition

Initial simulations considered singular composition thin films. The model was used to shift T_C to explore minimum and maximum values that meet X7R specifications. $C_{MAX} = 1000 \text{ pF}$ and $\delta = 175 \text{ }^\circ\text{C}$ replicated the temperature profile for a $(\text{Ba}_{0.5}, \text{Sr}_{0.5})\text{TiO}_3$ BST/Cu MIM device and were used for all simulations.

Simulations showed a BST dielectric with $292 \text{ K} < T_C < 330 \text{ K}$ can meet X7R specifications. These limiting cases are shown in figure 5.2 where the shaded area shows the X7R temperature and capacitance change boundaries.

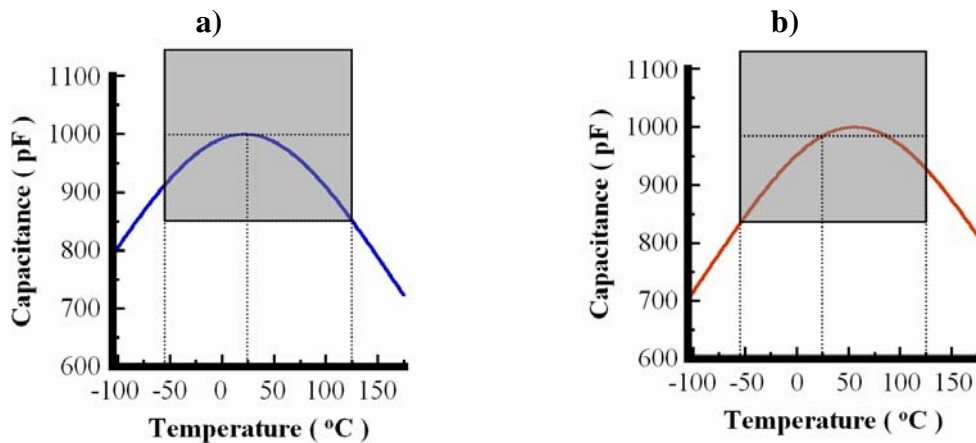


Figure 5.2: Simulated temperature dependence of capacitance for the limiting case of maximum and minimum T_C meeting X7R specifications. The shaded area shows the X7R temperature and capacitance change boundaries. a) Simulation of $T_C = 291.8 \text{ K}$ and b) $T_C = 329.3 \text{ K}$. In both cases the capacitance change is $\leq \pm 15\%$ from the room temperature capacitance within the temperature boundaries.

Both figures show the capacitance change is $\leq \pm 15\%$ from the room temperature capacitance over the $-55 \text{ }^\circ\text{C}$ to $125 \text{ }^\circ\text{C}$ temperature range. This treatment assumes that the temperature profile is independent of BST composition (an assertion that is supported by

experimentation later). The limiting T_C range corresponds to a composition of Ba mole fraction $0.66 < (Ba)/(Ba+Sr) < 0.77$.

A simulation for $T_C = 311$ K, directly between the observed limiting cases, can be evaluated for more stringent temperature specifications. Figure 5.3 shows the results of this simulation superimposed on shaded areas corresponding to the temperature and capacitance change boundaries for 9 more aggressive specifications.

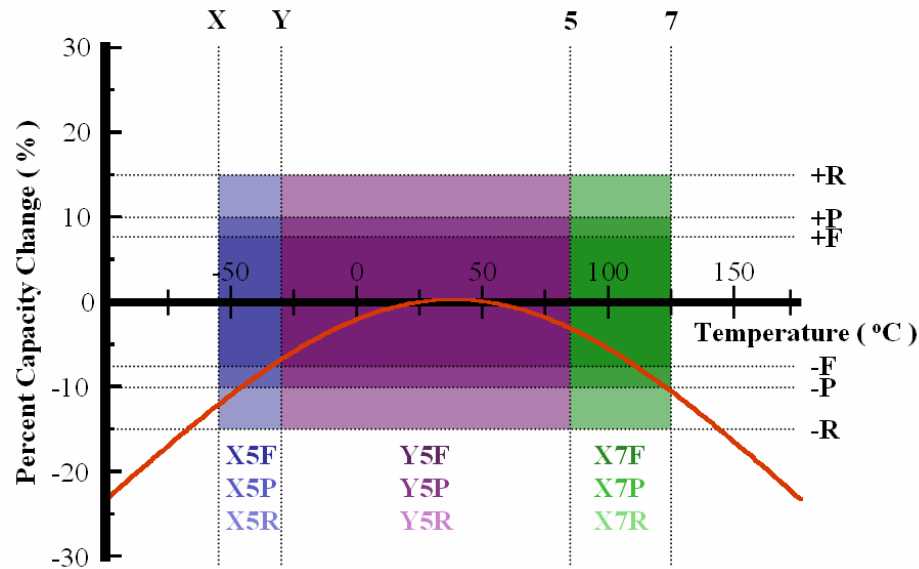


Figure 5.3: Simulation result for $T_C = 310.6$ K (red) exactly between the limiting cases for X7R compliance. The temperature boundaries are shown for Y5 by only the purple regions, the X5 by the combined blue & purple regions, and the X7 by the entire region shaded by blue, purple & green regions. The percentage capacitance change from room temperature capacitances are shown by the regions labeled $\pm F$, $\pm P$, and $\pm R$.

Over the narrowest temperature range, -30 °C to 85 °C (Y5), the capacitance changes $< \pm 7.5\%$ from the room temperature capacitance and meets all three of the displayed specifications. Over -55 °C to 85 °C (X5) the simulated capacitance change is $< \pm 15\%$ (R) but does not meet the (P) specification of $\pm 10\%$. In the largest temperature range, -55 °C to 125 °C (X7), a $\pm 10\%$ capacitance change is nearly met while approaching 125 °C yet the low temperature boundary shows only $< \pm 15\%$ (R) specification is achieved.

The majority of capacitors in service today in applications such as non-critical decoupling, filtering, transient voltage suppression, and timing delays typically require

only X7R temperature behavior. These results show that Film on Foil synthesized BST/Cu MIM devices can replace many of the core-shell based surface mounted MLCs in current service.

5.2. TEMPERATURE PROFILE SIMULATIONS

A thin film based high permittivity tunable dielectric would have greater utility if the temperature dependency is eliminated. This will move beyond X7 temperature ranges and capacitance change restrictions to less than $\pm 7.5\%$ (F). This section will describe simulations of dielectric stacks of two discrete compositions of BST combined in a composite. Two extremes will be considered: discrete composition films stacked perpendicular to applied electric fields and films stacked parallel to applied electric fields. These configurations are envisioned in a MIM device as seen in figure 5.4.

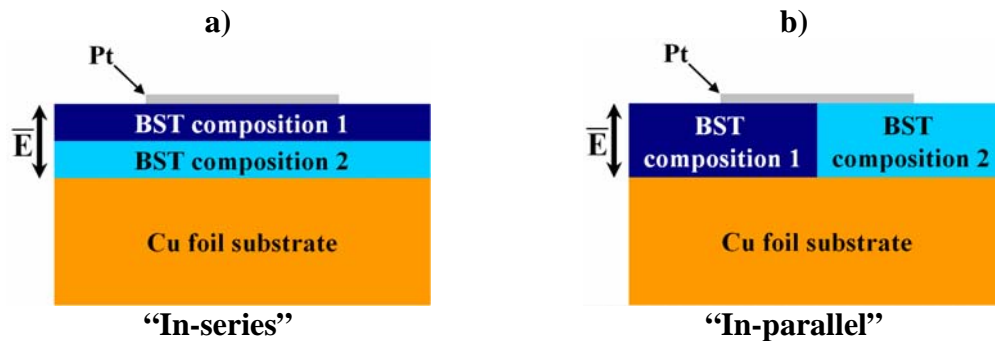


Figure 5.4: a) Schematic representation of series connected equi-thickness dual composition composite in a MIM configuration. b) Schematic representation of a parallel connected equi-thickness, equi-area dual composition composite in a MIM configuration.

When connectivity rules are applied to a composite, property values are weighted by volume fractions. For the following simulations, the area and thickness of individual composition component films is simply compensated by adjusting a C_{MAX} parameter appropriately. The Smolenskii model is rearranged to calculate capacitance temperature profiles, opposed to permittivity profiles.

$$\frac{1}{C(T)} = \frac{1}{C_{MAX}} + \frac{(T - T_{MAX})^2}{2C_{MAX}\delta^2} \quad \text{eqn [5.2]}$$

The stack thickness, device area, and permittivity of free space are all constants and can be removed from the model. For each component film, T_{MAX} is chosen to simulate a specific composition. C_{MAX} and δ are determined to simulate a $C(T)$ that closely matches the temperature profile of BST/Cu. The $C(T)$ of dual composition composites can then be mathematically combined as a model for assessment of potential temperature invariance.

5.2.1. Series connected dual composition composite simulations

The “in-series” configuration follows the mixing rules for 2-2 connectivity and is completely equivalent to two discrete capacitors in series as a lumped element circuit. Therefore the capacitance of a dual composition film where the component films are arranged in series is shown by the following relationship.

$$\frac{1}{C} = \sum_{i=1}^2 \frac{1}{C_i} \quad \text{eqn [5.3]}$$

This connectivity rule is applied to the adjusted Smolenskii $C(T)$ model for a dual composition composite.

$$C^{series}(T) = \frac{1}{\frac{1}{C_1^{MAX}} + \frac{(T - T_1^{MAX})^2}{2C_1^{MAX}\delta_1^2}} + \frac{1}{\frac{1}{C_2^{MAX}} + \frac{(T - T_2^{MAX})^2}{2C_2^{MAX}\delta_2^2}} \quad \text{eqn [5.4]}$$

For simplicity, an equivalent film thickness of each component film is assumed. A constant C_{MAX} can then be used for both components.

$$C^{MAX} = C_1^{MAX} = C_2^{MAX}$$

Also assumed is constant temperature profile broadness giving an equivalent δ for each component film in the composite.

$$\delta = \delta_1 = \delta_2$$

Redefining terms and simplifying the relation gives:

$$C^{series}(T) = \frac{2C^{MAX}\delta^2[4\delta^2 + (T - T_1^{MAX})^2 + (T - T_2^{MAX})^2]}{[2\delta^2 + (T - T_1^{MAX})^2][2\delta^2 + (T - T_2^{MAX})^2]} \quad \text{eqn [5.5]}$$

In series connectivity where equivalent component film thicknesses are assumed, C_{MAX} for each component film must be larger than the maximum capacitance of the total stack. The exact C_{MAX} is determined through trials to achieve a desired stack capacitance.

The end member BaTiO₃ has a T_C of 120 °C. Initial simulations showed the high temperature range limit of the X7R specification can only be met if one component has a $T_C = 120$ °C. Figure 5.5 shows the simulated temperature response of a BaTiO₃ film in series with BST films with $T_C = \{-173$ °C, -73 °C, and 27 °C}. Defining ΔT_C as the difference in Curie temperature between the two individual component films, the figure shows that as ΔT_C increases the T_C of the composite shifts to lower temperature and the temperature profile broadens. The capacitance change relative to room temperature is shown in figure 5.6 where the shaded region displays the boundaries of the X7R specification. Although the greatest ΔT_C stack showed the least change of capacitance with temperature, the T_C of the stack is shifted to such a low temperature it can not achieve X7R compliance. Only the $\Delta T_C = 193$ °C composite meets X7R specifications.

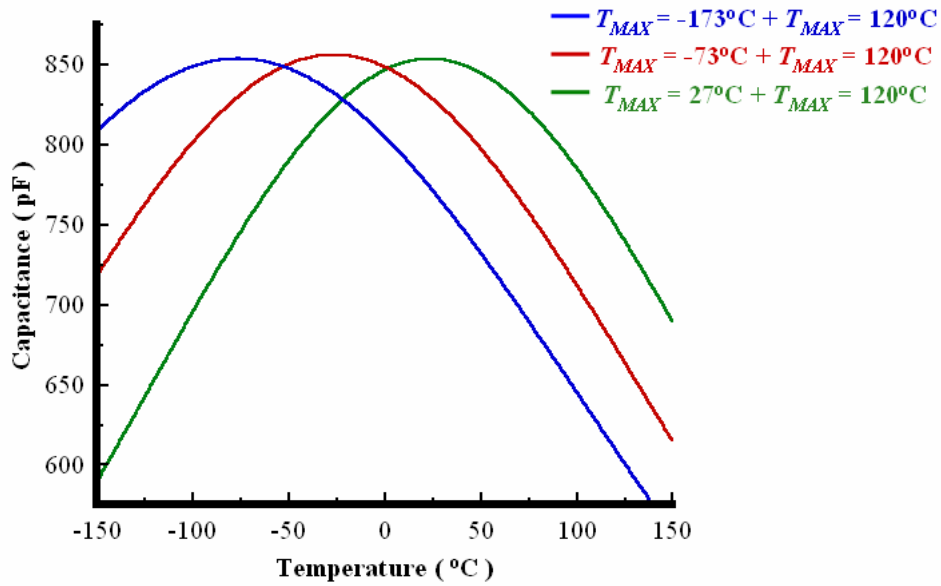


Figure 5.5: Simulated temperature profiles for series connected composites of equi-thickness dual composition films. BST films with a T_C of $-173\text{ }^\circ\text{C}$ (**blue**), $-73\text{ }^\circ\text{C}$ (**red**), and $27\text{ }^\circ\text{C}$ (**green**), are series connected to a pure BaTiO_3 film ($T_C = 120\text{ }^\circ\text{C}$).

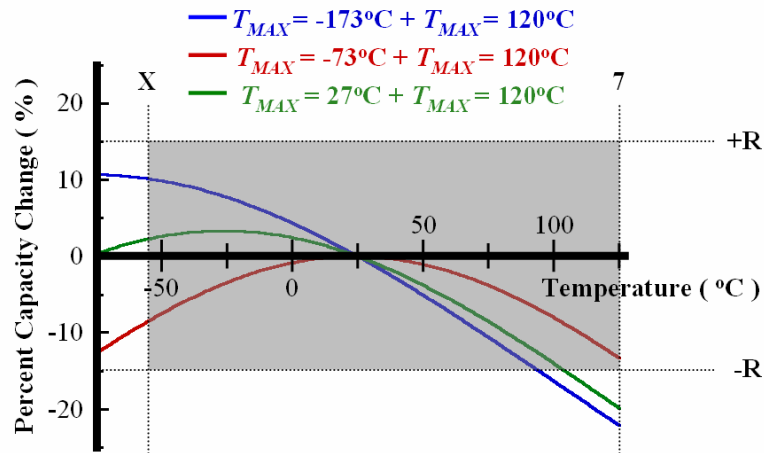


Figure 5.6: Simulated capacitance change relative to room temperature capacitance of series connected composites of equi-thickness dual composition films. BST films with a T_C of $-173\text{ }^\circ\text{C}$ (**blue**), $-73\text{ }^\circ\text{C}$ (**red**), and $27\text{ }^\circ\text{C}$ (**green**), are series connected to a pure BaTiO_3 film ($T_C = 120\text{ }^\circ\text{C}$). The shaded area shows the percent capacitance change and temperature range of X7R compliance.

The maximum and minimum ΔT_C to meet X7R specifications were explored while maintaining one component as BaTiO_3 . Simulations show $133\text{ }^\circ\text{C} < \Delta T_C < 213\text{ }^\circ\text{C}$ series

connected composites can achieve the required capacitance change relative to room temperature as seen in figure 5.7.

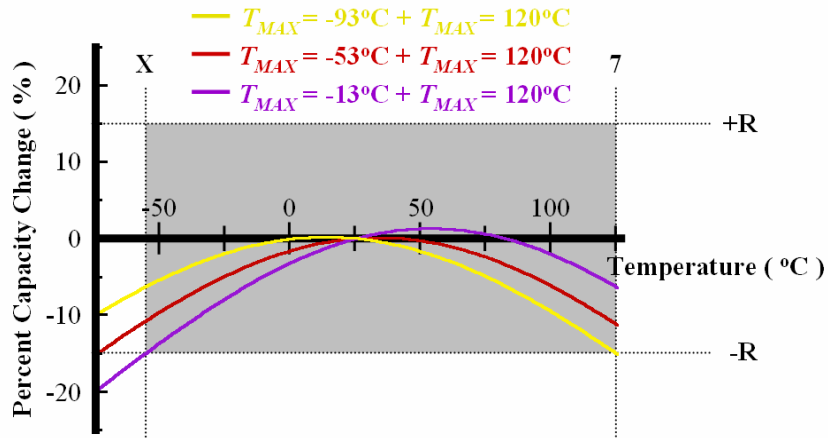


Figure 5.7: Simulated capacitance change relative to room temperature capacitance of series connected composites of equi-thickness dual composition films. BST films with a T_C of $-93\text{ }^\circ\text{C}$ (yellow), $-53\text{ }^\circ\text{C}$ (red), and $-13\text{ }^\circ\text{C}$ (purple), are series connected to a pure BaTiO_3 film ($T_C = 120\text{ }^\circ\text{C}$). The shaded area shows the percent capacity change and temperature range of X7R compliance. These results show the minimum and maximum T_C of the BST film to comply with X7R specifications.

A composite stack with a T_C equal to room temperature was simulated by series connection of a BaTiO_3 film and BST film with $T_C = -53\text{ }^\circ\text{C}$. This $\Delta T_C = 173\text{ }^\circ\text{C}$ series connected composite had the least capacitance change over the X7 temperature range yet X7P still could not be achieved by series connectivity.

To quantify the ability of series connectivity to broaden the temperature profile and mitigate TCC over a large temperature range, the largest ΔT_C available in the BST system, a pure SrTiO_3 film in series with a BaTiO_3 film ($\Delta T_C = 393\text{ }^\circ\text{C}$) was simulated and compared to a singular BST film with an identical T_C as the composite structure. The temperature profiles are displayed on the same plot in figure 5.8. Only a modest gain in temperature profile broadening is achieved with these series connected films of equal thickness. Additionally, the T_C of the composite is too low for this film to comply with X7R specifications.

Summarizing, equi-thickness dual composition BST films were simulated for series connectivity in a MIM capacitor. It was found that only modest temperature profile

broadening can be achieved with this configuration. A small subset of BST films in series with a pure BaTiO₃ film can meet X7R specifications allowing some latitude in choosing a stack with desired T_C . These results show there is little advantage of using series connected dual composition films because a singular composition BST film can achieve a similar result with a far less complicated processing route.

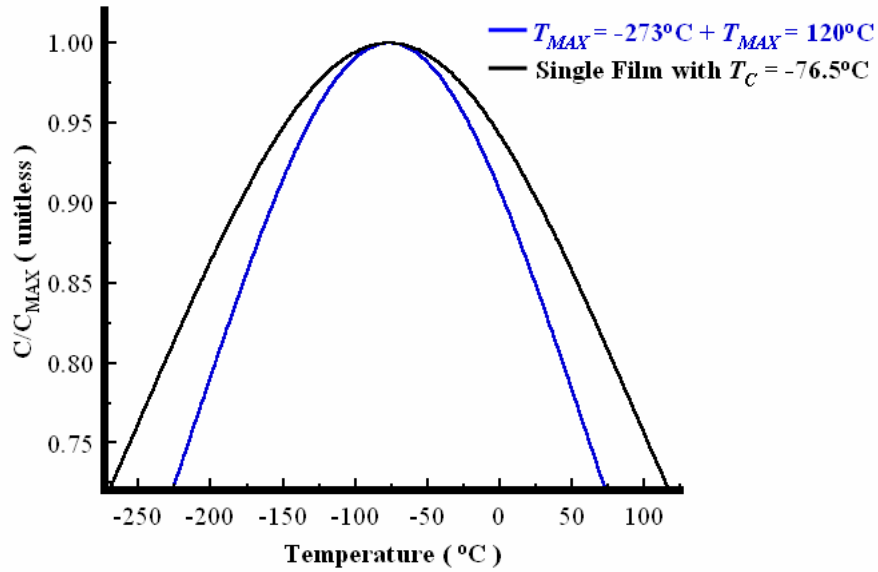


Figure 5.8: Simulated temperature profile for a series connected composite of equal thicknesses of pure BaTiO₃ and SrTiO₃ (**black**). The result is compared to a simulated BST film with an identical $T_C = -76.5$ °C (**blue**). Relative capacitance is plotted versus temperature to achieve exact overlap at the T_C .

5.2.2. Parallel connected dual composition composite simulations

The “in-parallel” configuration follows the mixing rules for 1-1 connectivity and is completely equivalent to two discrete capacitors in parallel as a lumped element circuit. The capacitance of a dual composition film where the component films are arranged in parallel is shown by the following relationship.

$$C = \sum_{i=1}^2 C_i \quad \text{eqn [5.6]}$$

Inserting the adjusted Smolenskii $C(T)$ model into this connectivity rule gives:

$$C^{para}(T) = \frac{2C_1^{MAX} \delta_1^2}{2\delta_1^2 + (T - T_1^{MAX})^2} + \frac{2C_2^{MAX} \delta_2^2}{2\delta_2^2 + (T - T_2^{MAX})^2} \quad \text{eqn [5.7]}$$

As before, C_{MAX} and δ are equivalent for each component film. Combining terms and rearranging the equation gives a more compact relation:

$$C^{para}(T) = \frac{2C^{MAX} \delta^2 [4\delta^2 + (T - T_1^{MAX})^2 + (T - T_2^{MAX})^2]}{[2\delta^2 + (T - T_1^{MAX})^2][2\delta^2 + (T - T_2^{MAX})^2]} \quad \text{eqn [5.8]}$$

In this parallel connected situation the thickness of the individual components is equivalent to the total stack thickness yet each component film constitutes only half the area under the electrodes. The C_{MAX} for each component film must be larger than the maximum capacitance of the total stack. The exact C_{MAX} is determined through trials to achieve a desired stack capacitance.

Composite stacks were simulated with trial T_{MAX} to identify the ΔT_C ($\Delta T_C = T_1^{MAX} - T_2^{MAX}$) required to realize the least change in capacitance over the widest temperature range. Figure 5.9 displays the results of these simulations.

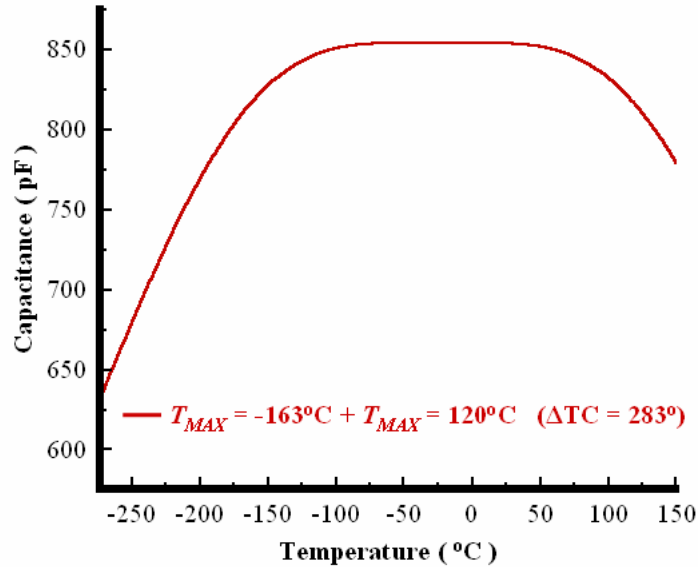


Figure 5.9: Simulated temperature profiles for parallel connected composites of equi-thickness, equi-area dual composition films. A BST film with a T_C of -163 °C is parallel connected to a pure BaTiO₃ film ($T_C = 120$ °C).

Parallel connection of BST films with $\Delta T_C = 283 \text{ }^\circ\text{C}$ gives almost no change in capacitance over a $75 \text{ }^\circ\text{C}$ temperature range. Shown in the figure is a pure BaTiO₃ film in parallel with a BST film with a T_C of $-163 \text{ }^\circ\text{C}$, yet as long as ΔT_C is maintained at $283 \text{ }^\circ\text{C}$ this flat temperature response can be shifted over a range of $110 \text{ }^\circ\text{C}$ and confined only by the T_C of the end members BaTiO₃ and SrTiO₃. The $R < \pm 15\%$ capacitance change relative to room temperature limit can be met over $407 \text{ }^\circ\text{C}$ temperature range. The simulated temperature profile far exceeds any common EIA Class II dielectric specification.

The ΔT_C of $283 \text{ }^\circ\text{C}$ is an ideal value for films with observed temperature profiles similar to BST/Cu specimens. Simulations using ΔT_C deviating from this ideal value are shown in figure 5.10.

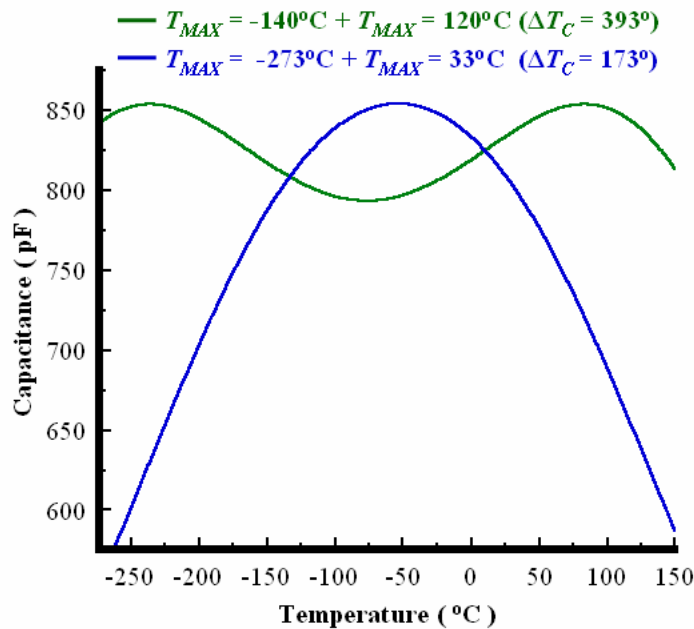


Figure 5.10: Simulated temperature profiles for parallel connected composites of equi-thickness, equi-area dual composition films. Shown in **green**, a BST film with a $T_C = -163 \text{ }^\circ\text{C}$ is parallel connected to a pure BaTiO₃ film ($T_C = 120 \text{ }^\circ\text{C}$). Shown in **blue**, a BST film with a $T_C = 33 \text{ }^\circ\text{C}$ is parallel connected to a pure SrTiO₃ film ($T_C \sim 0 \text{ }^\circ\text{C}$).

When a $\Delta T_C < 283 \text{ }^\circ\text{C}$ is simulated a narrower temperature profile results. When a $\Delta T_C > 283 \text{ }^\circ\text{C}$ is simulated reduction in capacitance is observed at temperatures between

the individual component films T_C . Any local minima can purportedly be eliminated by inclusion of an additional composition component film in the composite at the expense of even more complicated processing.

These results show the true success of the core-shell microstructure is from the parallel arrangement of volumes with different transition temperatures. Unfortunately, a parallel connected configuration is very difficult to achieve in a thin film MIM format. Simultaneous deposition of separating phases could achieve this microstructure, but perovskite oxide ferroelectrics have extensive miscibility making this route unattractive. Multi-multi-step lithography masking schemes and depositions may be able to produce the desired structures, but the process complexity will likely outweigh the gains of mitigating TCC.

5.2.3. Multi-composition composite temperature profiles simulations

Realizing series connected multi-composition composites are substantially simpler to fabricate; simulations were refined and so that more than two discrete films could be considered. Consecutive depositions of many component films of different composition can be integrated into a MIM capacitor. This synthesis technique requires no additional equipment or processes beyond those described in this thesis. Simulations were used to evaluate if any substantial mitigation of TCC can be achieved using this scheme.

When connectivity rules are applied to a composite, property values are weighted by volume fractions. Electrode area is considered simply as an adjusted parameter; therefore, for these simulations area is held constant and volume fractions are simply reduced to film thickness. This makes two independent degrees of freedom in the simulations: the temperature profile for a discrete BST composition and the thickness of the discrete layer in the composite structure. Simulations can be performed using the unadjusted Smolenskii model (equation 5.1). The series connection calculations must then use permittivity and component film thickness opposed to simply capacitance. This adapted series connectivity rule is shown below.

$$\frac{1}{C(T)} = \sum_{i=1}^n \frac{t_i}{\varepsilon(T)_i} \quad \text{eqn [5.9]}$$

$C(T)$ is the total capacitance temperature profile of the series connected composite and $\varepsilon(T)_i$ and t_i are the temperature dependent permittivity and thickness of individual component films, respectively. This equation allows n component films to be included in the composite and ε_{MAX} and δ are maintained equivalent for all component films to simulate BST/Cu specimen temperature profiles. To simplify the calculations, the total stack thickness is assumed to equal unity.

Simulations were performed for various situations including 3, 4, 5, and 21 separate equi-thickness films equally spaced T_C between films over all T_C available in the BST system. Figure 5.11 shows the simulated $C(T)$ for the 21 component series connected composite. Comparing this situation to the equi-thickness dual composition film and a singular composition film with the same T_C , the 21 component film shows a temperature profile between the singular composition film and a dual composition composite. The dual composition composite actually shows a broader transition due to the larger ΔT_C between the component films than is allowed in the 21 composition composite.

Other configurations were simulated such as a linearly increasing T_C gradient through thickness and component film thickness weighted to particular compositions. The simulations had little effect on the broadness of the temperature profile and simply shifted the observed T_C of the composite.

5.2.4. Temperature profile simulations summary

Methods for manipulating and minimizing the temperature profile were explored by mathematical simulations. The temperature profile of BST thin films on Cu foil substrates was characterized and data were fitted to a model. Simulation of singular composition BST thin films shows X7R specification can be met if composition is chosen to realize $19\text{ }^\circ\text{C} < T_C < 56\text{ }^\circ\text{C}$. Extending upon concepts from core-shell dielectrics, dual composition composites were considered in parallel and series connectivity. Series

connectivity revealed very modest ability to broaden the temperature profile, yet parallel connectivity was shown to create large temperature ranges where capacitance was virtually independent with temperature. A parallel connectivity multi-composition composite of BST thin film currently has no obvious synthesis scheme, a straightforward processing route can be envisioned however for series connected multi-composition composites. Therefore series connected simulations were refined. Results show that the use of a greater number of discrete component films with manipulated composition gradients could not broaden the temperature profile and mitigate TCC.

To experimentally verify these simulations, assumptions of the models must be addressed. The simulations assume that BST thin films of different compositions have similar temperature profiles. Bulk values of T_C for the BaTiO₃-SrTiO₃ system were used in calculations. A similar range of T_C must be achieved in thin film BST. Additionally, to achieve a target capacitance in a MIM device, film thickness must be adjusted. BST thin films must be synthesized in a range of thicknesses while achieving similar temperature profiles and maximum permittivity absent of a dependence of T_C on film thickness.

5.3. DEPENDENCE OF THICKNESS & COMPOSITION

The preceding chapter proved the success of the Film on Foil methodology to synthesize BST thin films on copper substrates while making comments on the utility of BST/Cu thin films for feature frequency-agile capacitors. This process was designed generally, without focusing on any specific circuit. The circuit designer must be able to adjust film thickness and electrode area to meet the capacitance and/or impedance requirements of a design. With the full solid solubility of the BST system and the ability to adjust T_C from absolute zero to 120 °C, the composition of the film can be adjusted to suit the operation temperature range for a wide range of applications. With these design criteria in mind, BST thin film properties were explored as a function of thickness and composition.

Many authors have noted the decrease of permittivity, shifts of T_C , and increased transition diffuseness with decreasing film thickness. Hypotheses for these observations can be attributed to effects of strain, existence of non-ferroelectric interface layers, scaling effects, and fundamental finite size effects. These hypotheses are still under development and no consensus has been reached that satisfactorily explains all observed phenomenon. This chapter will outline explorations of BST thin film thickness and composition on deposited on flexible Cu substrates. Since ferroelectricity is closely tied to lattice dynamics, it is important to not only characterize permittivity versus DC bias and temperature but also the grain morphology of the films to establish complete structure property relationships.

Simulations have provided routes to mitigate the temperature coefficient of capacitance (TCC) combining multiple BST compositions in a monolith composite. To realize mitigated TCC as simulations describe, films must be synthesized at various thickness with a predictable T_C without a significant change in the temperature profile.

A series of Pt/BST/Cu MIM devices were fabricated in a series of thickness and compositions. The tunability and phase transition were explored. These experiments permit evaluation of the utility of the Film on Foil process to realize highly tunable MIM capacitors with mitigated TCC.

5.4. DIELECTRIC PROPERTIES AS A FUNCTION OF THICKNESS

5.4.1. Film growth of thickness series

Films were processed by an identical procedure given in chapter # where the deposition time was varied. Films were sputtered for 15, 60, 75, 90, 105, 120, and 210 minutes from a $(\text{Ba}_{0.75}, \text{Sr}_{0.25})\text{TiO}_3$ target. The films were crystallized at 900 °C and 10^{-12} atm $p\text{O}_2$ in individual runs. “Re-ox” anneals were done on each sample to reduce electro-active defect concentrations. The specific “re-ox” conditions for each sample varied from 450 °C to 650 °C and 10^{-7} to 10^{-9} atm O_2 to obtain low $\tan \delta$ at high DC bias,

yet typically 550 °C, 10^{-8} atm O_2 was sufficient for most samples. Pt top electrodes were sputter deposited through a shadow mask to form MIM capacitors for measurement.

Film thicknesses were measured by profilometry and SEM measurement of cross sections. Random error was encountered in film thickness measurement and a constant deposition rate was assumed and determined from data by linear regression. A representative sample (105 min deposition) was TEM imaged to determine the grain morphology of the film and SEM images confirm this grain morphology is consistent throughout the thickness series. The grain size of each sample was determined by topographical AFM images and the linear intercept method.²²⁹ $C-V$ and $C-T$ data were obtained by the same procedure outlined previously. The complete characterization of physical and electrical properties allows conclusive discussion of structure property relationships as a function of film thickness.

5.4.2. Physical characterization of thickness series

Figure 5.12 below shows examples of SEM images used for quantitative film thickness measurements. Samples were cut and then mounted in the SEM so that the fractured film surface is approximately parallel to the electron beam. These fractured surfaces allow thickness measurement while giving a fracture surface to gain insight into the grain morphology of the film. Features associated with intra-grain fracture, inter-grain fracture, and grain pull out were observed. Multiple images at various locations on a sample film were obtained to increase confidence in thickness measurements and calculation of statistical confidence limits.

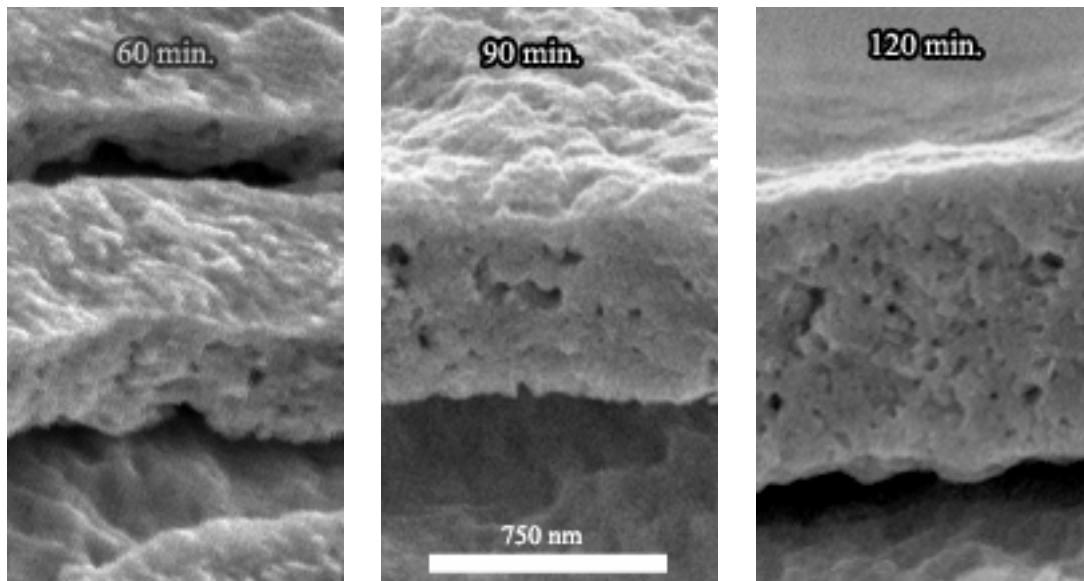


Figure 5.11: Three representative SEM images of the BST thin films in cross section. The films are fractured and aligned parallel to the electron beam when imaging. Left: 60 min. deposition. Center: 90 min. deposition, Right: 120 min. deposition. The scale bar in the center is valid for all three images. The fracture surface allows qualitative insight into the film microstructure since the fracture occurs by intergranular fracture, intragranular fracture, and grain pull out. Equiaxial grain morphology is observed throughout the film thickness and is consistent for all films in the thickness series.

Figure 5.13 shows a BF TEM image where the TEM specimen preparation utilizes the same wedge-sample technique mentioned earlier. Equiaxial polycrystalline microstructure is observed throughout the film thickness. Although previous experiments with the exact same sputtering conditions exhibited a partially columnar and random polycrystalline microstructure, the film observed here exhibited only an equiaxial microstructure throughout the film thickness. While acknowledging the differences in microstructure between original experiments and those shown in this section, the films produced from for the following experiments all exhibited an equiaxial microstructure. This is confirmed through data collected via XRD and the images shown here.

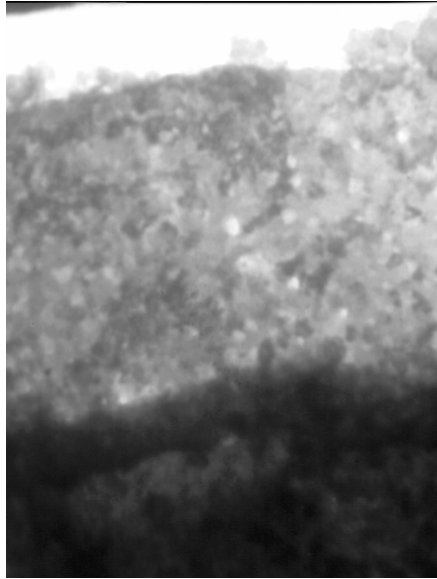


Figure 5.12: Uncalibrated BF TEM image of a BST/Cu film sputtered for 120 min. digitally captured at 590kX.

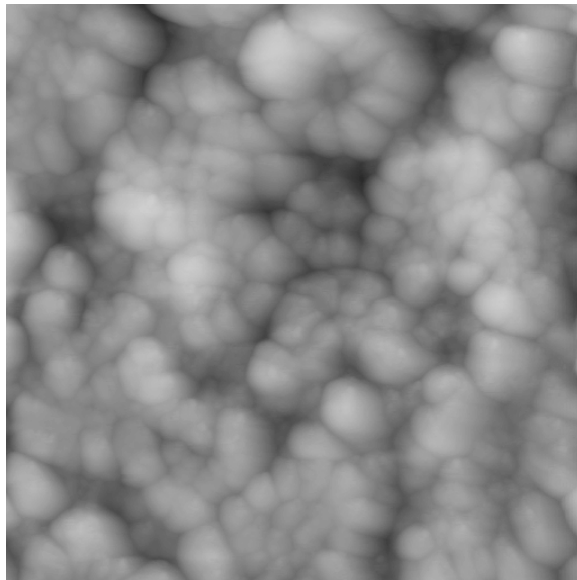


Figure 5.13: 1 μm X 1 μm topographical AFM image of a BST film sputtered for 75 min.

Figure 5.14 is an AFM image of the surface of a BST/Cu film. The linear intercept method was used to quantify grain diameters of the grains on the surface. This data enables the measurement of the overall grain size of the observed film while relying on the assumption that the grains imaged on the surface of the film are representative of the entire film and that the film has a uniform grain size throughout. A series of AFM

images were obtained and subsequent grain size measurements of the films were plotted versus film thickness as shown in Figure 5.15.

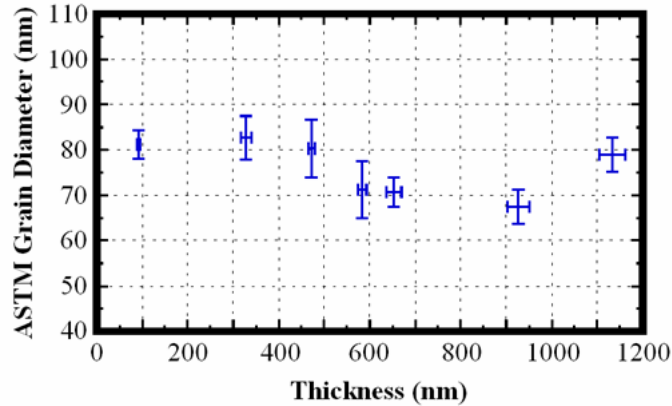


Figure 5.14: Measured ASTM grain diameter measured by AFM versus SEM measured film thickness for the thickness series.

Error bars are given as 95% confidence limits for the grain diameter and as one standard deviation for the film thickness. Although the data in Figure 5.15 shows some scatter in the resulting grain diameter versus film thickness, no relationship between grain diameter and film thickness was observed. In comparison to film thickness studies employing columnar fiber textured films, the grain size in the applied electric field direction is a much stronger function of film thickness. In this study the random equiaxial grain morphology gives a very weak function of grain size with thickness when considering the measurement direction in a MIM capacitor.

5.4.3. Dielectric properties as a function of thickness

The non-linear permittivity dependence on DC electrical field was measured for the thickness series. All samples were measured at room temperature, 100 kHz, and a constant oscillator level of 1.11 kV cm^{-1} using the same impedance analyzer and probe station described earlier. Figure 5.16 shows the results of these measurements.

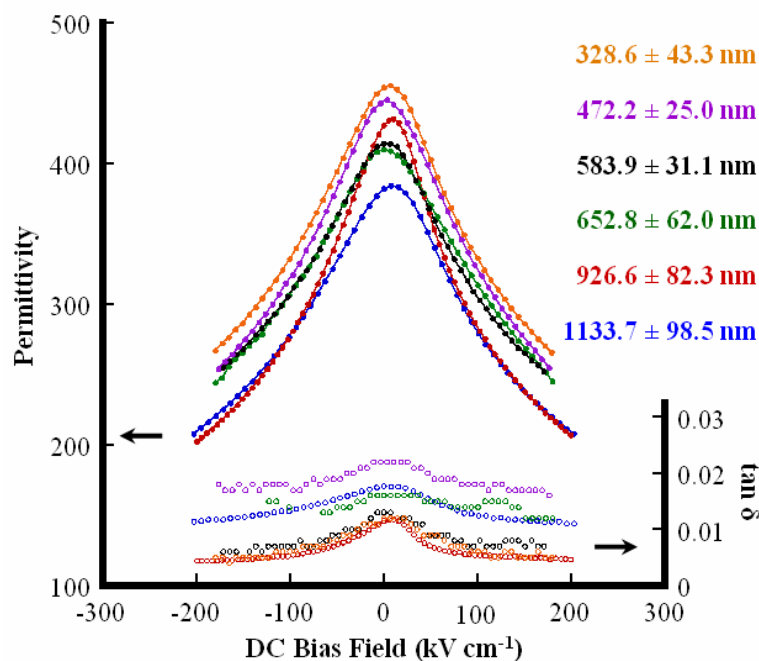


Figure 5.15: Room temperature permittivity versus DC bias for the thickness series. See the inset legend for the thicknesses associated with each curve.

All the curves have a similar shape and approach a similar saturated permittivity. $\tan \delta$ values for all samples were below 0.02 and some approached $<0.005 \tan \delta$ at high fields.

To evaluate the possible existence of a reduced permittivity interfacial layer, the inverse capacitance density is plotted versus film thickness. A non-zero inverse capacitance density at zero thickness has been used to support the existence of such features. A linear fit of data shows the permittivity is not a strong function of film thickness. Figure 5.17 shows the thickness series data plotted in this way.

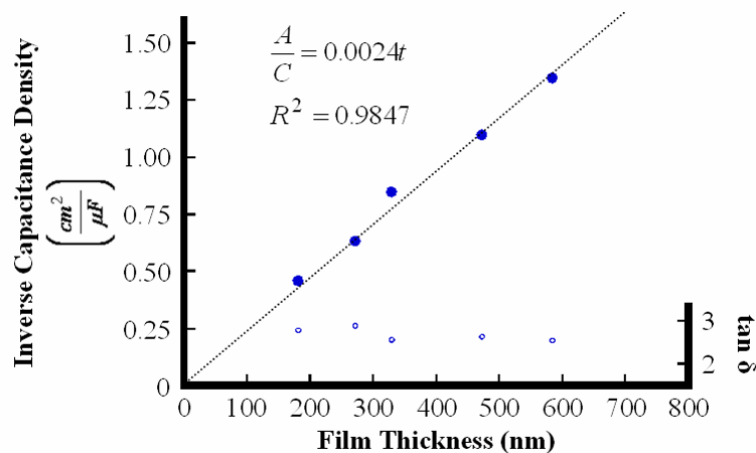


Figure 5.16: Room temperature inverse capacitance density versus film thickness. The data has a high degree of fit to a linear function with a zero intercept evident by the displayed equation and R^2 value of 0.9847.

The data fit a linear model with an origin intercept. Only data with a consistent $\tan \delta$ at zero DC bias were used for this analysis to avoid misinterpretation from inaccurate impedance measurements elevated by high loss. The measured R^2 value very close to unity for the equation displayed on the figure inset allows a high degree of confidence that linear fit is appropriate for the data set. These results indicate that permittivity is indeed not a strong function of film thickness.

As the previous series of data describe the examination of DC bias dependent dielectric properties, next, a similar examination will be made of temperature dependent dielectric properties.

Capacitance was measured versus temperature by the same procedure described previously and permittivity was calculated by measured film thickness and electrode diameter. Figure 5.18 shows the permittivity versus temperature for the thickness series measured at 10 kHz, 1.11 kV cm^{-1} , and zero DC bias while ramping temperature from 100 to 500 K at 4° min^{-1} .

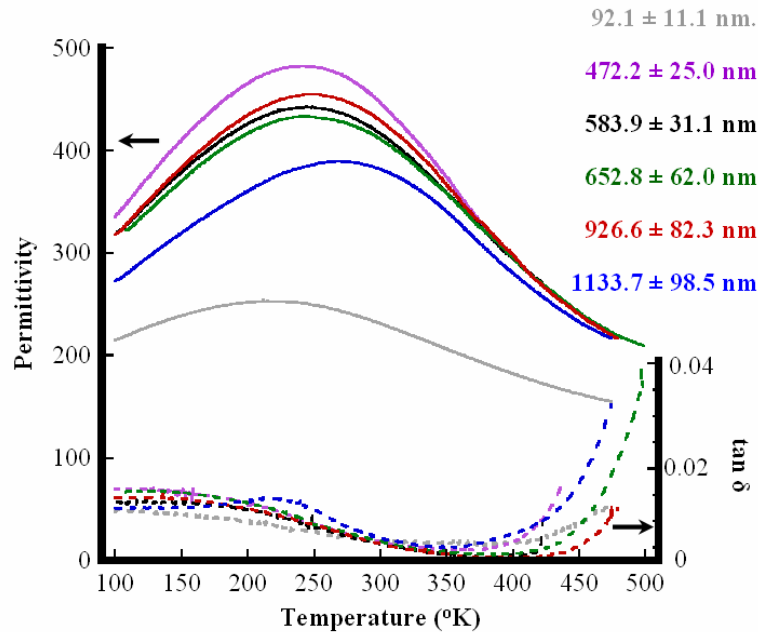


Figure 5.17: Permittivity temperature dependence for the thickness series. Film thicknesses are given in the inset.

Seen in the figure is a significant change in the temperature profiles for films with different thicknesses. For all the films above 100 nm the permittivity approaches an equivalent value at high temperatures. $\tan \delta$ values are consistently below 0.02 below 400 K and show characteristic increases preceding the phase transition. The loss increases at high temperatures, due in part to thermally stimulated charge carriers, giving decreased resistivity, and from increasing resistance of the conducting epoxy and solder at high temperatures. The melting point of the solder (~ 455 K) can be reached at high temperatures either leading to erroneous measurements or the loss of electrical contact, therefore not all measurements reach 500 K.

All intermediate thickness films show a similar functional dependence of permittivity with temperature and broadness of the profile changes little with film thickness. The existence of a broad diffuse transition was used previously to explain the high observed tunability at temperatures up to 100 °C away from the transition temperature. The films in this thickness study possess temperature profiles with the same

order of diffuseness which is attributed to the fine grained microstructure of the BST thin film.

The upper and lower film thickness extremes have substantially different dielectric properties than intermediate thickness films. The 100 nm sample was synthesized on an ultra-smooth substrate (see the Chapter 7) and this appears to result in a different behavior than rest of the thickness series. The substrates used for the intermediate thickness films did not allow formation of a fully coalesced film. The thickest film in the series, $> 1 \mu\text{m}$, also shows a different temperature response than intermediate thickness films. For film thicknesses greater than $1 \mu\text{m}$, processing induced mechanical stresses may be greater than the fracture strength of BST resulting in micron scale cracking. No MIM device shorts were observed on thick film samples indicating that film failure was contained to the film interior or the BST/Cu interface and not through the entire film thickness. These observations establish the limits on film thickness in BST thin film deposited on Cu foil substrates which are annealed at $900 \text{ }^\circ\text{C}$.

5.4.4. Thickness series summary

BST thin films in a series of thicknesses were synthesized using the Film on Foil methodology. The thickness, grain morphology, and grain size was characterized for each film and the data collected established the fine grained equiaxial microstructure was consistent throughout the series.

An analysis of inverse capacitance versus thickness establishes that permittivity is not a strong function of film thickness and the origin intercept at zero thickness suggests that a reduced permittivity interface layer is not strongly contributing to the properties in this thickness range.

Data concerning the DC bias and temperature dependent dielectric properties were analyzed versus film thickness. The dielectric properties are comparable to previous studies even when considering the fine grained microstructure of the films in this study compared to fiber textured films.^{85, 112} The $250 \text{ }^\circ\text{C}$ higher processing temperature is hypothesized to be responsible for this observation. Small grain size results in

temperature profile broadening which sustains high tunability over a large temperature range while mitigating TCC. The consistent grain size irrespective of film thickness provides only a weak function of tunability, maximum permittivity, and temperature profile shape with film thickness.

This study suggests film thickness can be adjusted to suit a particular application or circuit without encountering deleterious changes in dielectric properties over a thickness range that covers more than half an order of magnitude. The overall reduction of maximum permittivity and the constant transition broadening in these films is likely a consequence of scaling effects which can be attributed primarily to the extrinsic factors such as composition homogeneity, grain boundary volume, and defect concentrations. However, when viewed within the context of microwave devices, mitigated TCC are advantageous for the design of practical circuits.

5.5. DIELECTRIC PROPERTIES AS A FUNCTION OF COMPOSITION

5.5.1. Film growth of composition series

Multiple sputter targets with of a series of Ba:Sr compositions (Ba:Sr = {75:25, 60:40, 50:50, & 25:75}) were obtained from Super Conducting Materials, Inc. Films were sputtered for 90 minutes from each target using the conditions outlined in table 3.2 and crystallized, re-ox, and MIM capacitor defined in an identical way as in the thickness series experiments. XRD was used to determine lattice parameter of fully processed film and allowed determination of the film composition by Vegard's law.²³⁴ The exact thicknesses of these samples were not measured therefore data is plotted as relative capacitance (C/C_{MAX}) allowing measurement of tunability and T_C .

5.5.2. BST thin film composition

The compositions of the fully processed films were measured indirectly by unit cell parameter calculations from XRD data. θ - 2θ XRD measurements were performed to

accurately determine the θ value for the (110), (220), and (330) peaks for each BST thin film. The {110} family was used for analysis due to the appreciable intensity of the (330) reflection in the BST thin films, (300) and (400) could not be resolved above the background, and the XRD goniometer could reach all of the three lowest index reflections (versus only two for the {111} family).

From the measured θ value for each peak the lattice parameter can be calculated and the Nelson-Riley function used to correct for errors due to sample height alignment and X-ray adsorption. The Nelson-Riley function gives a corrected lattice parameter, a_0 , from the measured lattice parameter, a , and the Bragg angle, θ , value for the desired reflection.²³⁵

$$a = a_0 + a_0 k_2 \left(\frac{\cos^2 \theta}{\sin \theta} + \frac{\cos^2 \theta}{\theta} \right) \quad \text{eqn [5.10]}$$

Since there is total solid solubility between SrTiO₃ and BaTiO₃ with only one equilibrium phase, perovskite (Ba_x, Sr_{1-x})TiO₃, between the end members then lattice parameter for any x composition (Ba_x, Sr_{1-x})TiO₃ sample should follow Vegard's Law.²³⁴

$$a_{solution} = n_A a_A + n_B a_B \quad \text{eqn [5.11]}$$

Equation 5.11 is in the generic form of Vegard's Law. Since $n_A = x$ in (Ba_x, Sr_{1-x})TiO₃ and therefore $n_B = (1-x)$ then the Vegard relationship for BST can be shown by equation 5.12.

$$a_{BST} = x a_{BaTiO_3} + (1-x) a_{SrTiO_3} \quad \text{eqn [5.12]}$$

Using these assumptions, the lattice parameter determination for the BST thin films with various compositions can be tied to film composition.

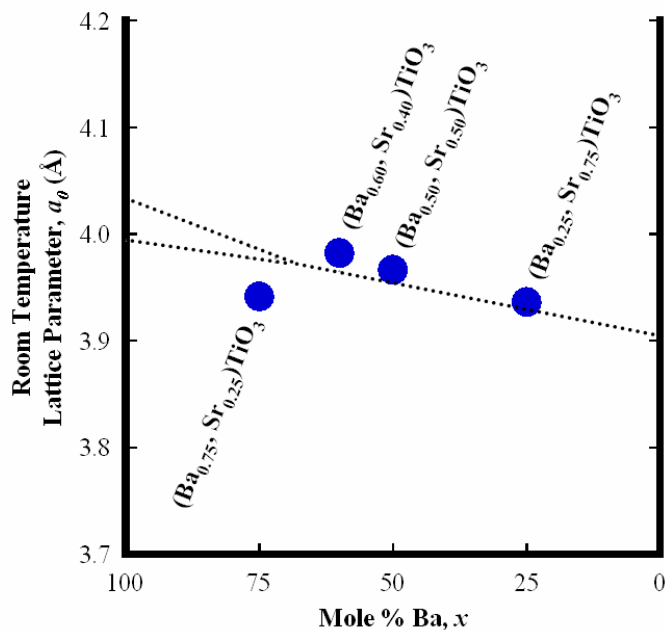


Figure 5.18: Lattice parameter of BST thin films based on extrapolation by the Nelson-Riley function. The dotted line shows the expected lattice parameter for all compositions based on Vegard's Law and the accepted values of the end members.

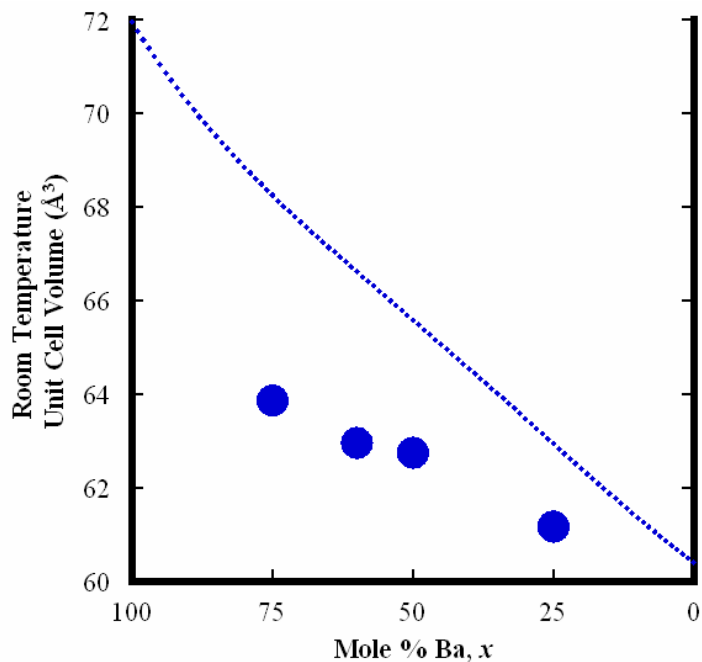


Figure 5.19: Room temperature unit cell volume of BST thin films from XRD data and extrapolation using the Nelson-Riley function. The dotted line shows the accepted values for bulk room temperature BST unit cell volume.⁶³

Figure 5.19 shows the measured lattice parameter for the BST film in the composition series compared against known lattice parameters²³⁶ extrapolated for the full composition range according to Vegard's Law and figure 5.20 shows unit cell volume compare to equilibrium bulk data.⁶³ The room temperature lattice parameter and unit cell volume of the $x = 25$ film agrees well with the bulk value for that composition. There is deviation of the film lattice parameter and unit cell volume from bulk values as the composition becomes increasingly Ba rich. An elemental characterization technique such as medium energy ion scattering (MEIS) or X-ray fluorescence (XRF) would allow direct measurement of the Ba:Sr ratio in these films but was not available during this work and remains a point of future work. For the film with composition $x \leq 0.6$ the deviations from bulk values is minute enough to definitively distinguish films as separate compositions.

5.5.3. Dielectric properties as a function of composition

Figure 5.21 shows temperature dependence of relative capacitance, C/C_{MAX} , for all compositions in this study. These measurements were made using a 10 kHz, 0.10 V oscillator level, and zero DC bias voltage signal while ramping the temperature from 100 K to 500 K at $4 \text{ }^\circ\text{C min}^{-1}$. All curves display a similar diffuseness of the temperature profile and in all cases $\tan \delta$ is below 0.03 for $T < 400$ K. The Curie temperature can be determined from these data as the temperature where relative capacitance is equivalent to unity. An appreciable shift of T_C is seen for Sr rich composition films as is expected, yet the Ba rich films appear to all have a similar T_C .

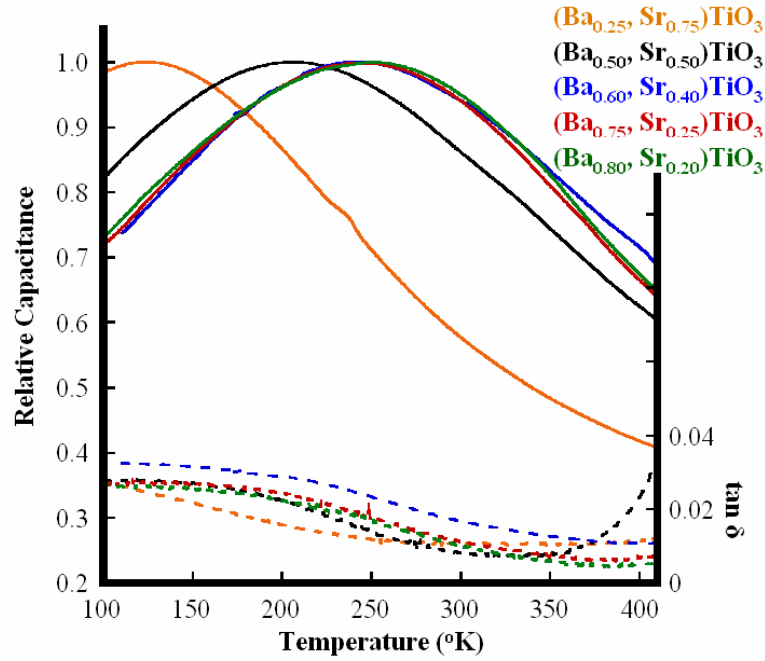


Figure 5.20: Relative capacitance temperature dependence for the composition series. Target composition used to grow each film are given in the inset.

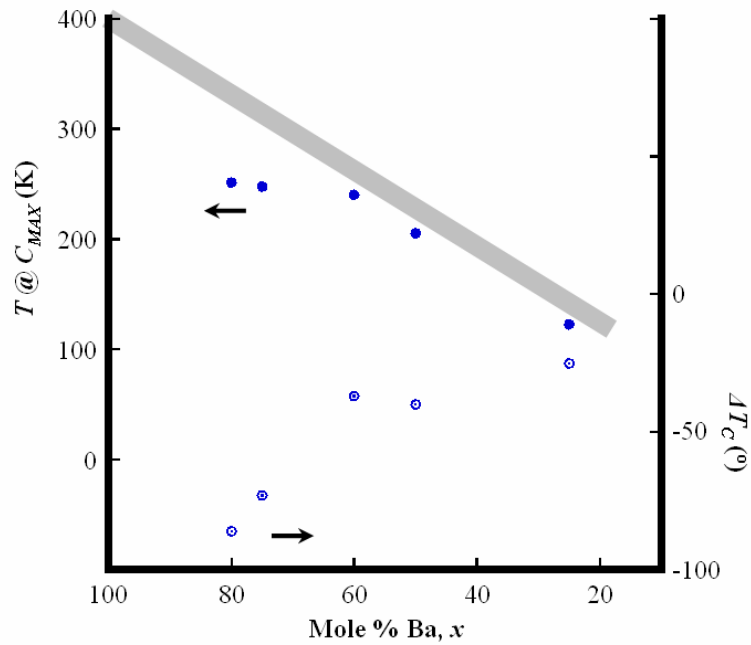


Figure 5.21: Observed T_C (closed circles) and the shift from the accepted bulk BST values, ΔT_C (open circles), versus film composition. The grey line represents the accepted T_C values for bulk BST and is given as reference to comparing the observed T_C for the films in this study.

To quantifiably address the T_C shift in Ba rich films, figure 5.22 displays the measured T_C versus composition for the data shown in figure 5.21. The ΔT_C is given by the open circles and the right axis as the observed shift in the transition temperature relative to accepted bulk values for BST.⁶⁵ This method of plotting the data displays the divergence away from the bulk ΔT_C with increasing Ba composition. For films where $x \leq 0.6$, a linear dependence of the transition temperature is followed with a constant $\Delta T_C = -40$ °C. For $x > 0.6$ the ΔT_C is invariant with increasing Ba composition and ΔT_C increases in magnitude to increasingly lower temperatures with increasing Ba composition. It is unclear to the physical origins of the suppression of the ferroelectric transition in Ba rich thin films. This deviation from bulk T_C is consistent with the broad temperature profiles observed. Finite scaling and size effects frustrate the transition making difficult to realize the tetragonal ferroelectric phase.

Although it appears that within the confines of these studies a T_C above room temperature cannot be realized in thin film BST. Hysteretic behavior is to be avoided in frequency-agile circuits so the observation of an ability to shift the temperature profile to lower temperatures allows T_C tailoring for room temperature use. This observation makes it difficult to realize some conclusions of the previous simulations. Analysis of BST/Cu samples with respect to composition show a smaller range of T_C is attainable in a thin film format compared to bulk BST. This limits the available ΔT_C for multi-composition composite stacks to mitigate TCC.

The room temperature voltage dependence capacitance was measured for films in the composition series to assess tunability as a function of composition (figure 5.23). These measurements were made using a 100 kHz, 0.1 V oscillator level voltage signal.

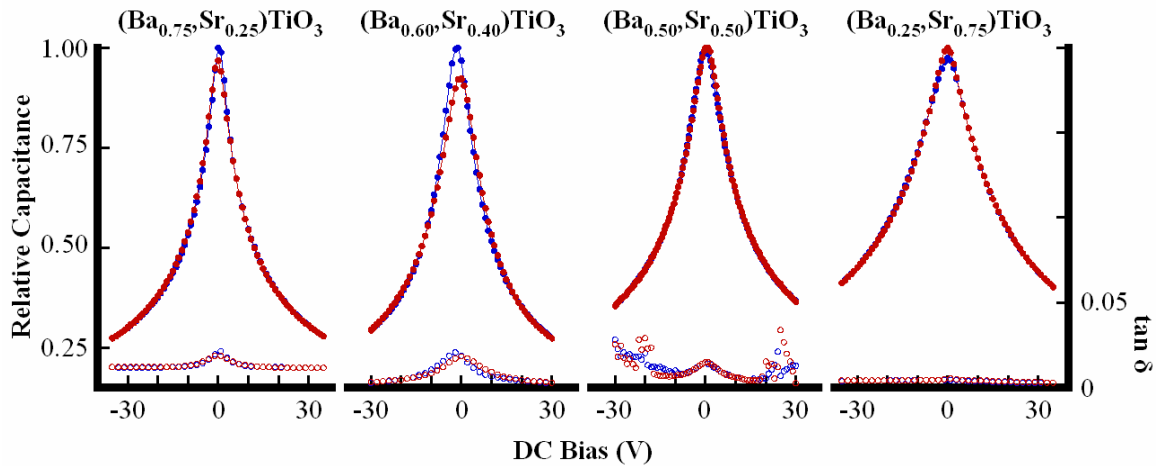


Figure 5.22: C-V curves for films in the composition series. The multiple curves for each film are from successive forward and reverse sweeps of voltage to display any apparent hysteresis. The axis on the extreme right, relative capacitance (**closed circles**), and extreme left, $\tan \delta$ (**open circles**), are valid for all four data sets.

In the figure, the films are increasingly Ba rich as viewing from left to right and therefore measurements made at room temperature are progressively closer to the transition temperature as viewed from left to right. Ferroelectric theory predicts increasing permittivity and $\tan \delta$ as measurements are made closer to T_C approaching from the high temperature paraelectric side of the phase transition. The data show a slight increase in tunability and a general increase in $\tan \delta$, both zero bias and saturated $\tan \delta$, as Ba composition increases. Since film thicknesses were not quantified, tunability cannot be unambiguously and quantitatively determined because there is no way to ensure a constant maximum DC electric field is applied. Yet, all films were deposited for an equivalent period of time and, barring unforeseen implication of using different sputtering targets, all film thicknesses should be similar. Theory suggests that tunability generally increases with increased permittivity³⁸ and permittivity increases as the phase transition is approached. Therefore the results of these measurements are self consistent.

A more significant observation lies in the high apparent tunability observed when measurements are made at a large difference in temperature from T_C . The $(\text{Ba}_{0.25}, \text{Sr}_{0.75})\text{TiO}_3$ film, where room temperature measurements are 180 °C above T_C , a 60% relative tunability is measured versus 72% relative tunability for the

(Ba_{0.75}, Sr_{0.25})TiO₃ film where room temperature measurements are only 50 °C from T_C . This is yet another observation of sustainability of tunability over a wide temperature range attributed to the fine grained equiaxial microstructure characteristic to the Film on Foil sputtering methodology used to synthesize these films.

5.5.4. Composition series summary

BST thin films in a series of compositions were synthesized using the Film on Foil methodology using identical sputter deposition time and anneals. The temperature dependent and DC bias dependent capacitance and $\tan \delta$ were measured for each composition. The analysis yielded insight into how the temperature profile and tunability vary across the BaTiO₃ - SrTiO₃ solid solution in a thin film embodiment. These observations are important when the temperature profile has to be tailored to suit circuit specifications.

In conclusion, this study established some important concepts concerning tunability over a wide range of compositions for BST thin films. A fine grained equiaxial microstructure gives the films a broad temperature profile which allows for substantial tunability to be observed when measurements are made >150 °C away from the phase transition temperature. The shift of T_C is not a linear function of Ba composition as suggested by measurements in bulk (Ba_x, Sr_{1-x})TiO₃ samples. The linear dependence is observed with a constant $\Delta T_C = -40$ °C when $x \leq 0.6$, yet the T_C approaches a constant value for Ba rich compositions. XRD determination of lattice parameter to gauge composition in Ba rich thin films was inconclusive yet the analysis of $C-V$ curves implied increasing the Ba composition of the films allowed room temperature measurements to be increasingly close to the transition temperature.

5.6. SUMMARY

Ferroelectrics have a varying permittivity with temperature limiting their use in electronic circuits. A concept for reducing the dependence of permittivity on temperature was explored by modeling the temperature profile of Pt/BST/Cu MIM capacitors. The

modeled temperature profiles were combined to simulate multiple compositions stacks of BST thin films in series and parallel connectivity. Simulations showed that parallel connectivity was effective in creating large temperature ranges where capacitance was a weak function of temperature. Simulations also showed that series connection had only modest utility in broadening the temperature profile.

To determine if the simulated structures could be synthesized and realize a mitigated TCC, dielectric properties as a function of film thickness and composition were determined. The study showed films could be processed from 300 nm to 1 μm with little effect on maximum permittivity, tunability, and temperature profile shape. An increasing T_C shift was observed in increasingly Ba rich compositions due to size and scaling effects frustrating the ferroelectric transition. These observations provide confidence that aspects of the simulations can be realized and BST/Cu tunable MIM capacitors synthesized with mitigated TCC.

6. ADHESION IN THE BST/CU SYSTEM

The use of metal foils as substrates for ferroelectric thin film deposition is a novel concept and consequently, much of the knowledge base developed for rigid substrate technology is of limited applicability for these flexible and ductile substrates. For instance, the fundamentally different mechanical boundary conditions necessitate reconsidering the concepts of substrate induced residual stress. Additionally, the literature involving rigid substrates^{237, 238} identifies an in-depth understanding of the chemical compatibility and thin film adhesion. The desire to use base metal electrodes, specifically Cu, demands a similar technical understanding of these issues. The low pO_2 processing described in this thesis solves one significant hurdle: a processing methodology to avoid the oxidation of the copper substrate during BST crystallization. This chapter outlines an investigation of adhesion between BST and copper and explores how the characteristics of commercially available copper substrates affect adhesion in the BST/Cu system. In doing so, we address a second technical challenge in Film on Foil technology.

The Film on Foil technique can reproducibly synthesize BST thin films in thicknesses spanning 250 nm to 1 μ m on commercially available copper foils. Outside of this thickness range, film cracking and MIM capacitor shorting are often observed. The 25 - 150 nm RMS surface roughness of the commercial copper foils is suspected to interfere with film coalescence even in sputter deposition where film deposition approaches conformality. Additionally, this surface roughness provides interfacial irregularities which can lead to field concentration and premature failure. Therefore it was hypothesized that using copper foils with reduced surface roughness would improve device yield and performance under bias. To address this possibility, smooth foils were obtained from commercial sources and produced in-house by the procedures described in Chapter 7. BST thin films deposited on these foils exhibited film cracking and film delamination to an unacceptable extent, thus identifying the initial need to understand and control Cu-BST adhesion.

The need for photolithographic definition of device structures also supports the need for smooth foils. The high permittivity of ferroelectric materials makes impedance matching of MIM thin film capacitors to the 50 Ω standards difficult at high frequencies. A 0.3 pF capacitance has an equivalent impedance of 50 Ω at 10 GHz. Assuming a permittivity of 500 and a film thickness of 1 μm in a MIM configuration, a 8.5 μm X 8.5 μm square electrode or 9.5 μm round electrode would be required for a 0.3 pF device. To accurately and repeatably form electrodes with these dimensions, photolithographic pattern definition is necessary. The commercially available Cu foils are incompatible with photolithography due to large surface roughness. The surface roughness will cause diffuse scattering of the incident photon intensity used to expose the photoresist. This diffuse intensity edge profile will result in pattern transfer with blurred feature edges, and is especially problematic at small dimensions.²³⁹

The problems encountered with smooth foils suggest poor BST-Cu interface adhesion. To quantify adhesion, one of two methodologies is generally employed. Mechanical tests can measure the force to separate the film from the substrate.^{173, 174, 176} These tests are performed on solid samples in their intended application format. Alternatively, wetting tests allow straightforward measurement of adhesion energy.¹⁸⁶ In these tests, one component of the system is melted in contact with the other solid component and the balance of surface energies gives a measurable contact angle at the liquid-solid-vapor triple point. Adhesion in thin films depends on chemical forces and interfacial morphology. The two common methods of measuring adhesion obfuscate chemical and interfacial morphology influences, thus care is needed during interpretation of experimental data.

Mechanical tests involve peeling, pulling, or scratching a thin film adhered to a substrate. The force required to cause delamination allows quantification of adhesion force. This force is determined by the chemical bonding across the interface and mechanical/physical interlocking due to interface morphology. The film and substrate can interlock in the reentrant sections caused by substrate roughness and conformal thin film growth. The peeling stresses can cause plastic deformation and/or fracture of these

interlocked regions and add to the measured adhesion force.¹⁷³ Interface roughness can also allow more bonding sites per apparent interface area leading to a potential artifact. The need for external attachment to both the film and substrate stronger than the adhesion forces makes mechanical adhesion tests impractical for flexible systems. Understanding BST/Cu adhesion requires comparison of rougher commercial Cu foils to smoother Cu foil variants. Since commercial Cu foils have chemical surface treatments affecting adhesion and mechanical tests are predominated by interface roughness an alternative method for characterizing adhesion more sensitive to intrinsic interface properties is needed.

Wetting experiments require only one solid component of the material system. When a liquid is brought in contact with a solid surface a portion of the previously solid-vapor interface is replaced by a liquid-solid interface and a liquid-vapor interface. The amount of solid-vapor interface area replaced is determined by the balance of all the surface energy terms and an excess energy term. The excess energy term is known as the work of adhesion, W_a , which corresponds to the energy per unit area needed to separate the two materials.

$$W_a = \gamma_{solid-vapor} + \gamma_{liquid-vapor} - \gamma_{solid-liquid} \quad \text{eqn [6.1]}$$

If the surface energy, or surface tension, of the liquid is known then the Young-Dupré equation¹⁷⁸ allows calculation of W_a without knowledge of the surface energies of the solid interfaces.

$$W_a = \gamma_{liquid-vapor} (1 + \cos \theta) \quad \text{eqn [6.2]}$$

The work of adhesion is affected by interface roughness. On an atomic level, a rough surface has more available bonding sites per macroscopic interface area changing the solid interface surface energies. Macroscopically, the difference between the energy of surfaces created, $\gamma_{liquid-vapor} + \gamma_{solid-liquid}$, and the surface destroyed, $\gamma_{solid-vapor}$, determines an equilibrium contact area. If the solid-liquid interface is perfectly flat, i.e. apparent area = interfacial area, the interfacial area is maximized, the contact angle, θ , is minimized. In

reality, interface roughness makes the interfacial area greater than the apparent area and larger contact angle is measured. This error due to roughness is smaller than in mechanical adhesion force tests since there is no strain in a liquid-solid system and solid-state compliance does not play a role. Sessile drop experiments allow measurement of the macroscopic contact angle from a drop of molten material resting on a solid substrate. Pillar and Nutting measured equilibrium faceting of small Cu particles on alumina and fit the measured shapes to Wulff plots to calculate the solid-solid interfacial energy. Pillar's and Nutting's measurements establish sessile drop measured work of adhesion is within 20% of interfacial energy in solid-solid systems.²⁰⁵

Sessile drop experiments are better suited for making an assessment of adhesion in the BST-Cu system if surface roughness is kept consistent. This allows measurement of interfacial adhesion forces between Cu and BST are how surface treatments can perturb the pure Cu-BST system.

Metallic Cu melted on BST thin films deposited on alumina substrates allowing measurement of W_a^{BST-Cu} . Interpreting this data, in turn allows us to make assessments of adhesion in the BST-base metal system, and to form predictions that will improve film properties. X-ray photoelectron spectroscopy (XPS) of Oak Mitsui PLSP copper foil surfaces identified zinc, which is not present in the smooth variants of other foils used in this study. Therefore, molten (Cu_x, Zn_{1-x}) and ZnO substrates were explored to identify the role of Zn in BST/Cu adhesion. Although there are reports of W_a for Cu-BaTiO₃ in the literature²⁰⁶⁻²⁰⁸, no reports of W_a in Zn - metal oxide systems could be found. This study explores fundamental issues for adhesion of copper substrates to BST thin films and allows assessment of the utility of copper electrodes and/or substrates for electroceramic oxides.

6.1. ANALYSIS OF COMMERCIAL/CONVENTIONAL CU FOIL SUBSTRATES

Experiments show BST thin films are robust when deposited on Oak Mitsui PLSP copper foil substrates, yet films crack and delaminate when deposited on pure copper foil

substrates. The Oak Mitsui PLSP surface was analyzed by XPS. Key findings are shown in figure 6.1.

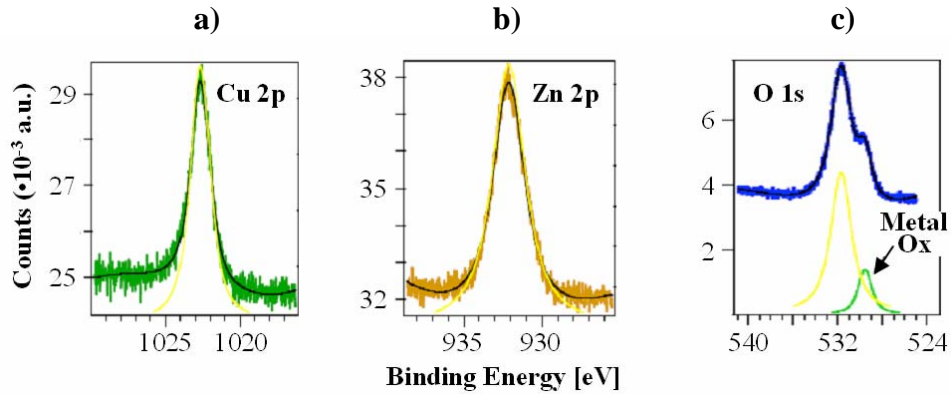


Figure 6.1: XPS spectra of the PLSP copper foil surface. a) XPS peak for the binding energy associated with the Cu 2p electrons. b) XPS peak for the binding energy associated with the Zn 2p electrons. c) XPS peak for the binding energy associated with the O 1s electrons showing a binding energy shift due to metal-oxide bonds.

XPS revealed the existence of copper, zinc, and oxygen on the PLPS surface evident by spectral peaks at binding energies corresponding to the 2p electrons of the metals and the 1s electrons of oxygen. A shoulder in the O 1s electron binding energy corresponds to a binding energy shift consistent with metal-oxygen bonds.

The spectroscopic analysis revealed PLSP copper foils have several monolayers of oxidized copper and zinc at the surface. These chemical components are absent in pure copper foil substrates where film cracking and delamination was observed. Therefore the possibility that Zn or ZnO promotes adhesion must be explored.

6.2. EXPERIMENTAL SETUP FOR CONTACT ANGLE MEASUREMENT

In the $BST/(Cu_x, Zn_{1-x})$ system, the metallic component has the lower melting temperature; therefore, to measure a contact angle the system must involve a ceramic substrate and a metal drop. The metal drop is imaged and contact angles on either side of the drop are measured. The metals must be melted while avoiding oxidation. For copper, annealing under controlled pO_2 conditions has already been demonstrated. For zinc at

temperatures near its melting point the situation is substantially more complex given the high vapor pressure of Zn and the low pO_2 necessary to keep Zn metallic.

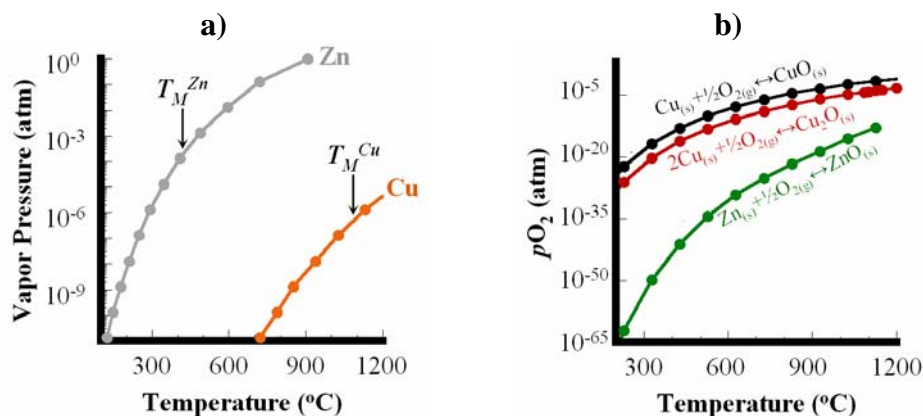


Figure 6.2: a) Vapor pressure curves for pure metallic Zn and Cu. The melting point for each metal is labeled on the plot. b) pO_2 -T plots of zero free energy of formation for the oxidation reactions of the binary oxides of Cu and Zn.

Figure 6.2a shows the vapor pressure curves for pure Cu and Zn where the arrows indicate the melting points, 420 °C and 1083 °C for Cu and Zn, respectively.²⁴⁰ The equilibrium vapor pressure of Zn is $> 10^{-3}$ atm at temperatures above 420 °C. This high vapor pressure allows for significant loss of Zn from the molten drop to the vapor phase making it difficult to maintain a constant composition of (Cu_x, Zn_{1-x}) with time. The equilibrium vapor pressure of Zn is determined by the activity of Zn in mixtures with Cu. The activity of Zn in Cu has a negative deviation from Raoultian behavior, yet the vapor pressure still reduces monotonically with decreasing Zn content in (Cu_x, Zn_{1-x}) .¹⁵⁸ In all cases the amount of Zn loss during the experiment can be substantial. Figure 6.2b shows the zero free energy of formation curves with respect to pO_2 and T for the reaction of the pure metals and molecular oxygen to form the binary oxides of Cu and Zn.¹⁵⁴⁻¹⁵⁷ Flowing 5% H_2 forming gas can establish the necessary conditions to maintain metallic molten copper, yet the required pO_2 to maintain metallic zinc at its melting point is 36 orders of magnitude lower. Therefore, experiments must be done in substantially more reducing conditions.

To achieve the necessary temperature and atmospheric control, a sealed tube furnace was constructed that allowed pO_2 control through process gas mixtures while allowing sample viewing *in situ*. A schematic of this furnace is given in figure 6.3.

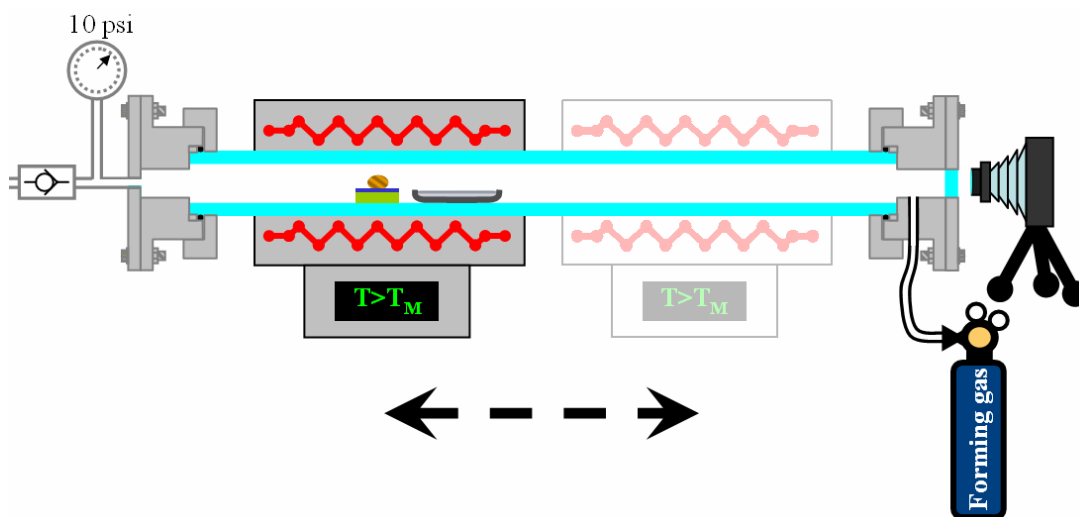


Figure 6.3: Schematic of furnace designed to measure contact angle.

A 4 ft long 25 mm OD X 20 mm ID fused silica tube is sealed with Viton™ o-ring compression seals to stainless steel conflat vacuum flanges. The flange at the right side of the figure has a 1" diameter glass window to allow viewing down the length of the tube.

A 12" long resistively heated furnace was built by winding Kanthal heating wire (Kanthal, Bethel, CT, USA) around a 2" diameter alumina mandrel. The heating elements are insulated by alumina fiber within a stainless steel sheet metal and machinable ceramic box. Temperature is controlled by a Eurotherm 818S PID temperature controller (Eurotherm Ltd., Durrington, West Sussex, UK) through temperature feedback from a K-type thermocouple situated in close proximity above the heating elements. This furnace has a ~ 6" hot zone and is capable of reaching temperatures of 1200 °C. The furnace is set on precision linear motion rails parallel to the silica tube to allow placement and *in situ* motion of the hot zone at any point along the center 2 ½ ft of the silica tube.

Pre-mixed high purity gases (99.999% purity) were used. The hydrogen/inert forming gas (8.55% H₂, balance He or 5% H₂, balance N₂) was metered using a mechanical rotameter. Back streaming of contaminants is prevented by a 10 psi check

valve at the outlet, and the interior pressure is monitored using a diaphragm gauge. The furnace is continuously purged during periods between experiments using dry N₂ gas supplied from a liquid N₂ dewar.

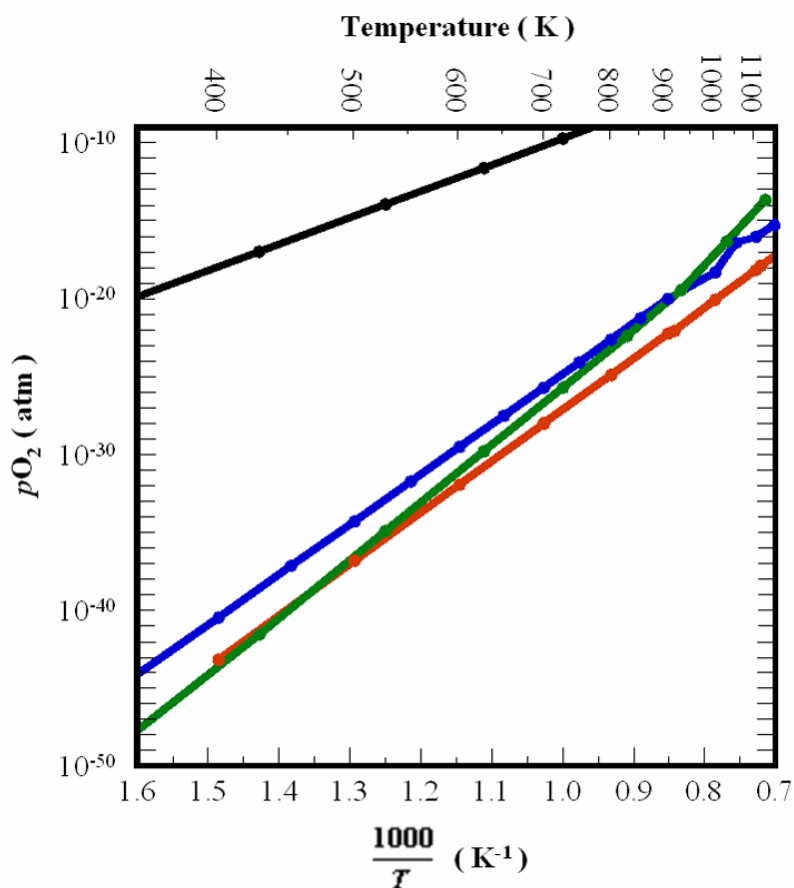


Figure 6.4: pO_2 versus temperature curves for the free energy of oxide formation for Cu (black) and Zn (green). These curves are compared the pO_2 conditions created by the 8.55% H₂:balance He (red), and 5% H₂:balance N₂ (blue) forming gas measured *in situ* in a sealed tube furnace.

The achievable pO_2 versus temperature were estimated by flowing process gases in a similarly sealed furnace where pO_2 is measured *in situ* with a doped zirconia oxygen sensor (Australian Oxytrol Systems, Victoria, Australia, DS-Series solid-state pO_2 sensor). Figure 6.4 shows these measurements compared to the necessary pO_2 to maintain metallic Zn or Cu. Either variant of forming gas is sufficient to maintain metallic Cu. The red 8.55% H₂ (balance He) curve and the green curve corresponding to the free energy of formation for zinc oxide (green) cross at 465 °C. Above this temperature the necessary

conditions to maintain metallic Zn can be achieved and at lower temperatures ZnO is stable.

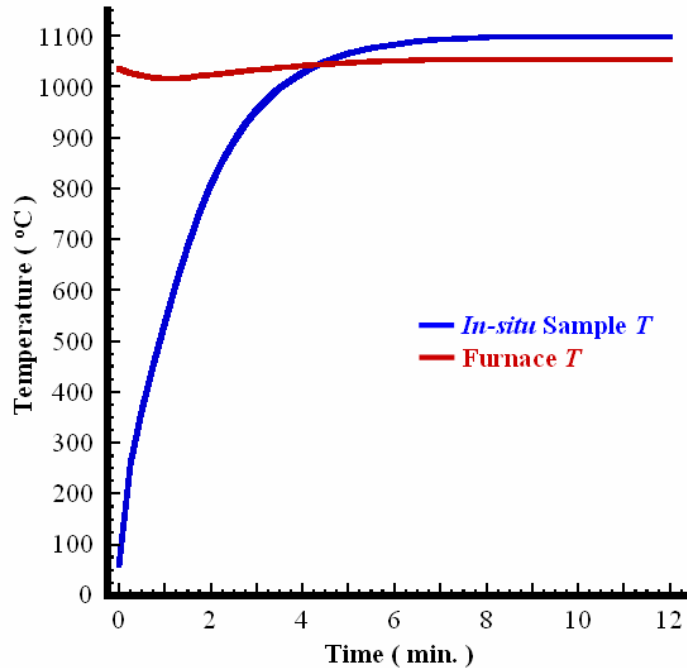


Figure 6.5: Temperature profile created by sliding the furnace at 1035 °C over a room temperature sample. The *in situ* temperature (blue) is compared to the furnace temperature (red).

For experiments where $x < 1$ ($\text{Cu}_x, \text{Zn}_{1-x}$), oxidation in this low temperature region must be kinetically bypassed by a high rate temperature ramp. Sliding the hot furnace over the room temperature sample an initially rapid temperature ramp rate can be achieved ($\leq 800 \text{ }^\circ\text{C min}^{-1}$) which decays as the sample reaches the dwell temperature of the furnace and effectively eliminates substantial formation of ZnO. The sample temperature is measured *in situ* with a K-type Inconel sheathed thermocouple. Seen in figure 6.5, the fast temperature ramp can bypass the low temperature oxidizing region in approximately 1 minute.

Samples consisted of the ceramic substrate and the metallic raw material. Intertec (Intertec Southwest, Inc., Tucson, AZ) 1.3 cm X 1.3 cm polycrystalline alumina substrates (>99.6% purity, 3.9 g cc^{-1} , 625 μm thickness) were obtained with one surface polished (< 50 nm RMS roughness over $1 \mu\text{m} \times 1 \mu\text{m}$ area measured by AFM¹⁰⁵). Samples

labeled as “Al₂O₃” use these substrates in their virgin state. (Ba_{0.75}, Sr_{0.25})TiO₃ thin films, 500 nm thick, were deposited on alumina substrates at 450 °C using the sputtering conditions described in the experimental procedure section of this thesis. The films are annealed in air at 900 °C for 20 hours to ensure full crystallization. The BST thin films on alumina substrates are labeled “BST/Al₂O₃” in this chapter. Zinc oxide (labeled “ZnO”) substrates (Eagle-Pitcher Industries, Inc, Miami, OK, USA) were obtained and polished using diamond films to a < 1 μm polish. All substrates were rinsed with methanol (MeOH) and dried with flowing dry N₂ compressed gas prior to experiments.

Pure metals were obtained from Alfa Aesar (Ward Hill, MA, USA). The Cu used is Puratronic® 99.998% (metals basis) oxygen free foil 30 μm thickness. Cu foil is cut to achieve the desired mass, methanol (MeOH) rinsed, and dried by flowing purified N₂ compress gas. The Zn used is 99.9+%(metals basis) ½ inch diameter rods. The rod is cut to achieve the desired mass. To remove native surface oxides the cut Zn rod is surface ground using standard alumina sandpaper (120 grit). Zn samples are then MeOH rinsed, MeOH soaked for 15 min, then rinsed again in MeOH with a subsequent N₂ dry to remove hydrocarbon contamination. The zinc is then etched in a 15 volume % acetic acid (99.7+% purity, Alfa Aesar) - deionized water (DI H₂O) solution for 20 minutes, DI H₂O rinsed, and N₂ dried. A final rinse in isopropyl alcohol (IPA) and N₂ dry is used to remove any remaining water. Alloy samples are made by massing appropriate ratios of Cu and Zn and wrapping the Zn piece with the copper foil as tightly as possible to minimize Zn vapor loss during the pre-melt and pre-alloyed low temperature portion of the ramp. All substrate/metal samples were massed prior to experiment. Total metal mass was kept to between 1 and 2 grams for all experiments.

After images were captured and the experiment finished, samples are quenched while maintaining the controlled atmosphere. This is achieved by sliding back the hot furnace away from the sample. This quickly cools the sample and minimizes post experiment Zn evaporation. In this manner, the final measured composition can be estimated by massing the solidified metal drop after cooling. Samples are massed after the experiment and any weight loss/gain is assumed from the evaporation or condensation

of Zn. The final mass ratio is used to estimate the alloy composition. The post experiment quench gives confidence the final measured composition by mass is accurate.

To further minimize Zn loss during ($\text{Cu}_x, \text{Zn}_{1-x}$) measurements, a Zn overpressure is created upstream by an upstream bath of molten Zn. A sintered SiO_2 crucible (Technical Glass Products, Inc., Painesville Twp., OH, USA) is filled with Zn foil (99.98% purity, 0.01 inch thickness, Alfa Aesar) prepared to remove native surface oxides. Prior to heating the sample, the furnace is positioned over the Zn bath until condensation of Zn vapor is observed downstream from the furnace. The Zn bath is positioned so it partially sits outside the furnace hot zone when the furnace is centered on the sessile drop sample. This procedure allows a rapid temperature ramp of the Zn bath thereby avoiding oxidation. When sessile drop samples are measured, the furnace maintains the bath at a temperature approximately equal to the sample creating an equilibrium vapor pressure of $\text{Zn}_{(v)}$ above the molten drop. This procedure can maintain the composition of the ($\text{Cu}_x, \text{Zn}_{1-x}$) drop to ± 3 mass %.

A digital Nikon D50 single lens reflex (SLR) camera fitted with a FIVE STAR MC auto macro zoom 75-200mm 1:4.5 lens (Toyo Seiki Kogaku, Toko, Japan) was used to capture images of the molten drop. This camera allows appropriate optical zoom at small working distances and digital capture of the images on a 6 mega pixel CCD. Images were acquired at ISO 200 sensitivity, $f = 4.5$ aperture setting, $1/50^{\text{th}}$ sec exposure and full zoom approximately 1 m from the sample with the camera mounted on a tripod. Images were stored and analyzed in the Nikon compressed raw NEF file format to avoid data loss artifacts from more aggressive image compression algorithms.

A wetting experiment is conducted by first cleaning and removing of surface oxides and contaminates of all materials. Metal raw materials are massed and combined to make the final desired composition. The sealed tube is opened while maintaining the flow of N_2 . The Zn bath is slid into position, and the samples are positioned over the internal thermocouple. The furnace is sealed and allowed to purge for 10 minutes with N_2 . The furnace is positioned upstream away from the Zn bath and samples, and is ramped from $150\text{ }^\circ\text{C}$ to the measurement temperature at $30\text{ }^\circ\text{C min}^{-1}$ while flowing the

appropriate forming gas. The furnace is allowed to purge and equilibrate for approximately 15 minutes after the temperature ramp is completed. The camera is positioned to fully image the sample. The furnace is then slid over the Zn bath until Zn condensation is observed and then moved over the sample. The sample is viewed through the camera to observe the melting of the metal drop. In all cases, the drop melted at the predicted temperature (see the Zn-Cu phase diagram in Appendix figure B.4). When the drop fully melts, images were taken of the sample. Approximately 10 to 15 images were taken of the molten drop over a 10 minute period while noting the *in situ* temperature measurement for each exposure. Multiple exposures are used to gauge if the drop is at an equilibrium shape. After all images are captured, the furnace is slid back and the sample allowed to air quench to < 100 °C while maintaining the flow of forming gas. Before opening the sealed tube, the furnace is purged with N₂. The drop is then assessed for axial symmetry and massed for final composition. If an axisymmetric drop shape is not observed, the experiment is considered a failed run and the data is not included in analyses.

Table 6.1 summarizes the specific experimental conditions for each substrate and metal composition.

Table 6.1: Experimental conditions used for all wetting experiments.

Molten Metal	Substrate	Forming Gas Content	Measurement Temperature	Zn Bath
Cu	Al ₂ O ₃	8.55% H ₂ (balance He)	1100 °C	-----
Cu	BST/Al ₂ O ₃	8.55% H ₂ (balance He)	1100 °C	-----
Zn	Al ₂ O ₃	8.55% H ₂ (balance He)	690 °C - 725 °C	-----
Zn	BST/Al ₂ O ₃	8.55% H ₂ (balance He)	690 °C - 725 °C	-----
(Cu _x Zn _{1-x})	BST/Al ₂ O ₃	8.55% H ₂ (balance He)	1100 °C	Yes
Cu	Al ₂ O ₃	5% H ₂ (Balance N ₂)	1100 °C	-----
Cu	BST/Al ₂ O ₃	5% H ₂ (Balance N ₂)	1100 °C	-----
Cu	ZnO	5% H ₂ (Balance N ₂)	1100 °C	-----

These experimental procedures are designed to avoid metal oxidation and minimize impurity concentration. Contact angle measurements are used in combination with literature values for surface tension¹⁸³ to calculate W_a . Experiments of pure metals are repeated on alumina substrates for comparison to literature reports and assess the validity of the experimental procedure.

6.3. ADHESION OF PURE COPPER & ZINC TO ALUMINA

Cu-Al₂O₃ sessile drop experiments were performed to compare against literature values and validate experimental procedures. Sessile drop data given in the literature often employs single crystal epitaxial ready wafers of the substrate material while taking great care to achieve a contaminate-free environment. The experimental procedure outlined in this thesis uses polycrystalline Al₂O₃ with a < 50 nm RMS roughness. The complications associated with the high vapor pressure of Zn do not allow for similar interfacial cleanliness. Comparing the experimental data for Cu-Al₂O₃ with literature reports will enable assessment of the experimental procedure.

Figure 6.6 shows images of Zn (a) and Cu (b) at 725 °C and 1100 °C, respectively.

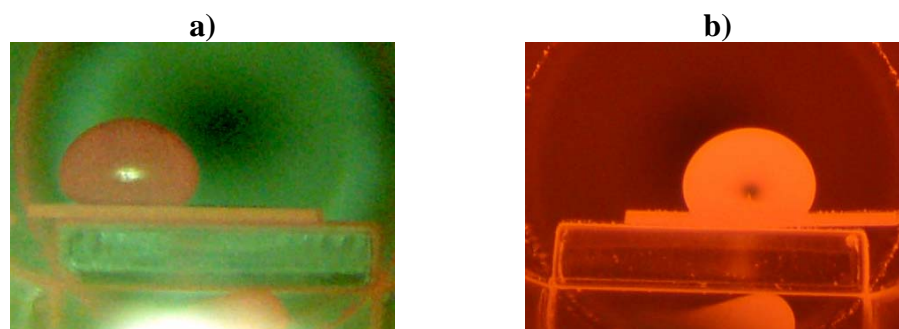


Figure 6.6: Images of a) molten Zn on Al₂O₃ at 725 °C and b) molten Cu on Al₂O₃ at 1100 °C.

The red hue of image 6.6b is from the higher measurement temperature. The sessile drops are axisymmetric and show the characteristic shape of a molten metal on a flat rigid surface when gravitational and surface tension forces are acting on the liquid drop.^{177, 180} Additionally, reflections can be seen in the middle of each drop resulting from the shiny luster. The contact angle > 90° is considered a “non-wetting” sessile drop and is common

for metal-oxide sessile drop measurements where the metal has a low formation enthalpy of oxidation, ΔH_f^{ox} .¹⁸⁶

Table 6.2 shows data for contact angle and W_a from the literature. The last row in the table gives the data collected in the present work.

Table 6.2: Contact angle and W_a values measured by sessile drop experiments for pure Cu on alumina (sapphire and polycrystalline Al_2O_3). $\text{Cu-Al}_2\text{O}_3$ values are compared to those found in the literature for 1100 °C, $\sim 10^{-19}$ atm $p\text{O}_2$.^{189,199}

Substrate	Molten Metal	Contact Angle, θ (°)	W_a (J m ⁻²)
Sap- Al_2O_3 [†]	Cu	130	0.480
Sap- Al_2O_3 [‡]	Cu	126	0.559
Poly- Al_2O_3	Cu	125 ± 4	0.620 ± 0.076

[†] V. Ghetta et al, Acta mater., 1996.

[‡] P. Darrell Ownby & Jenq Liu, J. Adhesion Sci. Technol., 1988.

The data for Cu on polycrystalline substrates of this study agree with literature data taken on sapphire at similar temperatures and $p\text{O}_2$, 1100 °C and 10^{-19} atm, respectively. The agreement of the data in this study to accepted literature values for $W_a^{\text{Cu-Al}_2\text{O}_3}$ validate the experimental procedure and instrumentation.

Pure Zn was melted on polycrystalline alumina substrates; this data has not previously been reported. Zn data was collected between 690 °C and 700 °C, significantly above the 420 °C melting point. This high temperature was necessary to allow rapid heating at low temperatures, to avoid Zn oxidation, and allow sufficient thermal radiation for imaging. In comparison, Cu drops were measured at 1100 °C, just above the T_M^{Cu} of 1084 °C. The change of surface tension with temperature for Cu and Zn are $-0.26 \cdot 10^{-3} \text{ J m}^{-2} \text{ °C}^{-1}$ and $-0.227 \cdot 10^{-3} \text{ J m}^{-2} \text{ °C}^{-1}$, respectively.¹⁸³ This small temperature coefficient represents a change of surface tension from the T_M^{Zn} to the measurement temperature of 725 °C of only 8% which is small compared to the error associated with sessile drop determination of W_a .

Table 6.3 gives the measured contact angle and W_a for Cu and Zn on polycrystalline alumina substrates. The Zn result is compared to data for metals commonly used in ferroelectric thin film devices^{237, 241, 242}.

Table 6.3: Measured contact angle and W_a of Cu and Zn on alumina substrates. Values for other common BST electrode metals are given from the literature.^{209, 211}

Molten Metal	Contact Angle, θ (°)	W_a (J m ⁻²)
Pt [•]	Not reported	1.050 ± 0.080
Pd [◇]	Not reported	0.737
Au [◇]	131 ± 3	0.277
Cu	125 ± 4	0.620 ± 0.076
Zn	136 ± 8	0.220 ± 0.078

- Measured by observation of grain boundary grooving and reported in M. McLean and E. D. Hondros, J. Mater. Sci., 1971.
- ◇ D. Chatain et al, Revue Phys. Appl., 1988

This comparison shows $W_a^{Au-Al_2O_3} \ll W_a^{Cu-Al_2O_3} \ll W_a^{Pd-Al_2O_3} \ll W_a^{Pt-Al_2O_3}$, or copper adheres to alumina stronger than gold yet weaker than palladium and platinum. $W_a^{Zn-Al_2O_3}$ is the lowest of all the metals listed; the first indication that metallic Zn adversely affects adhesion for Zn-oxide interfaces.

6.4. ADHESION OF PURE COPPER & ZINC TO BST

BST thin films were deposited on alumina substrates identical to those used in previous experiments. These BST/Al₂O₃ substrates will extend the analysis of Cu and Zn adhesion to a system mirroring BST thin films on copper foil substrates. Alumina was used as a carrier substrate for BST thin films to replicate the surface roughness of previous experiments. Polycrystalline alumina has a similar thermal expansion coefficient to BST ($\alpha_{poly-Al_2O_3} = 8 \text{ ppm } ^\circ\text{C}^{-1}$ at 1000 °C²⁴³ versus $\alpha_{BST} \approx 10 \text{ ppm } ^\circ\text{C}^{-1}$ by linear superposition of the solid solution end members $\alpha_{SrTiO_3} = 7.6 \text{ ppm } ^\circ\text{C}^{-1}$ and $\alpha_{BaTiO_3} = 11 \text{ ppm } ^\circ\text{C}^{-1}$ ²³⁶) maintaining crack free BST thin films at the sessile drop measurement temperatures.

Figure 6.7 shows optical images of the samples before and after experiment. The BST thin film becomes dark after the high temperature, low pO_2 conditions. This is a well documented phenomenon where extreme reduction of BST causes a change in optical properties from transparent to opaque.²⁴⁴

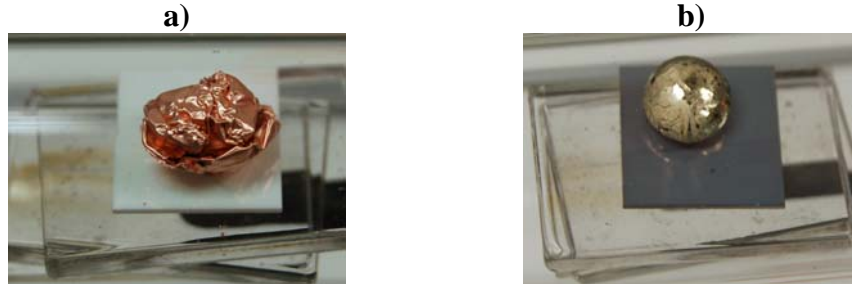


Figure 6.7: a) Cu wrapped Zn on BST/Al₂O₃ sealed in the furnace tube prior to the experiment. The white color of the substrate is alumina ceramic viewed through the transparent BST thin film. b) A solidified (Cu_x, Zn_{1-x}) drop on a BST/Al₂O₃ substrate viewed after an experiment and still sealed in the furnace tube. The substrate appears dark due to the change in optical properties of BST from the extreme reducing, high T conditions the sample encounters during experiment.

X-ray diffraction characterization of BST films on Al₂O₃ after high temperature measurement showed secondary phase development. XRD θ - 2θ data, shown in figure 6.8, show peaks corresponding to reflections from (Ba_{0.75}, Sr_{0.25})TiO₃, Al₂O₃, and an unidentified phase.

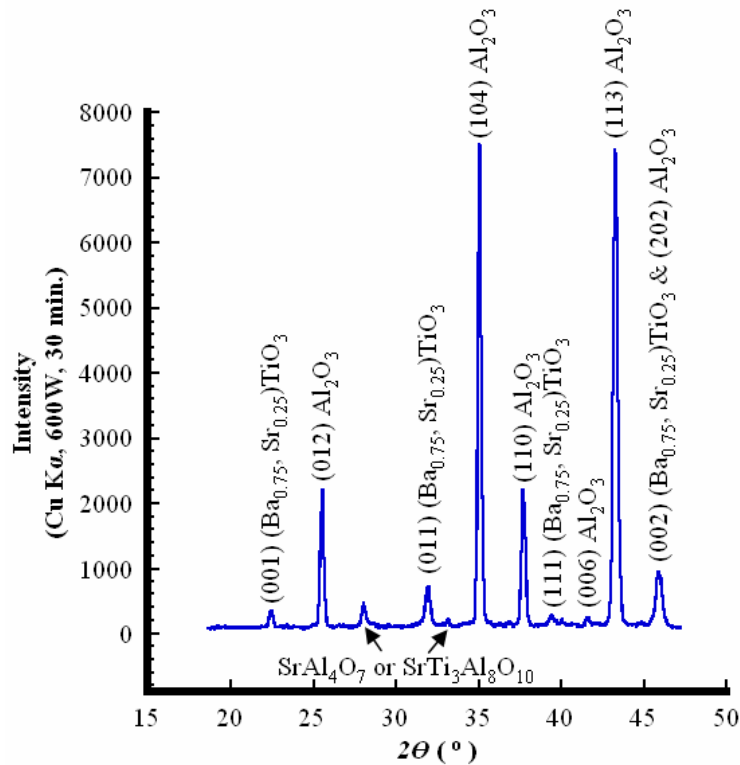


Figure 6.8: XRD θ - 2θ of the BST/ Al_2O_3 substrate after a sessile drop experiment. The BST and alumina phases are clearly evident. Weak intensity from a secondary phase could not be identified as reflection from any one particular phase. It is proposed that these data show a small interfacial reaction of BST and Al_2O_3 but by peak intensities it appears this phase is confined to the interface.

This additional phase (presumably a Ba, Sr, and Ti-containing aluminate) is believed to result from interfacial reaction between BST and alumina. (Powder diffraction files and a SrO- Al_2O_3 phase diagram are given in Appendices B and C for equilibrium phases of Ba, Sr, and Ti-containing aluminates. To ensure that this extra phase (which presumably forms at the alumina interface) does not confound the wetting experiments, surface composition of the post heat-treated BST films was measured using XPS. XPS data (figure 6.9) show no indication of Al, thus we can sensibly assume that the surface remains BST, and that wetting angle measurements are meaningful. The comparatively weak intensity of the secondary phase XRD reflections suggests that the volume fraction is small, further supporting our surface assumptions.

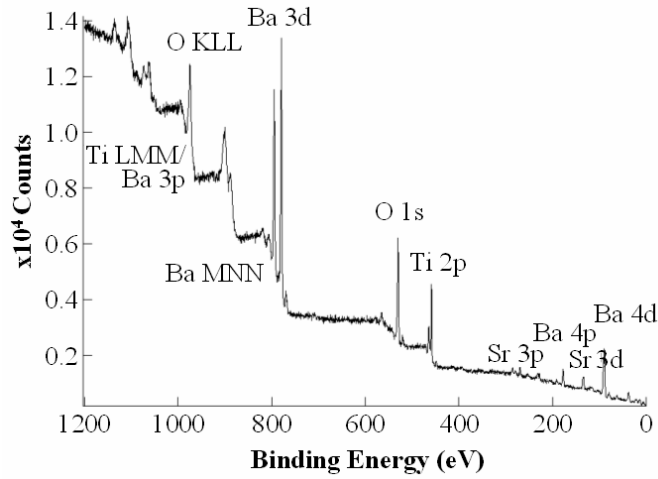


Figure 6.9: XPS survey scan of the BST surface after a sessile drop experiment. No signal from Al can be seen assuring that the reaction phase observed in XRD is confined to the interface and does not affect contact angle measurements on BST thin films.

Table 6.4: Measured contact angle and W_a of Cu and Zn on BST/ Al_2O_3 substrates. Values for Cu on polished bulk BaTiO_3 substrates are given from the literature.^{206, 208}

Substrate	Molten Metal	Contact Angle, θ (°)	W_a (J m^{-2})
Bulk- BaTiO_3 [†]	Au	124 ± 2	0.520 ± 0.040
Bulk- BaTiO_3 [†]	Cu	102 ± 4	1.080 ± 0.090
Bulk- BaTiO_3 [‡]	Cu	102	1.042
Thin film - BST/ Al_2O_3	Cu	127 ± 9	0.554 ± 0.164
Thin film - BST/ Al_2O_3	Zn	146 ± 5	0.133 ± 0.042

[†] D. P. Cann, Ph.D. Thesis, The Pennsylvania State University, 1997.

[‡] S.-F. Wang, J. Mater. Sci., 2001.

Table 6.4 gives the measured contact angle and W_a for Cu and Zn on BST/ Al_2O_3 substrates. The data is compared to similar data for Cu on polished bulk polycrystalline BaTiO_3 .^{206, 208} The measured $W_a^{\text{Cu-BST}}$ is significantly lower than $W_a^{\text{Cu-BaTiO}_3}$ reported for bulk BaTiO_3 . Two major differences between the experiment outlined in this thesis and the experiment on polished bulk BaTiO_3 can be identified.

Bulk BaTiO_3 is polished prior to measurement to remove the as-sintered surface, and typically, sintered samples exhibit lower density, and grain sizes 1000X larger than

thin films. Both factors lead to larger surface roughness values, however, this does not explain the differences in W_a , because a smoother surface should give less interfacial area per volume and reduce the contact angle as predicted by the Young-Dupré equation.^{178, 179}

Secondly, the work of adhesion is highly dependent on the oxygen activity during measurement. This has been shown for Cu-Al₂O₃¹⁹⁹ and Cu-BaTiO₃²⁰⁸ where increasing oxygen activity causes a higher work of adhesion and a transition from non-wetting to wetting. In the study of metal-oxide adhesion, similar to the study of surface tension¹⁸³, the intrinsic property values minimize or eliminate the effects of oxygen contamination. The studies presented in this thesis were conducted at $<10^{-19}$ atm pO_2 to maintain the metallic character of Zn and were extended to the measurements of Cu for consistency. Literature reports do not provide *in situ* measurements or estimations of pO_2 for their studies, yet comparisons of data suggest higher oxygen activity for experiments from literature reports.

In comparing Cu-BST and Zn-BST adhesion, the W_a^{Zn-BST} is significantly less than W_a^{Cu-BST} . Therefore, the hypothesis that metallic Zn interlayer is responsible for increased BST adhesion to Oak Mitsui PLSP copper foils cannot be supported.

6.5. ADHESION OF (Cu_x, Zn_{1-x}) TO BST

To further investigate the impact of metallic Zn on BST adhesion to copper foils, the sessile drop experiments were extended across the Cu-Zn solid solution. There is total miscibility of the two elements in both the liquid and solid phase (see Appendix figure B.4 for Cu-Zn phase diagram) allowing (Cu_x, Zn_{1-x}) samples to be prepared of $x = \{25, 50, 75\}$ mass%. Alloys were melted on BST/Al₂O₃ substrates at 1100 °C and 10^{-19} atm pO_2 while using an upstream bath of molten Zn to establish a Zn_(v) overpressure and mitigate Zn loss through evaporation.

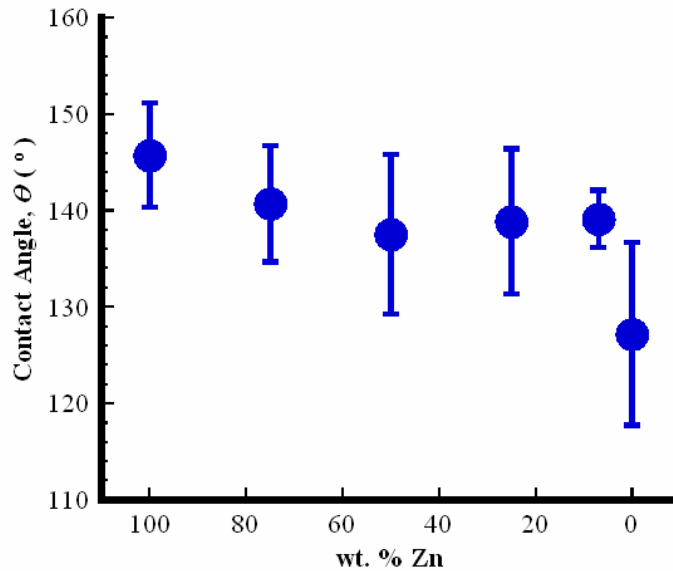


Figure 6.10: Contact angle for $(\text{Cu}_x, \text{Zn}_{1-x})$ on $\text{BST}/\text{Al}_2\text{O}_3$ substrates given versus the mass percent Zn in the molten alloy.

Figure 6.10 shows the results of contact angle measurements for the metallic $(\text{Cu}_x, \text{Zn}_{1-x})$ on $\text{BST}/\text{Al}_2\text{O}_3$ substrates. The intermediate composition Cu-Zn alloys give between 139° and 141° contact angle in contact with BST. All Cu-Zn alloys show a substantial improvement in contact angle over pure Zn, yet the Cu-BST contact angle is significantly lower than any Zn containing alloy. Error associated with these measurements prohibits determination of an exact dependence of contact angle with Zn content, yet by cursory analysis a weak trend is observed until dilute alloys are reached. A stronger trend may exist for W_a versus composition but W_a could not be determined for these data since the surface tension of a $(\text{Cu}_x, \text{Zn}_{1-x})$ alloy is not present in the literature. Most importantly, the inclusion of any amount of Zn to the metal drop induces a reduction in contact angle on BST and a reduction in adhesion strength.

The tendency for liquid alloys to segregate one species preferentially to the surfaces and/or interfaces must be considered. To test this possibility, a post experiment quench was performed on several metal beads to freeze in the composition profile after sessile drop imaging. These samples were then embedded in epoxy, cross sectioned with a diamond saw, and polished to a $3 \mu\text{m}$ surface finish. The cross sections were imaged

using a Rutherford Backscatter electron detector in a Hitachi S-3200 SEM (Hitachi High Technologies America, Inc., Pleasanton, CA, USA) operating in a high pressure (80 Pa) environment mode. Elemental analysis is performed using energy dispersive X-ray spectroscopy (EDS) line scans by an Oxford Link PentaFET® (Oxford Instruments, Witney, Oxon, UK) across the liquid-vapor interface. A 25kV accelerating voltage was used for imaging and microanalysis.

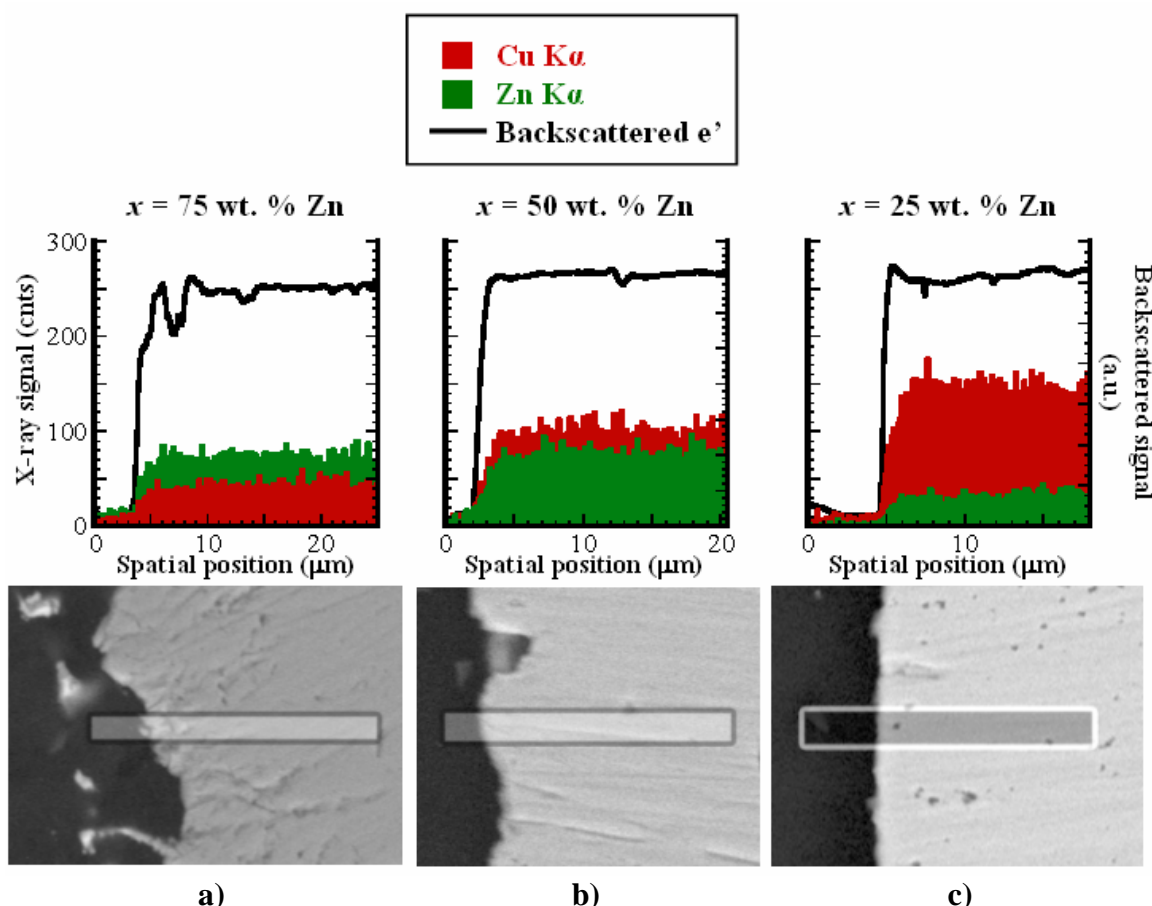


Figure 6.11: SEM backscattered electron images and EDS line scan data for three intermediate $(\text{Cu}_x, \text{Zn}_{1-x})$ alloys. a) $x = 75$ mass% Zn b) $x = 50$ mass% Zn c) $x = 25$ mass% Zn.

Shown in figure 6.11a-c are the measured signals for the backscattered electrons, $\text{K}\alpha$ Cu X-rays, and $\text{K}\alpha$ Zn X-rays along the lines shown in the corresponding backscattered electron SEM images for each Cu-Zn alloys. The spatial and composition resolution of SEM-EDS is 1 atomic % at $1 \mu\text{m}$. This analysis qualitatively shows that the

(Cu_x, Zn_{1-x}) alloys show surfaces which are 1 - 5 atomic % Zn rich within the first 2 μm compared to the bulk composition. This slight difference between the surface and bulk compositions is consistent across alloys. Even in the 25 wt. % Zn sample, the surface is still Cu rich at the surface. Also, difference in surface composition is smaller than the Δx chosen for the specific (Cu_x, Zn_{1-x}) alloys analyzed giving confidence the observed trend of increasing contact angle with increasing Zn content observed is real.

These observations suggest that the addition of Zn to Cu increase the equilibrium contact angle, thus reduce the adhesion of the BST-base metal interface. However, one final aspect of the original hypothesis remains, oxidation state of the Zn present on the commercial PLSP foils. The resident Zn on the copper foil surfaces could be oxidized and represent a ZnO interfacial layer that promotes adhesion to both Cu and the BST thin film.

6.6. ADHESION OF COPPER TO ZNO

The previous experiments establish metallic zinc at the BST/Cu interface reduces adhesion. One final aspect of this study's hypothesis remains: how ZnO influences adhesion in the BST/Cu system. This possibility is explored by sessile drop experiments with copper on three substrates: alumina, BST/Al₂O₃, and ZnO. Assuming BST/ZnO adhesion is stronger than any metal-oxide interface, the Cu-ZnO interface was characterized.

Polished single crystal ZnO oxygen polar substrates were used to measure Cu-ZnO contact angle. This set of experiments was performed at higher pO_2 conditions using 5% H₂ (balance N₂) content forming gas than the previous experiments so as to not reduce the ZnO substrate (see figure 6.4). Cu contact angle measurements on Al₂O₃ and BST/Al₂O₃ substrates were repeated at this pO_2 condition for direct comparison.

Shown in table 6.5 are the measured contact angles and W_a for copper on the three substrates measured from the corresponding images in figure 6.12a-c.

Table 6.5: Adhesion measurements of Cu on three ceramic substrates measured at 1100 °C while flowing 5%H₂ (balance N₂) forming gas.

Substrate	Contact Angle, θ (°)	W_a (J m ⁻²)
Al ₂ O ₃	133 ± 6	0.480 ± 0.142
BST/ Al ₂ O ₃	120 ± 6	0.691 ± 0.127
ZnO	62 ± 5	2.012 ± 0.097

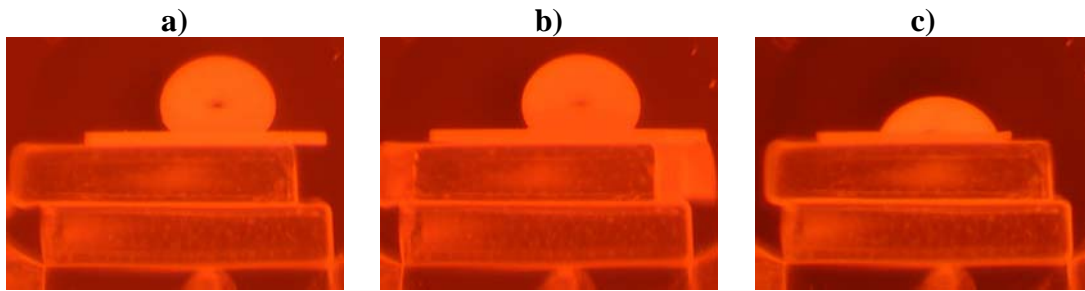


Figure 6.12: Images of molten Cu on a) Al₂O₃, b) BST/Al₂O₃, and c) ZnO. Cu-ZnO represents a wetting system where $\theta < 90^\circ$ whereas Cu-Al₂O₃ and Cu-BST are non-wetting systems ($\theta > 90^\circ$).

A pronounced shift from non-wetting behavior in Cu-Al₂O₃ and Cu-BST to a wetting behavior for Cu on ZnO was observed. In comparison, the changes in W_a are minute when comparing experiments for metallic drops on Al₂O₃ and BST described in the previous sections. The $\sim 3X$ increase of W_a^{Cu-ZnO} shows a ZnO interlayer at the BST/Cu interface increase adhesion while promoting the durability of films on commercially obtained copper foils. This mechanism is unique to Zn-treated Cu foil substrates.

6.7. SUMMARY AND CONCLUSIONS

When BST thin films are deposited on reduced surface roughness Cu foil substrates, film cracking and delamination is encountered. These issues were attributed to poor adhesion between Cu and BST. Additionally, a Zn-Cu-O surface treatment was identified by XPS on commercially obtained copper foils that allowed robust BST thin film processing. Sessile drop experiments were conducted to quantify the adhesion of

metallic Cu, Zn, and $(\text{Cu}_x, \text{Zn}_{1-x})$ to the oxide surfaces of alumina, BST thin films, and ZnO single crystals. These experiments quantify interface energy through work of adhesion. Collectively these data allow the influences of metal and oxide surface composition to be determined with regard to adhesion in the BST-base metal interface..

The key results, observations and conclusions are given below.

- The experimental setup and procedures successfully reproduced results found in the literature for Cu sessile drops on alumina substrates. Although, these experiments employed polished polycrystalline alumina substrates, opposed to single crystal sapphire, a $125^\circ \pm 4^\circ$ contact angle is measured and is within the experimental error of previously published reports. This validates the experimental procedures described in this thesis.
- Contact angle and W_a were measured for the Zn-alumina system. These data are unreported in the current literature. No definitive determination of how fundamental variables determine the work of adhesion in all elements and compounds; limiting the ability to predict adhesion in new systems. The addition of Zn-alumina data to the literature provides additional data for evaluation and/or determination of adhesion theories.
- Literature data and the results of these experiments suggest Cu-BST adhesion is within the range proven adequate for ferroelectric perovskite oxide electrodes and substrates. The work of adhesion for Cu-BaTiO₃ (or Cu-BST) is intermediary to Au-BaTiO₃ and Pd-BaTiO₃, both common electrode metals. It is unclear if the flexible foils substrates require a more durable interface. The complex inhomogeneous strains that a flexible configuration will generate compared to rigid substrate systems may require high work of adhesion in metal-oxide thin films.

- Across the Zn-Cu alloy system, and on both alumina and BST thin film substrates, increasing metallic Zn content reduces W_a . Specifically in the BST/Cu systems of which this thesis is concerned, a Zn metal surface treatment is detrimental to adhesion. If this is indeed the case, solely the larger surface roughness of the PLSP copper foils is responsible for adequate adhesion for BST thin robustness.
- Experimentally determined $W_a^{Cu-ZnO} = 2.0 \text{ mJ m}^{-2}$, a roughly 3 X increase over W_a^{Cu-BST} . The adhesion of Cu to ZnO is stronger than Pt-oxides. Pt is successfully used as electrodes and/or substrates for ferroelectric oxide devices and provides an appropriate benchmark for comparison of adhesion strength. If the surface treatments of commercially obtained copper foils do enable more robust thin film adhesion, it must be through a ZnO interlayer.

These results provide a methodology to increase interfacial durability by employing a ZnO interlayer in BST/Cu samples. This is a key insight for depositing BST thin films on copper foil substrates with reduced surface roughness. The ability to deposit BST thin films on smooth copper foils enables micron scale electrode definition by photolithography providing a methodology to adapt the Film on Foil process and synthesize impedance matched frequency agile capacitive elements in a flexible format.

7. LITHOGRAPHY-COMPATIBLE COPPER FOIL SUBSTRATES

The Film on Foil process methodology can produce high quality BST thin films directly on copper foils. This technology provides an advantage over traditional ferroelectric thin film technologies where very thick and low resistivity metallization is integrated directly with a tunable dielectric film. This presents an attractive component in a microwave circuit where finite metallization resistance imparts a substantial component of the high frequency energy loss.^{114, 245, 246} Though this embodiment incorporates an attractive complement of material properties, a substantial practical challenge remains: foil surfaces are rough, and the diffuse reflections associated with foil surface roughness dramatically limit the feature dimensions that can be generated using optical lithography.^{239, 247} This situation is particularly detrimental to microwave components in the GHz range which require very low capacitance values for 50 Ω impedance matching. Achieving these low capacitance values while using high permittivity ferroelectric films necessitates feature sizes in the μm to sub- μm range, and such resolution is not possible when substrate surfaces exhibit micron-scale RMS surface roughness values.

To overcome this limitation, a new copper substrate preparation method offering ultra smooth surfaces was developed. This substrates, termed “UltraFoil”, were proven compatible with the low oxygen pressure and high temperature process needed for $(\text{Ba}_{1-x}\text{Sr}_x)\text{TiO}_3$ (BST) preparation.^{149, 159} Using the knowledge gained through the adhesion experiments, a Zn adhesion layer was employ between the Cu substrate and the BST thin film and this Zn layer is oxidized during subsequent anneals forming a robust interface and avoid film delamination. The ultra smooth Cu/BST allows lithographic patterning and demonstration of micron-scale features.

7.1. ULTRAFoil SYNTHESIS

Thin copper foils were prepared by evaporating high purity copper onto glass slides, then subsequently peeling the Cu layer from its parent SiO_2 surface. Evaporation

was performed using a custom thermal source operated in a diffusion pumped vacuum chamber (schematically shown in figure 7.1).

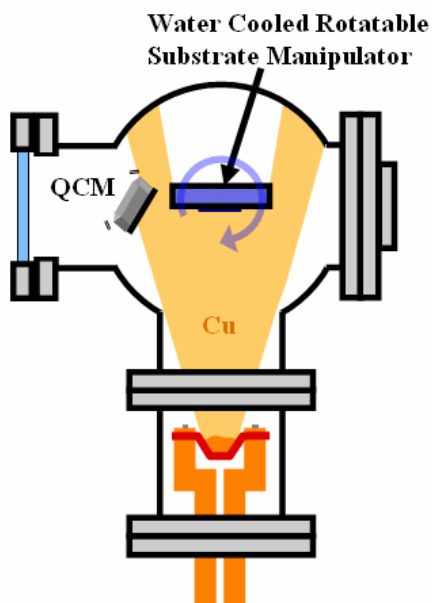


Figure 7.1: Schematic representation of the thermal evaporator system used to produce copper foils on glass slides.

The evaporator is diffusion pumped with a base pressure of $2 \cdot 10^{-8}$ Torr. Molybdenum boats were filled with copper blocks and a constant 500 watts of DC electrical power is used to heat this source and evaporate Cu. Sections of conventional copper conflat flange gaskets were used as the Cu metal source. In order to maintain a constant power, the voltage was monitored and increased to compensate for changes in boat resistance associated with source heating and exhaustion of Cu. *In situ* flux measurement, using the crystal quartz microbalance (QCM), confirmed that constant power was most effective to maintain a nearly constant deposition rate. A deposition rate of 5 nm sec^{-1} was achieved at a source-to-substrate distance of 15 cm. The X-ray diffraction pattern in figure 7.4 shows the copper to be crystalline as deposited. Four-point probe measurements of the copper layers determined the copper resistivity to be roughly $2.5 \mu\Omega \cdot \text{cm}$ in the as deposited state. Free standing Cu substrates were produced by this method from 5 to 30 μm , yet a 15 μm substrate thickness yielded the best results.

After deposition, the Cu foils were peeled from the glass substrate. A razorblade was used to lift a corner from the slide, and once initiated, the Cu removal occurred easily and without tearing or plastic deformation. The peeled-off foils exhibited minor curling, but were easily handled. Figure 7.2 shows an atomic force microscope analysis of an UltraFoil foils in comparison to a standard Oak-Mitsui PLSP ½ oz. Cu electroplated copper sheet (Oak-Mitsui, Hoosick Falls, NY).

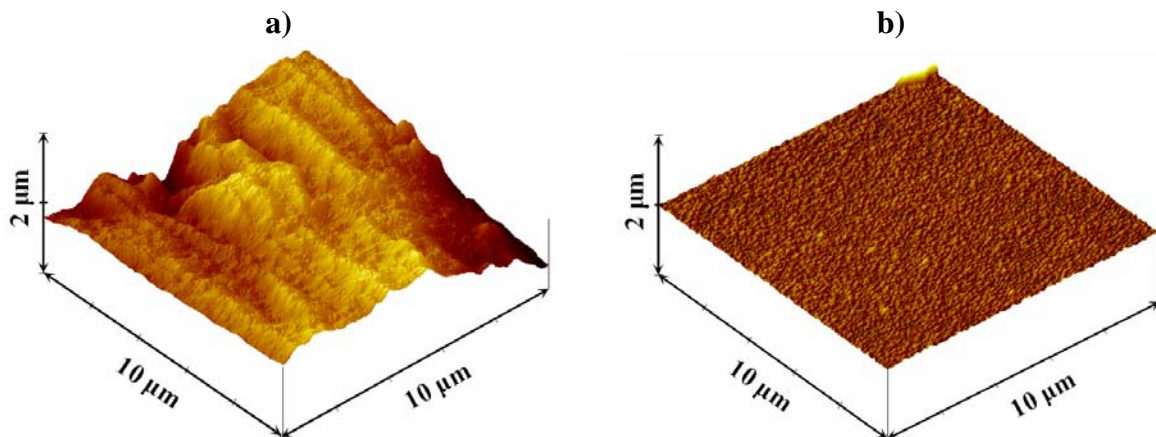


Figure 7.2: a) 10 μm X 10 μm AFM scan (rendered in 3-D) for the smooth (or shiny) side of Oak Mitsui PLSP ½ oz. Cu foil. b) 10 μm X 10 μm AFM scan (rendered in 3-D) for thermally evaporated UltraFoil. Data taken of the smooth side of the UltraFoil originally mated to the glass slide and is the intended deposition surface. Roughness values were measured at 150 nm and 9.0 nm RMS, respectively.

The RMS roughness of the ultra-foil is 1.5 nm over a 25 μm² area and 9.0 nm RMS over a 100 μm² area, while the conventional foil surface shows 25 nm and 150 nm of RMS roughness when measured over the same ranges. This represents an order of magnitude improvement in substrate surface roughness apparent macroscopically; PLSP Cu foils have a dull luster and the UltraFoil has a specular mirror-like appearance.

BST films with 75:25 barium to strontium ratio were prepared on the UltraFoil surfaces using RF magnetron sputtering. Attempts to synthesize BST thin film on virgin UltraFoil resulted in BST film delamination: the observation that was the genesis of the adhesion experiments. Prior to sputtering BST, a Zn layer was sputter deposited on the smooth side of the UltraFoil. Zn was magnetron sputtered from a 2" diameter Zn foil (99.99+% purity, Alfa Aesar, Ward Hill, MA, USA) using 1 W cm⁻² RF power and

$4 \cdot 10^{-3}$ Torr flowing Ar at 6 cm target-to-substrate distance. Zn is deposited at a rate of 45 \AA min.^{-1} by these sputtering conditions. BST thin films are deposited and annealed on the Zn coated UltraFoil using the methodology described in the Experimental Procedures Chapter 3. A range of thicknesses for the BST thin film, Zn adhesion layer, and UltraFoil substrate were explored by changing deposition times for the associated processes.

7.2. ULTRAFoil/ZN/BST THICKNESS DEPENDENCES

As established in the previous chapter, BST/Cu interfaces have moderate adhesion energy. Cursory attempts to deposit $\frac{1}{2}$ to $1 \text{ }\mu\text{m}$ thick films on virgin UltraFoil substrates resulted in delamination, film cracking, and ultimately shorted devices. Upon heat treatment, BST/Cu stacks are subjected to $900 \text{ }^\circ\text{C}$ where the difference in thermal expansion coefficients can generate considerable strain during processing. When the materials' mechanical responses are extremely unbalanced, the result is typically negative and may include cracking, plastic deformation, and or delamination. As strain energy is a volume term there is a thickness dependence to the mechanical response of the film/substrate stack, and most often, the problems are exacerbated when either or both layers become thicker.

A matrix of BST and UltraFoil thicknesses were explored to determine the optimum configuration. BST thin films were grown from 450 nm to $1.3 \text{ }\mu\text{m}$ on $10 \text{ }\mu\text{m}$ to $18 \text{ }\mu\text{m}$ thick untreated UltraFoil substrates. Films were annealed at $900 \text{ }^\circ\text{C}$ while maintaining $p\text{O}_2$ at 10^{-12} atm. Pt top electrodes were sputter deposited through a shadow mask and $C-V$ data collected at 10 kHz and 0.1V oscillation level from multiple capacitors on a singular sample. This matrix generated a large amount of data and is included in Appendix E. Results were evaluated on device yield, dielectric loss, and high field tolerance. This experiment established that a 450 nm BST film on a $15 \text{ }\mu\text{m}$ thick UltraFoil substrate generated the highest device yield, minimized film delamination, and generated the optimum dielectric properties.

Using the knowledge gained through wetting experiments, the ability of ZnO to act as an adhesion layer was explored. A $10 \text{ }\mu\text{m}$ thick UltraFoil was sectioned and metallic

Zn in a range of thickness {virgin, 10 Å, 25 Å, 50 Å, & 100 Å} was sputter deposited on the UltraFoil growth surface. A 450 nm thick BST film was simultaneously sputter deposited on all samples. The samples were then crystallized in the same furnace run. Pt top electrodes were deposited and $C-V$ data taken at 10 kHz and 1.11 kV cm^{-1} oscillation field. Figure 7.3a shows the raw $C-V$ data and figure 7.3b gives a summary of the maximum capacitance (linearly proportional to permittivity since the dielectric thickness and electrode area are constant throughout the series), 0-25V tunability, and zero bias $\tan \delta$ versus deposited Zn layer thickness.

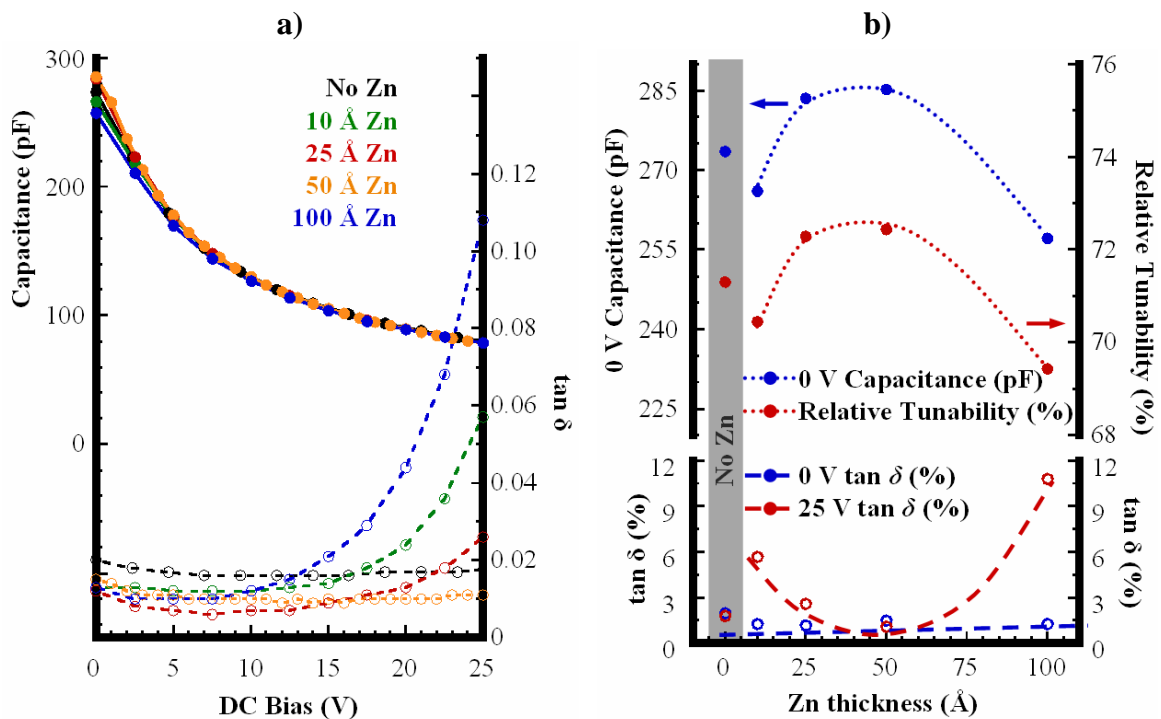


Figure 7.3: a) Room temperature $C-V$ data versus Zn adhesion layer thickness measured at 10 kHz and 1.11 kV cm^{-1} oscillator field. b) Critical parameters extracted from the raw data including maximum capacitance, tunability, dielectric loss at 0 V DC bias and dielectric loss at 25 V DC bias. Dielectric properties are maximized using 50 Å of deposited Zn as an adhesion layer.

With no Zn the maximum capacitance is 273 pF, tunability 71 %, and zero bias $\tan \delta$ 0.020 saturating to 0.18 at 25 V. With 10 Å Zn the capacitance drops slightly and the zero bias $\tan \delta$ reduces to 0.013 yet at high field the $\tan \delta$ rises significantly. The 50 Å Zn sample has the highest maximum capacitance, 285 pF, the highest tunability, 72.4%, and

the lowest $\tan \delta$ over all voltages, 0.015 at zero bias saturating to 0.011 at 25 V. As the Zn layer thickness is increased to 100 Å, the dielectric properties degrade and the sample shows high loss at high DC bias.

In the entire series, the metallic Zn adhesion layer is assumed to oxidize during the 900 °C, 10^{-12} atm pO_2 crystallization anneal as shown in the pO_2 - T phase diagram (see figure 6.2b). These data show an optimum ZnO thickness leads to the best device yield and dielectric properties. This finding is understood by considering competing processes occurring during subsequent processing.

First, metallic Zn has a substantial vapor pressure (see figure 6.2a) therefore Zn can be lost at the 130 °C sputter deposition temperature and exacerbated by the vacuum ambient. Second, ZnO is partially miscible in barium titanate. The crystallization anneal provides sufficient thermal energy to kinetically allow solution. Whether Zn^{2+} incorporates by A-site substitution²⁴⁸ or B-site substitution^{249, 250} is still under debate, yet in either case the incorporation of Zn^{2+} point defects into the BST lattice results in electro-active defects which if present in excessive concentrations, can degrade dielectric properties. If a substantially thick discrete and continuous ZnO layer still exists after deposition and anneals, the low linear permittivity of ZnO ($\epsilon_{ZnO} \sim 4.3$) can reduce the effective permittivity of the dielectric stack and mitigate tunability. Finally, XPS analysis of commercially obtained copper foils reveals only a few monolayers of Zn surface treatment and these foils show adequate adhesion while allowing excellent dielectric properties as a BST thin film substrate. Therefore, it can be assumed only a minute thickness of ZnO is needed to promote adhesion. The optimal 50 Å Zn adhesion layer results in a similarly minute volume after losses from Zn evaporation and ZnO dissolving in BST. The thin ZnO layer which survives provides sufficient interface adhesion strengthening, yet does not cause significant degradation of dielectric properties though large concentrations of Zn^{2+} point defects.

7.3. BST THIN FILM PROPERTIES ON ULTRAFoil SUBSTRATES

X-ray diffraction data for a 450 nm BST film deposited on an UltraFoil Cu substrate are shown in figure 7.4 for the BST film as-deposited and fully processed.

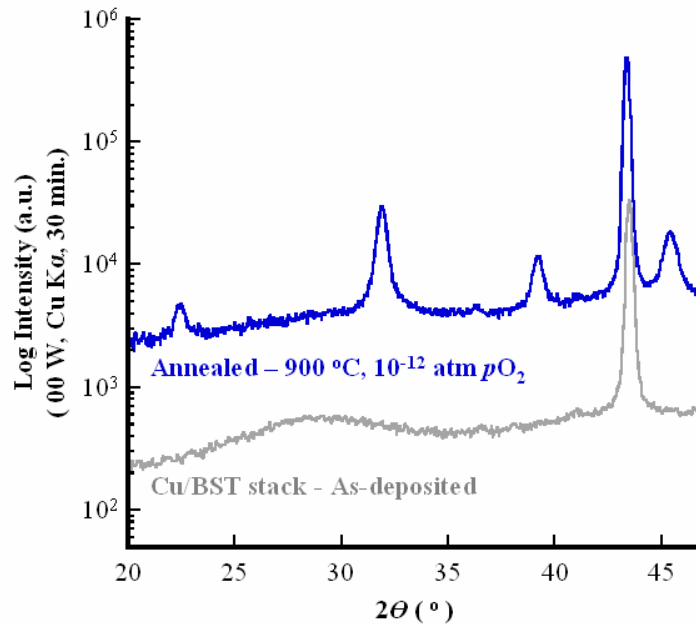


Figure 7.4: XRD θ - 2θ data for a 450 nm BST thin film as-deposited on UltraFoil Cu (gray) and the same BST/Cu stack after full processing (blue).

As-deposited, the UltraFoil substrate is crystalline and the BST film is “proto-”crystalline. The BST film is fully crystallized when annealed at 900 °C and 10^{-12} atm pO_2 . The high T anneals causes significant Cu grain growth in the UltraFoil substrate yet copper oxidation is avoided.

After annealing, Pt top electrodes were deposited through a shadow mask. The Cu/BST/Pt devices were electrically characterized using the impedance analyzer. Permittivity versus voltage curves were collected at 10 kHz and a 2.22 kV/cm oscillator field. The ϵ - E data is shown in Fig. 7.5.

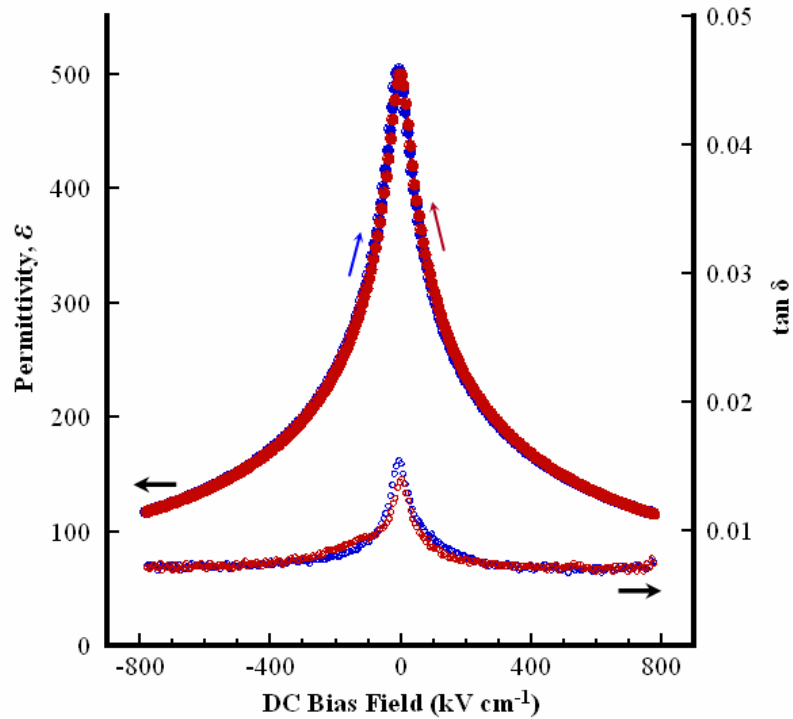


Figure 7.5: Dielectric constant versus DC electric field data for an MIM dot capacitor with Pt top electrode taken at room temperature. The oscillator voltage was 2.22 kV/cm RMS, and the measurement frequency was 10 kHz. This film was 450 nm in thickness, thus the maximum field applied was approximately 750 kV cm⁻¹.

A tunability of 5:1 and loss tangents below 1% at fields in excess of 750 kV cm⁻¹ are observed. This tunability is afforded by the ability to apply large DC biases without causing dielectric breakdown. The UltraFoil reduced surface roughness minimizes field concentrating interface asperities typically responsible for premature breakdown. Therefore, fields can be applied further approaching saturation resulting in greater apparent tunability. Figure 7.6 gives the frequency dependence between 100 and 10,000 Hz measured at 0 V DC bias and a 1.11 kV cm⁻¹ oscillator field.

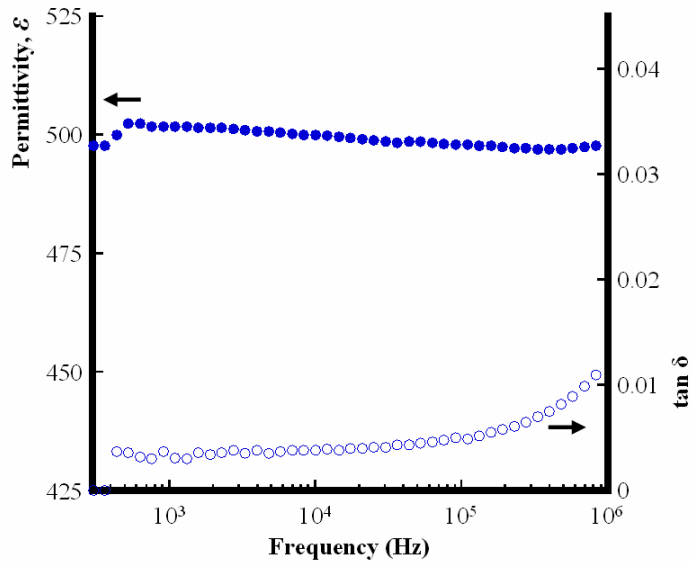


Figure 7.6: Permittivity frequency dispersion measurements for the same sample in figure 7.5. Note that the increase in loss above 10 kHz corresponds to the onset of capacitor resonance, not an increase in the material's loss tangent.

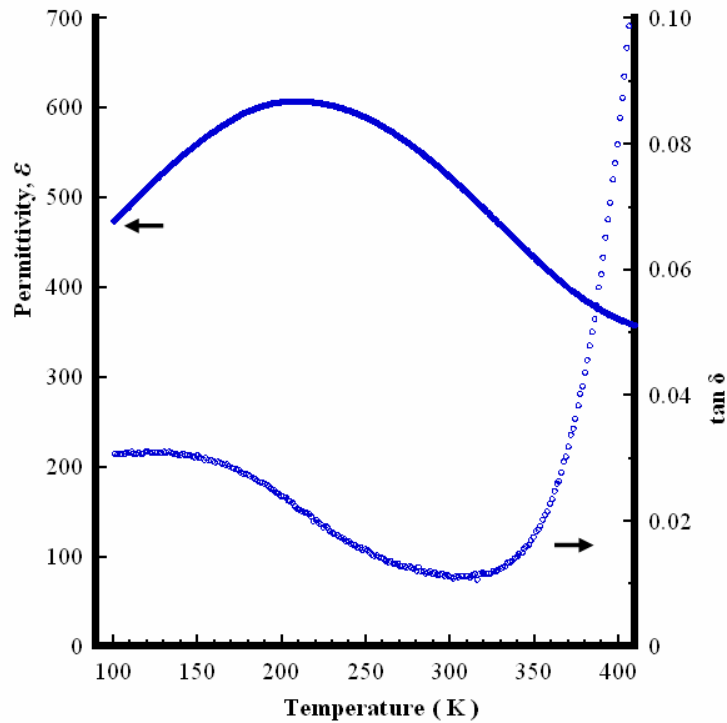


Figure 7.7: Permittivity temperature response for a fully processed 700 nm BST thin film deposited on an UltraFoil Cu substrate. The broad temperature profile allows > 3:1 tunability by 30 V applied over the entire temperature range.

No significant frequency dispersion is observed. The temperature dependence of a 700 nm thick film is shown in Fig. 7.7. The diffuse nature of the ferroelectric transition provides for substantial tuning well above the dielectric maximum, and tuning in the absence of hysteresis well below the dielectric maximum. The relative tunability as a function of temperature for 30 V applied over the same temperature range was measured and is similar to the observation of tunability versus temperature on PLSP ½ oz. Cu foil. Greater than 1½:1 tunability is sustained 150 °C away from the temperature at maximum permittivity.

These values are comparable to several of the finest literature examples of thin film BST^{96, 100, 104, 251, 252}, however, in this case, the substrate is a simple copper foil. These results prove an unadapted Film on Foil process can deposit BST thin films on UltraFoil substrates without adversely impacting device properties. A ZnO adhesion layer is employed to resolve film delamination issues that arose from using a smoother deposition surface. Although permittivity is slightly reduced in the presence of the thin ZnO low permittivity adhesion layer, the extrinsic contribution to BST permittivity is unaffected by the use of an UltraFoil substrate resulting in identical tunability as BST films on commercially obtained Cu foils. The smooth BST/Cu interface provides higher field tolerance and lower dielectric loss ultimately allowing realization of higher tunability.

7.4. PHOTOLITHOGRAPHIC PATTERNING & DEVICE DEFINITION

The motivation of this work lies in the application of these Cu-dielectric stacks in microwave circuit elements. As previously discussed, the electrode dimensions customary in microwave devices are in the range of microns necessitating lithographic patterning. Fully processed BST coated UltraFoil were evaluated for this purpose.

The BST/UltraFoil stacks were first laminated to a silicon carrier substrate using a room temperature curing epoxy designed for Cu bonding (Copper-Bond®, The Noble Co., Grand Haven, MI). The bonding process was conducted by sandwiching the Cu foil

between the silicon carrier and a glass slide between the jaws of a precision vice shown schematically in figure 7.8.

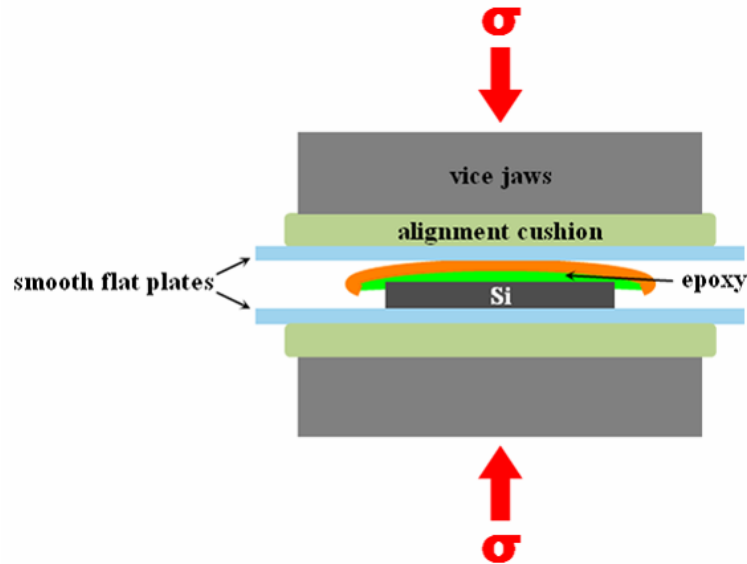


Figure 7.8: Schematic representation of the vice used to laminate BST/UltraFoil Cu specimens to Si wafer carriers.

The epoxy was applied between the exposed Cu side of the UltraFoil and the silicon carrier which was slightly smaller in lateral dimensions than the foil sample to avoid extrusion of the epoxy onto the critical BST surface during lamination. Microscope slides mated the silicon and BST surface to achieve flat smooth surfaces. Paper sheets were used as alignment cushions to compensate for any slight misalignments and homogenize the applied stress. After this process, the foils maintained their mirror-like finish, and were free from wrinkles.

The bonded foil surfaces were subsequently coated with a bilayer photoresist consisting of Microchem LOR 5A lift-off resist (Newton, MA) and Shipley 1813 imaging resist (Marlborough, MA), into which interdigitated electrodes (IDE) were imaged by contact lithography. Pt electrodes, 1000 Å thick, were DC magnetron sputter deposited, and a lift-off procedure was conducted to develop the pattern.

Figure 7.9 shows the result of this procedure. As evident in the image, interdigitated fingers with 10 μm width and 4 μm spacing are patterned with ease.

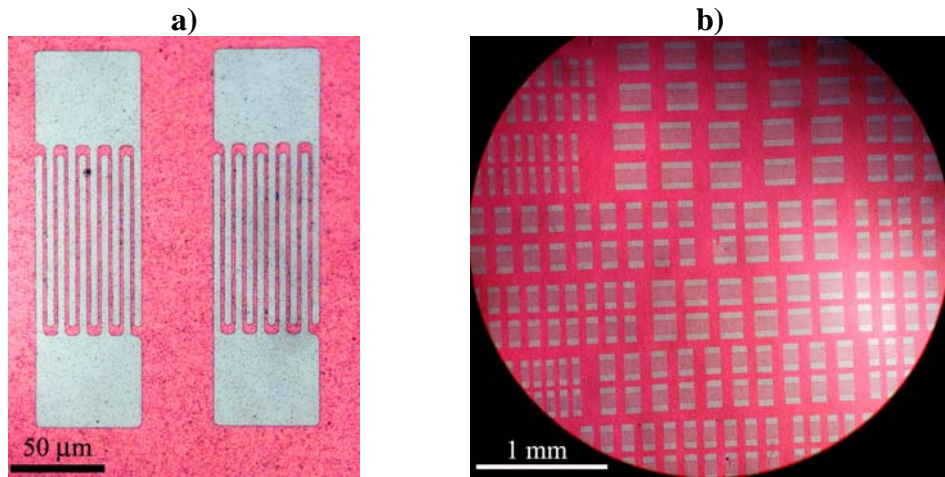


Figure 7.9: a) Optical micrograph of an interdigitated Pt electrode patterned by contact lithography and lift-off. 4 μm gaps and features are demonstrated. Prior to lithographic patterning, the foil-BST capacitor stack was laminated onto a silicon wafer. B) Large area optical micrograph of IDC Pt electrodes defined by photolithography. Few pattern transfer flaws are seen over a large area although the BST/Cu stack was processed outside of the cleanroom environment.

Due to the presence of the thin dielectric and a conducting substrate these electrodes do not allow the device to function as a planar IDE capacitor. Alternatively, probing the IDE pads results in an electrical response of two MIM capacitors with an area equivalent to the defined Pt pattern connected in series by the substrate Cu. The specific photo mask was chosen for the challenging geometry and evaluation of the lithographic patternability in the feature sizes of interest. These dimensions are consistent with GHz range microwave structures, thereby validating the utility of UltraFoil copper substrates.

C - V measurements were performed on the photolithographically defined Pt IDE electrodes to explore if the lamination and lithography process adversely affected the properties of the BST/Cu stack. C - V data is shown in figure 7.10.

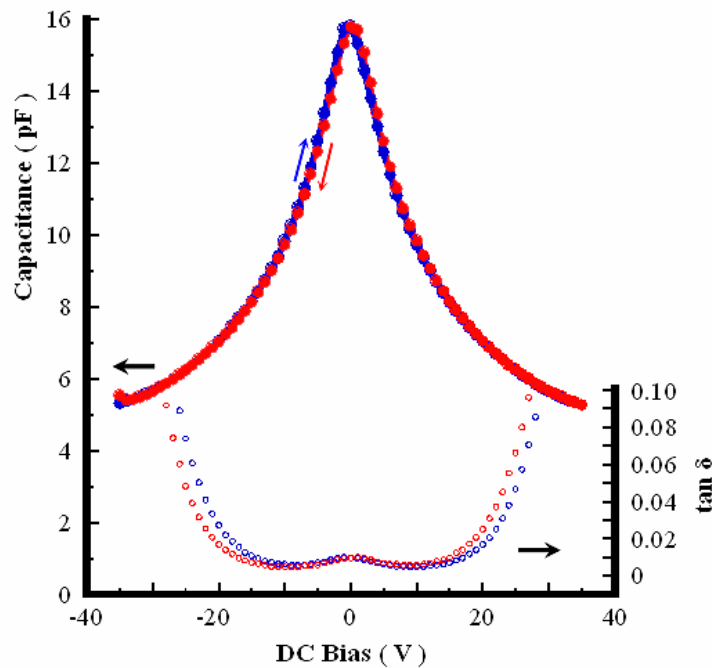


Figure 7.10: Room temperature C - V data of IDE structures. These data show an electrical MIM response due to the existence of the high conductivity Cu substrate.

Lamination imparts considerable strain on the brittle BST film yet no device shorting was observed in the IDE structures. The lithography process involves PR bakes approaching 190 °C and exposure to aggressive alkaline solutions and alcohol solvents. Dielectric measurements after these processes show degradation of the high field tolerance yet > 3:1 tunability is still apparent. Further experimentation into adapted lithography processes is expected to allow pattern transfer without adversely affecting dielectric properties.

These experiments establish that capacitance values on the order of several pF can be realized in a ferroelectric thin film format while using thick, high conductivity metal foil substrates. This allows the application of high DC bias fields with modest voltages to achieve large tunabilities while meeting the microwave circuit requirement of high quality factor, impedance matched devices.

7.5. CONCLUSION

A technique for preparing ultra-smooth copper foil substrates by evaporation onto a glass slide carrier and subsequent peel-off was demonstrated. BST deposition by RF magnetron sputtering, and crystallization at high temperatures in a reduced pO_2 environment were also shown. The ultra-smooth foil / BST stack exhibited electrical properties, including voltage tolerance, consistent with several literature examples of well-prepared BST. Tunabilities of 5:1, and high field loss tangent values below 1% were observed. Finally, foil lamination and lithographic patterning were demonstrated on these BST/Cu stacks, and the possibility of defining fine structures suitable for high frequency microwave devices was validated.

There are several issues regarding application of film-on-foil capacitors in microwave circuits, several of these have been addressed in this work and are noted below:

- Ferroelectric thin film MIM devices are fabricated on thick, high conductivity foils. This embodiment allows realization of 5:1 tunability using moderate voltages while avoiding degradation of device quality factor at high frequencies due the electrode series resistance.
- A Process was developed to make smooth Cu foils by thermal evaporation. With respect to commercial foil substrates, the evaporated foils offer an order of magnitude reduction in surface roughness.
- ZnO adhesion layers allowed promoted adhesion between BST and smooth copper without negatively impacting dielectric properties.
- Reduced surface roughness Cu foils allow electrode definition by photolithographic techniques with micron scale features.

8. CONCLUSIONS AND FUTURE WORK

The studies contained in this thesis address materials engineering issues associated with areas of practical concern for the use of BST thin films for microwave tunable dielectric in MIM varactors. The applicability of this technology was addressed and technological hurdles that may potentially limit the commercial viability were identified. The accomplishments are associated with both technical improvements, and economic considerations. This manuscript presents a commercially viable processing methodology for sputter deposition of BST thin films on thick, high conductivity Cu foil substrates. Post deposition controlled atmosphere heat treatments produce a dense dielectric while preserving the metallic substrate. Studies show device properties appropriate for frequency agile circuits. Technological barriers of TCC, thin film adhesion, and micron scale device definition are addressed in experiments which lead to material solutions that overcome these hurdles.

8.1. CONCLUSIONS

A sputter deposition process was developed to synthesize BST thin films on Cu foil substrates. Stoichiometric targets were used in low temperature depositions in an off-axis configuration to produce 300 nm to $> 1 \mu\text{m}$ thick films. The equipment utilized is consistent with large scale production. Post deposition controlled atmosphere heat treatments transformed as-deposited films to a dense dielectric while avoiding oxidation of the metallic substrate. The fully processed BST/Cu specimens exhibit high dielectric tunability, $> 3:1$ with a 700 maximum room temperature permittivity, and low dielectric loss, zero bias $\tan \delta = 0.02$ saturating to $\tan \delta = 0.003$ at high fields. Dielectric properties are demonstrated on a thick, low resistivity metal substrate. Collectively, these features can lead to high quality factor tunable varactors suitable for the microwave regime.

A processing study was performed to identify structure-process-property relationships in the BST/Cu system. The ability to grow BST thin films over a range of

thicknesses while maintaining a 55 - 80 nm equiaxial grain size was demonstrated. Temperature dependent dielectric properties were explored as a function of BST composition. The thickness independent microstructure allowed selection film thickness and BST composition without changing the permittivity temperature profile broadness allowing demonstration of large tunabilities even when T_C is 100 °C from room temperature. This was the first study of its kind.

A multi-composition stacked film concept was presented which can lead to a reduce temperature dependence of permittivity. The temperature profile of multiple compositions of discrete thin film layers of BST in parallel and series connectivity were simulated through appropriate mathematical models. Simulations showed that single composition BST/Cu specimens can achieve X7R performance and parallel connected multi-composition film stacks can create an effectively temperature independent response over several hundred degrees Centigrade.

BST-Cu adhesion was studied through sessile drop wetting experiments. The BST-Cu work of adhesion, $W_a^{Cu-BST} = 0.554 \pm 0.164 \text{ J m}^{-2}$, is comparable to adhesion energies between electro-ceramics and noble metals. XPS characterization identified Zn surface treatments on commercially obtained Cu foils. Wetting between BST and the Cu-Zn system was investigated. In doing so, Zn metal was shown to reduce adhesion, while ZnO was identified as an excellent adhesion a layer as $W_a^{Cu-ZnO} = 2.012 \pm 0.097 \text{ J m}^{-2}$.

A reduced surface roughness Cu foil substrate was synthesized by thermal evaporation. BST thin films were processed on these UltraFoil substrates allowing stability against higher DC bias and greater tunability. Fully processed BST thin film deposited on UltraFoil substrates were used to demonstrate photolithographic electrode definition with 4 μm resolution.

The process methodology and demonstrations contained in this work provide significant advancements towards realizing ferroelectric thin film devices for wide scale commercial proliferation. Research efforts similar to this work have only surfaced in the last decade and previous research efforts confined ferroelectric thin film use to high cost

niche applications. To compete with and potentially replace the bulk processed and semiconductor devices currently utilized in frequency-agile circuits, further studies similar to this thesis must be undertaken. The results presented in this manuscript provide material solutions to some major technological barriers for practical use, but many challenges, already apparent and still unforeseen, still need to be overcome.

8.2. FUTURE WORK

As in any major effort, the process of solving problems reveals further questions. The ideas presented in this thesis provide material solutions that are expected to have straightforward implementation into actual devices. If this indeed the case is only provide by demonstration in actual circuits.

BST/Cu MIM structures were electrically characterized using an impedance analyzer appropriate for measurements < 10 MHz. Using UltraFoil substrates, photolithographic device definition, and a high frequency network analyzer, measurements should be extended to the microwave region. This would require defining electrode features with appropriate pitch for connection to a high frequency network analyzer. High frequency reflection coefficients, s_{11} and s_{12} , can be determined for pairs of MIM devices electrically connected in series through the substrate Cu. Devices synthesis will require micron scale top electrode definition to satisfy impedance matching requirements.

The multi-composition stack film concept is only a mathematical proof and needs experimental verification. Specimens can be created using a sequence of depositions of predetermined BST compositions and thicknesses, and temperature profiles can be measured and compared against simulation predictions. Additionally, planar IDE devices provide a significant component of applied electric field parallel to stacked films. An IDE configuration can be used as a vehicle to assess if parallel connectivity can create a flat capacitance temperature response over a wide temperature range.

In the composition series, lattice parameter and T_C measurement determinations showed an increasing deviation from expected bulk BST values. This observation is

supported by the work of other researcher, but no satisfactory explanation has been unambiguously proven. Continuation of the experiments begun in this work can provide data using a novel material set and processing scheme that can be compared against the established results. The origin of observed effects is only elucidated by characterization elemental composition and microstructure.

Finally, attempts were made to integrate BST/Cu MIM structures in a QorTek designed synthetic aperture, SAR, RADAR array.^{230, 253, 254} This effort stalled when trying to electrically connect BST/Cu onto the insertion points on the PWB array. Wirebonding proved unsuccessful and crude epoxy connections did not allow accurate placement. To successfully demonstrate a frequency-agile SAR RADAR device, large area BST/Cu samples should be laminated onto an appropriate polymer substrate and the design's electrodes defined using modern integration schemes.

9. BIBLIOGRAPHY

- 1 nGimat. "Dielectrics & Conductors." (October 1, 2006)
<<http://www.ngimat.com/electronics/dielectrics.html>>.
- 2 Agile Materials & Technologies Inc. "'Tune In' to the Technology Leader in
Tunable Wireless Components." (October 1, 2006)
<<http://www.agilematerials.com/>>.
- 3 Robert E. Newnham, "Properties of Materials: Anisotropy, Symmetry, Structure."
New York: Oxford Univ. Press. (2005).
- 4 E. J. Murphy and S. O. Morgan, "The Dielectric Properties of Insulating
Materials," *Bell system Technical Journal*, 17 640-669.(1938).
- 5 Jack C. Burfoot and George W. Taylor, "Polar dielectrics and their applications ".
Los Angeles, CA: University of California Press. (1979).
- 6 Franco Jona and G. Shirane, "Ferroelectric Crystals,"1st ed. In *International Series
of Monographs on Solid State Physics*, Vol. 1 Edited by R. Smoluchowski and N.
Kurti. New York: Pergamon Press Inc. (1962).
- 7 Sidney B. Lang, "Sourcebook of pyroelectricity," In *Ferroelectric and related
phenomena*, Vol. 2 Edited by G. A. Smolenskii. New York: Gordon and Breach
Science Publishers. (1974).
- 8 Bernard Jaffe, William R. Cook and Hans Jaffe, "Piezoelectric Ceramics," In *Non-
Metallic Solids: A series of monographs*, Vol. 3 Edited by J. P. Roberts and P.
Popper. New York: Academic Press. (1971).
- 9 J. Valasek, "Piezo-Electric and Allied Phenomena in Rochelle Salt," *Physical
Review*, 17[4] 475.(1921).
- 10 W. Mandell, "Change in elastic properties on replacing the potassium atom of
rochelle salt by the ammonium group," *Proceedings of the Royal Society of
London*, 121 122-130.(1928).
- 11 W. J. Merz, "Lithium ammonium tartrate monohydrate, a new ferroelectric
crystal," *Physical Review*, 82 562.(1951).
- 12 B. T. Matthias and J. K. Hulm, "New ferroelectric tartrates," *Physical Review*, 82
108-109.(1951).

- 13 G. Busch and P. Scherrer, "Eine neue seignette-elektrische Substanz," *Naturwissenschaften*, 23[43] 737-737.(1935).
- 14 G. Busch, "New 'Rochelle-electrics'," *Helvetica Physica Acta*, 11[4] 269-298.(1938).
- 15 H. Thurnauer, *The Rochester Engineer*, 21 74-75, 77.(1942).
- 16 H. Thurnauer and J. Deaderick, U.S. Patent No. 2,429,588 (October 21, 1941).
- 17 E. Wainer and A. N. Salomon. Electrical Report No. 8 Titanium Alloy Mfg. Co. (1942).
- 18 E. Wainer and A. N. Salomon. Electrical Report No. 9 Titanium Alloy Mfg. Co. (1943).
- 19 E. Wainer, "High titania dielectrics," *Transactions of the Electrochemical Society*, 89 331-356.(1946).
- 20 B. M. Wul and I. M. Goldman, "Dielectric hysteresis in barium titanate," *Academie des Sciences de l'URSS -- Comptes Rendus*, 51[1] 21-23.(1946).
- 21 P. R. Coursey and K. C. Brand, "Dielectric constants of some titanates," *Nature*, 157 297-298.(1946).
- 22 S. Miyake and R. Ueda, "On polymorphic change of BaTiO₃," *Journal of the Physical Society of Japan*, 1 32-33.(1946).
- 23 A. Von Hippel, R. G. Breckenridge, F. G. Chesley and L. Tisza, "High dielectric constant ceramics," *Industrial and Engineering Chemistry*, 38 1097-1109.(1946).
- 24 G. Shirane and D. A. Takeda, "Phase transitions in solid solutions of PbZrO₃ and PbTiO₃. I. Small concentrations of PbTiO₃," *Journal of the Physical Society of Japan*, 7 5-11.(1952).
- 25 B. Jaffe, R. S. Roth and S. Marzullo, "Piezoelectric properties of lead zirconate-lead titanate solid-solution ceramics," *Journal of Applied Physics*, 25 809-810.(1954).
- 26 V. M. Goldschmidt, "Construction of crystals," *Zeitschrift fur Technische Physik*, 8[7] 251-264.(1927).
- 27 R. D. Shannon, "Revised Effective Ionic-Radii and Systematic Studies of Interatomic Distances in Halides and Chalcogenides," *Acta Crystallographica Section A*, 32[SEP1] 751-767.(1976).

- 28 R. D. Shannon and C. T. Prewitt, "Effective Ionic Radii in Oxides and Fluorides," *Acta Crystallographica Section B-Structural Crystallography and Crystal Chemistry*, B 25 925-&.(1969).
- 29 S. V. Halilov, M. Fornari and D. J. Singh, "Lattice instabilities and ferroelectricity in AScO₃ perovskite alloys," *Physical Review B*, 69[17].(2004).
- 30 R. E. Cohen, "Origin of Ferroelectricity in Perovskite Oxides," *Nature*, 358[6382] 136-138.(1992).
- 31 R. E. Cohen and H. Krakauer, "Lattice-Dynamics and Origin of Ferroelectricity in BaTiO₃ - Linearized-Augmented-Plane-Wave Total-Energy Calculations," *Physical Review B*, 42[10] 6416-6423.(1990).
- 32 W. Zhong, D. Vanderbilt and K. M. Rabe, "First-Principles Theory of Ferroelectric Phase-Transitions for Perovskites - the Case of BaTiO₃," *Physical Review B*, 52[9] 6301-6312.(1995).
- 33 W. Zhong, D. Vanderbilt and K. M. Rabe, "Phase-Transitions in BaTiO₃ from First Principles," *Physical Review Letters*, 73[13] 1861-1864.(1994).
- 34 A. D. Hilton and B. W. Ricketts, "Dielectric properties of Ba_{1-x}Sr_xTiO₃ ceramics," *Journal of Physics D-Applied Physics*, 29[5] 1321-1325.(1996).
- 35 N. A. Pertsev, A. G. Zembilgotov, S. Hoffmann, R. Waser and A. K. Tagantsev, "Ferroelectric thin films grown on tensile substrates: Renormalization of the Curie-Weiss law and apparent absence of ferroelectricity," *Journal of Applied Physics*, 85[3] 1698-1701.(1999).
- 36 A. F. Devonshire, "Theory of Ferroelectrics," *Advances in Physics*, 3[10] 85-130.(1954).
- 37 R. Landauer, D. R. Young and M. E. Drougard, "Polarization Reversal in the Barium Titanate Hysteresis Loop," *Journal of Applied Physics*, 27[7] 752-758.(1956).
- 38 A. K. Tagantsev, V. O. Sherman, K. F. Astafiev, J. Venkatesh and N. Setter, "Ferroelectric materials for microwave tunable applications," *Journal of Electroceramics*, 11[1-2] 5-66.(2003).
- 39 V. L. Gurevich and A. K. Tagantsev, "Intrinsic Dielectric Loss in Crystals," *Advances in Physics*, 40[6] 719-767.(1991).

- 40 X. X. Xi, H. C. Li, W. D. Si, A. A. Sirenko, I. A. Akimov, J. R. Fox, A. M. Clark and J. H. Hao, "Oxide thin films for tunable microwave devices," *Journal of Electroceramics*, 4[2-3] 393-405.(2000).
- 41 M. J. Lancaster, J. Powell and A. Porch, "Thin-film ferroelectric microwave devices," *Superconductor Science & Technology*, 11[11] 1323-1334.(1998).
- 42 I. M. Buzin, "Dielectric Losses of Strontium Titanate at Vhf," *Vestnik Moskovskogo Universiteta Seriya 3 Fizika Astronomiya*, 18[6] 70-76.(1977).
- 43 L. C. Sengupta, S. Stowell, E. Ngo, M. E. Oday and R. Lancto, "Barium strontium titanate and non-ferroelectric oxide ceramic composites for use in phased array antennas," *Integrated Ferroelectrics*, 8[1-2] 77-88.(1995).
- 44 Takaaki Tsurumi, Takashi Teranishi, Takakiyo Harigai, Hirofumi Kakemoto, Satoshi Wada, Masafumi Nakada and Jun Akedo, "Ultra Wide Band Dielectric Spectroscopy of Perovskite Dielectrics," in *Proceedings of the International Symposium on the Applications of Ferroelectrics*. Edited by D. P. Cann. Sunset Beach, NC, USA, (2006).
- 45 J. P. Remeika, "A Method for Growing Barium Titanate Single Crystals," *Journal of the American Chemical Society*, 76[3] 940-941.(1954).
- 46 W. J. Merz, "Double Hysteresis Loop of BaTiO₃ at the Curie Point," *Physical Review*, 91[3] 513-517.(1953).
- 47 H. H. Wieder, "Ferroelectric Hysteresis in Barium Titanate Single Crystals," *Journal of Applied Physics*, 26[12] 1479-1482.(1955).
- 48 W. J. Merz, "The Electric and Optical Behavior of BaTiO₃ Single-Domain Crystals," *Physical Review*, 76[8] 1221-1225.(1949).
- 49 W. J. Merz, "The Dielectric Behavior of BaTiO₃ Single-Domain Crystals," *Physical Review*, 75[4] 687-687.(1949).
- 50 B. Jaffe, R. S. Roth and S. Marzullo, "Piezoelectric Properties of Lead Zirconate-Lead Titanate Solid-Solution Ceramics," *Journal of Applied Physics*, 25[6] 809-810.(1954).
- 51 D. Damjanovic, "Ferroelectric, dielectric and piezoelectric properties of ferroelectric thin films and ceramics," *Reports on Progress in Physics*, 61[9] 1267-1324.(1998).

- 52 D. Berlincourt, B. Jaffe, H. Jaffe and H. H. A. Krueger, "Transducer properties of lead titanate zirconate ceramics," *IRE -- National Convention Record*, 7[Part 6] 227-240.(1959).
- 53 G. Arlt, D. Hennings and G. Dewith, "Dielectric-Properties of Fine-Grained Barium-Titanate Ceramics," *Journal of Applied Physics*, 58[4] 1619-1625.(1985).
- 54 S. Roberts, "Dielectric Constant of Barium Titanate at High Temperatures," *Physical Review*, 75[6] 989-990.(1949).
- 55 M. E. Drougard and D. R. Young, "Dielectric Constant Behavior of Single-Domain, Single Crystals of Barium Titanate in the Vicinity of the Curie Point," *Physical Review*, 95[5] 1152-1153.(1954).
- 56 A. Linz, "Some Electrical Properties of Strontium Titanate," *Physical Review*, 91[3] 753-754.(1953).
- 57 J. K. Hulm, "The Dielectric Properties of Some Alkaline Earth Titanates at Low Temperatures," *Proceedings of the Physical Society of London Section A*, 63[370] 1184-1185.(1950).
- 58 G. A. Smolenskii, "Novye Segnetoelektriki," *Doklady Akademii Nauk Sssr*, 70[3] 405-408.(1950).
- 59 G. A. Smolenskii, "*Segnetoelektricheskie Svoistva Nekotorykh Titanatov I Tsirkonatov Dvukhvalentnykh Metallov, Imeyushchikh Strukturu Tipa Perovskita," *Zhurnal Tekhnicheskoi Fiziki*, 20[2] 137-148.(1950).
- 60 J. H. Haeni, P. Irvin, W. Chang, R. Uecker, P. Reiche, Y. L. Li, S. Choudhury, W. Tian, M. E. Hawley, B. Craigo, A. K. Tagantsev, X. Q. Pan, S. K. Streiffer, L. Q. Chen, S. W. Kirchoefer, J. Levy and D. G. Schlom, "Room-temperature ferroelectricity in strained SrTiO₃," *Nature*, 430[7001] 758-761.(2004).
- 61 H. E. Weaver, "Dielectric Properties of Single Crystals of SrTiO₃ at Low Temperatures," *Journal of Physics and Chemistry of Solids*, 11[3-4] 274-&.(1959).
- 62 J. A. Basmajian and R. C. Devries, "Phase Equilibria in the System BaTiO₃-SrTiO₃," *Journal of the American Ceramic Society*, 40[11] 373-376.(1957).
- 63 M. McQuarrie, "Structural Behavior in the System (Ba,Ca,Sr) TiO₃ and Its Relation to Certain Dielectric Characteristics," *Journal of the American Ceramic Society*, 38[12] 444-449.(1955).
- 64 W. Jackson and W. Reddish, "High Permittivity Crystalline Aggregates," *Nature*, 156[3972] 717-717.(1945).

- 65 G. A. Smolenskii and K. I. Rozgachev, "*Segnetoelektricheskie Svoistva Tverdykh Rastvorov V Sisteme Titanat Bariya Titanat Strontsiya," *Zhurnal Tekhnicheskoi Fiziki*, 24[10] 1751-1760.(1954).
- 66 S. Kisaka, S. Ikegami and H. Sasaki, "Dielectric Properties of Mixed Crystals of Barium-Strontium Titanate," *Journal of the Physical Society of Japan*, 14[12] 1680-1685.(1959).
- 67 W. J. Merz, "The Effect of Hydrostatic Pressure on the Curie Point of Barium Titanate Single Crystals," *Physical Review*, 78[1] 52-54.(1950).
- 68 D. F. Rushman and M. A. Strivens, "The permittivity of polycrystals of the perovskite type [with discussion]," *Transactions of the Faraday Society*, 42 A 231.(1946).
- 69 D. Hennings and G. Rosenstein, "Temperature-Stable Dielectrics Based on Chemically Inhomogeneous BaTiO₃," *Journal of the American Ceramic Society*, 67[4] 249-254.(1984).
- 70 H. Saito, H. Chazono, H. Kishi and N. Yamaoka, "X7R Multilayer Ceramic Capacitors with Nickel Electrodes," *Japanese Journal of Applied Physics Part 1- Regular Papers Short Notes & Review Papers*, 30[9B] 2307-2310.(1991).
- 71 AVX Corporation. "AVX Surface Mount Ceramic Capacitor Products ver. 6.1." (September 29, 2006) <<http://www.avxcorp.com/docs/masterpubs/smccp.pdf>>.
- 72 V. P. Dudkevich, V. M. Mukhortov, Y. I. Golovko, V. A. Bukreev, V. M. Mukhortov, Y. G. Sineev and E. G. Fesenko, "On Dielectric Property Dependence of Condensed BaTiO₃ Films on Coherent Scattering Region Sizes," *Fizika Tverdogo Tela*, 23[2] 612-614.(1981).
- 73 H. Ikawa, "Dependent Behavior for Perovskite Ferroelectrics," *Ceramic Transactions*, 32 19-28.(1993).
- 74 J. Junquera and P. Ghosez, "Critical thickness for ferroelectricity in perovskite ultrathin films," *Nature*, 422[6931] 506-509.(2003).
- 75 K. Ishikawa, K. Yoshikawa and N. Okada, "Size Effect on the Ferroelectric Phase-Transition in PbTiO₃ Ultrafine Particles," *Physical Review B*, 37[10] 5852-5855.(1988).
- 76 W. L. Zhong, Y. G. Wang, P. L. Zhang and B. D. Qu, "Phenomenological Study of the Size Effect on Phase-Transitions in Ferroelectric Particles," *Physical Review B*, 50[2] 698-703.(1994).

- 77 D. D. Fong, G. B. Stephenson, S. K. Streiffer, J. A. Eastman, O. Auciello, P. H. Fuoss and C. Thompson, "Ferroelectricity in ultrathin perovskite films," *Science*, 304[5677] 1650-1653.(2004).
- 78 D. D. Fong, A. M. Kolpak, J. A. Eastman, S. K. Streiffer, P. H. Fuoss, G. B. Stephenson, C. Thompson, D. M. Kim, K. J. Choi, C. B. Eom, I. Grinberg and A. M. Rappe, "Stabilization of monodomain polarization in ultrathin PbTiO₃ films," *Physical Review Letters*, 96[12].(2006).
- 79 W. R. Buessem, L. E. Cross and A. K. Goswami, "Phenomenological Theory of High Permittivity in Fine-Grained Barium Titanate," *Journal of the American Ceramic Society*, 49[1] 33-&.(1966).
- 80 K. Kinoshita and A. Yamaji, "Grain-Size Effects on Dielectric Properties in Barium-Titanate Ceramics," *Journal of Applied Physics*, 47[1] 371-373.(1976).
- 81 M. H. Frey, Z. Xu, P. Han and D. A. Payne, "The role of interfaces on an apparent grain size effect on the dielectric properties for ferroelectric barium titanate ceramics," *Ferroelectrics*, 206[1-4] 337-353.(1998).
- 82 D. McCauley, R. E. Newnham and C. A. Randall, "Intrinsic size effects in a barium titanate glass-ceramic," *Journal of the American Ceramic Society*, 81[4] 979-987.(1998).
- 83 K. Uchino, E. Sadanaga and T. Hirose, "Dependence of the Crystal-Structure on Particle-Size in Barium-Titanate," *Journal of the American Ceramic Society*, 72[8] 1555-1558.(1989).
- 84 C. B. Parker, J. P. Maria and A. I. Kingon, "Temperature and thickness dependent permittivity of (Ba,Sr)TiO₃ thin films," *Applied Physics Letters*, 81[2] 340-342.(2002).
- 85 Charles Bernard Parker, "Size effects and reliability of (Ba,Sr)TiO₃ thin films," Ph.D. dissertation. (Advisor: Prof. A.I. Kingon) Raleigh, NC: North Carolina State University. (2002).
- 86 M. Tanaka and Y. Makino, "Finite size effects in submicron barium titanate particles," *Ferroelectrics Letters Section*, 24[1-2] 13-23.(1998).
- 87 K. Binder and P. C. Hohenberg, "Phase-Transitions and Static Spin Correlations in Ising Models with Free Surfaces," *Physical Review B*, 6[9] 3461-&.(1972).
- 88 E. Ising, "Report on the theory of ferromagnetism," *Zeitschrift Fur Physik*, 31 253-258.(1925).

- 89 J. F. Scott, H. M. Duiker, P. D. Beale, B. Pouligny, K. Dimmler, M. Parris, D. Butler and S. Eaton, "Properties of Ceramic KNO₃ Thin-Film Memories," *Physica B & C*, 150[1-2] 160-167.(1988).
- 90 S. P. Li, J. A. Eastman, Z. Li, C. M. Foster, R. E. Newnham and L. E. Cross, "Size effects in nanostructured ferroelectrics," *Physics Letters A*, 212[6] 341-346.(1996).
- 91 T. M. Shaw, S. Trolier-McKinstry and P. C. McIntyre, "The properties of ferroelectric films at small dimensions," *Annual Review of Materials Science*, 30 263-298.(2000).
- 92 A. I. Kingon, J. P. Maria and S. K. Streiffer, "Alternative dielectrics to silicon dioxide for memory and logic devices," *Nature*, 406[6799] 1032-1038.(2000).
- 93 P. C. Fazan, "Trends in the development of ULSI DRAM capacitors," pp. 247-256. Vol. 4. Colorado Springs, CO, USA, (1994).
- 94 C. Feldman, "Thin Films of BaTiO₃," *Physical Review*, 96[3] 819-819.(1954).
- 95 J. R. Slack and J. C. Burfoot, "Electrical Properties of Flash Evaporated Ferroelectric BaTiO₃ Thin Films," *Journal of Physics Part C Solid State Physics*, 4[8] 898-&.(1971).
- 96 T. R. Taylor, P. J. Hansen, B. Acikel, N. Pervez, R. A. York, S. K. Streiffer and J. S. Speck, "Impact of thermal strain on the dielectric constant of sputtered barium strontium titanate thin films," *Applied Physics Letters*, 80[11] 1978-1980.(2002).
- 97 T. R. Taylor, P. J. Hansen, N. Pervez, B. Acikel, R. A. York and J. S. Speck, "Influence of stoichiometry on the dielectric properties of sputtered strontium titanate thin films," *Journal of Applied Physics*, 94[5] 3390-3396.(2003).
- 98 E. J. Cukauskas, S. W. Kirchoefer and J. M. Pond, "Low-loss Ba_{0.5}Sr_{0.5}TiO₃ thin films by inverted cylindrical magnetron sputtering," *Journal of Applied Physics*, 88[5] 2830-2835.(2000).
- 99 R. A. York, A. S. Nagra, P. Periaswamy, O. Auciello, S. K. Streiffer and J. Im, "Synthesis and characterization of (B_xSr_{1-x})Ti_{1+y}O_{3+z} thin films and integration into microwave varactors and phase shifters," *Integrated Ferroelectrics*, 34[1-4] 1617-1628.(2001).
- 100 J. Im, O. Auciello, P. K. Baumann, S. K. Streiffer, D. Y. Kaufman and A. R. Krauss, "Composition-control of magnetron-sputter-deposited (Ba_xSr_{1-x})Ti_{1+y}O_{3+z} thin films for voltage tunable devices," *Applied Physics Letters*, 76[5] 625-627.(2000).

- 101 J. Im, O. Auciello, P. K. Baumann, S. K. Streiffer, D. Y. Kaufman and A. R. Krauss, "Magnetron sputter-deposited multilayer $(\text{Ba}_x\text{Sr}_{1-x})\text{Ti}_{1+y}\text{O}_{3+z}$ thin films for passive and active devices," *Integrated Ferroelectrics*, 34[1-4] 1703-1710.(2001).
- 102 W. J. Lee, H. G. Kim and S. G. Yoon, "Microstructure dependence of electrical properties of $(\text{Ba}_{0.5}\text{Sr}_{0.5})\text{TiO}_3$ thin films deposited on Pt/SiO₂/Si," *Journal of Applied Physics*, 80[10] 5891-5894.(1996).
- 103 P. Padmini, T. R. Taylor, M. J. Lefevre, A. S. Nagra, R. A. York and J. S. Speck, "Realization of high tunability barium strontium titanate thin films by rf magnetron sputtering," *Applied Physics Letters*, 75[20] 3186-3188.(1999).
- 104 T. Horikawa, N. Mikami, T. Makita, J. Tanimura, M. Kataoka, K. Sato and M. Nunoshita, "Dielectric-Properties of $(\text{Ba}, \text{Sr})\text{TiO}_3$ Thin-Films Deposited by RF-Sputtering," *Japanese Journal of Applied Physics, Part 1: Regular Papers, Brief Communications & Review Papers*, 32[9B] 4126-4130.(1993).
- 105 Dipankar Ghosh, "Tunable Microwave Devices Using BST (Barium Strontium Titanate) And Base Metal Electrodes," Ph.D. dissertation. (Advisor: Prof. J. P. Maria) Raleigh, NC: North Carolina State University. (2005).
- 106 D. Ghosh, B. Laughlin, J. Nath, A. I. Kingon, M. B. Steer and J. P. Maria, "Tunable high-quality-factor interdigitated $(\text{Ba}, \text{Sr})\text{TiO}_3$ capacitors fabricated on low-cost substrates with copper metallization," *Thin Solid Films*, 496[2] 669-673.(2006).
- 107 J. C. Shin, J. Park, C. S. Hwang and H. J. Kim, "Dielectric and electrical properties of sputter grown $(\text{Ba},\text{Sr})\text{TiO}_3$ thin films," *Journal of Applied Physics*, 86[1] 506-513.(1999).
- 108 J. W. Jang, S. J. Chung, W. J. Cho, T. S. Hahn and S. S. Choi, "Thickness dependence of room temperature permittivity of polycrystalline BaTiO_3 thin films by radio-frequency magnetron sputtering," *Journal of Applied Physics*, 81[9] 6322-6327.(1997).
- 109 L. J. Sinnamon, R. M. Bowman and J. M. Gregg, "Investigation of dead-layer thickness in $\text{SrRuO}_3/\text{Ba}_{0.5}\text{Sr}_{0.5}\text{TiO}_3/\text{Au}$ thin-film capacitors," *Applied Physics Letters*, 78[12] 1724-1726.(2001).
- 110 A. Lookman, R. M. Bowman, J. M. Gregg, J. Kut, S. Rios, M. Dawber, A. Ruediger and J. F. Scott, "Thickness independence of true phase transition temperatures in barium strontium titanate films," *Journal of Applied Physics*, 96[1] 555-562.(2004).

- 111 B. Chen, H. Yang, L. Zhao, J. Miao, B. Xu, X. G. Qiu, B. R. Zhao, X. Y. Qi and X. F. Duan, "Thickness and dielectric constant of dead layer in Pt/(Ba_{0.7}Sr_{0.3})TiO₃/YBa₂Cu₃O_{7-x} capacitor," *Applied Physics Letters*, 84[4] 583-585.(2004).
- 112 C. Basceri, S. K. Streiffer, A. I. Kingon and R. Waser, "The dielectric response as a function of temperature and film thickness of fiber-textured (Ba,Sr)TiO₃ thin films grown by chemical vapor deposition," *Journal of Applied Physics*, 82[5] 2497-2504.(1997).
- 113 G. T. Stauff, R. Carl, S. Bilodeau, P. Van Buskirk and K. Watts, "Thin film high k dielectrics for integrated passive devices," pp. 349-354. Minneapolis, MN, USA, (1996).
- 114 G. T. Stauff, C. Ragaglia, J. F. Roeder, D. Vestyck, J. P. Maria, T. Ayguavives, A. Kingon, A. Mortazawi and A. Tombak, "Thick electrodes for high frequency high Q tunable ferroelectric thin film varactors," *Integrated Ferroelectrics*, 39[1-4] 1271-1280.(2001).
- 115 D. M. Tahan, A. Safari and L. C. Klein, "Preparation and characterization of Ba_xSr_{1-x}TiO₃ thin films by a sol-gel technique," *Journal of the American Ceramic Society*, 79[6] 1593-1598.(1996).
- 116 J. Ihlefeld, B. Laughlin, A. Hunt-Lowery, W. Borland, A. Kingon and J. P. Maria, "Copper compatible barium titanate thin films for embedded passives," *Journal of Electroceramics*, 14[2] 95-102.(2005).
- 117 S. Hoffmann and R. Waser, "Control of the morphology of CSD-prepared (Ba,Sr)TiO₃ thin films," *Journal of the European Ceramic Society*, 19[6-7] 1339-1343.(1999).
- 118 S. K. Streiffer, C. Basceri, C. B. Parker, S. E. Lash and A. I. Kingon, "Ferroelectricity in thin films: The dielectric response of fiber-textured (Ba_xSr_{1-x})Ti_{1+y}O_{3+z} thin films grown by chemical vapor deposition," *Journal of Applied Physics*, 86[8] 4565-4575.(1999).
- 119 Jon Fredrick Ihlefeld, "Synthesis and properties of barium titanate solid solution thin films on copper substrates," Ph.D. dissertation. (Advisor: Prof. J. P. Maria) Raleigh, NC: North Carolina State University. (2006).
- 120 M. M. Saad, P. Baxter, R. M. Bowman, J. M. Gregg, F. D. Morrison and J. F. Scott, "Intrinsic dielectric response in ferroelectric nano-capacitors," *Journal of Physics-Condensed Matter*, 16[41] L451-L456.(2004).

- 121 Don Morgan Smyth, "The defect chemistry of metal oxides." New York: Oxford University Press. (2000).
- 122 F. A. Kroger and H. J. Vink, "Relations between the Concentrations of Imperfections in Crystalline Solids," *Solid State Physics-Advances in Research and Applications*, 3 307-435.(1956).
- 123 N. H. Chan, R. K. Sharma and D. M. Smyth, "Nonstoichiometry in Acceptor-Doped BaTiO₃," *Journal of the American Ceramic Society*, 65[3] 167-170.(1982).
- 124 N. H. Chan, R. K. Sharma and D. M. Smyth, "Non-Stoichiometry in Undoped BaTiO₃," *Journal of the American Ceramic Society*, 64[9] 556-562.(1981).
- 125 Y. Tsur and C. A. Randall, "Point defect concentrations in barium titanate revisited," *Journal of the American Ceramic Society*, 84[9] 2147-2149.(2001).
- 126 J. Nowotny and M. Rekas, "Defect Chemistry of BaTiO₃," *Solid State Ionics*, 49 135-154.(1991).
- 127 A. E. Paladino, L. G. Rubin and J. S. Waugh, "Oxygen Ion Diffusion in Single Crystal SrTiO₃," *Journal of Physics and Chemistry of Solids*, 26[2] 391-&.(1965).
- 128 S. Shirasaki, H. Yamamura, H. Haneda, K. Kakegawa and J. Mouri, "Defect Structure and Oxygen Diffusion in Undoped and Ladoped Polycrystalline Barium-Titanate," *Journal of Chemical Physics*, 73[9] 4640-4645.(1980).
- 129 J. Plücker, *Annalen der Physik und Chemie*, 105[Series 2] 67-84.(1858).
- 130 W. R. Grove, "On the electro-chemical polarity of gases.," *Transactions of the Royal Society of London*, 142 87-101.(1852).
- 131 Dr. Wright, *The American Journal of Sciences and Arts*, 12[Third Series] 49-(1877).
- 132 William Crookes, "On electrical evaporation," *Proceedings of the Royal Society of London*, 50 88-105.(1891).
- 133 J. J. Thomson, "Structure of the atom," *Philosophical Magazine*, 7 237-265.(1904).
- 134 J. J. Thomson, "Charge carried by Röntgen ions," *Philosophical Magazine*, 46 528-545.(1898).
- 135 Thomas A. Edison, "PROCESS OF COATING PHONOGRAPH-RECORDS." U.S. Patent No. 713,863 (1902).

- 136 R. K. Waits, "Edison's vacuum coating patents," *Journal of Vacuum Science & Technology A*, 19[4] 1666-1673.(2001).
- 137 G. Betz and K. Wien, "Energy and Angular-Distributions of Sputtered Particles," *Int. J. Mass Spectrom. Ion Process.*, 140 1-110.(1994).
- 138 R. F. Bunshah, "Handbook of deposition technologies for films and coatings : science, technology, and applications," 2nd ed. Park Ridge, N.J.: Noyes Publications. (1994).
- 139 H. Oechsner, "Sputtering - Review of Some Recent Experimental and Theoretical Aspects," *Applied Physics*, 8[3] 185-198.(1975).
- 140 Milton Ohring, "The materials science of thin films." Boston: Academic Press. (1992).
- 141 Donald L. Smith, "Thin-film deposition : principles and practice." New York: McGraw-Hill. (1995).
- 142 F. Paschen, *Annalen der Physik und Chemie*, 37 69.(1889).
- 143 J. S. Townsend, "Electrons in Gases." London: Hutchinson. (1947).
- 144 Peter Sigmund, "Mechanisms and theory of physical sputtering by particle impact," *Nuclear Instruments and Methods in Physics Research Section B: Beam Interactions with Materials and Atoms*, 27[1] 1-20.(1987).
- 145 H. R. Koenig and L. I. Maissel, "Application of RF discharges to sputtering," *IBM Journal of Research and Development*, 14[2] 168-.(1970).
- 146 J. L. Vossen, "Control of Film Properties by Rf-Sputtering Techniques," *Journal of Vacuum Science & Technology*, 8[5] S12-&.(1971).
- 147 J. L. Vossen and J. J. O'Neill, "R-F Sputtering Processes," *RCA Review*, 29[2] 149-&.(1968).
- 148 Y. Sakabe and T. Reynolds, "Base-metal electrode capacitors," *American Ceramic Society Bulletin*, 81[10] 24-26.(2002).
- 149 D. F. K. Hennings, "Dielectric materials for sintering in reducing atmospheres," *Journal of the European Ceramic Society*, 21[10-11] 1637-1642.(2001).
- 150 J. M. Herbert, "Thin Ceramic Dielectrics Combined with Nickel Electrodes," *Proceedings of the Institution of Electrical Engineers-London*, 112[7] 1474-&.(1965).

- 151 J. M. Herbert, "High-permittivity ceramics sintered in hydrogen," *British Ceramic Society -- Transactions*, 62[8] 645-658.(1963).
- 152 H. Kishi, Y. Mizuno and H. Chazono, "Base-metal electrode-multilayer ceramic capacitors: Past, present and future perspectives," *Japanese Journal of Applied Physics Part I-Regular Papers Short Notes & Review Papers*, 42[1] 1-15.(2003).
- 153 T. H. Song and C. A. Randall, "Copper cofire X7R dielectrics and multilayer capacitors based on zinc borate fluxed barium titanate ceramic," *Journal of Electroceramics*, 10[1] 39-46.(2003).
- 154 Ihsan Barin, Ottmar Knacke and O. Kubaschewski, "Thermochemical properties of inorganic substances." New York: Springer-Verlag. (1973).
- 155 Ihsan Barin, Ottmar Knacke and O. Kubaschewski, "Thermochemical properties of inorganic substances (supplement)." New York: Springer-Verlag. (1977).
- 156 Ottmar Knacke, O. Kubaschewski and Klaus Hesselmann, "Thermochemical properties of inorganic substances," 2nd ed. New York: Springer-Verlag. (1991).
- 157 Jr. Malcolm W. Chase, C. A. Davies, Jr. J. R. Downey, D. J. Frurip, R. A. McDonald and A. N. Syverud, "JANAF Thermochemical Tables," 3rd ed. In *Journal of Physical and Chemical Reference Data*, Vol. 14 Supplement No. 1. Midland, MI: American Chemical Society, American Institute of Physics, and National Bureau of Standards. (1985).
- 158 D. B. Downie, "Thermodynamic + Structural Properties of Liquid Zinc/Copper Alloys," *Acta Metallurgica*, 12[8] 875-&.(1964).
- 159 J. T. Dawley and P. G. Clem, "Dielectric properties of random and < 100 > oriented SrTiO₃ and (Ba,Sr)TiO₃ thin films fabricated on < 100 > nickel tapes," *Applied Physics Letters*, 81[16] 3028-3030.(2002).
- 160 G. H. Yi, Z. Wu and M. Sayer, "Preparation of Pb(Zr,Ti)O₃ Thin-Films by Sol-Gel Processing - Electrical, Optical, and Electro-Optic Properties," *Journal of Applied Physics*, 64[5] 2717-2724.(1988).
- 161 G. Yi, M. Sayer, Z. Wu, C. K. Jen and J. F. Bussiere, "Piezoelectric Lead Zirconate Titanate Coatings on Metallic Wires," *Electronics Letters*, 25[14] 907-908.(1989).
- 162 J. Y. Chen, Q. C. Xu, M. Blaszkiewicz, R. Meyer and R. E. Newnham, "Lead Zirconate Titanate Films on Nickel Titanium Shape Memory Alloys - Smarties," *Journal of the American Ceramic Society*, 75[10] 2891-2892.(1992).

- 163 P. G. Mercado and A. P. Jardine, "Smart Thin-Film TiNi Piezoelectric Heterostructures," *Journal of Vacuum Science & Technology a-Vacuum Surfaces and Films*, 13[3] 1017-1021.(1995).
- 164 D. J. Kim, D. Y. Kaufman, S. K. Streiffer, T. H. Lee, R. Erck and O. Auciello, "Chemical solution deposition of PLZT films on base metal foils," pp. 457-462. Boston, MA, USA, (2003).
- 165 S. Seifert, P. Lobmann and D. Sporn, "Influence of processing parameters on dielectric properties of PZT thin films on steel substrates," *Journal De Physique Iv*, 8[P9] 61-64.(1998).
- 166 Q. Zou, H. E. Ruda and B. G. Yacobi, "Improved dielectric properties of lead zirconate titanate thin films deposited on metal foils with LaNiO₃ buffer layers," *Applied Physics Letters*, 78[9] 1282-1284.(2001).
- 167 Q. Zou, H. E. Ruda, B. G. Yacobi, K. Saegusa and M. Farrell, "Dielectric properties of lead zirconate titanate thin films deposited on metal foils," *Applied Physics Letters*, 77[7] 1038-1040.(2000).
- 168 J. P. Maria, K. Cheek, S. Streiffer, S. H. Kim, G. Dunn and A. Kingon, "Lead zirconate titanate thin films on base-metal foils: An approach for embedded high-permittivity passive components," *Journal of the American Ceramic Society*, 84[10] 2436-2438.(2001).
- 169 T. Kim, A. I. Kingon, J. P. Maria and R. T. Crosswell, "Ca-doped lead zirconate titanate thin film capacitors on base metal nickel on copper foil," *Journal of Materials Research*, 19[10] 2841-2848.(2004).
- 170 J. T. Dawley, R. J. Ong and P. G. Clem, "Chemical solution deposition of < 100 >-oriented SrTiO₃ buffer layers on Ni substrates," *Journal of Materials Research*, 17[7] 1678-1685.(2002).
- 171 M. D. Losego, L. H. Jimison, J. F. Ihlefeld and J. P. Maria, "Ferroelectric response from lead zirconate titanate thin films prepared directly on low-resistivity copper substrates," *Applied Physics Letters*, 86[17].(2005).
- 172 Mark Daniel Losego, "The chemical solution deposition of lead zirconate titanate (PZT) thin films directly on copper surfaces " M.S. dissertation. (Advisor: Prof. J. P. Maria) Raleigh, NC: North Carolina State University. (2005).
- 173 B. N. Chapman, "Thin-Film Adhesion," *Journal of Vacuum Science & Technology*, 11[1] 106-113.(1974).

- 174 P. R. Chalker, S. J. Bull and D. S. Rickerby, "A Review of the Methods for the Evaluation of Coating-Substrate Adhesion," *Materials Science and Engineering a-Structural Materials Properties Microstructure and Processing*, 140 583-592.(1991).
- 175 L. F. Goldstein and T. J. Bertone, "Evaluation of Metal-Film Adhesion to Flexible Substrates," *Journal of Vacuum Science & Technology*, 12[6] 1423-1426.(1975).
- 176 C. Weaver, "Adhesion of Thin-Films," *Journal of Vacuum Science & Technology*, 12[1] 18-25.(1975).
- 177 P. S. de Laplace, *Mecanique Celeste. Suppl. au Xe livre*.(1805).
- 178 Thomas Young, "An Essay on the Cohesion of Fluids," *Philosophical Transactions of the Royal Society of London*, 95 65-87.(1805).
- 179 August Dupré, "Theorie Mechanique de la Chaleur." Paris: Gauthier-Villars. (1869).
- 180 Bashford and Adams, "An attempt to test the theories of capillary attraction." Cambridge, UK: Cambridge University Press. (1883).
- 181 N. Ernest Dorsey, "A new equation for the determination of surface tension from the form of a sessile drop or bubble," *Journal of the Washington Academy of Sciences*, 18[19] 505-509.(1928).
- 182 W. D. Kingery and M. Humenik, "Surface Tension at Elevated Temperatures .1. Furnace and Method for Use of the Sessile Drop Method - Surface Tension of Silicon, Iron and Nickel," *Journal of Physical Chemistry*, 57[3] 359-363.(1953).
- 183 B. J. Keene, "Review of Data for the Surface-Tension of Pure Metals," *International Materials Reviews*, 38[4] 157-192.(1993).
- 184 F. Ernst, "Metal-Oxide Interfaces," *Materials Science & Engineering R-Reports*, 14[3] 97-156.(1995).
- 185 L. J. Brillson, "Metal-Semiconductor Interfaces," *Surface Science*, 300[1-3] 909-927.(1994).
- 186 N. Eustathopoulos and B. Drevet, "Determination of the nature of metal-oxide interfacial interactions from sessile drop data," *Materials Science and Engineering a-Structural Materials Properties Microstructure and Processing*, 249[1-2] 176-183.(1998).

- 187 D. Chatain, F. Chabert, V. Ghetta and J. Fouletier, "New Experimental Setup for Wettability Characterization under Monitored Oxygen Activity .1. Role of Oxidation-State and Defect Concentration on Oxide Wettability by Gold," *Journal of the American Ceramic Society*, 76[6] 1568-1576.(1993).
- 188 D. Chatain, F. Chabert, V. Ghetta and J. Fouletier, "New Experimental Setup for Wettability Characterization under Monitored Oxygen Activity .2. Wettability of Sapphire by Silver Oxygen Melts," *Journal of the American Ceramic Society*, 77[1] 197-201.(1994).
- 189 P. Darrell Ownby and Jenq Liu, "Surface-Energy of Liquid Copper and Single-Crystal Sapphire and the Wetting Behavior of Copper on Sapphire," *Journal of Adhesion Science and Technology*, 2[4] 255-269.(1988).
- 190 L. Espi e, B. Drevet and N. Eustathopoulos, "Experimental-Study of the Influence of Interfacial Energies and Reactivity on Wetting in Metal-Oxide Systems," *Metallurgical and Materials Transactions a-Physical Metallurgy and Materials Science*, 25[3] 599-605.(1994).
- 191 D. Chatain and W. C. Carter, "Wetting dynamics - Spreading of metallic drops," *Nature Materials*, 3[12] 843-845.(2004).
- 192 A. Mortensen, B. Drevet and N. Eustathopoulos, "Kinetics of diffusion-limited spreading of sessile drops in reactive wetting," *Scripta Materialia*, 36[6] 645-651.(1997).
- 193 Y. Rotenberg, L. Boruvka and A. W. Neumann, "The Shape of Nonaxisymmetric Drops on Inclined Planar Surfaces," *Journal of Colloid and Interface Science*, 102[2] 424-434.(1984).
- 194 R. A. Brown, F. M. Orr and L. E. Scriven, "Static Drop on an Inclined Plate - Analysis by the Finite-Element Method," *Journal of Colloid and Interface Science*, 73[1] 76-87.(1980).
- 195 M. E. R. Shanahan, "Meniscus Shape and Contact-Angle of a Slightly Deformed Axisymmetric Drop," *Journal of Physics D-Applied Physics*, 22[8] 1128-1135.(1989).
- 196 J. F. Oliver, C. Huh and S. G. Mason, "Experimental-Study of Some Effects of Solid-Surface Roughness on Wetting," *Colloids and Surfaces*, 1[1] 79-104.(1980).
- 197 C. Huh and S. G. Mason, "Effects of Surface-Roughness on Wetting (Theoretical)," *Journal of Colloid and Interface Science*, 60[1] 11-38.(1977).

- 198 R. N. Wenzel, "Surface Roughness and Contact Angle," *Journal of Physical and Colloid Chemistry*, 53[9] 1466-1467.(1949).
- 199 V. Ghetta, J. Fouletier and D. Chatain, "Oxygen adsorption isotherms at the surfaces of liquid Cu and Au-Cu alloys and their interfaces with Al₂O₃ detected by wetting experiments," *Acta Materialia*, 44[5] 1927-1936.(1996).
- 200 Andrew Zangwill, "Physics at surfaces." Cambridge, UK: Cambridge University Press. (1988).
- 201 G. Wulff, "On the question of speed of growth and dissolution of crystal surfaces," *Zeitschrift Fur Krystallographie Und Mineralogie*, 34[5/6] 449-530.(1901).
- 202 C. Herring, "Structure and properties of solid surfaces," pp. 491. Edited by Robert Gomer and Cyril Stanley Smith. National Research Council. Lake Geneva, Wisconsin, (1952).
- 203 B. E. Sundquist, "Direct Determination of Anisotropy of Surface Free Energy of Solid Gold Silver Copper Nickel + Alpha + Gamma Iron," *Acta Metallurgica*, 12[1] 67-&.(1964).
- 204 A. Dinghas, "On Wulff's geometric theorem for the balanced form of crystals," *Zeitschrift Fur Kristallographie*, 105[4] 304-314.(1944).
- 205 R. M. Pilliar and J. Nutting, "Solid-Solid Interfacial Energy Determinations in Metal-Ceramic Systems," *Philosophical Magazine*, 16[139] 181-&.(1967).
- 206 David P. Cann, "Thermochemical Interactgions at Electrode Interfaces in Electroceramic Applications," Ph.D. dissertation. (Advisor: Prof. Clive A. Randall) State College, PA: The Pennsylvania State University. (1997).
- 207 D. P. Cann, J. P. Maria and C. A. Randall, "Relationship between wetting and electrical contact properties of pure metals and alloys on semiconducting barium titanate ceramics," *Journal of Materials Science*, 36[20] 4969-4976.(2001).
- 208 Sae-Fue Wang, Thomas C. K. Yang and Shiao-Ching Lee, "Wettability of electrode metals on barium titanate substrate," *Journal of Materials Science*, 36[4] 825-829.(2001).
- 209 D. Chatain, L. Coudurier and N. Eustathopoulos, "Wetting and Interfacial Bonding in Ionocovalent Oxide-Liquid Metal Systems," *Revue De Physique Appliquee*, 23[6] 1055-1064.(1988).
- 210 K. Nogi, K. Oishi and K. Ogino, "Wettability of Solid Oxides by Liquid Pure Metals," *Materials Transactions JIM*, 30[2] 137-145.(1989).

- 211 M. McLean and E. D. Hondros, "Study of Grain-Boundary Grooving at Platinum/Alumina Interface," *Journal of Materials Science*, 6[1] 19-&(1971).
- 212 R. Standing and M. Nicholas, "Wetting of Alumina and Vitreous Carbon by Copper-Tin-Titanium Alloys," *Journal of Materials Science*, 13[7] 1509-1514.(1978).
- 213 N. Eustathopoulos and L. Coudurier, "Influence of Alloying Elements on Wettability and Adhesion Energy in Liquid Metal-Ceramic Systems," *Journal of Adhesion Science and Technology*, 6[9] 1011-1022.(1992).
- 214 J. G. Li, L. Coudurier and N. Eustathopoulos, "Work of Adhesion and Contact-Angle Isotherm of Binary-Alloys on Ionocovalent Oxides," *Journal of Materials Science*, 24[3] 1109-1116.(1989).
- 215 J. G. Li, D. Chatain, L. Coudurier and N. Eustathopoulos, "Wettability of Sapphire by Sn-Al Alloys," *Journal of Materials Science Letters*, 7[9] 961-963.(1988).
- 216 R. Novakovic, E. Ricci, M. L. Muolo, D. Giuranno and A. Passerone, "On the application of modelling to study the surface and interfacial phenomena in liquid alloy-ceramic substrate systems," *Intermetallics*, 11[11-12] 1301-1311.(2003).
- 217 A. R. Miedema, "Surface Segregation in Alloys of Transition-Metals," *Zeitschrift Fur Metallkunde*, 69[7] 455-461.(1978).
- 218 T. Tanaka, K. Hack, T. Iida and S. Hara, "Application of thermodynamic databases to the evaluation of surface tensions of molten alloys, salt mixtures and oxide mixtures," *Zeitschrift Fur Metallkunde*, 87[5] 380-389.(1996).
- 219 P. J. Spencer, "A Thermodynamic Evaluation of the Cu-Zn System," *CALPHAD-Computer Coupling of Phase Diagrams and Thermochemistry*, 10[2] 175-185.(1986).
- 220 Ralph Hultgren, Pramod D. Densai, Donald T. Hawkins, Molly Gleiser and Kenneth K. Kelly, "Selected Values of the Thermodynamic Properties of Binary Alloys." In. American Society for Metals, Metals Park, OH (1973).
- 221 M. C. Salvadori, L. L. Melo, M. Cattani, O. R. Monteiro and I. G. Brown, "Measurement of critical exponents of platinum thin films," *Surface Review and Letters*, 10[1] 1-5.(2003).
- 222 H. N. Al-Shareef, K. D. Gifford, S. H. Rou, P. D. Hren, Orlando Auciello and Angus I. Kingon, "Electrodes for Ferroelectric Thin Films," *Integrated Ferroelectrics*, 3[4] 321-332.(1993).

- 223 Gale A. Norton and P. Patrick Leahy, "Minerals Commodity Summaries 2006," pp. 199. U.S. Department of the Interior and U.S. Geological Survey. United States Government Printing Office: Washington, (2006).
- 224 William Frank McClune and Joint Committee on Powder Diffraction Standards, "Powder diffraction file : inorganic and organic ". In. ICDD-International Centre for Diffraction Data, Swarthmore, PA (1992).
- 225 T. K. Li, P. Zawadzki, R. A. Stall, S. H. Liang and Y. C. Lu, "High dielectric constant $Ba_xSr_{1-x}TiO_3$ (BST) thin films made by MOCVD techniques for DRAM applications," *Integrated Ferroelectrics*, 17[1-4] 127-&. (1997).
- 226 H. J. Cho, J. B. Park, S. S. Yu, J. S. Roh and H. K. Yoon, "Low temperature MOCVD of BST thin film for high density DRAMs," pp. 55-58 in *Proceedings of the Proceedings of the 2000 12th IEEE International Symposium on Applications of Ferroelectrics (ISAF) (IEEE Cat. No.00CH37076)*. Vol. vol. 1. Honolulu, HI, USA, (2001).
- 227 F. Fitsilis, S. Regnery, P. Ehrhart, R. Waser, F. Schienle, M. Schumacher, M. Dauelsberg, P. Strzyzewski and H. Juergensen, "BST thin films grown in a multiwafer MOCVD reactor," *Journal of the European Ceramic Society*, 21[10-11] 1547-1551.(2001).
- 228 W. Fan, B. Kabius, J. M. Hiller, S. Saha, J. A. Carlisle, O. Auciello, R. P. H. Chang and R. Ramesh, "Materials science and integration bases for fabrication of $(Ba_xSr_{1-x})TiO_3$ thin film capacitors with layered Cu-based electrodes," *Journal of Applied Physics*, 94[9] 6192-6200.(2003).
- 229 E 112 - 96: Standard Test Methods for Determining Average Grain Size ASTM International (2003).
- 230 Paul H. Shuch. "Updating the Multiband Reconfigurable Synthetic Aperture Radar Antenna." *ESTC 2005 Proceedings* (October 2006) <<http://www.estc.nasa.gov/conferences/estc2005/papers/b5p1.pdf>>.
- 231 W. L. Zhong, B. D. Qu, P. L. Zhang and Y. G. Wang, "Thickness Dependence of the Dielectric Susceptibility of Ferroelectric Thin-Films," *Physical Review B*, 50[17] 12375-12380.(1994).
- 232 R. E. Newnham, D. P. Skinner and L. E. Cross, "Connectivity and Piezoelectric-Pyroelectric Composites," *Materials Research Bulletin*, 13[5] 525-536.(1978).

- 233 G. A. Smolensky, "Physical phenomena in ferroelectrics with diffuse phase transition," pp. 8-10 in *Proceedings of the 2nd International Meeting on Ferroelectricity*. Kyoto, Japan, (4-9 Sept. 1969).
- 234 L. Vegard, "The constitution of the mixed crystals and the filling of space of the atoms," *Zeitschrift Fur Physik*, 5 17-26.(1921).
- 235 B.D. Cullity and S.R. Stock, "Elements of X-Ray Diffraction,"3rd ed. Upper Saddle River, NJ: Prentice Hall. (2001).
- 236 T. Mitsui and S. Nomura, "Landolt-Börnstein: Group III: Crystal and Solid State Physics, Ferroelectrics and Related Substances, Subvolume a: Oxides." In *Landolt-Börnstein: Numerical Data and Functional Relationships in Science and Technology*. Vol. 16 (a). Edited by K.-H. Hellwege, A. M. Hellwege, Richard Börnstein and Hans Landolt. Springer-Verlag, New York (1981).
- 237 K. Sreenivas, I. Reaney, T. Maeder, N. Setter, C. Jagadish and R. G. Elliman, "Investigation of Pt/Ti Bilayer Metallization on Silicon for Ferroelectric Thin-Film Integration," *Journal of Applied Physics*, 75[1] 232-239.(1994).
- 238 T. Nakamura, Y. Nakao, A. Kamisawa and H. Takasu, "Preparation of Pb(Zr,Ti)O₃ Thin-Films on Ir and IrO₂ Electrodes," *Japanese Journal of Applied Physics Part I-Regular Papers Short Notes & Review Papers*, 33[9B] 5207-5210.(1994).
- 239 Arthur C. Hardy and Fred H. Perrin, "The principles of optics,"Second Impression, First ed. In *International series in physics* Edited by F. K. Richtmyer. New York: McGraw-Hill. (1932).
- 240 D. Stull, "American Institute of Physics Handbook,"3rd ed. Edited by D. E. Gray. New York: McGraw Hill. (1972).
- 241 S. Yamamichi, T. Sakuma, K. Takemura and Y. Miyasaka, "SrTiO₃ Thin-Film Preparation by Ion-Beam Sputtering and Its Dielectric-Properties," *Japanese Journal of Applied Physics Part I-Regular Papers Short Notes & Review Papers*, 30[9B] 2193-2196.(1991).
- 242 P. W. M. Blom, R. M. Wolf, J. F. M. Cillessen and Mpcm Krijn, "Ferroelectric Schottky Diode," *Physical Review Letters*, 73[15] 2107-2110.(1994).
- 243 R. G. Munro, "Evaluated material properties for a sintered alpha-alumina," *Journal of the American Ceramic Society*, 80[8] 1919-1928.(1997).

- 244 T. Zhao, Z. H. Chen, F. Chen, H. B. Lu, G. Z. Yang and H. S. Cheng, "Electrical and optical properties of strongly reduced epitaxial BaTiO_{3-x} thin films," *Applied Physics Letters*, 77[26] 4338-4340.(2000).
- 245 J. P. Maria, B. A. Boyette, A. I. Kingon, C. Ragaglia and G. Stauff, "Low loss tungsten-based electrode technology for microwave frequency BST varactors," *Journal of Electroceramics*, 14[1] 75-81.(2005).
- 246 D. C. Dube, J. Baborowski, P. Muralt and N. Setter, "The effect of bottom electrode on the performance of thin film based capacitors in the gigahertz region," *Applied Physics Letters*, 74[23] 3546-3548.(1999).
- 247 James D. Plummer, Michael Deal and Peter B. Griffi, "Silicon VLSI technology: fundamentals, practice and modeling ". Upper Saddle River, NJ: Prentice Hall. (2000).
- 248 Y. L. Wang, L. T. Li, J. Q. Qi and Z. L. Gui, "Frequency response of ZnO-doped BaZr_xTi_{1-x}O₃ ceramics," *Materials Chemistry and Physics*, 76[3] 250-254.(2002).
- 249 A. C. Caballero, J. F. Fernandez, C. Moure and P. Duran, "ZnO-doped BaTiO₃: Microstructure and electrical properties," *Journal of the European Ceramic Society*, 17[4] 513-523.(1997).
- 250 A. C. Caballero, J. F. Fernandez, C. Moure, P. Duran and Y. M. Chiang, "Grain growth control and dopant distribution in ZnO-doped BaTiO₃," *Journal of the American Ceramic Society*, 81[4] 939-944.(1998).
- 251 W. Choi, B. S. Kang, Q. X. Jia, V. Matias and A. T. Findikoglu, "Dielectric properties of < 001 >-oriented Ba_{0.6}Sr_{0.4}TiO₃ thin films on polycrystalline metal tapes using biaxially oriented MgO/gamma-Al₂O₃ buffer layers," *Applied Physics Letters*, 88[6].(2006).
- 252 N. K. Pervez, P. J. Hansen and R. A. York, "High tunability barium strontium titanate thin films for rf circuit applications," *Applied Physics Letters*, 85[19] 4451-4453.(2004).
- 253 Paul H. Shuch. "Multiband Reconfigurable Synthetic Aperture Radar Antenna." *ESTC 2004 Proceedings* (October 2006) <<http://www.estc.nasa.gov/conferences/estc2004/papers/b1p1.pdf>>.
- 254 Paul H. Shuch. "Built from Unobtainium: an ATDM Multiband Reconfigurable Synthetic Aperture Radar Antenna." *ESTC 2006 Proceedings* (October 2006) <<http://www.estc.nasa.gov/conferences/estc2006/papers/b6p1.pdf>>.

- 255 D. E. Rase and R. Roy, "Phase Equilibria in the System BaO-TiO₂," *Journal of the American Ceramic Society*, 38[3] 102-113.(1955).
- 256 K. W. Kirby and B. A. Wechsler, "Phase-Relations in the Barium Titanate-Titanium Oxide System," *Journal of the American Ceramic Society*, 74[8] 1841-1847.(1991).
- 257 Mirosława Dryś and Włodzimierz Trzebiatowski, *Roczniki Chemii*, 31 492.(1957).
- 258 W. Kwestroo and H. A. M. Paping, "The Systems BaO-SrO-TiO₂, BaO-CaO-TiO₂, and SrO-CaO-TiO₂," *Journal of the American Ceramic Society*, 42[6] 292-299.(1959).
- 259 Franco Massazza, *Chim. Ind. (Milan)*, 41 112.(1959).

APPENDICES

A. CERTIFICATE OF ANALYSIS FOR BST SPUTTER TARGETS

The following tables are representative certificates of analysis for the BaTiO₃ and SrTiO₃ powders used to make sputter targets as reported by Super Conducting Materials, Inc. (Suffern, NY, USA). The starting powders are listed as 99.95% purity and table A.1 lists the impurities that are found above detection limits.

Table A.1: Measured impurity levels in raw powders to make BST sputter targets. Values are reported by the manufacturer.

Impurity	BaTiO₃	SrTiO₃
Ba	n/a	100 ppm
Ca	10 ppm	100 ppm
Cr	20 ppm	B.D.L.
Mg	B.D.L.	<100 ppm
Si	B.D.L.	100 ppm
Sr	100 ppm	n/a

*B.D.L - below detection limit

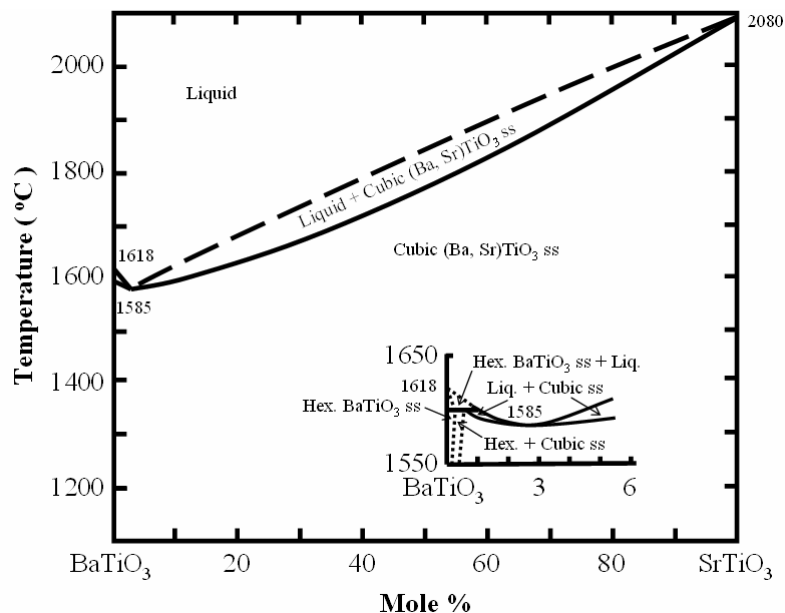


Figure B.3: BaTiO₃ - SrTiO₃ phase diagram showing full miscibility between the two perovskite oxides.⁶²

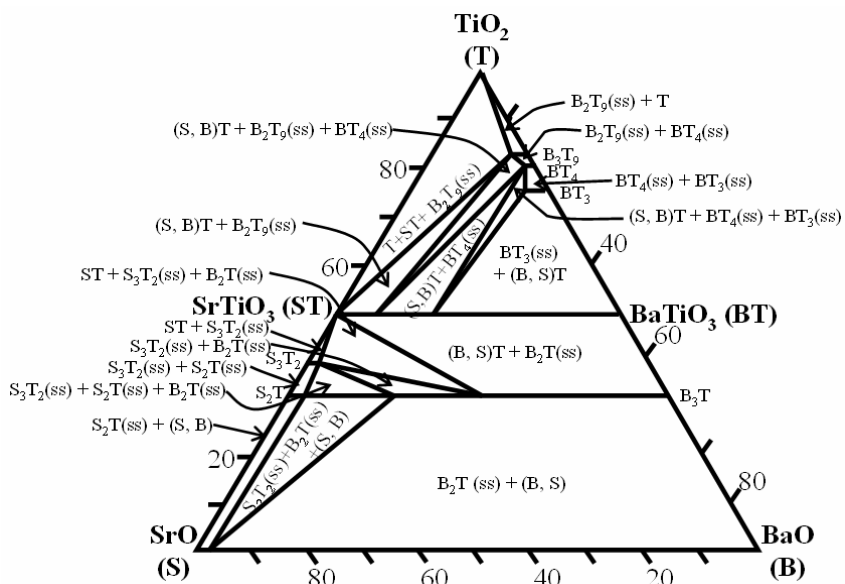


Figure B.4: The BaO - SrO - TiO₂ ternary phase diagram at 1400 °C. The labels in the figure correspond to: B = BaO, S = SrO, T = TiO₂, BT = BaTiO₃, ST = SrTiO₃, (B, S)T = (Ba_x, Sr_{1-x})TiO₃.²⁵⁸

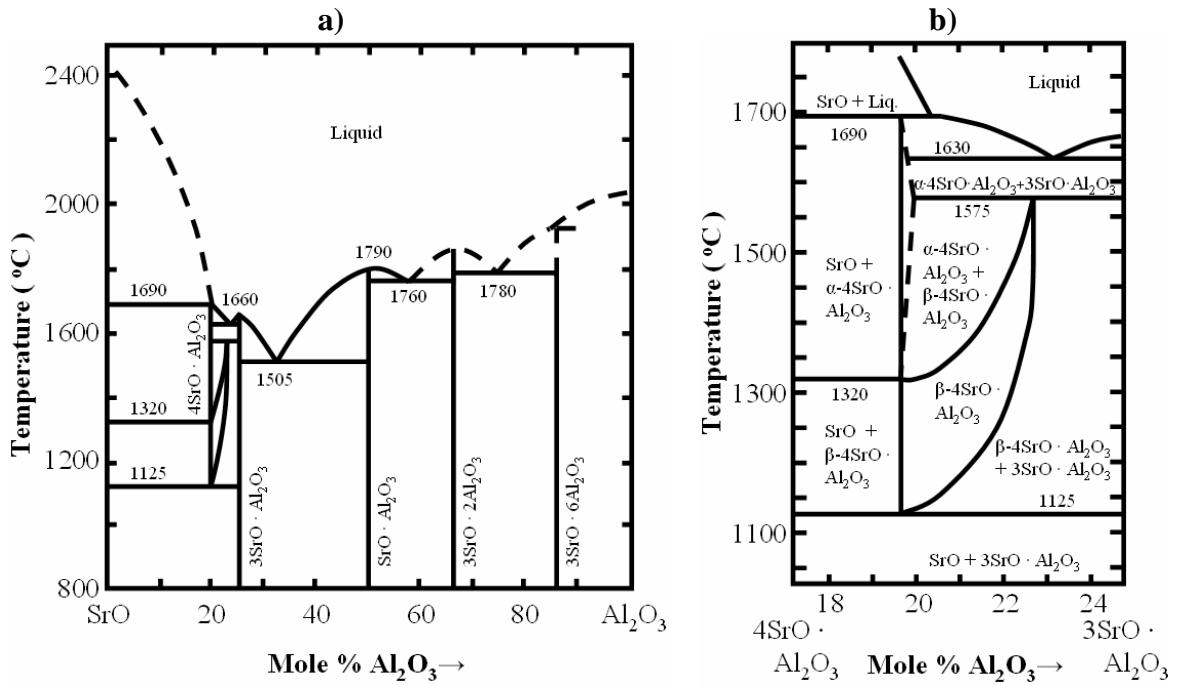


Figure B.5: SrO - Al₂O₃ phase diagram showing possible reaction products of BST on alumina. The entire composition range is shown in a) while b) shows the details of the phase field from 18 < mole % Al₂O₃ < 24.²⁵⁹

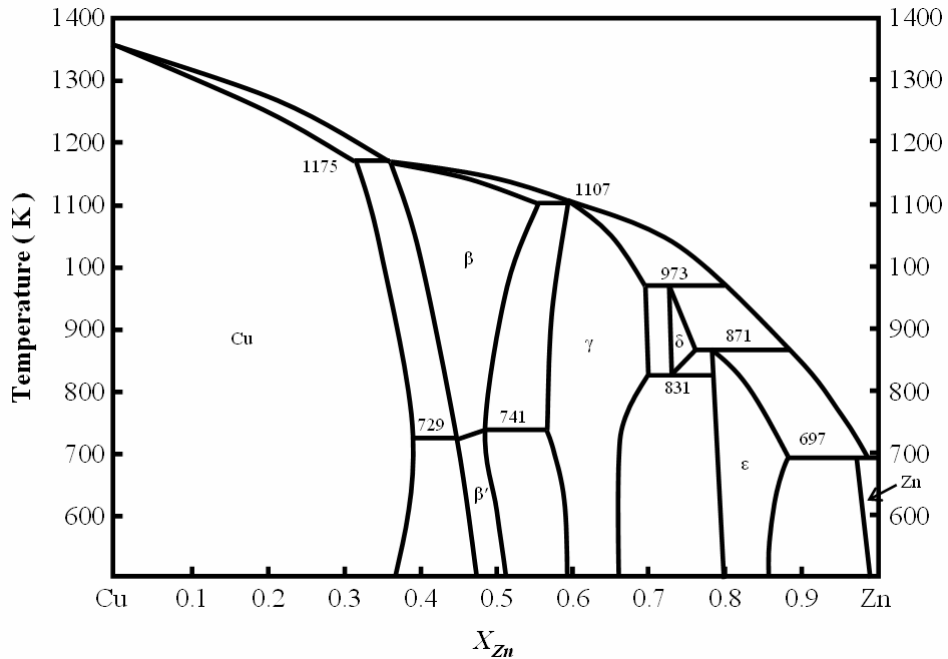


Figure B.6: The copper - zinc phase diagram showing total solid and liquid miscibility over the entire composition range.²¹⁹

C. POWDER DIFFRACTION FILES

A powder diffraction files (PDF) are given from the compiled data of the Joint Committee on Powder Diffraction Standards (JCPDS).²²⁴

Table C.1: Powder diffraction file for FCC Cu.

4- 836 JCPDS-ICDD Copyright 1993 QM=*

Cu

Copper Copper, syn

Rad: CuK α 1 Lambda: 1.5405 Filter: Ni d-sp:
 Cutoff: Int: Diffractometer I/Icor:
 Ref: Swanson, Tatge, Natl. Bur. Stand. (U.S.), Circ. 539, 1 15 (1953)

Sys: Cubic S.G.: Fm3m (225)
 a: 3.6150 b: c: A: C:
 A: B: C: Z: 4 mp: 1083°
 Ref: Ibid.
 Dx: 8.94 Dm: 8.95 SS/FOM: F8=89(.011,8)

Color: Red
 Pattern taken at 26 C. Sample from metallurgical laboratory of NBS, Gaithersburg, Maryland, USA. CAS no.: 7440-50-8. It had been heated in an H₂ atmosphere at 300 C. Impurities from 0.001-0.01%, Ag, Al, Bi, Fe, Si, Zn. Opaque mineral optical data on specimen from unspecified locality, R_{3R}%=60.65, Disp.=Std., VHN100=96-104, Ref.: IMA Commission on Ore Microscopy QDF. Measured density and color from Dana's System of Mineralogy, 7th Ed., I 99. Cu type. Gold group, gold subgroup. PSC: cF4. Mwt: 63.55. Volume[CD]: 47.24.
 Strong lines: 2.09/X 1.81/5 1.28/2 1.09/2 0.83/1 0.81/1 1.04/1 0.90/1

8 reflections in pattern. Radiation= 1.54060

2-theta	Int.	h k l	2-theta	Int.	h k l
43.298	100	1 1 1			
50.434	46	2 0 0			
74.133	20	2 2 0			
89.934	17	3 1 1			
95.143	5	2 2 2			
116.923	3	4 0 0			
136.514	9	3 3 1			
144.723	8	4 2 0			

Table C.2: Powder diffraction file for copper oxide, Cu₂O.

5- 667 JCPDS-ICDD Copyright 1993 QM=*

Cu₂O

Copper Oxide Cuprite, syn

Rad: CuK α 1 Lambda: 1.5405 Filter: Ni d-sp:

Cutoff: Int: Diffractometer I/Icor:
 Ref: Swanson, Fuyat, Natl. Bur. Stand. (U.S.), Circ. 539, II 23 (1953)

Sys: Cubic S.G.: Pn3m (224)
 a: 4.2696 b: c: A: C:
 A: B: C: Z: 2 mp:
 Ref: Ibid.
 Dx: 6.11 Dm: SS/FOM: F13=56(.012,20)

Color: Violet-red

X-ray pattern at 26 C. Sample prepared at NBS, Gaithersburg, Maryland, USA by sintering CuCl and Na2CO2 at ~800 C, then leaching with water and drying. Spectroscopic analysis: <1% Ca, Si; <0.1% Al, Mg; <0.01% Ag, B, Ba, Fe, Ti; <0.001% Mn, Pb, Sn. Opaque mineral optical data on specimen from Liskeard, Cornwall, England, UK. Pattern reviewed by Martin, K., McCarthy, G., North Dakota State University, Fargo, North Dakota, USA, ICDD Grant-in-Aid (1990). Agrees well with experimental and calculated patterns. Additional weak reflection [indicated by brackets] was observed. Ag2O type. PSC: cP6. Mwt: 143.09. Volume[CD]: 77.83.

Strong lines: 2.47/X 2.14/4 1.51/3 1.29/2 3.02/1 1.23/1 0.98/1 0.95/1

13 reflections in pattern. Radiation= 1.54060

2-theta	Int.	h k l	2-theta	Int.	h k l
29.555	9	1 1 0			
36.419	100	1 1 1			
42.298	37	2 0 0			
52.455	1	2 1 1			
61.345	27	2 2 0			
[69.571]	1	3 1 0			
73.528	17	3 1 1			
77.326	4	2 2 2			
92.383	2	4 0 0			
103.705	4	3 3 1			
107.562	3	4 2 0			
124.228	3	4 2 2			
139.292	3	5 1 1			

Table C.3: Powder diffraction file for copper oxide, CuO.

41-254

JCPDS-ICDD Copyright 1993

QM=*

CuO

Copper Oxide

Tenorite, syn

Rad: CuK α 1 Lambda: 1.54056 Filter: Mono. d-sp: Guin. -114.6
 Cutoff: Int: Diffractometer I/Icor: 2.8
 Ref: Geyer, A., Eysel, W., Mineral. Petrograph. Institut der Universitaet
 Heidelberg, Germany, ICDD Grant-in-Aid, (1989)

Sys: Monoclinic S.G.: C2/c (15)
 a: 4.685 b: 3.423 c: 5.132 A: C:
 A: B: 99.52 C: Z: 4 mp:
 Ref: Asbrink, S., Norrby, L., Acta Crystallogr., Sec. B, 26 8 (1970)
 Dx: 6.51 Dm: 6.45 SS/FOM: F22=56(.011,35)

Color: Black

Sample from Merck, purity >99.0%. CuO type. Also called: melaconite. C.D. Cell: a=5.132, b=3.423, c=4.685, β =99.52, a/b=1.4993, c/b=1.3687, S.G.=A2/a (15). Si used as internal standard. PSC: mC8. To replace 5-661. Mwt: 79.55. Volume[CD]: 81.17. Strong lines: 2.52/X 2.31/X 2.53/6 1.87/3 1.51/2 1.41/1 1.38/1 1.58/1

22 reflections in pattern. Radiation= 1.54060

2-theta	Int.	h k l	2-theta	Int.	h k l
32.509	8	1 1 0	75.262	7	-2 2 2
35.438	60	0 0 2	80.191	2	-2 0 4
35.539	100	-1 1 1	82.378	4	-3 1 3
38.941	100	2 0 0	83.105	4	2 2 2
46.264	3	-1 1 2	83.687	4	4 0 0
48.743	25	-2 0 2	86.570	2	-4 0 2
53.466	7	0 2 0	89.818	5	-1 3 1
58.312	12	2 0 2			
61.549	16	-1 1 3			
65.823	12	0 2 2			
66.276	14	-3 1 1			
67.934	9	1 1 3			
68.147	14	2 2 0			
72.436	6	3 1 1			
74.990	6	0 0 4			

Table C.4: Powder diffraction file for perovskite barium titanate.

5- 626

JCPDS-ICDD Copyright 1993

QM=*

BaTiO

3

Barium Titanium Oxide

Rad: CuK α 1 Lambda: 1.5405 Filter: Ni d-sp:
 Cutoff: Int: Diffractometer I/Icor: 8.343
 Ref: Swanson, Fuyat, Natl. Bur. Stand. (U.S.), Circ. 539, 3 45 (1954)

Sys: Tetragonal S.G.: P4mm (99)
 a: 3.994 b: c: 4.038 A: C: 1.0110
 A: B: C: Z: 1 mp:
 Ref: Ibid.
 Dx: 6.012 Dm: SS/FOM: F30=19(.049,32)

Color: Colorless

X-ray pattern at 26 C. Sample from National Lead Company. CAS no.: 12047-27-7. Annealed at 1480 C in MgO. Spectroscopic analysis: <0.1% Bi, Sr; <0.01% Al, Ca, Fe, Mg, Pb, Si; <0.001% Mn, Sn. Inverts to cubic form at 120 C. Merck Index, 8th Ed., p. 122. PSC: tP5. Plus 10 additional reflections. Mwt: 233.23. Volume[CD]: 64.41.
 Strong lines: 2.83/X 2.31/5 2.00/4 1.63/4 3.99/3 1.64/2 4.03/1 2.02/1

40 reflections in pattern. Radiation= 1.54060

2-theta	Int.	h k l	2-theta	Int.	h k l
22.039	12	0 0 1	70.663	2	3 0 0
22.263	25	1 0 0	74.336	5	1 0 3
31.498	100	1 0 1	75.094	7	3 0 1
31.647	"	1 1 0	75.164	9	3 1 0
38.888	46	1 1 1	78.768	3	1 1 3
44.856	12	0 0 2	79.472	5	3 1 1
45.378	37	2 0 0	83.492	7	2 2 2
50.614	6	1 0 2	86.966	1	2 0 3
50.978	8	2 0 1	87.287	1	[3 0 2]
51.100	7	2 1 0	88.069	1	3 2 0
55.955	15	1 1 2	91.586	7	2 1 3

56.253	35	2 1 1	92.060	12	3 1 2
65.755	12	2 0 2	92.328	12	3 2 1
66.123	10	2 2 0	99.495	1	0 0 4
70.359	5	2 1 2	100.984	2	4 0 0
103.869	1	1 0 4			
104.502	1	2 2 3			
104.991	1	3 2 2			
105.362	1	4 1 0			
108.256	3	1 1 4			
108.946	1	3 0 3			
109.733	5	4 1 1			
113.556	2	3 1 3			
114.362	2	3 3 1			
117.506	3	2 0 4			

Table C.5: Powder diffraction file for perovskite strontium titanate.

35-734 JCPDS-ICDD Copyright 1993 QM=*

SrTiO
3

Strontium Titanium Oxide Tausonite, syn

Rad: CuKα1 Lambda: 1.5405 Filter: Ni d-sp: Diff.
Cutoff: Int: Diffractometer I/Icor: 6.222
Ref: Swanson, H., Fuyat, Natl. Bur. Stand. (U.S.), Circ. 539, 3 44 (1954)

Sys: Cubic S.G.: Pm3m (221)
a: 3.9050 b: c: A: C:
A: B: C: Z: 1 mp:
Ref: Ibid.
Dx: 5.12 Dm: SS/FOM: F18=47(.018,21)

Pattern taken at 25 C. Sample from Nat. Lead Co. Spectrographic analysis: <0.01% Al, Ba, Ca, Si; <0.001% Cu, Mg. Perovskite group, loperite subgroup. PSC: cp5. To replace 5-634 and 40-1500. Mwt: 183.52. Volume[CD]: 59.55.
Strong lines: 2.76/X 1.95/5 1.59/4 2.25/3 1.38/3 1.04/2 1.24/2 3.90/1

18 reflections in pattern. Radiation= 1.54060

2-theta	Int.	h k l	2-theta	Int.	h k l
22.783	12	1 0 0	123.832	10	4 2 0
32.424	100	1 1 0	135.423	6	3 3 2
39.985	30	1 1 1	150.147	9	4 2 2
46.485	50	2 0 0			
52.358	3	2 1 0			
57.796	40	2 1 1			
67.805	25	2 2 0			
72.545	1	3 0 0			
77.177	15	3 1 0			
81.724	5	3 1 1			
86.206	8	2 2 2			
95.131	16	3 2 1			
104.154	3	4 0 0			
113.613	10	4 1 1			
118.590	3	3 3 1			

Table C.6: Powder diffraction file for perovskite barium strontium titanate, $(\text{Ba}_{0.5}, \text{Sr}_{0.5})\text{TiO}_3$.

39-1395 JCPDS-ICDD Copyright 1993 QM=*

Ba Sr TiO
0.5 0.5 3

Barium Strontium Titanium Oxide Tausonite, barian, syn

Rad: CuK α 1 Lambda: 1.540598 Filter: Mono. d-sp: Diff.
Cutoff: 17.7 Int: Diffractometer I/Icor:
Ref: Wong-Ng, W., McMurdie, H., Paretzkin, B., Hubbard, C., Dragoo, A., NBS (USA), ICDD Grant-in-Aid, (1988)

Sys: Cubic S.G.: Pm3m (221)
a: 3.94710(7) b: c: A: C:
A: B: C: Z: 1 mp:
Ref: Wong-Ng, W. et al., Powder Diffraction, 4 116 (1989)
Dx: 5.63 Dm: SS/FOM: F21=97(.010,21)

Color: Yellowish white
Peak height intensities. The approximate temperature of data collection was 25 C. Stoichiometric amounts of BaTiO₃ and SrTiO₃ were mixed and heated overnight at 1000 C, 1300 C, and 1400 C with regrinding. The compound is isostructural with the high temperature form of BaTiO₃. Perovskite group, loparite subgroup. Ag, FP used as internal standards. PSC: cP5. Structure reference: 1. Edwards, J., Speiser, R., Johnston, H., J. Am. Chem. Soc., 73 2934 (1951). Mwt: 208.37. Volume[CD]: 61.49.

Strong lines: 2.79/X 1.61/8 1.97/7 2.28/6 1.40/6 1.06/5 1.25/5 3.95/4

21 reflections in pattern. Radiation= 1.54060

2-theta	Int.	h k l	2-theta	Int.	h k l
22.494	38	1 0 0	111.792	27	3 3 0
32.032	100	1 1 0	116.559	8	3 3 1
39.498	64	1 1 1	121.560	24	4 2 0
45.944	74	2 0 0	126.836	4	4 2 1
51.755	21	2 1 0	132.528	14	3 3 2
57.114	78	2 1 1	145.943	23	4 2 2
67.011	64	2 2 0			
71.674	10	3 0 0			
76.225	50	3 1 0			
80.679	20	3 1 1			
85.052	22	2 2 2			
89.459	3	3 2 0			
93.808	53	3 2 1			
102.630	8	4 0 0			
107.131	5	4 1 0			

Table C.7: Powder diffraction file for corundum alumina.

42-1468 JCPDS-ICDD Copyright 1993 QM=*

Al O
2 3

Aluminum Oxide Corundum, syn

Rad: CuK α 1 Lambda: 1.54056 Filter: Mono. d-sp: Diff.

Cutoff: 15.0 Int: Diffractometer I/Icor: 1.00
 Ref: Welton-Holzer, J., McCarthy, G., North Dakota State University, Fargo,
 North Dakota, USA, ICDD Grant-in-Aid, (1989)

Sys: Rhombohedral (Hex) S.G.: R-3c (167)
 a: 4.7588(1) b: c: 12.992(1) A: C: 2.7301
 A: B: C: Z: 6 mp: 2050°
 Ref: Ibid.
 Dx: 3.99 Dm: 4.05 SS/FOM: F30=221(.004,31)

ea: 1.7604 nwB: 1.7686 ey: Sign: - 2V:
 Ref: Winchell, A., Winchell, H., Microscopic Character of Artificial Inorg.
 Solid Sub., 60 (1964)
 Color: White

Peak height intensities. Sample is the National Institute of Standards and Technology
 corundum standard reference material 674. $\sigma(\text{Iobs}) \pm 0.01$. Al₂O₃ type. Corundum group,
 corundum subgroup. Also called: alumina. Also called: alundum. Also called: diamonite.
 Si used as internal standard. PSC: hR10. To replace 10-173 and validated by calculated
 pattern Z-860. Structure reference: Ishizawa, N. et al., Acta Crystallogr., Sec. B, 26
 228 (1980). Mwt: 101.96. Volume[CD]: 254.80.

Strong lines: 2.09/X 2.55/X 1.60/8 3.48/7 1.37/5 2.38/4 1.74/4 1.40/3

49 reflections in pattern. Radiation= 1.54060

2-theta	Int.	h k l	2-theta	Int.	h k l
25.577	70	0 1 2	76.882	13	1 0 10
35.151	97	1 0 4	77.237	6	1 1 9
37.785	42	1 1 0	80.426	2	2 1 7
41.685	1	0 0 6	80.695	5	2 2 0
43.363	100	1 1 3	83.219	1	3 0 6
46.184	1	2 0 2	84.369	4	2 2 3
52.559	42	0 2 4	85.147	<1	1 3 1
57.504	82	1 1 6	86.359	4	3 1 2
59.773	2	2 1 1	86.502	3	1 2 8
61.135	5	1 2 2	89.000	5	0 2 10
61.305	7	0 1 8	90.708	2	0 0 12
66.522	30	2 1 4	91.193	6	1 3 4
68.209	45	3 0 0	95.251	12	2 2 6
70.420	1	1 2 5	98.397	2	0 4 2
74.302	1	2 0 8	101.067	9	2 1 10
102.835	1	1 1 12	131.125	4	2 0 14
103.319	2	4 0 4	132.214	<1	3 2 7
109.544	<1	3 2 1	132.646	<1	2 1 13
109.872	<1	1 2 11	136.101	16	4 1 6
110.837	2	2 3 2			
110.998	2	3 1 8			
114.073	2	2 2 9			
116.105	9	3 2 4			
116.594	7	0 1 14			
117.843	5	4 1 0			
120.216	<1	2 3 5			
122.053	3	4 1 3			
124.602	2	0 4 8			
127.683	10	1 3 10			
129.894	4	3 0 12			

Table C.8: Powder diffraction file for reaction product of strontium oxide and alumina.

SrAl₂O₇SrO·2Al₂O₃

Strontium Aluminum Oxide

Rad: Cu Lambda: 1.54056 Filter: Ni d-sp:
 Cutoff: Int: Diffractometer I/Icor:
 Ref: Appendino, Rev. Int. Hautes Temp. Refract., 9 297 (1972)

Sys: Monoclinic S.G.:
 a: 13.04 b: 9.00 c: 5.55 A: C:
 A: B: 106.31 C: Z: mp:
 Ref: Ibid.
 Dx: Dm: SS/FOM: F30=13(.023,102)

Metastable modification. Stable near 1400 C. C.D. Cell: a=12.657, b=9.000, c=5.550, β=98.58, a/b=1.4063, c/b=0.6167. Mwt: 307.54. Volume[CD]: 625.14.
 Strong lines: 3.54/X 2.77/8 2.46/8 6.25/8 3.65/7 2.00/5 4.50/4 2.92/4

67 reflections in pattern. Radiation= 1.54060

2-theta	Int.	h k l	2-theta	Int.	h k l
12.114	6	1 1 0	33.653	40	0 0 2
14.159	75	2 0 0	33.995	40	-1 3 1
18.947	8	-1 1 1	34.882	35	-4 2 0
19.713	40	0 2 0	36.116	7	1 3 1
22.206	17	1 1 1	36.496	80	-5 1 1
23.517	3	3 1 0	36.837	15	-3 3 0
24.367	65	2 2 0	37.785	5	1 1 2
25.136	100	-3 1 1	39.277	4	0 2 2
25.956	10	0 2 1	40.004	6	-3 2 2
27.250	35	-2 2 1	40.359	8	2 0 2
28.494	10	4 0 0	43.254	35	3 3 1
30.591	40	1 3 0	43.363	12	6 0 0
31.855	35	2 2 1	44.508	30	-1 3 2
32.304	80	-1 0 2	45.330	50	2 2 2
32.619	7	-2 0 2	46.159	7	-3 3 2
47.150	18	-6 0 2	59.472	4	-8 0 2
47.675	12	1 3 2	60.026	25	4 3 2
49.874	15	4 4 0	60.198	18	7 3 0
50.917	12	2 3 2	61.526	5	-2 5 2
51.008	12	7 0 0	61.936	3	3 4 2
51.533	2	-4 0 3	62.634	6	7 2 1
53.514	6	-2 2 3	63.204	4	3 1 3
54.025	4	-1 2 3	63.541	5	-6 4 2
54.972	6	1 5 1	63.785	4	2 6 0
55.116	10	1 1 3	64.328	4	-1 6 1
55.623	18	0 2 3	65.135	5	-2 6 1
56.141	3	-4 4 2	66.817	18	8 0 1
58.195	8	1 2 3	67.034	14	6 4 1
58.888	15	7 0 1	67.362	8	7 3 1
59.179	20	-4 5 0	67.805	5	-5 5 2
69.231	5	-4 1 4			
69.407	4	1 4 3			
70.118	3	-9 2 2			

70.299	30	3 5 2		
70.724	5	-7 3 3		
72.675	4	-6 0 4		
73.662	4	-8 4 0		

Table C.9: Powder diffraction file for reaction product of strontium titanate and alumina.

37-1231 JCPDS-ICDD Copyright 1993 QM=i

SrTi Al O
3 8 19

Strontium Aluminum Titanium Oxide

Rad: CuK α Lambda: 1.54178 Filter: Mono. d-sp: Diff.
Cutoff: Int: Diffractometer I/Icor:
Ref: Morgan, P., Rockwell International Science Center, California, USA,
Private Communication, (1985)

Sys: Monoclinic S.G.: C*/c
a: 22.7020 b: 11.0639 c: 9.7689 A: 2.0519 C: 0.8830
A: B: 98.652 C: Z: 8 mp:
Ref: Morgan, P., Koutsoutis, M., J. Mater. Sci., 4 321 (1985)
Dx: 4.114 Dm: SS/FOM: F30=12(.040,64)

Color: White

Coprecipitation and firing at 1400-1600 C. Cell constants refined from higher angle lines with coincident hkl values with isotypes CaTi3Al8O19 and LaTi2Al9O19. For lines over 40° 2theta CuK α 1 was used. Si used as external standard. PSC: mC248. Mwt: 751.16. Volume[CD]: 2425.76.

Strong lines: 2.85/G 2.78/G 2.09/G 2.38/G 1.40/G 1.89/G 2.15/G 3.12/G

152 reflections in pattern. Radiation= 1.54060

2-theta	Int.	h k l	2-theta	Int.	h k l
7.865	21	2 0 0	24.472	31	1 3 0, 0 2 2
8.959	42	1 1 0	24.763	4	3 1 2
13.250	4	1 1 1	25.337	10	4 2 1
14.274	1	3 1 0	26.413	22	1 3 1
16.010	3	3 1 -1	26.941	13	3 3 0
17.952	2	3 1 1	27.895	46	6 0 -2, 3 3 -1
18.458	4	0 2 1	28.614	156	1 1 -3
19.594	75	2 2 -1	29.127	80	3 3 1
20.703	7	2 2 1	29.662	55	3 1 -3
21.034	15	2 0 2	30.257	6	5 1 2
21.413	6	5 1 0	30.388	5	1 3 -2
22.088	11	5 1 -1	31.406	999	5 3 0, 6 2 1
22.446	12	4 0 -2	31.829	111	7 1 1
23.513	36	4 2 -1	32.145	251	2 2 -3
23.845	3	6 0 0	32.403	142	6 0 2
32.733	85	5 1 -3	40.203	25	10 0 0
33.400	41	2 4 0	41.313	78	6 0 -4
33.655	70	5 3 1	42.074	182	4 4 2
33.852	88	3 3 2	42.964	128	4 0 4, 6 2 3
34.064	28	2 2 3	43.277	226	6 4 -2

34.446	12	8 0 -2	44.189	10	7 3 -3
35.030	9	2 4 1	44.774	6	11 1 -1
35.864	65	8 2 -1	45.006	4	3 3 -4
36.225	22	4 4 0	45.773	48	8 0 -4
36.828	96	-9 1 1	46.468	53	6 4 2
37.219	38	0 0 4	47.174	6	10 0 2
37.776	214	2 4 -2, 1 1 -4	47.430	19	-3 1 5
38.286	4	4 0 -4	47.817	109	6 0 4
38.962	26	1 1 4	48.042	193	3 3 4
39.506	22	9 1 1	48.666	4	10 2 -3
49.119	2	5 1 -5	59.419	11	14 2 -1, 6 2 5
49.846	13	11 1 -3	60.065	14	14 2 0, 7 1 5
51.143	16	11 3 0	60.454	133	7 5 3
51.261	18	2 6 1	60.956	5	3 7 1, 7 5 -4
51.946	68	8 4 2	61.317	23	13 3 1
52.173	7	4 6 0	61.474	36	9 3 -5, 6 2 -6
53.139	20	13 1 -1	62.124	6	1 7 2
53.809	31	10 4 -2	62.510	20	5 5 4, 5 7 -1
54.832	18	4 6 -2	63.562	1	5 7 1
55.261	18	12 0 2	64.089	3	8 4 4
56.158	58	13 1 1	64.816	72	4 2 6
57.154	80	8 4 -4	65.531	150	12 4 2
57.768	11	14 0 -2	66.663	196	16 0 0
58.367	13	10 4 2	67.380	11	7 7 1
58.509	20	13 3 -1, 5 1 -6	67.785	128	14 4 -2
68.526	6	10 2 -6, 5 1 -7	77.600	11	18 2 -1
69.387	5	-2 2 7	78.521	11	14 6 -1
69.778	4	8 6 3	79.927	5	9 5 5
70.484	7	[-9 7 0]	80.818	4	7 7 4
70.985	6	-2 8 2	81.339	5	19 1 -2, 2 0 8
71.212	8	4 8 1	82.010	4	19 1 0
71.873	8	3 1 7	82.227	5	13 7 -1
72.833	8	6 8 0	82.516	6	6 8 -4
73.375	7	14 4 2	83.595	8	4 8 4
73.876	5	11 3 -6, 10 6 -4	84.833	2	9 7 -5
74.273	8	14 4 -4	85.374	8	19 3 -1
75.326	15	4 2 7	86.682	20	20 0 0
75.712	19	4 8 -3	87.982	2	2 8 5
76.176	6	15 5 -1	88.482	2	6 8 -5, 9 9 -1
77.374	7	11 3 5	89.130	3	
89.833	10	20 2 -3	101.179	37	3 11 0
90.294	13	18 2 3	102.983	4	2 4 9
90.912	4	19 3 -4	103.965	3	20 2 -6
91.553	3	21 1 -1, 8 8 4	104.781	6	3 11 2
92.928	9	12 8 2, 19 3 2	105.283	5	16 8 1, 21 5 -2
93.264	13	4 6 7	106.564	4	1 11 -3
94.018	9	19 1 3	107.525	4	13 9 -4
94.425	13	6 10 1	107.875	16	20 6 -3
94.755	12	20 4 -2	108.327	13	15 7 -6
95.329	22	10 6 -7	109.671	7	10 4 8
96.180	7	2 8 6	111.980	10	20 2 -7
96.880	6	8 10 -1	113.684	6	14 4 7
97.221	18	10 8 4	114.783	6	11 9 -6, 22 4 2
98.914	3	4 8 6	117.978	13	18 8 -4, 21 3 4

100.447	11	6 4 -9	119.903	7	8 10 -6
120.836	5	24 4 0			
122.469	27	25 1 1			

Table C.10: Powder diffraction file for hexagonal metallic zinc.

4- 831 JCPDS-ICDD Copyright 1993 QM=*

Zn

Zinc Zinc, syn

Rad: CuK α 1 Lambda: 1.5405 Filter: Ni d-sp:
Cutoff: Int: Diffractometer I/Icor: 3.80
Ref: Swanson, Tatge, Natl. Bur. Stand. (U.S.), Circ. 539, 1 16 (1953)

Sys: Hexagonal S.G.: P63/mmc (194)
a: 2.665 b: c: 4.947 A: C: 1.8563
A: B: C: Z: 2 mp: 420°
Ref: Ibid.
Dx: 7.14 Dm: 7.05 SS/FOM: F20=55(.018,20)

ea: nwB: 2.58 ey: Sign: 2V:
Ref: Winchell, Elements of Optical Mineralogy, 1 (1927)
Color: Bluish white
Pattern taken at 26 C. Sample from New Jersey Zinc Company, Sterling Hill, New Jersey, USA. CAS no.: 7440-66-6. Spectroscopic analysis shows faint traces of Pb, Cu, Mg, Si. Mg type. Zinc group. PSC: hP2. Mwt: 65.38. Volume[CD]: 30.43.
Strong lines: 2.09/X 2.47/5 2.31/4 1.69/3 1.34/3 1.17/2 1.33/2 1.12/2

20 reflections in pattern. Radiation= 1.54060

2-theta	Int.	h k l	2-theta	Int.	h k l
36.297	53	0 0 2	124.054	5	2 1 0
38.993	40	1 0 0	127.493	9	2 1 1
43.233	100	1 0 1	131.847	2	2 0 4
54.337	28	1 0 2	138.219	1	0 0 6
70.058	25	1 0 3	138.955	9	2 1 2
70.663	21	1 1 0			
77.030	2	0 0 4			
82.105	23	1 1 2			
83.767	5	2 0 0			
86.560	17	2 0 1			
89.923	3	1 0 4			
94.903	5	2 0 2			
109.133	8	2 0 3			
115.803	6	1 0 5			
116.390	11	1 1 4			

Table C.11: Powder diffraction file for zinc oxide.

36-1451 JCPDS-ICDD Copyright 1993 QM=*

ZnO

Zinc Oxide Zincite, syn

Rad: CuK α 1 Lambda: 1.540598 Filter: Mono. d-sp: Diff.

Cutoff: 17.7 Int: Diffractometer I/Icor:
 Ref: McMurdie, H. et al., Powder Diffraction, 1 76 (1986)

Sys: Hexagonal S.G.: P63mc (186)
 a: 3.24982(9) b: c: 5.20661(15) A: C: 1.6021
 A: B: C: Z: 2 mp:
 Ref: Ibid.
 Dx: 5.68 Dm: SS/FOM: F27=131(.007,29)

ea: nwB: 2.013 ey: 2.029 Sign: + 2V:
 Ref: Dana's System of Mineralogy, 7th Ed., I 504
 Color: Colorless

Peak height intensities. The approximate temperature of data collection was 26 C. References to other early patterns may be found in reference (5). The sample was obtained from the New Jersey Zinc Co., Bethlehem, Pennsylvania, USA. CAS no.: 1314-13-2. The structure was determined by Bragg (1) and refined by Abrahams, Bernstein (2). $\sigma(I_{obs}) = \pm 1$. A high pressure cubic NaCl-type of ZnO is reported by Bates et al. (3) and a cubic, sphalerite type is reported by Radczewski, Schicht (4). SZn type. Wurtzite group, zincite subgroup. Also called: chinese white. Also called: zinc white. PSC: hP4. To replace 5-664 (5). Structure references: 1. Bragg, W., Philos. Mag., 39 647 (1920); 2. Abrahams, S., Bernstein, J., Acta Crystallogr., Sec. B, 25 1233 (1969). Polymorphism references: 3. Bates, C., White, W., Roy, R., Acta Crystallogr., Sec. B, 137 993 (1962); 4. Radczewski, O., Schicht, R., Naturwissenschaften, 56 514 (1969). Additional powder pattern reference: 5. Swanson, H., Fuyat, R., Natl. Bur. Stand. (U.S.), Circ. 539, 2 25 (1953). Mwt: 81.38. Volume[CD]: 47.62. Strong lines: 2.48/X 2.81/6 2.60/4 1.62/3 1.48/3 1.91/2 1.38/2 1.36/1

27 reflections in pattern. Radiation= 1.54060

2-theta	Int.	h k l	2-theta	Int.	h k l
31.770	57	1 0 0	98.613	4	1 1 4
34.422	44	0 0 2	102.946	2	2 1 2
36.253	100	1 0 1	104.134	5	1 0 5
47.539	23	1 0 2	107.430	1	2 0 4
56.603	32	1 1 0	110.392	3	3 0 0
62.864	29	1 0 3	116.279	8	2 1 3
66.380	4	2 0 0	121.572	4	3 0 2
67.963	23	1 1 2	125.188	1	0 0 6
69.100	11	2 0 1	133.932	3	2 0 5
72.562	2	0 0 4	136.520	1	1 0 6
76.955	4	2 0 2	138.513	2	2 1 4
81.370	1	1 0 4	142.918	3	2 2 0
89.607	7	2 0 3			
92.784	3	2 1 0			
95.304	6	2 1 1			

D. REOX STUDY $C-V$ RESULTS

Results of systematic reox anneals from one BST/Cu sample from a 90 min. deposition from a $(\text{Ba}_{0.75}, \text{Sr}_{0.25})\text{TiO}_3$ target. $C-V$ data are collected at 100 kHz and 0.05 V oscillation level. All data are plotted on identical scale and each figure is labeled with the O_2 pressure in Torr (T) and the furnace temperature in $^\circ\text{C}$ (C). All reox anneals were for 30 minutes. Shown in the data are trends representing minimized dielectric loss and increased tunability for optimum $p\text{O}_2$ - T conditions.

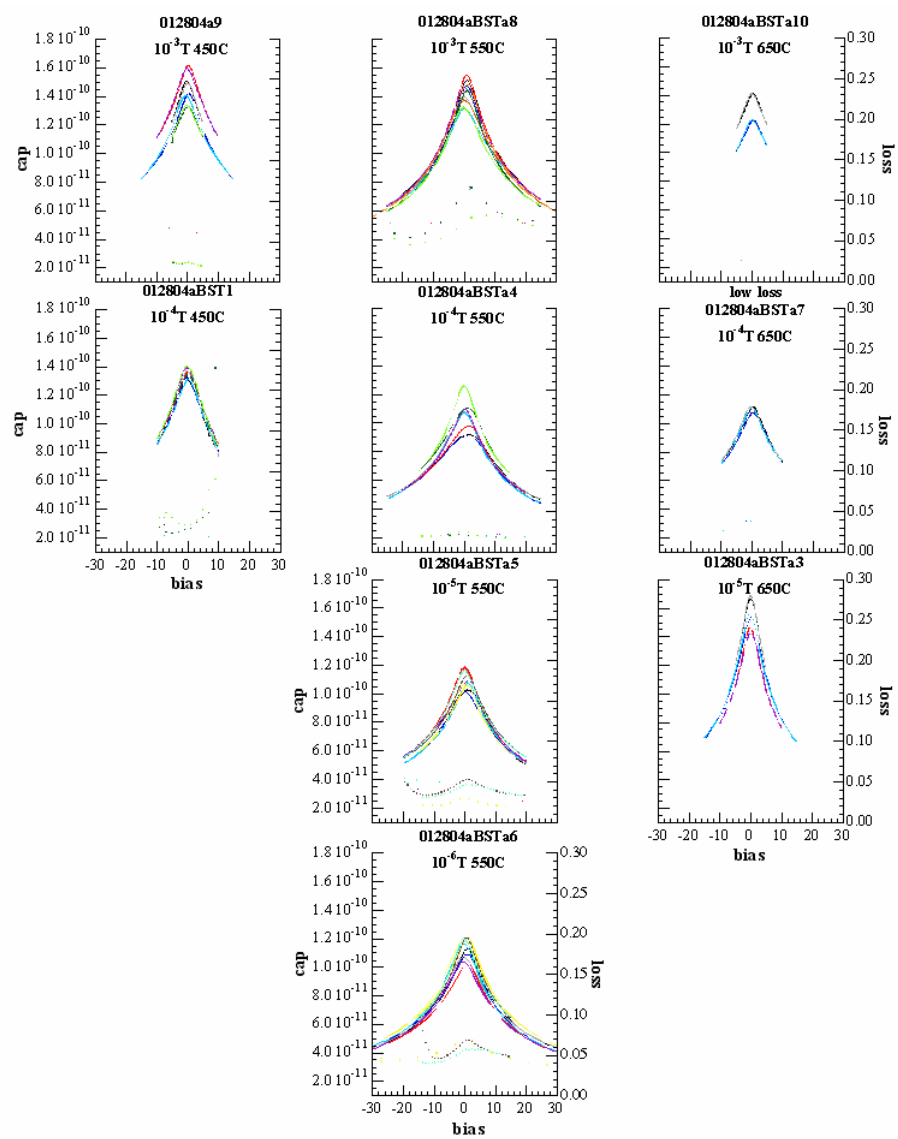


Figure D.1: C - V data from sample reoxed by a range of pO_2 - T combinations.

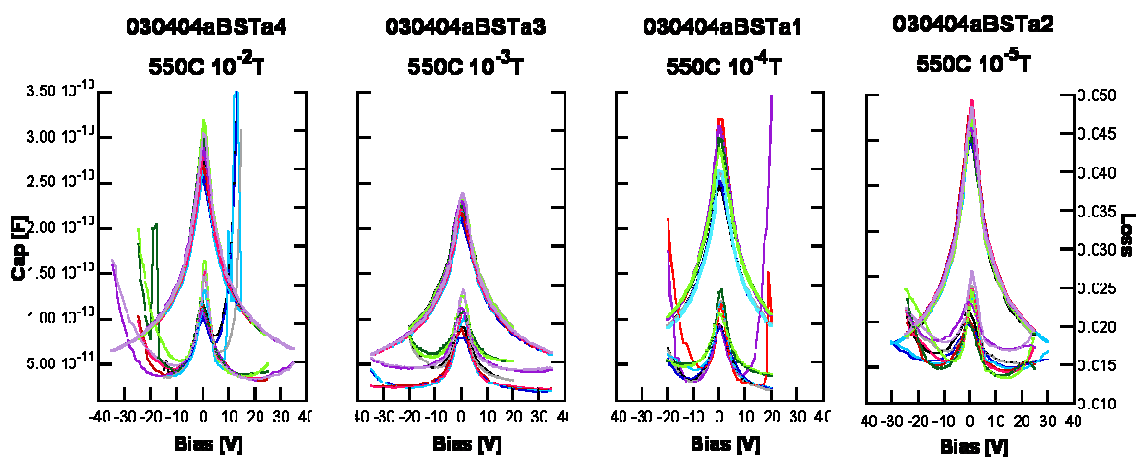


Figure D.2: Similar data set to figure D.1 for a different sample of identical composition and thickness. Reox anneals were all performed at 550 °C and total O_2 systematically varied.

E. BST-ULTRAFOIL THICKNESS STUDY: RAW $C-V$ DATA

Raw $C-V$ data used to assess optimum UltraFoil thickness versus BST thickness to achieve optimum BST/Cu dielectric properties. Data were collected at 100 kHz and 0.05 V oscillation level.

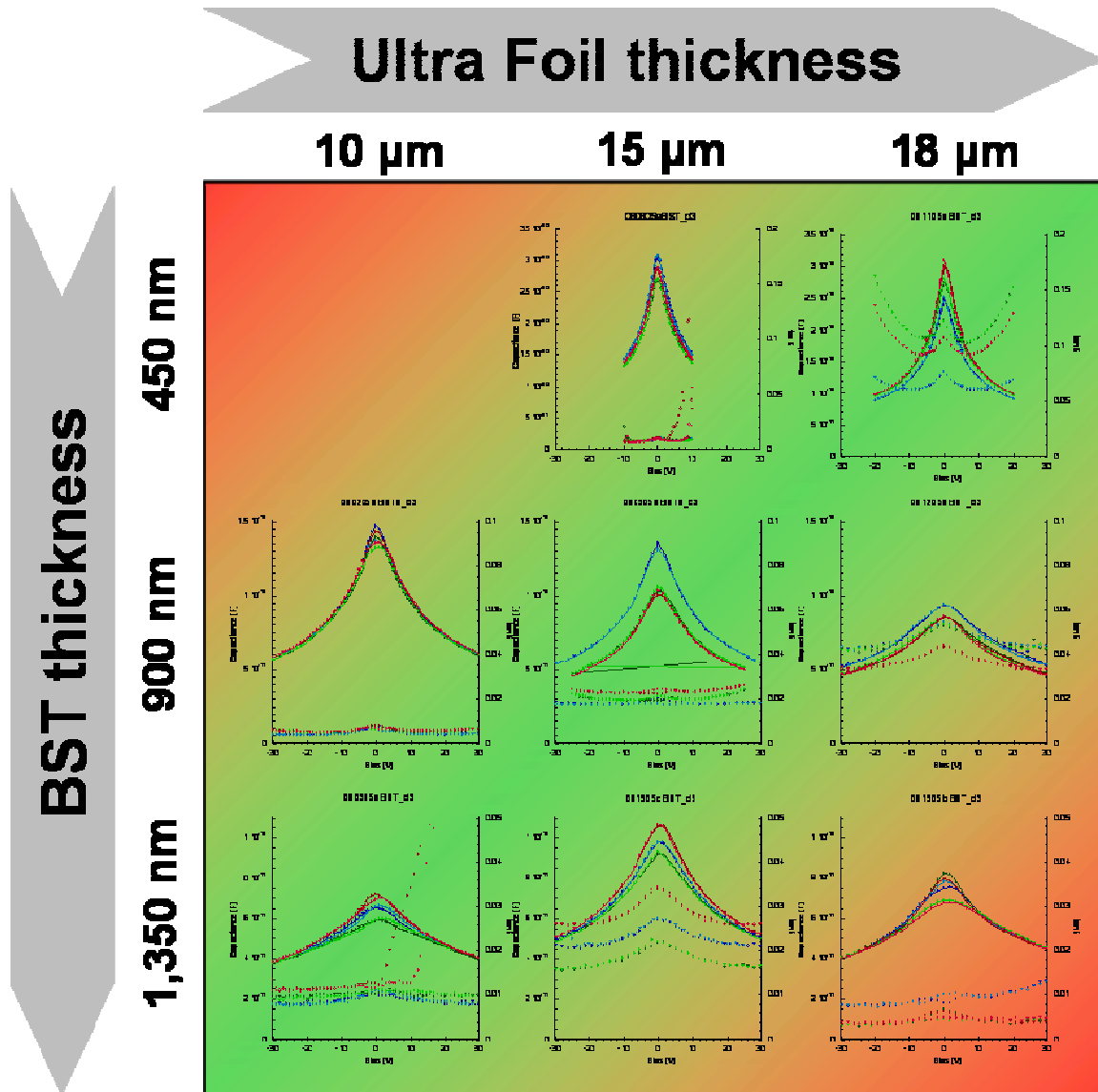


Figure E.1: Raw $C-V$ data for BST thickness of 450 - 1350 nm on UltraFoil substrates 10 - 18 μm . Data along row in the figure are plotted on the sample capacitance scale and all plots have a voltage range of -30 to 30 V.